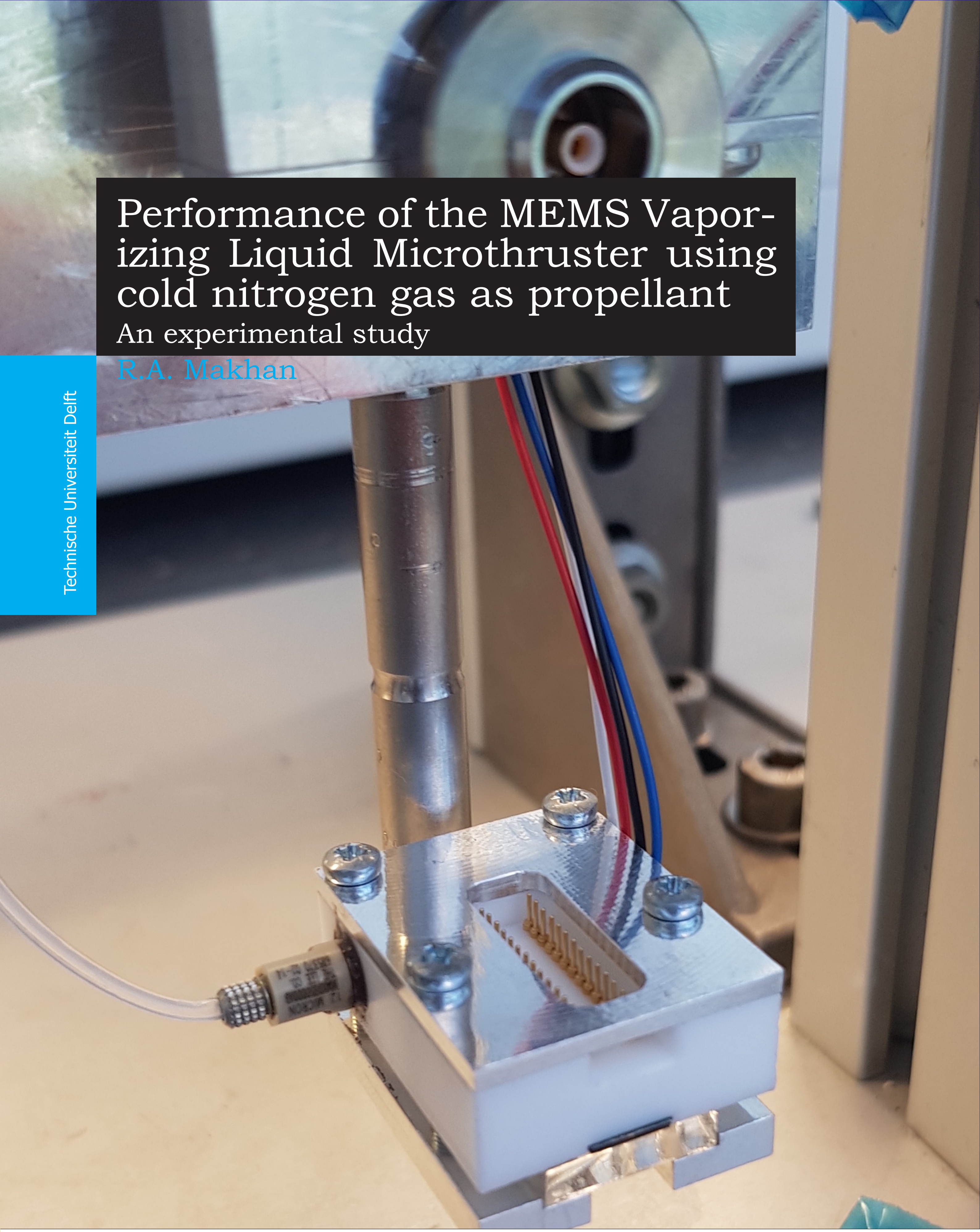

Performance of the MEMS Vaporizing Liquid Microthruster using cold nitrogen gas as propellant

An experimental study

R.A. Makhan

Technische Universiteit Delft

Delft University of Technology

Challenge the future

Performance of the MEMS Vaporizing Liquid Microthruster using cold nitrogen gas as propellant

An experimental study

Delft University of Technology
Faculty of Aerospace Engineering

December 13, 2018

by

R.A. Makhan 4081102

Supervisor: B.T.C. Zandbergen

Preface

This thesis concludes the final phase of my master in space engineering. Though all the difficult times and all the challenges that were opposed upon me, the overall experience has been great and I am honored that I had the opportunity to make a contribution to the space engineering department of the faculty of Aerospace Engineering.

I would like to express my deepest thanks to all the people that have supported me in getting to this point in my life. I would like to thank all my fellow ”Space Penguins”, who helped me during my thesis project and made it much more fun. I would specifically like to thank the Space Penguin Didier Maxence, with whom I’ve spent many hours working in the cleanroom and who provided a lot of support during my experiments. Furthermore, I would like to thank my fellow students and friends, who made the past few years at the university a wonderful experience. During my thesis project I also met the love of my life, my future wife, and words cannot describe the value of the support that she gave to me.

Finally, I would like to especially thank:

- Barry Zandbergen, my supervisor, who helped me in maturing into a real engineer and more importantly: who provided me support on every imaginable aspect related to my thesis and life in general, while being really understanding and patient.
- Marsil de Athay de Costa e Silva, a Ph.D. student who practically supervised me during my whole thesis project.
- Dadui Cordeiro Guerrieri, another Ph.D. student who also supported me a lot during my thesis.
- Mehmet Sevket Uludag, the supervisor of the cleanroom at the space engineering department, who helped out with everything related to hardware and the cleanroom.
- Frans Oostrum, the supervisor of the Physics and Chemistry Lab, who helped out with the microscopic tests.

May it be my supervisors and fellow students, or my friends, family and loved ones, all have helped me in some way for which I am truly grateful! As for the people reading this thesis: I hope it will be a pleasant experience for you and that you can gain something valuable from it!

Rajeev A. Makhan
Delft, December 2017

Abstract

TU Delft has successfully demonstrated miniaturization of spacecrafts with the Delfi-C3 and Delfi-n3Xt. The Delfi-n3Xt included the T3μPS, which is a micro-propulsion system based on cold gas thrusters. Since micro-propulsion systems can increase mission capabilities (e.g. formation flying), TU Delft is currently researching improved micro-propulsion systems, on of which is a micro-resistojet that can increase the performance by adding heat to the propellant. The micro-resistojet, created by MEMS (Micro-Electro-Mechanical Systems) technology, was called the MEMS - Vaporizing Liquid Microthruster (VLM) chip as it is intended to vaporize liquid water with the heaters within this chip.

Several master students of TU Delft performed thesis studies related to the MEMS-VLM chip, but more research was still needed before a flight model could be created. For example, there were many problems with the (previous) 2nd gen. MEMS-VLM chip and the previous interface that was used to connect it to the electrical and feed system. Also, the nozzle performance was low ($0.2 - 0.3[-]$) compared to results found in literature. Therefore, the 3rd gen. MEMS-VLM chip and the 1st gen. interface were manufactured. Furthermore, it was found in literature that a low nozzle performance could be improved by operating at higher Reynolds numbers.

The aim of the thesis project was therefore to investigate the relationship between the throat Reynolds number and the performance characteristics of the 3rd gen. MEMS-VLM chip. This was translated to the following research question: *"What do experiments, within an accuracy of 10%, reveal about the influence of different throat Reynolds numbers on the performance characteristics by controlling the operating conditions of the 3rd gen. MEMS-VLM chip?"* This research question was expanded and translated into subgoals and explored in this thesis study. This was done by performing thrust bench tests with cold nitrogen gas during which the thrust force, mass flow, chamber pressure and chamber temperature were measured. Note that the following preliminary tests were also important: calibration of the instruments and sensors, optical characterization tests and leak tests. The preliminary tests were needed to verify different components of the MEMS-VLM chip and the set-up of the thrust bench test. This makes these tests equally important as the thrust bench test.

At the end of the thesis study the following conclusions were made. The main research question could be partially answered. The accuracy of $10[\%]$ was found to be an overestimation since for the nozzle quality (and Isp quality) the uncertainties were between $15 - 25[\%]$ and despite the high uncertainty a relationship was established between the throat Reynolds number and the nozzle quality: increasing the Reynolds number from $600[-]$ to $2000[-]$ increased the nozzle quality from $0.19[-]$ to $0.60[-]$. Including viscous loss and divergence loss corrections (applied to ideal rocket theory) resulted in a nozzle quality between $0.37[-]$ and $0.82[-]$. As for the relationship with the discharge factor, this range increased between $0.77 - 0.91[-]$, which corresponded well to the predicted range of $0.93 - 0.97[-]$ based on an analytical equation found in literature. The corresponding operating conditions were as follows: the temperature was uncontrolled and on average at $295[K]$, while the pressure range was controlled and varied between $2[bar]$ and $5[bar]$ with increments of $1[bar]$. This indicates that there is still room for future experiments, where for example the heater influence is investigated with liquid water as propellant. Furthermore, it is still unclear why the experimental nozzle performance is lower compared to data found in literature. A hypothesis is that the 2D conical design of the MEMS-VLM chip is greater influenced by boundary layer formation. However, it can be concluded that increasing the Reynolds number is recommended in order to improve the nozzle performance.

Contents

Glossary

List of Acronyms

DAQ

Data Acquisition System 23, 38, 43, 67, 71, 72, 73, 129

DASML

Delft Aerospace Structures and Materials Laboratory 30

GPF

General Purpose Feed system xix, 22, 23, 43, 58, 59, 61, 63, 65, 73, 85

MEMS

Micro-Electro-Mechanical Systems 1

PCB

Printed Circuit Board xix, 6, 65, 73, 119, 120, 121, 129

PSU

Power Supply Unit 23, 37, 38, 40, 43, 66, 73, 116, 129

RMSE

Root Mean Square Error 49, 51

TU Delft

Delft University of Technology 1

VLM

Vaporizing Liquid Microthruster 1

VTDC

Varying Turn-Density Coil xiii, xviii, 4, 21, 37, 38, 39, 40, 41, 43, 46, 51, 52, 53, 86, 88, 89, 129

List of Symbols

FCF Force correction factor [-] vii, xiii, 21, 53, 52, 53, 89
P_c Chamber pressure [Pa] xv, xx, 12, 18, 19, 22, 55, 56, 58, 66, 79, 93, 95, 96, 97, 98
P_{int} Measured absolute pressure in the interface [bar] xv, 66, 67, 73, 77, 79, 80, 81, 88, 90, 93, 96
$(\dot{m})_{exp}$ Experimental mass flow [mg/s] xv, xx, 14, 18, 22, 58, 77, 85, 90, 94, 95, 96, 98, 100
$(\dot{m})_{adj.}$ Adjusted experimental mass flow [mg/s] xv, xx, 94, 95, 96, 98, 100, 104
C_A Divergence loss factor [-] xvii, 15
$(C_F)_{visc\_loss}$ Theoretical thrust coefficient including viscous loss [-] xvii, 16, 104, 106
R^* Radius of curvature of the nozzle throat section [m] xvii, 16, 17, 100, 101
R_t Radius of the nozzle throat [m] xvii, 16, 17, 100
W_t Nozzle throat width [μm] xvii, 16, 29, 32, 33, 35, 100

Δ_{disp}	Change average displacement target w.r.t. displacement sensor $[\mu m]$	xviii, 37, 49, 50, 51, 86, 88, 89
$(\dot{m})_{ideal}$	Theoretical mass flow [mg/s]	xx, 14, 55, 56, 79, 94, 95, 96, 98, 101
$(F)_{exp}$	Experimental thrust force [mN]	xx, 18, 58, 77, 78, 86, 90, 96, 97, 143
$(F)_{ideal}$	Theoretical thrust force [mN]	xx, 55, 56, 78, 79, 96, 97
$(I_{sp})_{adj.}$	Adjusted specific impulse [s]	xx, 96, 98
$(I_{sp})_{ideal}$	Theoretical specific impulse [s]	xx, 14, 55, 56, 96, 98
$(R_e)_{exp}$	Throat Reynolds number based on experimental mass flow [-]	xx, xxi, 93, 100, 101, 102, 103, 104, 106
C_d	Nozzle discharge factor [-]	xx, 1, 2, 14, 16, 18, 19, 22, 29, 35, 55, 100, 101, 102
A_t	Nozzle throat area $[m^2]$	5, 12, 19, 29, 32, 33, 35
A_e	Nozzle exit area $[m^2]$	5, 12, 19, 29, 33, 35
AR	Area ratio: nozzle exit area over throat area $[-]$	5, 14, 15, 29, 32, 33
P_w	Wetted perimeter $[m]$	5, 14, 29, 33
D_H	Hydraulic diameter [m]	5, 14, 29, 32, 33
F	Thrust force [N]	12, 19, 55
$\dot{m}$	Mass flow [kg/s]	12, 19, 55
V_{eq}	Equivalent exhaust velocity [m/s]	12
V_e	Propellant exhaust velocity [m/s]	12
P_e	Nozzle exit pressure [Pa]	12
P_a	Ambient pressure [Pa]	12, 43, 55, 56, 58, 69, 71, 73, 77, 78, 79, 90
c^*	Characteristic velocity [m/s]	12
R_a	Universal gas constant [J/mol/K]	12
M	Molar mass [kg/mol]	12
T_c	Chamber temperature [K]	12, 55, 56, 58, 66, 81
R	Specific gas constant [J/kg/K]	12, 81
I_{sp}	Specific impulse [s]	12
g_0	Gravitational acceleration on Earth $[m/s^2]$	12
R_e	Reynolds number in the nozzle throat [-]	13, 14, 18, 19
$(A_t)_{eff}$	Effective nozzle throat area $[m^2]$	14
$(A_t)_{ideal}$	Geometrical nozzle throat area $[m^2]$	14
$(C_F)_{exp}$	Experimental thrust coefficient [-]	14, 18, 19, 103, 104, 106
$(C_F)_{ideal}$	Theoretical thrust coefficient [-]	14, 19, 96, 103, 104, 106
$C_F{}^\circ$	Characteristic thrust coefficient [-]	14
$(I_{sp})_{exp}$	Experimental specific impulse [s]	14, 22, 96
$(c^*)_{exp}$	Experimental characteristic velocity [m/s]	14, 96
$(c^*)_{ideal}$	Theoretical characteristic velocity [m/s]	14, 81, 96
T_t	Isentropic throat temperature [K]	14, 93
T_{tot}	Total temperature [K]	14
R_{mod}	Modified Reynolds number used for the Cd calculation of Tang&Fenn [-]	16, 17, 100
$(C_d)_{bd\_loss}$	Discharge factor including throat boundary layer loss [-]	16, 17, 94, 100, 101
W_{nd}	Nozzle divergent width $[\mu m]$	29, 32, 33, 35
h_t	Nozzle throat height $[\mu m]$	29, 33, 35
h_{nd}	Nozzle divergent height $[\mu m]$	29, 33
L_{nc}	Nozzle convergent length $[\mu m]$	29, 33, 35
L_{nd}	Nozzle divergent length $[\mu m]$	29, 32, 33, 35
W_{nc}	Nozzle convergent width $[\mu m]$	29, 33, 35
R^*	Angle between convergent and divergent part of the nozzle $[^\circ]$	29, 32, 33, 35
I	Current provided by the SM7020-D PSU [A]	37, 49
$F_{magnetic}$	Magnetic force produced by the VTDC actuactor [mN]	37, 49
X_{disp}	Measured displacement target w.r.t. displacement sensor $[\mu m]$	43, 49, 73, 77, 86, 89, 143
$(\dot{m})_{corr.}$	Tang&Fenn correction for ideal mass flow [mg/s]	56, 94, 95
$(F)_{corr.}$	Spisz, divergence loss and Tang&Fenn correction for ideal thrust force [mN]	56
$(I_{sp})_{corr.}$	Divergence loss and Tang&Fenn correction for ideal thrust force [mN]	56
$(R_e)_{ideal}$	Throat Reynolds number based on ideal mass flow [-]	56
$\dot{V}$	Measured volumetric flow rate in the feed system [mln/min]	63, 73, 77, 84

A	Temperature difference between T1 and T2 [K]	64
P	Constant of proportionality $[s^2 \cdot K^2/kJ^2]$ [25]	64
Cp	Specific heat at constant pressure $[kJ/kg \cdot K]$	64
T_{int}	Measured temperature in the interface [K]	66, 67, 73, 77, 81, 83, 90, 93
$\dot{V}_{corrected}$	Corrected volumetric flow rate in the feed system [mln/min]	84
R_{N2}	Specific gas constant for nitrogen gas [J/kg/K]	93
$(C_F)_{adj.}$	Adjusted experimental thrust coefficient [-]	96
$(C_F)_{div\_loss}$	Theoretical thrust coefficient including divergence loss [-]	104, 106
$(C_F)_{corrected}$	Theoretical thrust coefficient including viscous and divergence loss [-]	104, 106
SEM	standard error of the mean (unit depends on measured parameter)	79
std	standard deviation of the measurements (unit depends on measured parameter)	79
N	sample size or number of measurements [-]	79

γ_{N2}	Specific heat ratio of nitrogen gas [-]	xiv, 93
Γ_{N2}	Vandenkerckhove function applied for nitrogen gas [-]	xiv, 93
μ_{t_N2}	Dynamic viscosity of nitrogen gas at the nozzle throat $[Pa{\cdot}s]$	xiv, 93, 100
θ_{nd}	Nozzle divergence half angle [°]	xvii, 15, 29, 32, 33, 35, 104
γ	Specific heat ratio [-]	xvii, 12, 16, 17, 100
ξ_b	Heating quality [-]	xx, 12, 14, 55, 100, 103
ξ_F	Nozzle quality [-]	xx, xxi, 1, 2, 14, 19, 29, 55, 96, 100, 103, 104, 106
ξ_s	Isp quality [-]	1, 2, 14, 18, 19, 55, 96, 100
Γ	Vandenkerckhove function [-]	12, 81
μ_t	Dynamic viscosity at isentropic throat temperature $[Pa{\cdot}s]$	14
θ_{nc}	Nozzle convergence half angle [°]	29, 32, 33, 35
ρ_{N2_n}	Density viscosity of nitrogen gas at normal conditions $[kg/m^3]$	63, 85
ΔT	Temperature difference between T1 and $T2$ [K]	64
δ	Absolute error (unit depends on measured parameter)	79
ϵ	Relative error [%]	79

List of Tables

List of Figures

1

Introduction

1.1. Background

Delft University of Technology (TU Delft) has successfully demonstrated miniaturization of spacecrafts with the nano-satellites Delfi-C3 and Delfi-n3Xt. Further miniaturization was done by TU Delft with the Delfi-PQ, which is a pico-satellite. As for the miniaturization of propulsion systems, the Delfi-n3Xt has successfully implemented the T3μPS, a micro-propulsion system based on cold gas generators (Gill and Guo, 2012) [4]. Propulsion systems can increase the mission capability by enabling orbit raising and/or orbit change, formation flying, de-orbit, etcetera (Mueller *et al.*, 2010) [5]. Further improvement of the propulsion system could be achieved by using a micro-resistojet that is designed to heat up the propellant, which results in an increased specific impulse and consequently an increased Delta-V.

TU Delft developed a micro-resistojet that was created using Micro-Electro-Mechanical Systems (MEMS) technology, which was also called the MEMS Vaporizing Liquid Microthruster (VLM) chip. The chip has dimensions in the millimeter range and provides thrust by expelling and vaporizing liquids (e.g. water), which is turned into gas by added heat from heaters. Several master students have performed different thesis studies related to the MEMS-VLM chip. For example, Matthew (2011) [6] played a big role in the design and testing of the 1st gen. MEMS-VLM chip. Furthermore, Hanselaar (2016) [7] worked on computational models based on two-phase flow to predict the performance of the 2nd gen. MEMS-VLM chip, while Jansen (2016) [8] improved and validated the AE-TB-5M thrust bench that is able to measure the thrust of the MEMS-VLM chip. As for Van Wees (2017) [3], he focussed more on manufacturing, testing and characterization of the 2nd gen. MEMS-VLM chip.

Even though many researches have been performed, more steps are needed before a flight model can be achieved. For example, Van Wees (2017) [3] only managed to perform thrust tests with gaseous nitrogen as propellant instead of liquid water, which means that currently no experimental data is available for thrust tests with vaporized liquid water. Also, the nitrogen thrust tests provided only limited experimental data with large uncertainties. Based on the recommendations of Van Wees (2017) [3], two PhD students (M. de Athay de Costa e Silva and D. Cordeiro Guerrieri) designed and manufactured the 3rd gen. MEMS-VLM chips. Also, the interface that Van Wees (2017) [3] used for the 2nd gen. MEMS-VLM chip was also in need of improvements. This is why the two PhD students designed a new (1st gen.) type of interface for the 3rd gen. MEMS-VLM chip that provided: easier integration, increased robustness and more measurement capabilities.

This 1st gen. interface and the 3rd gen. MEMS-VLM chip were required to be tested as the performance was unknown. From literature it was concluded that the throat Reynolds number has a significant influence on important performance characteristics: Isp quality (ξ_s), nozzle discharge factor (C_d) and nozzle quality (ξ_F) (Grisnik *et al.*;Spisz *et al.*, 1987;1965) [2;9]. In order to obtain data about these characteristics, it was required to perform both thrust bench tests and preliminary tests, which included calibration tests, optical characterization tests, and leak tests. The purpose of preliminary tests was to increase the reliability of the experimental data obtained from the thrust bench tests. Thus, the main aim of the thesis project was to investigate the relationship between the throat Reynolds number and the performance characteristics of the 3rd gen. MEMS-VLM chip.

1.2. Research Goal

From the main aim, the following main research objective or goal was constructed:

"Determine the influence of the throat Reynolds number on the performance characteristics of the 3rd gen. MEMS-VLM chip within an accuracy of 10% through experimentation in order to gain insight on its operating conditions and the corresponding performance."

As mentioned before, the Reynolds number in the nozzle throat, which is defined in Equation 2.13, has an influence on the performance characteristics (ξ_s, C_d, ξ_F), which are defined in Equations 2.7-2.11. This relationship was needed to be investigated for different Reynolds numbers through experimentation. That is why thrust bench tests were performed, which are described in Chapter 4. Note that the required accuracy of ±10% was guessed since at the beginning of the thesis the author did not have any experience with the experiments and thus could not provide a realistic value. It was intended that the thrust bench tests would be done with both gaseous nitrogen and liquid water as propellant. Experimental data using gaseous nitrogen would be compared with the test results of Van Wees (2017) [3]. The data gathered from vaporized liquid water could be compared with the experimental data of gaseous nitrogen, which would provide insights on the efficiency of each propellant type. The Reynolds number would be varied during the tests between the range of 751-2622 [-] (see Subsection 4.1.3). The control of the range would be done by changing the operating conditions of the 3rd gen. MEMS-VLM chip: the heater power input and the mass flow or inlet pressure. The gathered data about the operating conditions could for example help in determining the requirements for the Delfi-PQ mission, in the case that the satellite would implement the MEMS-VLM chip in the propulsion system.

From the main objective, the following sub-goals were constructed with explanations and success criteria:

1. *Experimentally determine the relationship between the throat Reynolds number and the Isp quality / nozzle discharge factor / nozzle quality.*
    - The behavior of this relationship is expected to resemble the experiments performed by Grisnik *et al.* (1987) [2] and Spisz *et al.* (1965) [9]. However, the relationship differs for different nozzle types and nozzle dimensions. That is why experiments are needed to establish the exact relationship for the 3rd gen. MEMS-VLM chip.
    - This sub-goal is achieved when the experimental data is produced, documented and plotted in graphs.
2. *Explore the limit of the highest achievable Reynolds number and the corresponding performance characteristics at vacuum by controlling the operating conditions without damaging the 3rd gen. MEMS-VLM chip and 1st gen. interface.*
    - The importance of this sub-goal is that the limiting Reynolds number determines the highest achievable performance characteristics. Since the operating conditions determine the Reynolds number, the actual limitation lies in the design of the 1st gen. interface and the 3rd gen. MEMS-VLM chip as they hold a maximum allowable pressure and temperature.
    - This sub-goal is achieved when the experimental data is produced and documented.
3. *Obtain experimental data that is reproducible and accurate within 10% from both the preliminary tests and the thrust bench tests.*
    - It is important to obtain accurate data for all the tests that are carried out. However, reproducibility is also important; when the exact same tests are performed by others with the same MEMS-VLM chip, the test results should be about the same. The results will not be

  exactly the same because of measurement uncertainties. Thus, it shall be needed to repeat tests in order to guarantee reproducibility.
   - The preliminary tests include: optical characterization tests, leak tests and calibration tests (e.g. for the displacement sensor in the AE-TB-5M thrust bench).

4. *Create detailed test procedures for both the preliminary tests and the thrust bench tests.*
   - This sub-goal is important because proper documentation is currently lacking for the MEMS-VLM chips in general, whether it is design specification sheets or test procedures.
   - By achieving this sub-goal, it is prevented that the knowledge gained during testing is lost and the test procedures become available for others (e.g. future master students). This also enables the possibility for others to test the reproducibility of the experimental data obtained during this research.
5. *Investigate through experimentation the influences of using liquid water versus gaseous nitrogen as propellant.*
   - Though many influences are interesting, the most important one is investigating what the difference is in the performance characteristics of the propellants while maintaining the same operating conditions (heater power input and mass flow).
   - This sub-goal is reached when experimental data for the above mentioned influence has been produced and documented.
6. *Provide recommendations for the test procedures, the 1st gen. interface design, the 3rd gen. MEMS-VLM chip design and the operating conditions.*
   - Points of the improvement shall become apparent when carrying out the tests and analyzing the test results.
   - For the test procedures it can already be mentioned that the recommendations shall include how to make the process of testing more efficient.

In order to help achieve the main objective and its sub-goals, the main research question and its sub-questions were created. The thesis project can also be considered completed when the following main research question can be answered:

"What do experiments, within an accuracy of 10%, reveal about the influence of different throat Reynolds numbers on the performance characteristics by controlling the operating conditions of the 3rd gen. MEMS-VLM chip?"

From the main research question, the following sub-questions were constructed:

1. What relationship is found through experimentation for the Reynolds number and the Isp quality / nozzle discharge coefficient / nozzle quality?
   (a) How well does this relationship resemble other experimental data found in literature?
   (b) What are the maximum performance characteristics that are achieved during experiments?
   (c) What are the operating conditions that correspond to the maximum performance characteristics?
   (d) What is the Reynolds number that correspond to the maximum performance characteristics?
   (e) What is accuracy of the experimental data?
   (f) Is the experimental data reproducible?
2. In order to help those who have no prior experience in performing these experiments, how should the test procedures be written?
3. What is the influence of using liquid water versus gaseous nitrogen as propellant?
   (a) How is clogging of the nozzle throat with mineral residue prevented when using liquid water?

   (b) What method is effective in unclogging the nozzle throat?
   (c) What is the influence on the power required for the heaters?
   (d) What information can be gained about the percentage of vaporization when using liquid water?

4. What are the recommendations for the test procedures, the interface design, the MEMS-VLM chip design and its operating conditions?

1.3. Thesis Outline

This report is divided into multiple chapters. Chapter 2 contains theoretical background related to the MEMS-VLM chip. Both the previous and current MEMS-VLM chip and interface designs are described here. It is also explained how ideal rocket and corrections like viscous losses, throat boundary layer formation and divergences losses could be used to predict the performance of the MEMS-VLM chip. Experimental results found in literature are included as well.

In chapter 3 the preliminary tests are presented that were required. The leak tests are described, which are needed to validate that the feed lines of the set-up do not have any leakage. The optical characterization test is also explained, which was needed to determine the nozzle geometry that can be used to make performance predictions for the MEMS-VLM chip. Furthermore, the AE-TB-5m calibration test is described in which the Varying Turn-Density Coil (VTDC) actuator was used to relate the pendulum arm displacement with the induced magnetic force on the pendulum arm. Another test, was the AE-TB-5m FCF test and this was required to determine the force correction factor, which was needed because the magnetic force of the VTDC actuator is located higher compared to the thrust force of the MEMS-VLM chip.

Al these tests were needed such that the nitrogen thrust bench could properly be carried out. The test plan, set-up and procedure for the thrust bench test are described in Chapter 4. The experimental results that were obtained from the test are presented in Chapter 5. These results are analyzed in Chapter 6. Here, a comparison is made between not only experimental data and ideal rocket theory, but also with corrections based on viscous loss, boundary layer formation in the nozzle throat and divergence loss. Finally in Chapter 7 conclusions and recommendations are made for this thesis project.

2

Theoretical Background

In this chapter background information is given about the MEMS-VLM chip. This includes the evolution of the design of both the chip and the interface, which is presented in Section 2.1. Furthermore, the performance of the MEMS-VLM chip is described in Section 2.2, where ideal rocket theory including corrections are described and experimental data found in literature is presented.

2.1. Evolution of the MEMS-VLM Chip & Interface Designs

In Subsection 2.1.1 the characteristics of the 2nd gen. MEMS-VLM chip and the previous interface are presented, while in Subsection 2.1.2 the current MEMS-VLM chip and interface are described. Note that the 1st gen. MEMS-VLM chip is not described here.

2.1.1. Previous design

The 2nd gen. MEMS-VLM chip that was used by Van Wees (2017) [3] is presented in Figure 2.1. It can be seen in the figure that the MEMS-VLM chip is integrated with both the electrical and fluidic interface, including mechanical support. It has the following characteristics:

- There were seven suspended heating elements made from Silicon-Carbide that were located in the center of the silicon chamber.
- The heating chamber was the "S1" type of Figure 2.2.
- The nozzle is a 2D-equivalent of a (convergent-divergent) conical nozzle with the following geometry:
    - The designed throat width was 34 $[\mu m]$ and the real throat width was 38.7 $[\mu m]$.
    - The designed throat height was 50 $[\mu m]$ and the real throat height was 84.7 $[\mu m]$.
    - The designed throat area was 1700 $[\mu m]$ and the real throat area (A_t) was 3277.9 $[\mu m]$.
    - The designed exit width was 500 $[\mu m]$ and the real exit width was 495.6 $[\mu m]$.
    - The designed exit height was 50 $[\mu m]$ and the real exit height was 94.0 $[\mu m]$.
    - The designed exit area was 25000 $[\mu m]$ and the real exit area (A_e) was 46586 $[\mu m]$.
    - The designed nozzle area ratio was 14.7 $[-]$ and the real nozzle area ratio (AR) was 14.2 $[-]$.
    - The designed nozzle convergent angle was 30 [°] and the real nozzle convergent angle was 31.1 [°].
    - The designed nozzle divergent angle was 20 [°] and the real nozzle divergent angle was 19.8 [°].

  - The (real) wetted perimeter (P_w) was 247 [μm], which resulted in a (real) hydraulic diameter (D_H) of 53.1 [μm].

- The fluidic interface included a dispensing needle bonded (using ACC AS 1504 Acetoxy) to the inlet of the MEMS-VLM chip.

- The electrical interface used (highly fragile) thin golden bond wires that were looped between the bond pads of the Printed Circuit Board (PCB) and the bond pads of the MEMS-VLM chip. This process was performed by the Advanced Packaging Center in Duiven.

- The interfaces were mechanically supported by a 3D-printed support bracket and cover. The purpose of the cover was to prevent that the fragile golden bond wires would accidentally get damaged.

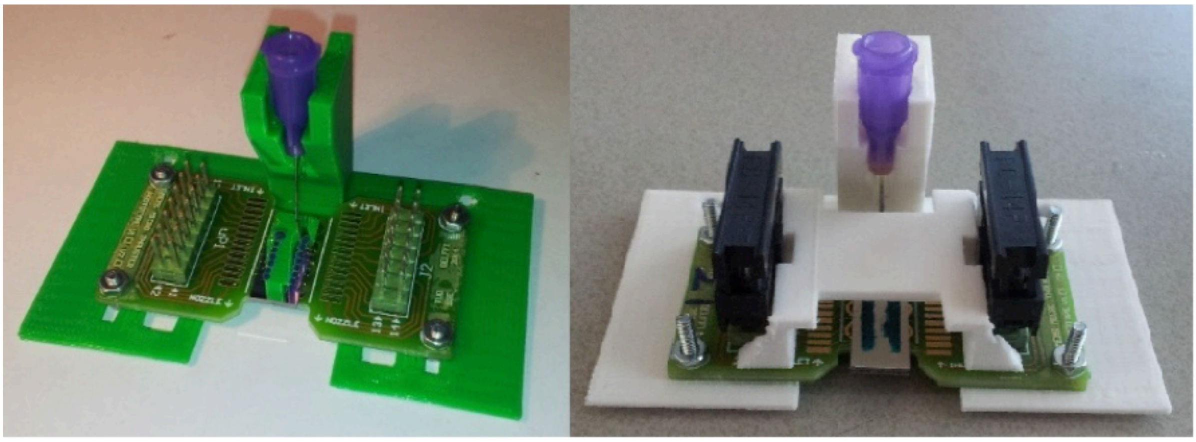

Figure 2.1: MEMS-VLM chip integrated with both the electrical and fluidic interface on a support bracket (left). Integrated MEMS-VLM chip with additional protection by support cover (right) [3].

Note that the above mentioned characteristics only apply to a specific MEMS-VLM chip design that was used during the tests performed by Van Wees (2017) [3]. Other designs had a variation in the amount of heaters, in the type of flow channel and the nozzle type. There was either an option for 7 heaters or 14 heaters, which meant these two designs would also differ in length. The heating chambers that are presented in Figure 2.2 show that there were four different types: small diamond-shaped pillars (D1), large diamond-shaped pillars (D2), small serpentine channels (S1) and large serpentine channels (S2). There were two different designs for the nozzle: a 2D-equivalent of a conical nozzle and a 2D-equivalent of a bell nozzle.

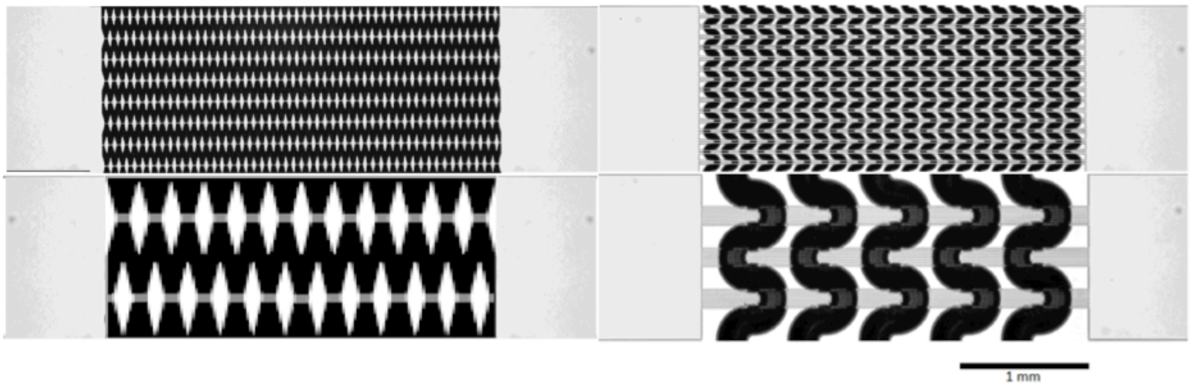

Figure 2.2: Top view of different heating chambers: Top left- D1, top right- S1, bottom left- D2 and bottom right- S2 [3].

2.1.2. Current design

In this section the current designs for the 3rd gen. MEMS-VLM chips and the 1st gen. interface are described based on the work of de Athayde Costa e Silva *et al.* (2017) [10].

3rd gen. MEMS-VLM chip

Compared to previous designs the current MEMS-VLM chip underwent a few changes that would either tackle problems of previous designs or improve their performance. The current MEMS-VLM chip has the following characteristics:

- Instead of the Silicon-Carbide heaters now metal (Molybdenum) heaters are used to heat up the propellant. One advantage of metal heaters is that they have a positive temperature coefficient of resistance that enables stable use of the heaters in constant voltage mode. Another advantage is that resistivity of metals is a few orders of magnitude lower than that of Silicon-Carbide, which means that the heaters can be designed for a lower (e.g. 5V) volt supply [3].
- Instead of suspended heaters in the center of the chamber cross-section, now the heaters are integrated within the silicon, which mitigates a few problems of the previous MEMS-VLM chip. The suspended heaters were found to be fragile and because of the increased complexity of the manufacturing process, large discrepancies were found between design and manufacturing results [3].
- In the current design transparent material is used for the heater chamber wall, such that the vaporization process of liquid propellant can be directly observed.
- The maximum temperature and pressure at which the MEMS-VLM chip can operate is unknown and should be researched. Note that this was not done in this thesis project.

Thus, many changes were incorporated in the 3rd gen. MEMS-VLM chip. The 3rd gen. MEMS-VLM chips have different design options as can be seen in Figures 2.3, 2.4 and 2.5. Note that it is recommended to read the work of de Athayde Costa e Silva *et al.* (2017) [10] for more information. Each chip that was manufactured, has a specific identifier. This will be explained using the "01-Ws2-01" chip as an example:

- The first part of the identifier, "01", is the wafer number on which the chip was manufactured.
- The "W" indicates that it has a wide nozzle, which is "Nozzle 2" in Figure 2.3.
- The "s" indicates that it has small serpentine channels flow channels, which is "Channel 3" in Figure
- The "2" indicates that there are 30 heater lines divided into sets of 2 lines, which is "Heater 2" in Figure 2.3.
- The "01" at the end of the identifier is the thruster number in case of repetition.

1st gen. interface

Apart from the MEMS-VLM chip, changes were also necessary for the interface. The previous interface was only designed for breadboard testing and was far from being representative as a flight-model design. Also, the process of integrating the MEMS-VLM chip with the interface is complicated. That is why a new type of interface design was created, about which a schematic is presented in Figure 2.6. The 1st gen. interface has the following characteristics:

- Compared to the previous design, the current interface has less volume, is more robust and provides protection to the MEMS-VLM chip as it mostly encapsulates the chip.
- Instead of a large dispensing needle, the current interface encapsulates the MEMS-VLM chip and there is a small hole through which the propellant can flow to the inlet of the MEMS-VLM chip. Furthermore, bolts are used to connect the interface with the MEMS-VLM chip instead of glue, which means that one interface can be used to test different MEMS-VLM chips of the same size. The usage of bolts also means that the integration process has become much easier and costs less time [3].

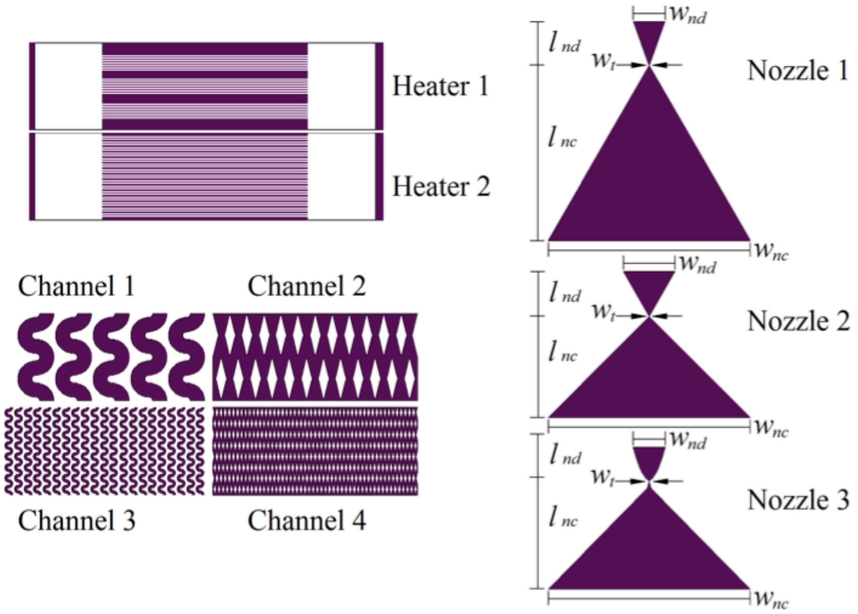

Figure 2.3: Visualization of different design options for the 3rd gen. MEMS-VLM chips with design variations in heaters, flow channels and nozzles. [10]

Type	w_{nd}	l_{nd}	w_{nc}	l_{nc}	w_t
L	500	645	3000	2600	45
W	780	660	3000	1500	45
B	500	500	3000	1600	45

	d_1	d_2
d	160	40
D	580	160
s	60	20
S	266	54

Figure 2.4: Metrics (in μm) of different design options for the 3rd gen. MEMS-VLM chips with design variations in heaters, flow channels and nozzles. [10]

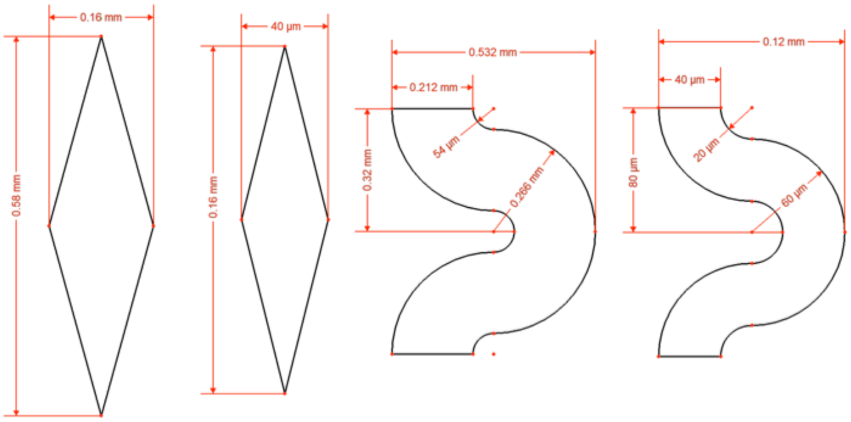

Figure 2.5: Designed dimensions of the different flow channels. From left to right: large diamonds (D), small diamonds (d), large serpentine (S), and small serpentine (s). [10]

- Instead of using thin golden electrical wires to provide power to the heater of MEMS-VLM chip, the 1st gen. interface utilizes gold plated spring loaded pins. The pins have the advantage of being more robust compared to the golden wires, which are really fragile due to their thin 25 [μm] diameter. Furthermore, for the bonding process of the golden wires the involvement of another company is needed, which means integration time and costs are saved when spring loaded pins are used [3].
- The 1st gen. interface has increased measurement capabilities, as a pressure and temperature sensor is integrated within the interface. This enables measuring the propellant inlet pressure and temperature. Note that this part is not included in Figure 2.6.
- The 1st gen. interface consists mostly of Teflon, a good thermal insulator and a natural sealant, which can reduce heat loss of the MEMS-VLM chip and reduce leakage of the integrated system. Note that the Teflon part limits the maximum operating temperature as teflon melts at 327 [$^\circ C$] [11].
- A glass piece is incorporated in the 1st gen. interface as well, since this enables to optically observe the vaporization process of propellants in the heating chamber during experiments.
- The interface has an aluminum base plate with four threaded holes, a U-shaped cavity and a support hole. The purpose of the threaded holes is to fasten the other parts of the interface utilizing bolts. The U-shaped cavity is needed to enable looking through the glass piece at the MEMS-VLM chip. The support hole is needed to fasten the interface to the AE-TB-5M thrust bench.
- The interface has an aluminum top plate with four holes and a U-shaped cavity. The holes are needed such that the bolts can go through them. The U-shaped cavity is important to create space for the spring loaded pins. Note that this part is not included in Figure 2.6.

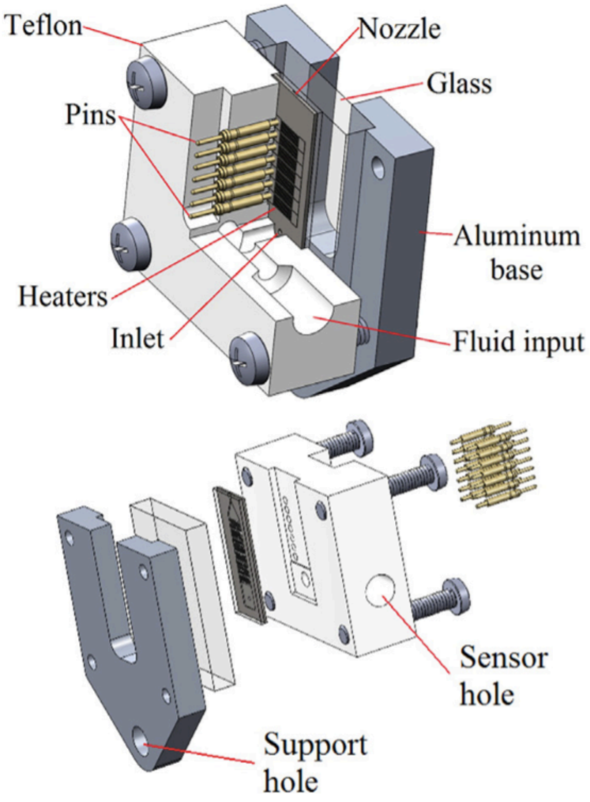

Figure 2.6: Schematic of the 1st gen. interface designed for the 3rd gen. MEMS-VLM chip that shall be used for testing. Upper part displays a partially cut-open-view and the lower part displays an exploded view. Note that this is an older schematic as the aluminum top plate was not included in this design. [10]

2.1.3. Chips used for experiments

During the first phases of the thesis project, it was intended to use the ”01-Ws2-01” chip (see Figure 2.7) for experiments. However, there was a leakage problem that could not be solved because the 1st gen. short interface (see Figure 2.9) was deformed slightly due to tests performed by others at high temperatures. The ”01-Ws2-01” chip, was the only short chip remaining that could be used for experiments since the other short chips were all damaged or had clocked nozzles during (water vaporization) tests. Luckily, there still multiple long chips available for experiments (see Figure 2.8). However, this meant that if a new interface was created, that it would be required to make adjustments due to the longer chips. Therefore the new interface was also longer, which can be seen when comparing Figure 2.9 to Figure 2.10. After the new interface was created, it was used for experiments with the ”01-LS2-02” chip

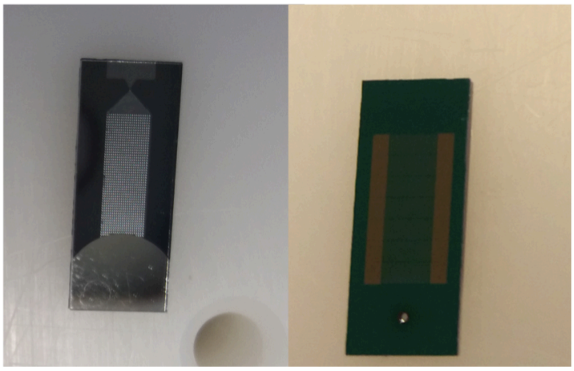

Figure 2.7: Picture of the 01-WS2-01 chip, which is a short 3rd gen. MEMS-VLM chip that shall be used for testing. Left picture displays the bottom of the chip and right picture the top of the chip.

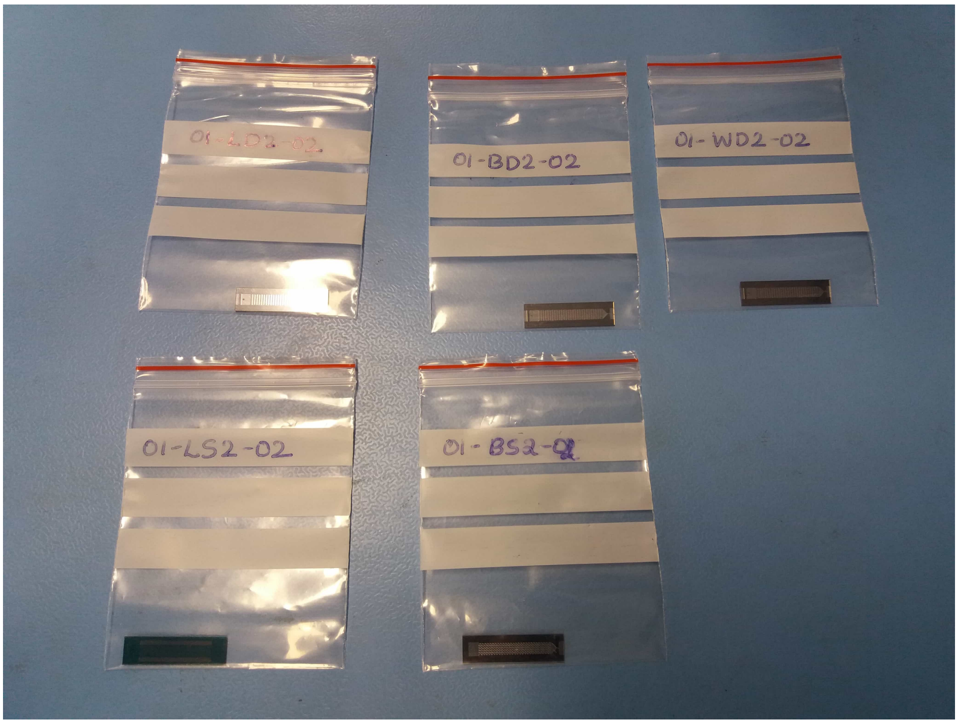

Figure 2.8: Picture of different long 3rd gen. MEMS-VLM chip that were available for testing.

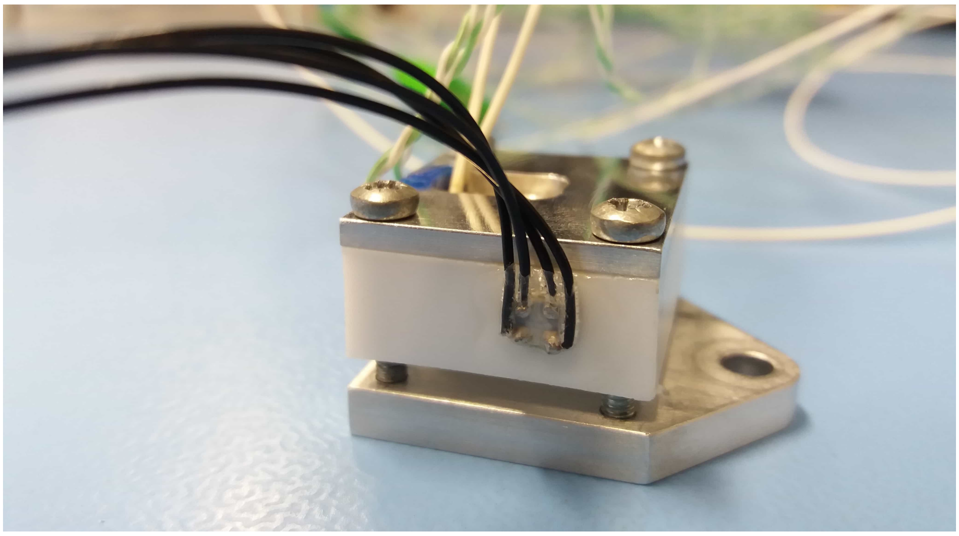

Figure 2.9: Picture of the short 1st gen. interface.

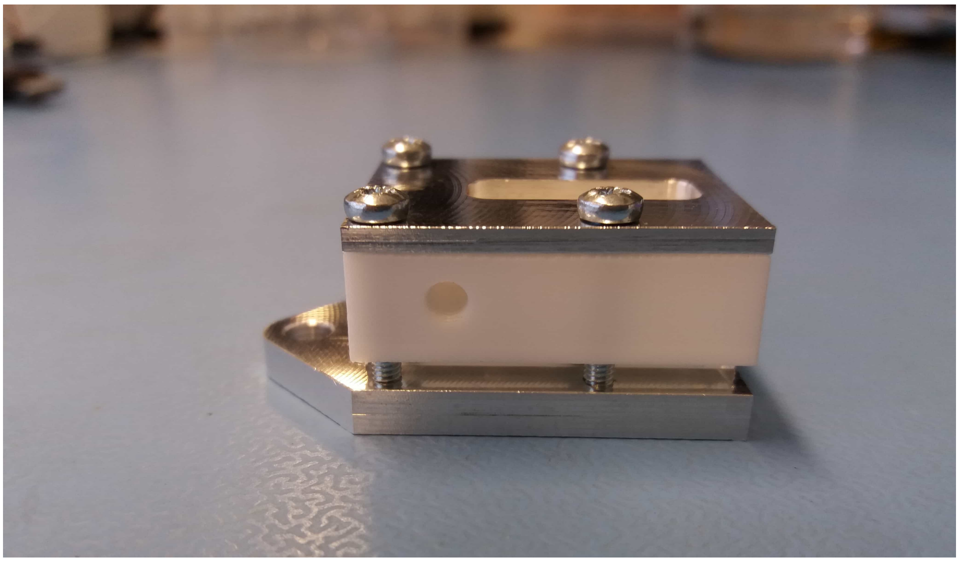

Figure 2.10: Picture of the long 1st gen. interface. Note that here the pressure/temperature sensor was not yet included.

2.2. Performance of the MEMS-VLM chip

As mentioned in the introduction, the main goal of the thesis is to find the performance of the MEMS-VLM chip. However, it is important to get an indication of what is expected from the outcome of the tests. First, in Subsection 2.2.1, it is explained how the expected results are computed using ideal rocket theory and how the performance parameters are defined. Because ideal rocket theory and experiments usually don't compare well, corrections exist that can provide a better prediction for the expected test results, which is presented in Subsection 2.2.2. Finally in Subsection 2.2.3 experimental data is presented that was found in literature.

2.2.1. Ideal Rocket Theory

It is important to know which parameters of the MEMS-VLM chip have influence on its performance and that is why the basics of rocketry need to be explained. All rockets produce force by expelling mass, which is in accordance with Newton's third law of motion (Larson and Wertz, 2005) [12]. This relationship can be found in Equation 2.1 [12], with mass flow, exhaust velocity and characteristic velocity in Equations 2.2, 2.3 and 2.4 as described by Zandbergen (2016) [13]:

$$F = \dot{m} \cdot V_{eq} = \dot{m} \cdot V_e + (P_e - P_a)A_e \tag{2.1}$$

$$\dot{m} = \frac{P_c \cdot A_t}{c^*} \tag{2.2}$$

$$V_e = \sqrt{\frac{2\gamma}{\gamma - 1} \cdot \frac{R_a \cdot T_c}{M} \cdot \left[1 - \left(\frac{P_e}{P_c}\right)^{\left(\frac{\gamma-1}{\gamma}\right)}\right]} \tag{2.3}$$

$$c^* = \frac{1}{\Gamma} \cdot \sqrt{R \cdot T_c} \tag{2.4}$$

Where:

- F is the thrust force [N]
- $\dot{m}$ is the mass flow [kg/s]
- V_{eq} is the equivalent exhaust velocity [m/s]
- V_e is the propellant exhaust velocity [m/s]
- P_e is the gas pressure at the exit nozzle or exit pressure [Pa]
- P_a is the ambient pressure [Pa]
- A_e is the nozzle exit area $[m^2]$
- P_c is the chamber pressure [Pa]
- A_t is the nozzle throat area $[m^2]$
- c^* is the characteristic velocity [m/s]
- γ is the specific heat ratio [-]
- R_a is the universal gas constant [J/mol/K]
- M is the molar mass [kg/mol]
- T_c is the chamber temperature [K]
- Γ is the Vandenkerckhove function [-]
- R is the specific gas constant [J/kg/K]

According to Zandbergen (2016) [13] maximum thrust is achieved when P_e is equal to P_a. Since the MEMS-VLM chip will be used in a space environment, the ambient pressure is equal to zero. However, the exit pressure can only be zero in case the nozzle is infinitely long. This implies that P_e will never be equal to P_a. Furthermore, it can be seen that thrust varies linearly with both the mass flow and exhaust velocity. In its turn, the exhaust velocity (in a space environment) depends on the propellant type and the propellant temperature in the combustion chamber [13]. This makes all these parameters important to investigate. How efficiently the energy content of the propellant is converted in thrust is described in Equation 2.5 [12]:

$$I_{sp} = \frac{F}{g_0 \cdot \dot{m}} \tag{2.5}$$

Where:

- I_{sp} is the specific impulse [s]

- g_0 is the gravitational acceleration on Earth $[m/s^2]$

From Equation 2.5 it can be deduced that for a higher specific impulse less propellant is needed per second for the same amount of thrust, which means less mass and therefore less costs. That is why the specific impulse is important and needs to be investigated. In reality the value for specific impulse is lower than the value predicted from theory. The ratio between the experimental and theoretical specific impulse is called the motor quality or Isp quality, which is considered an important performance parameter [13]. According to Van Wees (2017) [3] the nozzle discharge factor and the nozzle quality are also important performance parameters that should be determined for the MEMS-VLM chips, since these parameters relate experimental values to theoretical values. The nozzle discharge factor relates the experimental mass flow to the theoretical mass flow. It accounts for boundary layer effects and real gas effects (e.g. compressibility) [13]. The nozzle quality relates the experimental thrust coefficient to the theoretical thrust coefficient. It accounts for losses due to friction effects, divergence and shifting gas composition (Suton and Biblarz; Huzel and Huang; Spisz *et al.*, 2001; 1971; 1965) [14-9]. The (throat) Reynolds number has a big influence on the effective throat area and experimental thrust coefficient, which also means that it impacts the discharge factor and nozzle quality, respectively [13]. Note that heating quality ξ_b is included as well, which indicates the propellant heat loss for a non-chemical thermal rocket motor. Also, note that ξ_b for chemical rockets is called combustion quality, which indicates losses of the combustion process.

All these parameters are presented in Equations 2.6 - 2.13 [3,13]. It should be noted that Equation 2.13 is adapted to calculate the Reynolds number for a nozzle slit, which is different compared to a circular nozzle. Also, the wetted perimeter is the perimeter of the nozzle throat that interacts with the propellant. Furthermore, Equation 2.15 is an adaption of the isentropic flow relations, where a chocked flow is assumed (Mach number is 1) and thus the throat temperature can be calculated, which can be used to determine the dynamic viscosity (based on NIST). The dynamic viscosity is again needed to determine R_e.

$$C_d = \frac{(A_t)_{eff}}{(A_t)_{ideal}} \approx \frac{\dot{m}_{exp}}{\dot{m}_{ideal}} \tag{2.6}$$

$$\xi_F = \frac{(C_F)_{exp}}{(C_F)_{ideal}} = \frac{F(p_c \cdot A_t)^{-1}}{(C_F)_{ideal}} \tag{2.7}$$

$$(C_F)_{ideal} = C_F{}^\circ + \left(\frac{P_e}{P_c} - \frac{P_a}{P_c}\right) \cdot AR \tag{2.8}$$

$$AR = \frac{A_e}{A_t} \tag{2.9}$$

$$C_F{}^\circ = \frac{V_e}{c^*} \tag{2.10}$$

$$\xi_s = \frac{(I_{sp})_{exp}}{(I_{sp})_{ideal}} \tag{2.11}$$

$$\xi_b = \frac{(c^*)_{exp}}{(c^*)_{ideal}} = \frac{\xi_s}{\xi_F} \tag{2.12}$$

$$R_e = \frac{\dot{m} \cdot D_H}{\mu_t \cdot A_t} \tag{2.13}$$

$$D_H = \frac{4 \cdot A_t}{P_w} \tag{2.14}$$

$$\frac{T_t}{T_{tot}} = \frac{\gamma + 1}{2} \tag{2.15}$$

Where:

- C_d is the nozzle discharge factor [-]
- $(A_t)_{eff}$ is the effective throat area of the nozzle after boundary layer formation $[m^2]$
- $(A_t)_{ideal}$ is the geometrical throat area of the nozzle $[m^2]$
- $(\dot{m})_{exp}$ is the experimental mass flow [kg/s]
- $(\dot{m})_{ideal}$ is the theoretical mass flow according to ideal rocket theory [kg/s]
- ξ_F is the nozzle quality [-]
- $(C_F)_{exp}$ is the experimental thrust coefficient [-]
- $(C_F)_{ideal}$ is the theoretical thrust coefficient [-]
- AR is the nozzle area ratio [-]
- $C_F{}^\circ$ is the characteristic thrust coefficient [-]
- ξ_s is the Isp quality [-]
- $(I_{sp})_{exp}$ is the experimental specific impulse [s]
- $(I_{sp})_{ideal}$ is the theoretical specific impulse [s]
- ξ_b is the heating quality [-]
- $(c^*)_{exp}$ is the experimental characteristic velocity [m/s]
- $(c^*)_{ideal}$ is the theoretical characteristic velocity [m/s]
- R_e is the Reynolds number in the nozzle throat [-]
- D_H is the hydraulic diameter of the nozzle [m]
- μ_t is the dynamic viscosity of the propellant at isentropic throat temperature $[Pa{\cdot}s]$
- P_w is the wetted perimeter [m]
- T_t is the isentropic throat temperature [K]
- T_{tot} is the total temperature [K]

2.2.2. Corrections for Ideal Rocket Theory

According to Zandbergen (2016) [13], a better prediction of the performance can be obtained when the following three effects are taken together with ideal rocket theory: the loss factor caused by divergence of the flow (divergence loss), the loss factor caused by viscous effects (viscous loss) and the loss factor caused by a reduction in effective nozzle throat area and thus the nozzle area ratio (throat boundary layer loss).

Divergence loss

Incorporating divergence loss is required because ideal rocket theory assumes a 1D propellant flow at the nozzle exit. However, in reality the nitrogen particles have a velocity vector in the radial direction (w.r.t. the nozzle exit), which is basically the divergence loss and this affects the characteristic thrust coefficient ($C_F{}^\circ$). According to Farokhi (2014) [16] Equations 2.16-2.18 can be used to account for the divergence loss in a 2D or 3D (converging-diverging) conical nozzle:

$$(C_F)_{div\_loss} = CA \cdot C_F{}^\circ + \left(\frac{P_e}{P_c} - \frac{P_a}{P_c}\right) \cdot AR \tag{2.16}$$

$$CA_{2D\text{-}C} = \frac{sin(\theta_{nd})}{\theta_{nd}} \tag{2.17}$$

$$CA_{3D\text{-}C} = \frac{1 + cos(\theta_{nd})}{2} \tag{2.18}$$

Where:

- C_A is the divergence loss factor [-]
- θ_{nd} is the nozzle divergence half angle [rad]
- the subscript "2D-C" stands for the 2D conical nozzle.
- the subscript "3D-C" stands for the 3D conical nozzle.

It can be seen that Equation 2.16 is an adaption of Equation 2.8 where the divergence loss factor is included for the calculation of the thrust coefficient. The derivation for Equations 2.17 and 2.18 can be found in Farokhi (2014) [16]. The effect of the nozzle divergence half angle on the divergence loss factor is visualized in Figure 2.11 for both a 2D and 3D conical nozzle. It can be seen that a larger θ_{nd} has a greater effect on the C_A for a 3D conical nozzle compared to a 2D conical nozzle. Note that θ_{nd} needs to be in radians when using it in de denominator of Equation 2.17.

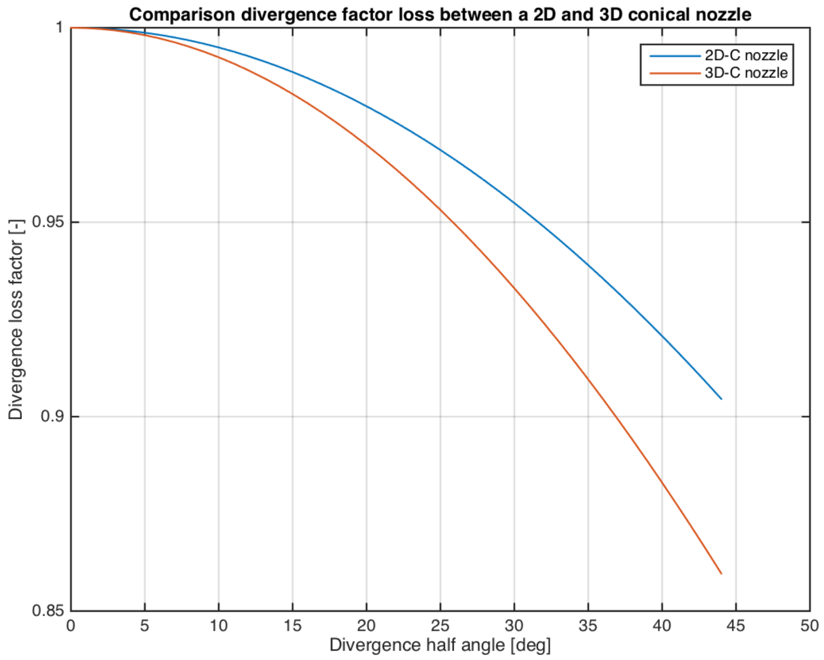

Figure 2.11: The divergence loss factor (C_A) as a function of the nozzle divergence half angle (θ_{nd}) plotted in MATLAB for both a 2D (upper curve) and 3D (lower curve) conical nozzle.

Viscous loss

Viscous loss, which is caused by boundary layer formation in the divergent part of the nozzle, also affects the thrust coefficient as was found by Spisz *et al.* (1965) [9]. Depending on the nozzle area ratio and the throat Reynolds number, the viscous loss can be calculated and used to correct the ideal thrust coefficient as can be seen in Equation 2.19. This equation is an empirical relation based on experiments with (3D) conical nozzles with different nozzle area ratios, which was carried out and established by Spisz *et al.* (1965) [9]. Note that the relation holds for a Reynolds number range of $2000-10000[-]$ and nozzle area ratio's between $25[-]$ and $150[-]$. Also, the experiments were carried out for a 3D conical nozzle and not a 2D conical nozzle. A visualization of the function is presented in Figure 2.12. It can be seen that compared to the nozzle area ratio (AR) increasing the Reynolds number has a much greater effect on reducing the viscous loss.

$$(C_F)_{visc\_loss} = (C_F)_{ideal} - (C_F)_{visc} = (C_F)_{ideal} - \frac{17.6 \cdot e^{0.0032 \cdot AR}}{\sqrt{R_e}} \tag{2.19}$$

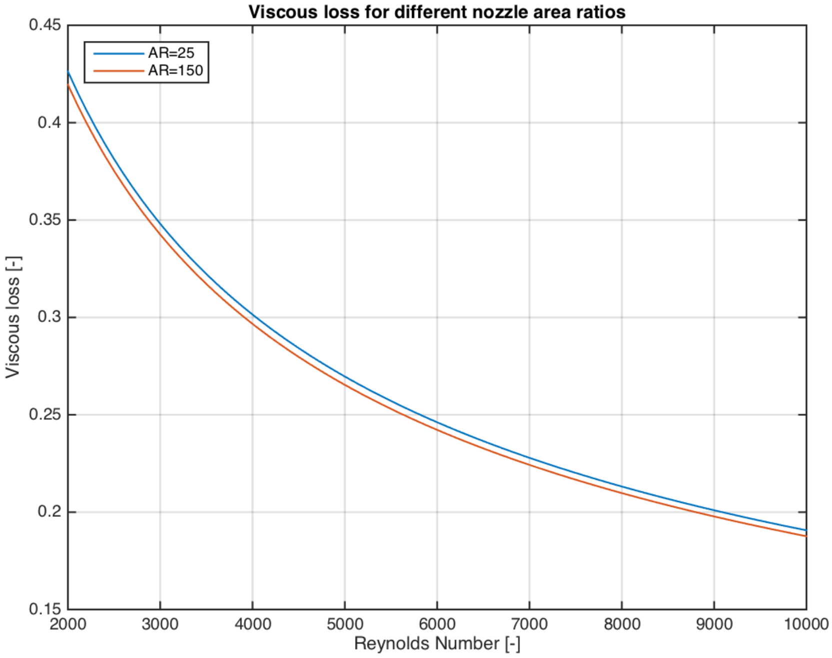

Figure 2.12: The viscous loss ($(C_F)_{visc\_loss}$) as a function of the throat Reynolds number plotted in MATLAB for different area ratios.

Throat boundary layer loss

As mentioned before, the discharge factor (C_d) takes into account the effect of the boundary layer inside the nozzle throat on the mass flow. Tang and Fenn (1978) [17] provided Equation 2.20, which is an analytical approach for determining the discharge factor based on the specific heat ratio (γ) and the modified Reynolds number (R_{mod}). This means that the equation can be used to give a better prediction for the theoretical mass flow. Furthermore, this equation applies to a chocked axi-symmetric nozzle where the shape of throat is not sharp. The effect of the throat shape is incorporated in R_{mod} as can be seen in Equation 2.21. As mentioned before, the nozzle of the MEMS-VLM chip has a parallel floor and ceiling, but the side walls converge and diverge. This means that R^* is the radius of curvature of the side walls and that R_t is half of W_t. A visualization of Equation 2.20 can be found in Figure 2.13. For the "Reference" curve a γ of $1.4[-]$, an R^* of $1[m]$ and an R_t of $1[m]$ were taken. For the other curves one of these input parameters were changed in order to investigate its effect. For example, the most upper (purple) curve corresponds to "Rt=10", which means that only R_t was changed to $10[m]$ while the other input parameters were the same as for the "Reference" curve. A few things can be said about the behavior of $(C_d)_{bd\_loss}$ when looking at Figure 2.13. A change in γ from $1.4[-]$ to $1.66[-]$, which for example can be caused by changing from nitrogen gas to helium gas (both at standard conditions), only results in a small change in the curve. Whereas a change in the nozzle throat shape has a much greater impact on the curve. However, it can be seen that for large Reynolds numbers that all curves converge to a discharge factor of $1.0[-]$.

$$(C_d)_{bd\_loss} = 1 - \left(\frac{\gamma+1}{2}\right)^{3/4}\left\{\frac{72-32\sqrt{6}}{3(\gamma+1)} + \frac{4\sqrt{6}}{3}\right\}\left(\frac{1}{\sqrt{R_{mod}}}\right) + \left(\frac{2\sqrt{2}(\gamma-1)(\gamma+2)}{3\sqrt{\gamma+1}}\right)\left(\frac{1}{R_{mod}}\right) \tag{2.20}$$

$$R_{mod} = R_e\sqrt{\frac{R^*}{R_t}} \tag{2.21}$$

Where:

- R_{mod} is the modified Reynolds number needed to calculate $(C_d)_{bd\_loss}$ [-]
- R^* is the radius of curvature of the nozzle throat section [m]
- R_t is the radius of the nozzle throat [m]

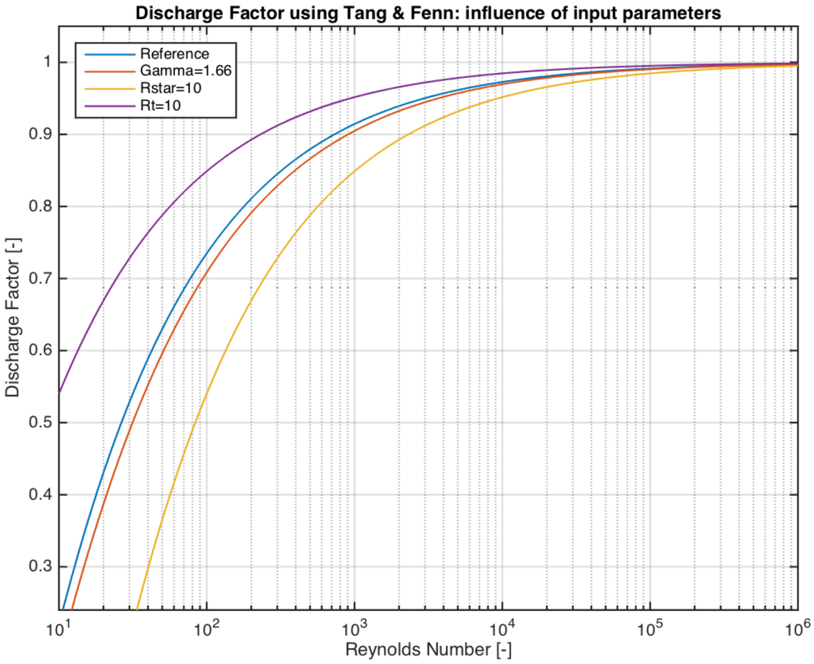

Figure 2.13: The discharge factor as a function of the throat Reynolds number using the analytical approach of Tang and Fenn (1978) [17] plotted in MATLAB with a log-scale for the x-axis. For the reference curve a γ of $1.2[-]$, a R^* of $1[m]$ and a R_t of $1[m]$ were taken. For the other curves the name indicates what parameter was changed compared to the reference line.

2.2.3. Experimental data found in literature

In this subsection different experimental data found in literature are compared to each other, which can also be seen in Table 2.2.

Van Wees (2017)

Regarding the testing campaign, Van Wees (2017) [3] determined the discharge factor and the nozzle performance for which the thrust, mass flow and pressure were measured. This was done in a vacuum environment using a mass flow sensor & controller (Brooks 5850S), a pressure sensor (PX181-200G5V) and the AE-TB-5M, which is a pendulum thrust bench. Note that the pressure sensor was placed in the feed system that was outside of the vacuum chamber, meaning that the sensor was upstream with respect to the heating chamber of the 2nd gen. MEMS-VLM chip. This also meant that in order to obtain the heating chamber pressure, the pressure losses between the feed system pressure and heating chamber pressure were estimated from theory. This drastically increased the uncertainty of the experiment. Also, from all the thrust tests that were performed, only FT13 (low pressure) and FT14 (medium pressure) were thoroughly analyzed as many other tests (FT1-FT13 and FT15) failed. The test results are presented in Table 2.1 and a few interesting points can be noted:

- Van Wees (2017) [3] compared the values for the nozzle discharge coefficient to literature and found out that his values were much lower. Matthew (2011) [6] tested for Reynolds numbers between 280 and 1400 and obtained discharge coefficient values between 0.5 and 0.8. Bayt (1999) [18] tested for a Reynolds number of 700 and obtained a discharge coefficient of 0.88 ± 0.08.
- Despite the high absolute uncertainty the values for the Isp quality or motor quality indicate that the 2nd gen. MEMS-VLM chip performs poorly, which might be due to increased viscous losses caused by the high aspect ratio of the nozzle exit [3].
- As a final note, with only two data sets no definitive conclusions can be given about the predictability of the 2nd gen. MEMS-VLM chip.

Table 2.1: Overview of the different parameters as was determined for the thrust bench tests (FT-13 and FT-14) by Van Wees (2017) [3].

Test Label	P_c [bar]	$(\dot{m})_{exp}$ [mg/s]	$(F)_{exp}$ [mN]	$(C_F)_{exp}$ [−]	C_d [−]	R_e [−]	ξ_s [−]
FT-13	1.53±0.11	0.76±0.01	0.10 ±0.03	0.22 ±0.08	0.66 ±0.06	6.88e2	0.2 ±0.06
FT-14	2.57±0.12	1.32±0.01	0.265±0.038	0.33 ±0.06	0.68 ±0.06	1.20e3	0.23 ±0.05

Jansen (2016)

The experiments of Jansen (2016) [8] also included thrust bench tests using the AE-TB-5M. Although, the tests were performed for the T3μPS, a cold-gas micro-thruster. The T3μPS was successfully demonstrated on board of the Delfi-n3Xt. Compared to the nozzle of the 2nd gen. MEMS-VLM chip the dimensions of the T3μPS nozzle are greater: the nozzle throat area is 37670 [μm^2] and the exit area is 52480 [μm^2]. According to Equation 2.2 the larger throat area means that higher mass flows can be achieved and therefore also higher thrust. It should be mentioned that even though a classical conical nozzle was designed, Jansen (2016) [8] found out via optical inspection that in reality the nozzle resembles a hole with tapered edges. Nevertheless, the T3μPS performed much better than the 2nd gen. MEMS-VLM chip: the discharge factor ranged between 0.85 and 0.87 [-], the thrust coefficient was in the range of 1.155-1.164 [-] and the nozzle quality ranged from 0.86 to 0.89 [-].

Spisz *et al.* (1965)

An investigation was performed by Spisz *et al.* (1965) [9], who determined the relationship between the Reynolds number and the thrust coefficient for seven nozzles that differed in size and/or geometry. The research was done with gas flows where no heat was added and for gas flows that included heat addition. From the research it was concluded that lower Reynolds numbers result in lower measured thrust coefficients and consequently lower nozzle efficiencies. For example, for one thruster the following can be observed when looking at the experimental data (see also Table 2.2). For a Reynolds number of 4660 [-] a thrust coefficient of 1.468 [-] is measured, while for a Reynolds number of 867 [-] a thrust coefficient of 1.014 was measured. This decrease in Reynolds number caused the nozzle quality drop from 0.889 to 0.614 [-]. It should be noted that all the nozzles that were tested by Spisz *et al.* (1965) [9] had much larger dimensions than the nozzle of the 2nd gen. MEMS-VLM chip. This could explain the low nozzle efficiencies of Van Wees (2017) [3], since for smaller nozzles the impact of low Reynolds numbers is likely greater. Since such low nozzle efficiencies are undesirable for a propulsion system, it is important to thoroughly investigate the effect of the Reynolds number on the quality.

Maurya *et al.* (2005)

Another example that is comparable to the 2nd gen. MEMS-VLM chip is the nozzle used by Maurya *et al.* (2005) [19], which had an even a smaller nozzle throat area of 900 [μm^2] that also performed poorly. The thrust measurements ranged from 10 to 110 [μN] for heater power inputs ranging from 1.1 to 2.4 [W], for which a constant mass flow of 1.6 [mg/s] was used. The test configuration for the thrust measurements included a thin copper foil strip that functioned as a cantilever. Using a 'lamp-and-scale arrangement' the deflection of the cantilever could be effectively magnified by several orders of magnitude. From the deflection of the cantilever the thrust force could be deduced. The measurement accuracy was about 20% for smaller thrust values and about 10% for higher thrust values. More information about the test configuration can be found in the article by Maurya *et al.* (2005) [20]. Hereafter, Maurya *et al.* (2005) [19] used the force measurement values together with the corresponding values for measured mass flow, nozzle throat area and heater power input, for a back-to-front iterative approach to obtain the values for the (effective) nozzle exit area, chamber temperature, chamber pressure and the exit pressure. A detailed explanation of the iteration process can be found in [19]. Note that it was predicted that the divergence angle of the nozzle exit was too large to match with the exhaust jet of the water vapor, which is supposedly more directional. This means that the effective exit area is smaller compared to the geometrical exit area of the nozzle. Since this is not easily determined, the iteration process was used to provide an estimate for the effective exit area. Furthermore, not all the wanted data was available in the article, which is why some parameters were calculated based on theory. For example, the characteristic velocity was calculated using Equation 2.4, after which the chamber pressure could determined using Equation 2.2. Ideal rocket theory was used (by the author of this thesis) to calculate the chamber pressure of 10.98 [bar], but this is quite high for a small nozzle as it needs to robust enough to withstand the high pressure. The chamber pressure together with the other calculated parameters are bold in Table 2.2. It can be seen that a nozzle quality of 0.093 [-] was calculated, which is even smaller compared to the 2nd gen. MEMS-VLM.

Cen and Xu (2010)

The experimental results for the nozzle tested by Cen and Xu (2010) [21] indicated a better performance compared to the nozzle of the 2nd gen. MEMS-VLM chip. As mentioned before, the better performance might be due to its larger nozzle geometries for which the Reynolds number effects are expected to be less significant. The micro-thruster was able to produce an average thrust value of 6.5 [mN] with a chamber pressure of 2.32 [bar], which had estimated uncertainties of ± 0.02 [mN] and ± 0.01 [bar], respectively. In the test configuration for obtaining the thrust measurements, the exhaust gas of the micro-thruster was pointed towards an impinging plate that was connected to a lever and the resulting impinging force was enlarged by the lever. At the other side of the lever there was a piezoelectric sensor that could measure the enlarged force. Note that the micro-thruster was attached to a copper heater block, which was mounted on a slide track that could move in vertical or horizontal direction in order to make slight adjustments in the relative position between the micro-thruster and the impinging plate on the end of the lever. Also, the whole test configuration was performed under vacuum conditions. More information about the test configuration can be found in [21]. The provided experimental data was incomplete as it only included the nozzle geometry (throat and exit area), the mass flow, the chamber pressure, the vacuum pressure and the measured thrust. Therefore, these known parameters were used to determine the ideal thrust coefficient, the experimental thrust coefficient and the nozzle quality. It can be seen in Table 2.2 that the nozzle quality is as high as 0.922 [-], which is much better compared to the 2nd gen. MEMS-VLM chip.

Table 2.2: Part 1 – Comparison of various parameters found from experimental / simulated data in literature. Note that some papers did not include information about all the parameters. Thus, some parameters were calculated, which are presented in bold.

Data source	Propellant	A_t [μm^2]	A_e [μm^2]	A_t/A_e [-]	$\dot{m}$ [mg/s]	P_c [bar]
Van Wees (2017) [3]	N2 gas	3,278	46,586	14.2	0.76−1.32	1.53−2.57
Jansen (2016) [8]	N2 gas	37,670	52,480	1.393	27.19	3.20
Spisz *et al.* (1965) [9]	H2 gas	4,277,411	106,935,275	25	226,796 – 566,990	0.34 – 1.61
Maurya *et al.* (2005) [19]	H2O liquid	900	3700	4.111	1.6	**10.98**
Cen and Xu (2010) [21]	H2O liquid	18,000	210,960	11.72	8.33	2.32

Table 2.3: Part 2 – Comparison of various parameters found from experimental / simulated data in literature. Note that some papers did not include information about all the parameters. Thus, some parameters were calculated, which are presented in bold.

Data source	F [mN]	$(C_F)_{ideal}$ [-]	$(C_F)_{exp}$ [-]	ξ_F [-]	ξ_s [-]	C_d [-]	R_e [-]
Van Wees (2017) [3]	0.1-0.265	1.61	0.22-0.33	0.2 – 0.3	0.2 – 0.3	0.66 – 0.68	688 – 1200
Jansen (2016) [8]	15.7	1.348	1.164	0.89	-	0.87	9968
Spisz *et al.* (1965) [9]	83,182 – 632,537	1.652	1.07 – 1,468	0.648 – 0.889	-	-	823 – 1895
Maurya *et al.* (2005) [19]	0.110	**1.199**	**0.111**	**0.093**	-	-	-
Cen and Xu (2010) [21]	6.5	**1.688**	**1.557**	**0.922**	-	-	-

3

Preliminary Tests

Many (preliminary) tests have been performed between the start and finish of this thesis, which are visualized in a flow chart in Figure 3.1. It can be seen that most of the tests can be performed in parallel, except for the thrust bench test sequence between the two leak tests. This sequence can be performed multiple times, but not before it has been verified that the leaks have been reduced to acceptable levels, which will be explained in more detail in Section 3.1. Another leak test after the sequence(s) was done, which was to check if the leak remained at the acceptable levels. As for the optical characterization test, this test was needed to determine the nozzle geometry, which will be described in Section 3.2. Analyzing the thrust bench test sequence, it can be seen that calibration test of the AE-TB-5m was done before and after thrust bench test, which will be explained in Section 3.3. Note that the calibration test of the Varying Turn-Density Coil (VTDC) was NOT performed, which will be explained in Subsection 3.3.4. Finally, in Section 3.4 the AE-TB-5m FCF test is presented in which it is described how the force correction factor was determined.

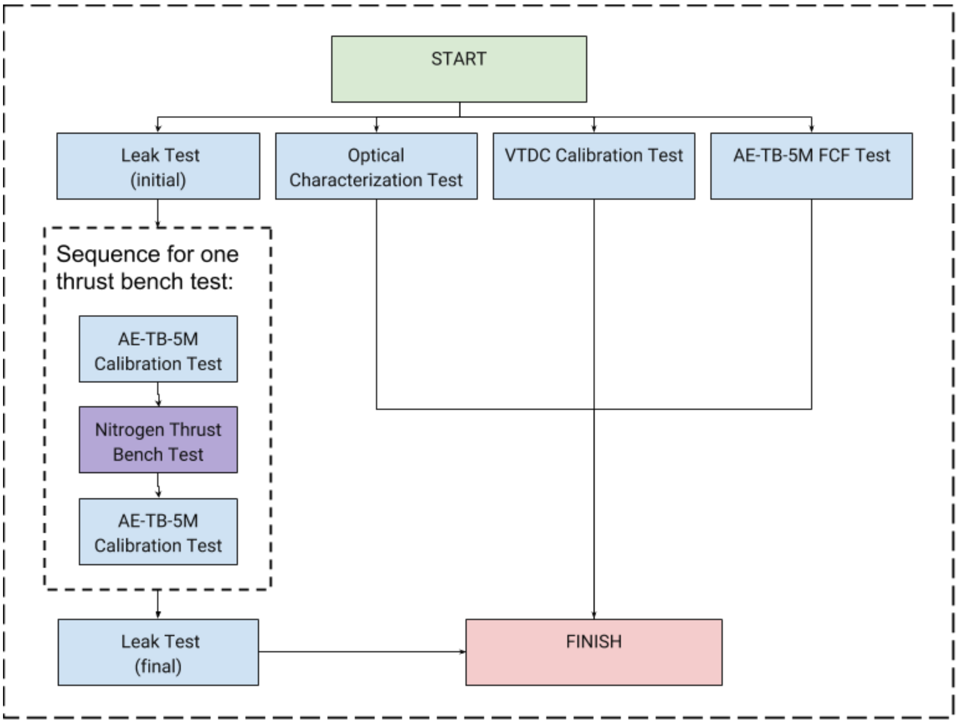

Figure 3.1: All the required tests for thrust bench tests with gaseous nitrogen for the 3rd gen. MEMS-VLM chip are presented here in a flow chart, where the preliminary tests are indicated with blue and the thrust bench test is indicated with purple. Note that the tests can be performed in parallel, except for the tests between and including the leak tests. Also, the thrust bench test sequence can be repeated multiple times, as long as before the first test and after the last test a leak test is carried out.

3.1. Leak Test

In this section the leak test is described. Firstly, in Subsection 3.1.1 the test plan is presented, which includes the goal of the test, the measured parameters and the success criteria. Hereafter, the test set-up and test procedure are presented in Subsections 3.1.2 and 3.1.3, respectively. As for the test results and analysis, these are presented in Subsection 3.1.4. Finally, a summary is presented in Subsection 3.1.5.

3.1.1. Test plan

Purpose

When the thrust bench test is carried out, a mass flow sensor will be used to measure the mass flow that moves through the nozzle of the MEMS-VLM chip. This mass flow sensor is integrated in the propellant feed system that is needed to provide the gaseous nitrogen. However, when there is a certain amount of leakage in the feed system, then the measurements made by the mass flow sensor will include both the mass flow caused by the leakage and the mass flow through the MEMS-VLM chip. This would then result in a false calculation of the performance, since the experimental mass flow is needed to determine the C_d and $(I_{sp})_{exp}$. Note that this only occurs when the leak rate is large enough for the mass flow sensor to measure it.

Therefore, it is required to perform a leak test: a MEMS-VLM chip with a blocked nozzle is placed in 1st gen. interface, after which the feed system is pressurized at a pressure range comparable to the thrust bench test and during this process the mass flow sensor should measure zero mass flow. Hence, this test will prove that there is no detectable leakage in the feed system. In case there is a detectable leak present, then this leakage needs to be reduced to an acceptable level. Furthermore, it was presented in Figure 3.1 that the leak test needs to be performed twice: once before the thrust bench tests (LT-01) and once afterwards (LT-02). The initial leak test was needed because the thrust bench tests could not be performed before it was proven that the leak rate was reduced to an acceptable level. The final leak test was done to check if the leak rate remained acceptable, since any damage that possibly occurred during the thrust bench test could increase the leak rate. Hence, the following objective was made:

"Ensure that the leak rate of the feed system is undetectable by the mass flow sensor in order to guarantee accurate measurements of the mass flow through the nozzle of the 3rd gen. MEMS-VLM chip."

Relevant parameters

The parameters that are relevant for this test can be found in Table 3.1. It can be seen that the chamber pressure is the control variable that would be varied between $3-7[bar]$ for leak test that was done before the thrust bench tests, and between $3-6[bar]$ for the leak test that was done afterwards. This is because the planned pressure range for the thrust bench test was $2-6[bar]$ (see Section 4.1.2), but the actual pressure range was $2-5[bar]$ (see Section 5.2). Note that the differences in pressure range between the leak test and the thrust bench test is exactly $1[bar]$. This is because the leak tests were done at (standard) atmospheric pressure and the thrust bench tests were done at (near) vacuum. To further elaborate: leakage is caused by a pressure difference and by increasing the pressure range with $1[bar]$, the leak tests better represent leak rates that would occur during the thrust bench test. The second parameter in Table 3.1 is the mass flow, which is expected to remain zero in case no leakage is detected and is thus independent of the chamber pressure.

Success criteria

In order to determine if the test was considered successful, a few success criteria were created, which are presented in Table 3.2. Note that in case of leakage, the test could still be considered successful if the following was carried out and documented: the location of the leakage was detected and the leakage was reduced to an undetectable value.

Table 3.1: Relevant parameters for the leak test.

Parameters	Description	Variable
P_c	Chamber pressure provided by the General Purpose Feed system (GPF) and increased with increments of $1[bar]$. Note the pressure range differs for the leak test that is done before the thrust bench tests and the one that is done afterwards.	Controlled: $3-7[bar]$ or $3-6[bar]$
$(\dot{m})_{exp}$	Mass flow measured by the Brooks 5850S, which is expected to remain zero.	Independent: $0[ml/min]$

Table 3.2: Success criteria for the leak test.

Criteria	Test Acceptance
SC-LT-01	All the parameters as described in Tables 3.1 have been measured and documented.
SC-LT-02	The measured mass flow was zero for the whole pressure range.

3.1.2. Test set-up

The test set-up for the leak test is almost the same as for the thrust bench test, which is described in Section 4.2. Therefore, in this subsection only the differences of the set-up will be described. Instead of the "01-LS2-02" chip, for this set-up a chip with a blocked nozzle is needed: the 01-Bs1-01. It is important to integrate this blocked chip in the 1st gen. interface, because if this set-up is pressurized and no leakage is detected, then it has been proven with this test that there is no detectable leakage between the N2-bottle and the inlet of the MEMS-VLM chip. The equipment needed to properly perform the leak test can be found in Table 3.3.

Table 3.3: Equipment needed to perform the leak tests.

Item Name:	Description:
Blocked MEMS-VLM chip: "01-Bs1-01"	The 01-Bs1-01 chip was incorrectly manufactured, which resulted in a nozzle throat that was fully blocked. This chip was placed integrated in the 1st gen. interface to block the nitrogen flow.
Pendulum thrust bench: AE-TB-5m (see Figure 3.10)	This is part of the set-up: the 1st gen. interface was integrated at the bottom of the pendulum arm of the AE-TB-5m.
Propellant feed system (see Figure 4.5)	Provides gaseous nitrogen from the N2-bottle all the way to the 01-Bs1-01 chip. The feed system also has the ability to measure mass flow using the Brooks 5850S mass flow controller.
Vacuum oven: Heraeus Vacutherm (see Figure 4.17)	This is part of the set-up. It also has the ability to measure the ambient pressure and to provide a vacuum environment.
Pressure sensor (MS5837-30BA) integrated in the 1st gen. interface [22]	Used to measure the pressure near the inlet of the 01-Bs1-01 chip, which is needed to verify if the planned input pressures were obtained.
DAQs and cleanroom computer (see Figures D.8-D.3)	Used to measure and digitalize all the experimental data. The available DAQs are: NI PXI-8331, NI PXI-6229 and NI PXI-4220.

3.1.3. Test procedure

All the required steps for the leak test are described in Tables 3.4 and 3.5 .

Table 3.4: Detailed test procedure for the leak test - Part 1

Step	**Description**	**Performed Y/N**	**Date & time**
1.	Use Subsection 3.1.2 and Table 3.3 to verify if the test set-up is complete: a blocked MEMS-VLM chip has been integrated in the 1st gen. interface and the interface has been attached to the AE-TB-5m thrust bench, the thrust bench has been configured and placed inside the vacuum chamber, all the tubes between the 1st gen. interface and the GPF are connected, all the sensors are connected to the cleanroom computer.		
2.	Turn on the required devices/equipment simultaneously and wait 1 hour for the devices to reach a stable temperature, before performing step 5:		
	1. Turn on the E030-10 and D030-10 Power Supply Unit (PSU) (See Figure 4.13a), which have a 1 hour warm-up time.		
	2. Turn on the Brooks 5850S sensor (See Figure 4.10a), which has a 45 minutes warm-up time.		
	3. Turn on the clean room computer and log in with the local administrator account. The current login is *".\localadmin"* and the current password is *"sse_cr03"*).		
	4. Turn on the USB hub that connects the cleanroom computer with the NI-USB-6008 (,NI-USB-9262) and NI-USB-8451 Data Acquisition System (DAQ).		
3.	Perform the following checks:		
	1. Open the *"main_marsil_TEST_wDisplacementSensor.vi"* LabVIEW file, check if the data will be saved to the right folder, run the file, check if all the sensors read out measurements (that make sense), check if the valve is able to open/close (produces clicking sound), stop the file and close the program. Note that if the program produces an error, the user should figure out the source of the error and solve it.		
	2. Check if the N2 storage bottle has a sufficient amount of pressurized nitrogen gas by opening the line-in rotary valve and reading the pressure indicator of the pressure gauge. In case this is false, stop the experiment and send an email to the cleanroom manager requesting to replace the N2 bottle.		

Table 3.5: Detailed test procedure for the leak test - Part 2

Step	Description	Performed Y/N	Date & time
4.	Open the *"main_marsil_TEST_wDisplacementSensor.vi"* LabVIEW file.		
5.	Perform the leak test:		
	1. Click on the arrow button at the top left of the LabVIEW interface in order to run the program.		
	2. Set the pressure regulator at X [bar] gauge pressure, which is X+1 [bar] absolute pressure.		
	3. Open both the shut-off valve and the flow path selector valve.		
	4. Open the VHS-M/M-24V valve by turning on the button *"Open valve"* in LabVIEW in order to let the nitrogen gas flow to the MEMS-VLM chip.		
	5. Observe if the Brooks 5850S measures a mass flow. In case this is false, there is no measurable leakage and thus move on to step 6. In case this is true, there is a leakage and the test has failed: stop the test, find the source of the leakage, find a solution and redo the leak test.		
	6. Close the VHS-M/M-24V valve by turning off the button *"Open valve"* in LabVIEW.		
	7. Close both the shut-off valve and the flow path selector valve.		
	8. Repeat steps 5.1-5.8 for the same/other pressure(s) if required.		
6.	Stop the LabVIEW program, localize the stored data and copy the experimental data to a separate folder or a USB device.		
7.	Make sure that the N2 bottle, line-in rotary, shut-off and flow path selector valves are properly closed.		
8.	Turn off all the devices described in step 2.		
9.	Remove the test set-up from the vacuum chamber if no other tests will be carried out.		

3.1.4. Test results & analysis

As mentioned before, it was required to perform two leak test: LT-01 was done before the thrust bench tests and LT-2 was done afterwards. However, the raw experimental data of LT-01 got lost due to improper documentation. However, the findings for the test were documented, which can be found in Table 3.6. In the table the results for LT-02 are included as well. Luckily for LT-02 the experimental data was not lost, which is why the raw data of the pressure sensor and mass flow sensor are presented in Figures 3.2-3.3.

Table 3.6: Detailed test procedure for the leak test.

Leak Test	Description
LT-01	Pressure was increased until 6.7 [bar] and no leakage was detected. Since this test was done at atmospheric pressure, this means that the pressure difference between the feed system and ambient environment was 5.7 [bar].
LT-02	Pressure was increased until about 5 [bar] and a leakage was detected, which was located somewhere between the tube adaptor in the interface and the inlet of the MEMS-VLM chip. This means that a leakage happened at a pressure difference of 4 [bar]

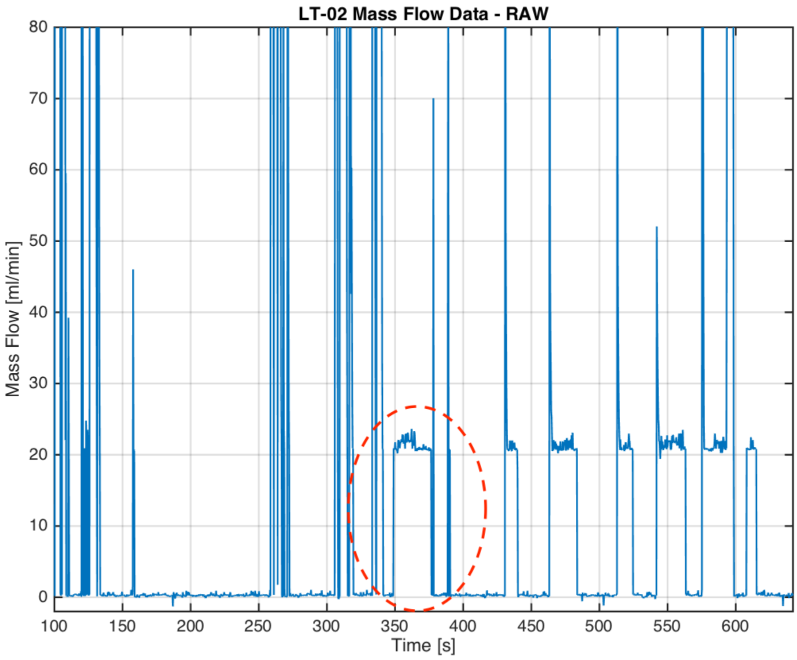

Figure 3.2: Raw experimental mass flow data plotted in MATLAB, where the red dotted circle indicates the moment leakage started.

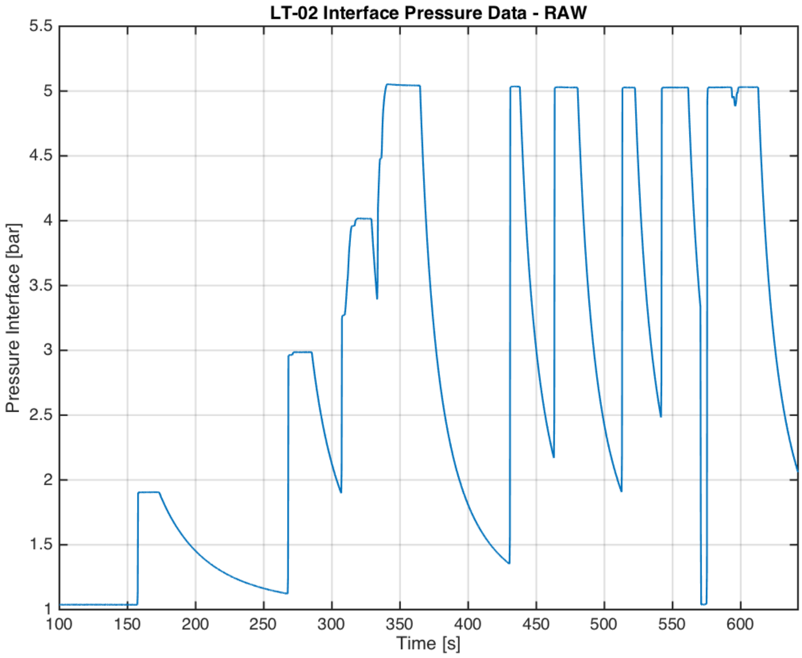

Figure 3.3: Raw experimental chamber pressure data plotted in MATLAB.

It can be seen that at $5[bar]$ or a pressure difference of $4[bar]$ leakage started: a mass flow of $21[ml/min]$ $(0.44[mg/s])$ was measured by the Brooks 5850S. Hereafter, the solenoid valve opened and closed a few times after making various adjustments to the setup. For example, the screws that hold the 1st gen. interface together and the tube connections were tightened. None of these actions had any effect on the leakage. Because during LT-01 a pressure of 6.7 [bar] resulted in no leakage and during LT-02 a leakage already occurred at a pressure of $5[bar]$, this means that the ”leak tightness” degraded during handling and performing the thrust bench tests. Since the pressure of $5[bar]$ was at atmosphere and the thrust bench test was done at vacuum, this means that during the thrust bench test a leakage could already occur at a pressure of $4[bar]$. Luckily, this was not the case for thrust bench tests TT-04 and TT-05 since the relation between the chamber pressure and experimental mass flow was linear as can be seen in Figure 6.1 in Subsection 6.1.2. If there would be a leakage of $0.44[mg/s]$, then this would definitely be seen in the graph.

Another important step was to localize the leakage. This was done by pressurizing different parts of the feed line (see Subsection 4.2.1) using the following order:

1. The Legris 4 5/32 push-in fitting (see Figure 4.5a) connected to the Brooks 5850S was disconnected, after which the system was pressurized up to $5[bar]$. After no leakage was found, the fitting was again connected to the feed system. Note that if the tube in this fitting is not properly connected, leakage could occur.

2. Inside the vacuum chamber the Swagelok SS-400-R-1 connector (see Figure 4.6a) was disconnected, after which the system was pressurized up to $5[bar]$. After no leakage was found, the connector was again connected to the feed system.

3. The tube that was connected to the output of the solenoid valve (see Figure 4.7) was disconnected, after which the system was pressurized up to $5[bar]$. After no leakage was found, the tube was again connected to the feed system.

4. The tube that was connected to the 1st gen. interface (see Figure 4.14) was plugged into another solenoid valve of the Lee Company, after which the system was pressurized up to $5[bar]$. After no leakage was found, the tube was again connected to the 1st gen. interface.

By following these steps it was proven that the leakage occurred between the tube connector of the 1st gen. interface and the inlet of the MEMS-VLM chip. The leakage could be caused by the tube connector, because the threads in the teflon block do not perfectly match with the tube connector, which is why silicon paste was added here to prevent leakage. It could be the case that during handling this connector was slightly turned, and because of that a gap between the silicon paste was opened/increased. It is recommended that this connector is glued in the teflon block in order to prevent possible leakage and to exclude this connector as a possible source of leakage. Another possible cause of the leakage could be deformations of the teflon block. It can be seen in Figure 3.4 that after all the experiments the teflon block has slightly bended (it used to be straight). Because the teflon block functions as a sealant, bending of the block could have caused the leakage.

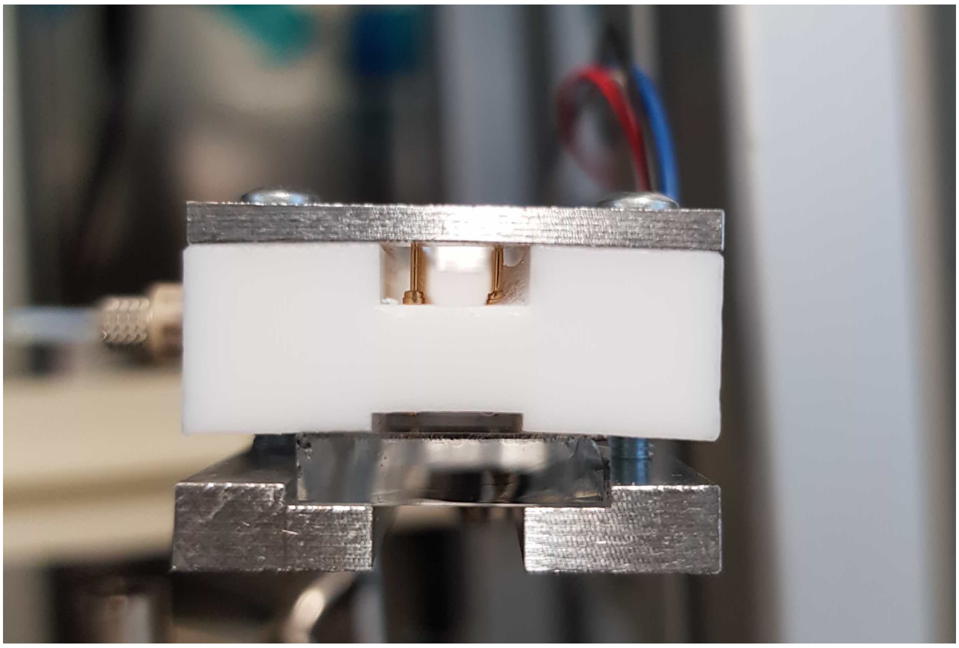

Figure 3.4: Bended teflon block of the 1st gen. interface after all the experiments.

3.1.5. Summary

Looking back at Table 3.2, the success criteria have not been met for all tests. For LT-01 no leakage was found at a pressure of $6.7[bar]$, but for LT-02 a leakage of $21[ml/min]$ ($0.44[mg/s]$) was found at a pressure of $5[bar]$. This means that LT-02 cannot be concluded successful. However, it can be concluded that no leakage occurred during thrust bench tests TT-04 and TT-05, since the relationship between the pressure and mass flow was linear. The source of leakage was either the bended teflon block of the 1st gen. interface or the tube connector inside the teflon block that required silicon paste to reduce leakage. Therefore, it is recommended that this tube connector is glued in the teflon block. This will either help reducing the leakage or help determine the true source of the leakage.

3.2. Optical Characterization Test

In this section the optical characterization test is described. Firstly the test plan is presented in Subsection 3.2.1; this includes the goal of the test as well as the measured parameters and the success criteria. This is followed by the test set-up and test procedure that are presented in Subsections 3.2.2 and 3.2.3, respectively. The test results and analysis are presented in Subsection 3.2.4. Finally, a summary is presented in Subsection 3.2.5.

3.2.1. Test plan

Purpose

The optical characterization test was used to determine the nozzle geometry, which was needed to help meet Subgoal 1 presented in Section 1.2. This is because the nozzle geometry is needed to calculate the ideal mass flow, the ideal thrust coefficient (or thrust force) and the ideal specific impulse which are needed to determine the performance parameters of Subgoal 1. Furthermore, the nozzle geometry is also required to calculate the throat Reynolds number. The designed nozzle geometry was already known from de Athayde Costa e Silva *et al.* (2017) [10]. However, it was not known what the precision was of the manufacturing method for the MEMS-VLM chip. Therefore the following question arose: how well do the manufactured dimensions and shape of the nozzle match with the designed ones? This question is important because the nozzle throat and exit area are used to calculate the ideal mass flow, thrust force and specific impulse. For example, a nozzle throat area that has increased twice in size will double the ideal mass flow (see Equation 2.2). Therefore, an optical characterization test was needed and the following objective was made:

"Experimentally determine the nozzle geometry of the manufactured 3rd gen. MEMS-VLM chip with design-code 01-LS2-02 in order to verify the designed parameters and to enable calculating the throat Reynolds number, ideal mass flow, ideal thrust force and ideal specific impulse."

Relevant parameters

The parameters for the nozzle geometry including the designed values can be found in Table 3.7 and a microscopic picture of the whole nozzle can be found in Figure 3.5. The nozzle parameters and the corresponding description are presented in the first and second column of the table, respectively. The third column consists of the designed values. which which were based on the article of de Athayde Costa e Silva *et al.* (2017) [10]. It was already mentioned before why the nozzle throat and exit area were needed. The reason why both the width and height are needed at the nozzle throat and exit (W_t, W_{nd}, h_t and h_{nd}), is because the corresponding areas (A_t and A_e) are not circular but rectangular, which is due to the nozzle being a 2D-conical (slit) nozzle instead of a 3D-conical nozzle. As for the nozzle convergence and divergence half angles (θ_{nc} and θ_{nd}), these were described in Zandbergen (2016) [13] as both affect the discharge factor (C_d) and the divergence half angle also affects the nozzle quality (ξ_F). However, during this thesis the effect of different half angles on the performance were not investigated due to lack of time. It is therefore recommended to investigate this by performing experiments with the other MEMS-VLM chips that have a different nozzle geometry in order to find the most favorable geometry. Finally, the P_w and D_H will be needed to determine the throat Reynolds number.

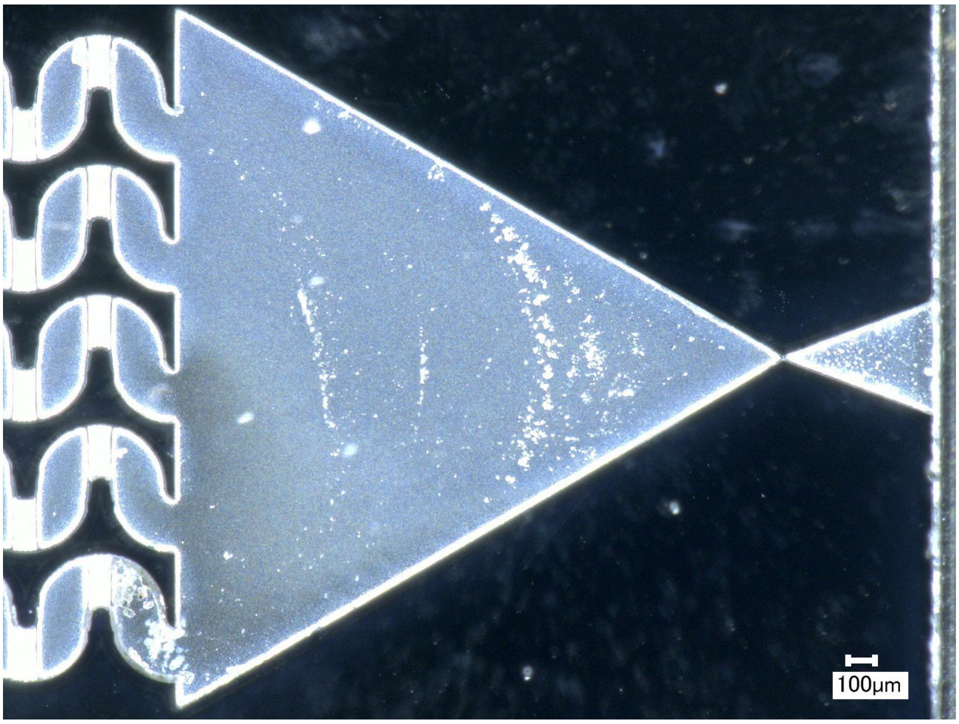

Figure 3.5: Image of the "01-LS2-02" MEMS-VLM chip produced by the VHX-2000E Digital Microscope at a magnification of 100x. During thrust bench tests the nitrogen gas will flow from the five serpentine flow channels at the left to the convergent part of nozzle, through the nozzle throat and exit through the divergent part of the nozzle.

Table 3.7: Designed values of the nozzle geometry of the ”01-LS2-02” chip as described by de Athayde Costa e Silva *et al.* (2017) [10].

Parameters	**Description**	**Designed values**
L_{nc}	Length of the convergent part of the nozzle.	2600 $[\mu m]$
L_{nd}	Length of the divergent part of the nozzle.	645 $[\mu m]$
W_{nc}	Width of the convergent part of the nozzle.	3000 $[\mu m]$
W_{nd}	Width of the divergent part of the nozzle.	500 $[\mu m]$
W_t	Width of the nozzle throat.	45 $[\mu m]$
h_{nd}	Height of the divergent part of the nozzle.	100 $[\mu m]$
h_t	Height of the nozzle throat.	100 $[\mu m]$
A_t	Nozzle throat area.	4500 $[\mu m^2]$
A_e	Nozzle exit area.	50000 $[\mu m^2]$
AR	Nozzle area ratio.	11.1 $[-]$
θ_{nc}	Nozzle convergence half angle.	29.6 $[^{\circ}]$
θ_{nd}	Nozzle divergence half angle.	19.4 $[^{\circ}]$
R^*	Angle between convergent and divergent part of the nozzle	131 $[^{\circ}]$
P_w	Wetted perimeter	290 $[\mu m]$
D_H	Hydraulic diameter	62 $[\mu m]$

Success criteria

In order to determine if the test was considered successful, a few success criteria were created which are presented in Table 3.8.

Table 3.8: Success criteria for the optical characterization test.

Criteria	**Test Acceptance**
SC-OCT-01	All the parameters as described in Tables 3.7 have been determined using a microscope, except for the parameters for which this was not possible.
SC-OCT-02	Every measurement of the parameters has been documented.
SC-OCT-03	A picture is made of every parameter including the reference scale.

3.2.2. Test set-up

The optical characterization test was performed with the VHX-2000E Digital Microscope of Keyence (see Figure 3.6), which is located in the Microscope Lab of the Delft Aerospace Structures and Materials Laboratory (DASML). Note that access to the DASML is granted after following the safety training, which is held each month for which a subscription can be done via Marianne de Knegt-Overduin (m.deknegt-overduin@tudelft.nl). Also, access to the Microscope Lab needs to be arranged via Frans Oostrum (F.G.C.Oostrum@tudelft.nl), who is the supervisor of the lab. Furthermore, a printed version of the user manual of the microscope is available in the Microscope Lab.

Figure 3.6 shows that the microscope is connected to both a controller and a computer. The controller can be used to operate the microscope, though this can also be done manually. The computer has software with a real-time display of the image captured by the microscope. With measurement tools that are included in the software it is possible to determine distances, angles, etc. Note that that these measurements are done by manually on points of the image, which means that the tool is prone to human errors as precise selection is difficult with a mouse. Nevertheless it was possible to make pictures of the image (including the indicated measurements) and store it on the computer. There were three lenses available: Lens 1 with a magnification range of 20x-200x, Lens 2 with a range of 100x-1000x and Lens 3 with a range of 500x-5000x. Note that the optical characterization test only required Lens 1 and Lens 3. Also note that because the equipment is very expensive, changing the lenses should always be done by the supervisor of the lab. Apart from the microscope, the experiment required other materials and resources as well. The complete list can be found in Table 3.9.

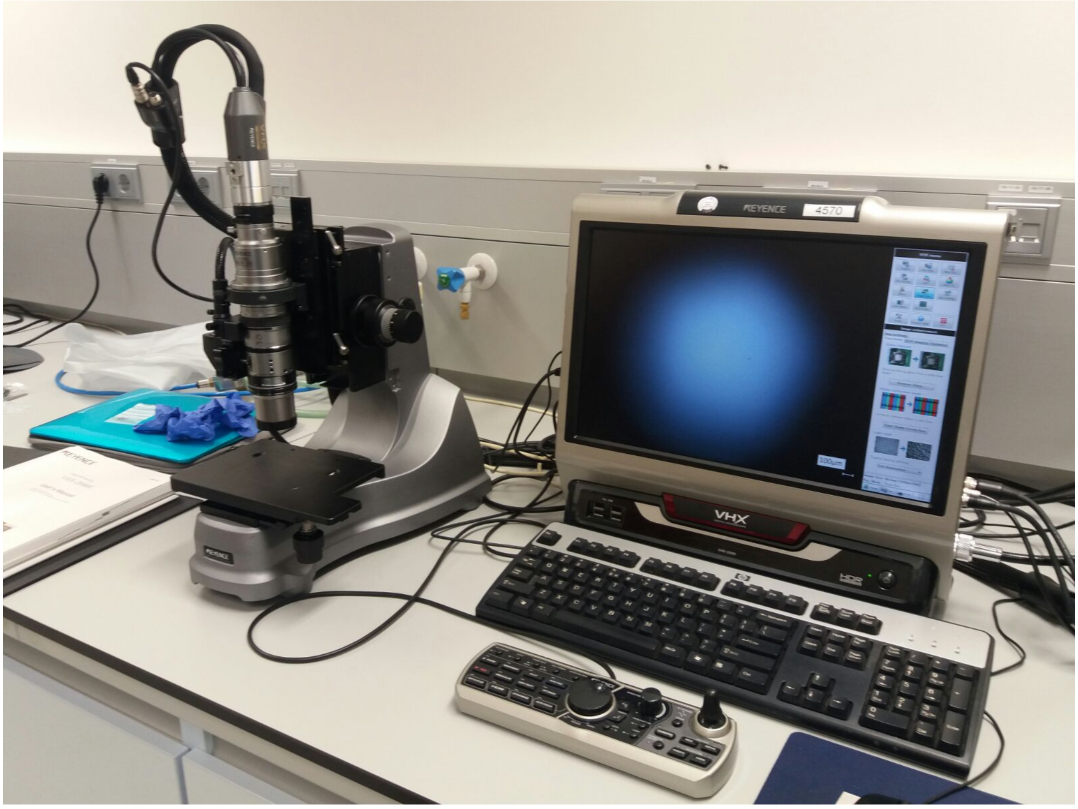

Figure 3.6: The VHX-2000E Digital Microscope including the computer and controller. Three lenses are available: the Lens 1 has a magnification range of 20x-200x, the Lens 2 has a range of 100x-1000x and the Lens 3 has a range of 500x-5000x.

Table 3.9: Equipment and resources needed for the optical characterization test.

Item Name	**Description**
VHX-2000E - Digital Microscope (Keyence)	Used to perform the test. Depending on the lens, different magnification ranges 20x-200x (Lens 1), 100x-1000x (Lens 2) or 500x-5000x (Lens 3) can be achieved.
USB-stick	Needed to store the test data.
3rd gen. MEMS-VLM chip	The sample that shall be tested.
Clamp	Enables an inside view of the nozzle of the chip.
Examination gloves - Finite P Indigo AF Nitrile (Polyco Bodyguards)	Needed to keep the chip clean.
Klerwipe 70|30 IPA (Ecolab)	Needed for cleaning the chip and test environment.
Supervisor of the Physics and Chemistry Lab (inside DASML)	Needed for instructions before testing and for changing the lenses in case needed. Current supervisor: Frans Oostrum.

3.2.3. Test procedure

All the required steps for the optical characterization test are described in Table 3.10.

Table 3.10: Detailed test procedure for the optical characterization test using the VHX-2000E Digital Microscope.

Step	**Description**	**Performed Y/N**	**Date & time**
1.	Use Table 3.9 to verify if the test set-up is complete. Note that in case a different lens is needed, the supervisor of the Physics and Chemistry Lab should always be consulted.		
2.	Turn on the computer connected to the microscope.		
3.	Remove plastic cover from the microscope.		
4.	Turn on the light with the microscope controller.		
5.	Remove protection cap from the microscope lens.		
6.	Clean the stage of the microscope and place the chip (test sample) straight on the stage w.r.t. the gridlines of the software, since any misalignments can inhibit making precise measurements with the software tools.		
7.	Adjust microscope to the required settings: 1. Use the magnification ring to set required the magnification. 2. Use the focus control knob to obtain an image that is in focus.		
8.	Perform the measurements: 1. Create a folder on the computer in which the measurement data needs to be stored. 2. Change the save location to this folder. 3. Optional: add grid lines as aid when using the measure-tool software on the computer. 4. Click on different points on the picture with the measure-tool in order to display the dimensions/angles of the parameters. 5. Repeat step 4 a few times to obtain the measurement inaccuracy.		
9.	Data storage: 1. Insert USB-stick in the computer. 2. Store data on USB-stick. 3. Remove USB-stick from computer		
10.	Remove the chip (test sample) from the stage.		
11.	Place protection cap on the microscope lens.		
12.	Turn off light with the microscope controller.		
13.	Place plastic cover over the microscope.		
14.	Turn off the computer.		

3.2.4. Test results & analysis

The results of the optical characterization test of the ”01-LS2-02” chip using the VHX-2000E Digital Microscope are presented in Table 3.11. In the first column of the table the nozzle parameters are presented. The second column explains the method that was used to determine the experimental values in the third column. Note that below each measurement the magnification is given between brackets and that the uncertainty becomes smaller for larger magnifications as these provide more detailed pictures. These uncertainties were determined by counting the pixels of the boundaries of the parameters and converting the number of pixels to metric values. In the fourth column the designed values are presented and in the final column the percentage difference between the experimental and designed values is presented. The table shows that these percentages vary for each parameter, where the largest percentage difference values are found for A_t, AR, W_t and D_H, and the smallest values are found for θ_{nc}, θ_{nd}, W_{nd}, L_{nd} and R^*. This indicates that either the manufacturing procedure of the MEMS-VLM chips needs to be improved regarding the precision, or that each manufactured chip needs to undergo an optical characterization test in order to determine real nozzle geometry. The large percentage difference values are unacceptable because the nozzle geometry is needed to determine the performance of the ”01-LS2-02” chip. For example, the real throat width is more than twice as small compared to the designed throat width, which means that for constant pressure and characteristic velocity the ideal mass flow would also reduce more than half and this again affects the discharge factor (see Subsection 2.2.1).

Table 3.11: Test results of the optical characterization test for the nozzle parameters. **Note that the percentage difference was calculated as follows: |A-B|/(0.5A+0.5B); with A and B being the the experimental and designed values.**

Nozzle Parameters	**Method**	**Experimental Value ± Uncertainty**	**Designed Value**	**Percentage Difference**
L_{nc}	Software tools	2.23e3 ± 2e1 $[\mu m]$ (100x magnification)	2600 $[\mu m]$	15.3 [%]
L_{nd}	Software tools	606.8 ± 5.3 $[\mu m]$ (500x magnification)	645 $[\mu m]$	6.1 [%]
W_{nc}	Software tools	2575 ± 27 $[\mu m]$ (100x magnification)	3000 $[\mu m]$	15.2 [%]
W_{nd}	Software tools / Pixel counting	471.4 ± 4.1 $[\mu m]$ 471.7 ± 4.1 $[\mu m]$ (500x magnification)	500 $[\mu m]$	5.8 [%]
W_t	Pixel counting	17.4 ± 1.2 $[\mu m]$ (5000x magnification)	45 $[\mu m]$	88.5 [%]
h_{nd}	Pixel counting	90 ± 5.6 $[\mu m]$ (200x magnification)	100 $[\mu m]$	10.5 [%]
h_t	Estimation	81 ± 5 $[\mu m]$	100 $[\mu m]$	21.0 [%]
A_t	Calculation	1.4e3 ± 1.3e2 $[\mu m^2]$	4500 $[\mu m^2]$	105 [%]
A_e	Calculation	4.2e4 ± 2.7e3 $[\mu m^2]$	50000 $[\mu m^2]$	17.4 [%]
AR	Calculation	30 ± 3	11.2 [−]	92.0 [%]
θ_{nc}	Calculation	29.8 [°]	29.6 [°]	0.7 [%]
θ_{nd}	Software tools	20.5 [°]	19.4 [°]	5.5 [%]
R^*	Calculation	127.5 [°]	131 [°]	2.7 [%]
P_w	Calculation	197 ± 18 $[\mu m]$	290 $[\mu m]$	38 [%]
D_H	Calculation	28.7 ± 3.7 $[\mu m]$	62 $[\mu m]$	74 [%]

Coming back to the second column, it can be noted that four different methods were used: software tools, pixel counting, estimation and calculation. As mentioned before the microscope was attached to a computer with "software tools", thus these were used to determine some of the experimental values. It was also mentioned before that this method is prone to human errors due to imprecise control of the mouse. The "pixel counting" method on the other hand does not have this problem. This method was performed with the standard Preview app of macOS, where the number of pixels (both in horizontal and vertical direction) could easily and precisely be counted by selecting a rectangular area. The number of pixels was then compared to the number of pixels of the reference scale in order to determine the metric value. This is all visualized in Figure 3.7 for W_t: the reference scale of 43.57 $[\mu m]$ corresponds to 1000 horizontal pixels and the nozzle throat width consists of 400 vertical pixels, which therefore corresponds to 17.4 $[\mu m]$. Note that in Figure 3.7b not all pixels of the reference scale have been selected as the white line is actually 1010 pixels long: the end blocks are each 10 pixels and line in between is 990 pixels wide. This means that only half of the end block pixels were selected, which was done because the software links the 43.57 $[\mu m]$ to this segment of the reference scale. Thus, the pixel counting method enables more precise measurements for straight lines compared to the standard software tools.

The precision of the software tool only tends to be a problem when the selection area is small and not when it is large. An example of a large selection area can be found in Table 3.11 where both the software tools and pixel counting were applied for determining W_{nd}. The difference was merely 0.3 $[\mu m]$, which was negligibly small compared to the measurement values (471.4 and 471.7 $[\mu m]$). An example of a small selection area can be found in Appendix H, where another optical characterization test is presented for the "01-Ws2-01" chip. In the appendix in Table H.1 (and Figures H.2-H.3) it can be seen that both the software tools and pixel counting were applied for determining W_t. The

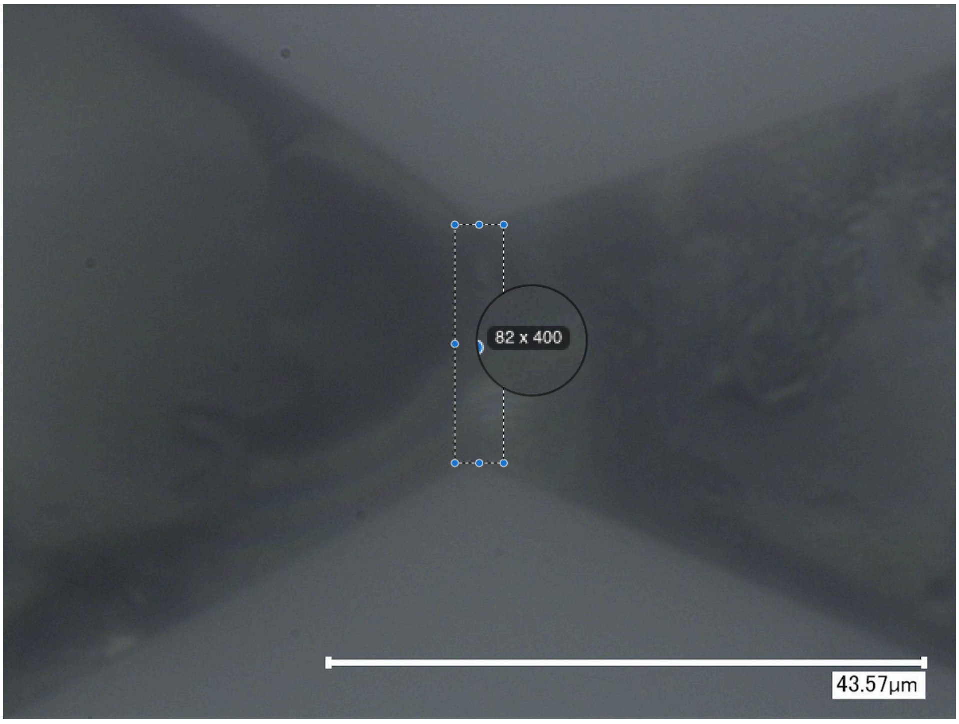

(a) It can seen that the height of the selected area has 400 pixels that correspond to the nozzle throat width.

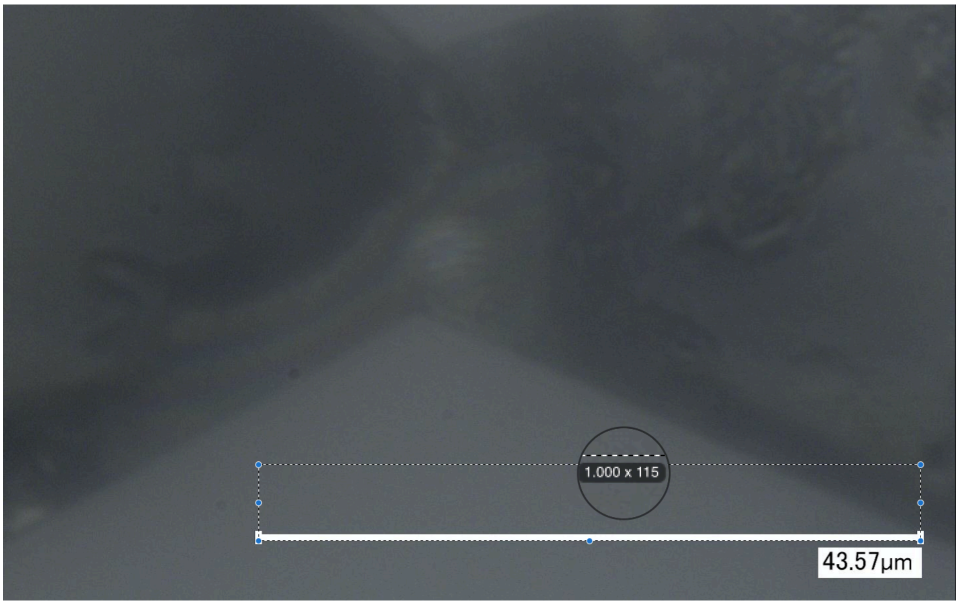

(b) It can seen that the width of the selected area has 1000 selected pixels that correspond to white line of the reference scale.

Figure 3.7: Demonstration of the pixel counting method taking W_t of the "01-LS2-02" as an example. Note that the white line of the reference scale is actually 1010 pixels wide: each thick end block is 10 pixels wide and the line in between is 990 pixels wide. However, the software only links 1000 pixels to the 43.57 $[\mu m]$, which means that only half of each thick end block were selected. Images of the were produced by the VHX-2000E Digital Microscope at a magnification of 5000x.

difference here was 1 $[\mu m]$, which is much bigger when compared to the measurement values (20.0 and 19.0 $[\mu m]$). The impact of this difference is also bigger. For example, letting nitrogen gas flow through a given MEMS-VLM chip with a constant height of 100.0 $[\mu m]$ throughout the whole nozzle and a constant chamber pressure/temperature. If for this MEMS-VLM chip the nozzle throat width would actually be 19.0 instead of 20.0 $[\mu m]$, this would result in a decrease of 5 [%] in the theoretical mass flow, which would also result in a 5 [%] decrease in the discharge factor. Imagine the possible impact on the discharge factor for the "01-LS2-02" chip if the actual throat width was not measured, since the designed value was 45 $[\mu m]$ and the experimental value was 17.4 $[\mu m]$.

As for the "estimated" method, this was required as it was not possible with Lens 1 (20x-200x) to get a complete picture of h_t as it was too deep inside the nozzle (see Figure 3.8). It should be noted that both Lens 2 and Lens 3 were not able to provide any picture of the nozzle throat due to lack of illumination. This could be explained by the difference in the configuration of the light source. Lens 2 and Lens 3 have a light source that is further away from the lens, while the light source of Lens 1 is much closer to the lens. This means that when Lens 1 is "looking" inside the nozzle throat the light can reach further as it shines more perpendicular compared to the light for Lens 2 and Lens 3. A solution for Lens 2 and Lens 3 could be illuminating the nozzle with another light source from the side, which should be possible as the top of the chip is made out off glass. It is recommended that this should be investigated as these lenses have a higher magnification factor, which results in better quality images and possibly lower uncertainties. Coming back to the "estimated" method, this was basically an assumption based on the work of Van Wees (2017) [3], who performed a scanning electronic microscopic test on a 2nd gen. MEMS-VLM chip. This test revealed that the manufacturing method (deep reactive ion etching) of the chip was less effective for narrow channels: at the nozzle throat the height was 84.7 $[\mu m]$ and the width was 38.7 $[\mu m]$, while at the nozzle exit the height was 94.0 $[\mu m]$ and the width was 495.6 $[\mu m]$. This is about a 10 [%] difference in etch height. Therefore it was assumed that the nozzle throat of the "01-LS2-02" chip would also be 10 [%] smaller than the at the nozzle exit. However, the throat width of 17.4 $[\mu m]$, being about twice as small compared to the throat width of the nozzle of Van Wees (2017) [3], should then result in an even smaller throat. Since this was not possible to verify, the estimated value does hold an uncertainty that was not possible to verify. Note that scanning electron microscopy was not used for the "01-LS2-02" chip because this test is destructive and makes the chip useless after running the test.

The final method, the "calculated" method, differed per parameter. Starting off with A_t and A_e, these were calculated by multiplying the corresponding width and length at each location. This is because the nozzle is in fact a slit, which means that the areas are not circular but rectangular. As for θ_{nc}, θ_{nd} and R^*, these were determined by applying basic trigonometry using L_{nc}, L_{nd}, W_{nc}, W_{nd} and W_t.

3.2.5. Summary

Looking back at Table 3.8, all the success criteria have been met, which means that this test can be concluded to be successful. This also indicates that the goal stated in Subsection 3.2.2 has been achieved. It can also be concluded that the difference between the designed values and the manufactured values of the nozzle of the "01-LS2-02" chip is unacceptable as these nozzle parameters are used to calculate the performance of the chip. The biggest difference was found for the nozzle throat width that was about a factor two smaller, which has a big influence on the discharge factor (C_d). Note that there was also a big discrepancy for the nozzle throat width of the 01-Ws2-01" chip that is described in Appendix H. It is therefore recommended that the precision of the manufacturing procedure for the MEMS-VLM chips should be improved. Otherwise, an optical characterization test needs to be carried out for each chip before a thrust bench test can be done. Furthermore, the nozzle throat height could not be determined with the microscope. It was therefore estimated based on the work of Van Wees (2017) [3], who found that that the throat was smaller compared to rest of the nozzle as the manufacturing method (deep reactive ion etching) was less effective in the narrow nozzle throat. Because h_t was estimated, this means that experimental value holds an unknown uncertainty. It is therefore recommended that during the manufacturing procedure of the MEMS-VLM chips, before the glass waver is bonded to the silicon waver, an optical characterization test is done such that the different heights inside the nozzle can be determined.

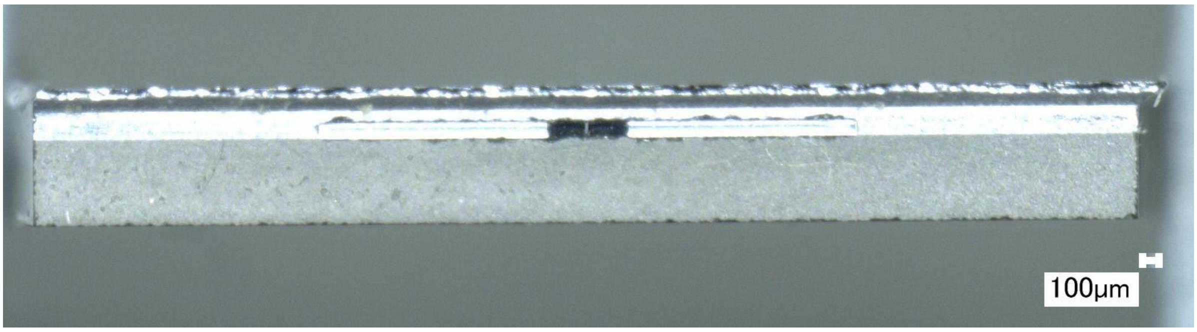

(a) Magnification factor of 50x.

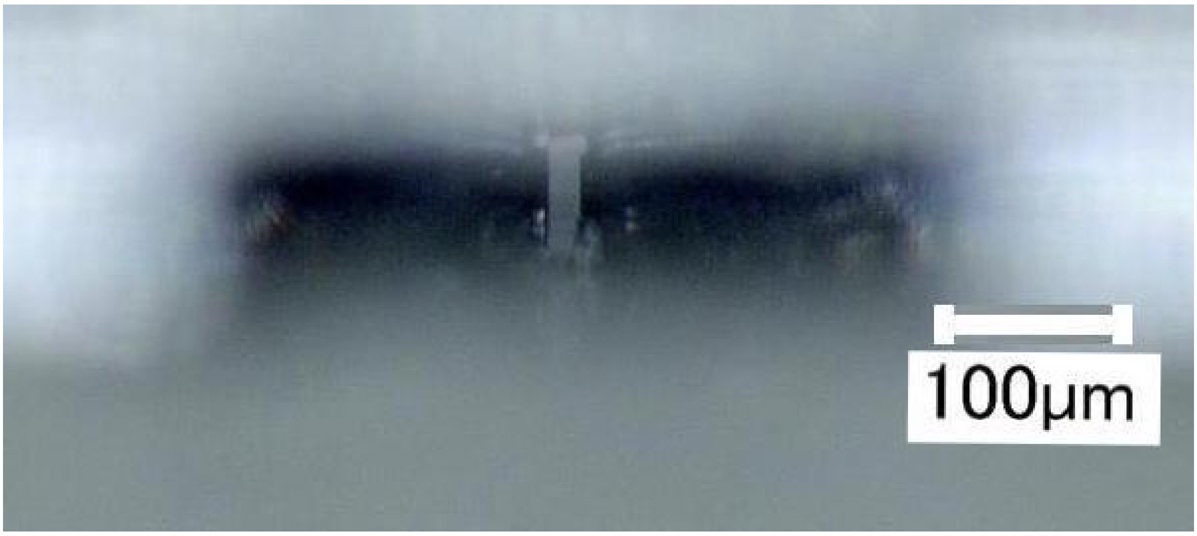

(b) Magnification factor of 200x.

Figure 3.8: Inside look of the ”01-LS2-02” MEMS-VLM chip produced by the VHX-2000E Digital Microscope. Note that the image of the nozzle throat is incomplete and seems distorted.

3.3. AE-TB-5m Calibration Test

In this section the calibration of the AE-TB-5m thrust bench (or pendulum calibration test) is described. First, in Subsection 3.3.1 the test plan is presented, which includes the goal of the test, the measured parameters and the success criteria. Hereafter, the test set-up and test procedure are presented in Subsections 3.3.2 and 3.3.3, respectively. As for the test results and analysis, these are presented in Subsection 3.3.4. Finally, a summary is presented in Subsection 3.3.5.

3.3.1. Test plan

Purpose

The AE-TB-5m, a pendulum thrust bench, is needed to determine the thrust values of the MEMS-VLM chip during the thrust bench test. However, the thrust bench can only be used to measure the displacement of its pendulum arm. This means that the change in pendulum arm displacement needs to be related to a known force. This known force came from the VTDC actuator as described in the thesis of Bijster (2014) [23], which is able to provide a magnetic force depending on the electrical input current. Therefore, the following objective was made:

"Experimentally determine the relationship between the change in pendulum arm displacement and the magnetic force of the VTDC applied to the pendulum arm in order to enable the AE-TB-5m to determine thrust values produced by the 3rd gen. MEMS-VLM chip(s).

Relevant parameters

The parameters that are relevant for this test can be found in Table 3.12. It can be seen that the control variable (I) varied from 0 to $2.5[A]$, which is done in ten steps and this means that the increments are $0.25[A]$. This variation process is done in the following manner: the current starts at zero and steadily increases with $50.0[mA/s]$ until it reaches the first plateau at $0.25[A]$ where it remains for $10[s]$, after this the current is decreased to zero with the same rate of $50.0[mA/s]$ and it remains at zero for $10[s]$, subsequently these steps are done for the remaining nine plateaus until the maximum of $2.5[A]$ is reached. Note that the reason why the current is steadily increased instead of a rapid jump, is because a rapid jump causes high unwanted fluctuations in the displacement. As for the reason why this electrical current range is taken, is because this range corresponds to a magnetic force range of $0-2[mN]$ produced by the VTDC and this was based on a sensitivity of $0.827[mN/A]$ as was determined by Jansen (2016) [8]. The magnetic force range is again based on the expected thrust range (see Section 4.1). As for the change in the average displacement (Δ_{disp}), this will be determined in Subsection 3.3.4. Note that the average is used, since the displacement of a pendulum fluctuates, which means that it keeps on increasing and decreasing at a certain balance point. Furthermore, it is expected that the change in the average displacement increases about linearly with the electrical current and the slope of this linear curve depends on the configuration of the AE-TB-5m (Jansen, 2016) [8].

Table 3.12: Relevant parameters for the AE-TB-5m pendulum calibration test.

Parameters	Description	Variable
I	The electrical current provided by the PSU and increased with increments of 0.25 $[A]$.	Controlled: 0-2.5 $[A]$
$F_{magnetic}$	Magnetic force produced by the VTDC as result of the induced currents. The sensitivity was determined to be 0.827 $[mN/A]$ by Jansen (2016) [8].	Dependent: 0-2 $[mN]$
Δ_{disp}	Change in the average displacement of the pendulum arm w.r.t. the displacement sensor.	Dependent $[\mu m]$

Success criteria

In order to determine if the test was considered successful, a few success criteria were created, which are presented in Table 3.13. Note that the SC-PCT-03 was included as the test is a failure when the average displacement does not increase for higher electrical currents.

Table 3.13: Success criteria for the AE-TB-5m pendulum calibration test.

Criteria	**Test Acceptance**
SC-PCT-01	The measurement data of the preset electrical current values produced by the PSU has been been stored.
SC-PCT-02	The measurement data of the displacement has been stored.
SC-PCT-03	The average displacement increases for higher electrical current values.
SC-PCT-04	It has been demonstrated that the AE-TB-5m calibration test is repeatable.

3.3.2. Test set-up

The equipment needed to properly perform the AE-TB-5m calibration test is elaborated in this section. As mentioned before the calibration test was done both before and after the thrust bench test. This means that the set-up for the calibration test is basically the same as the set-up for the thrust bench test. However, only the parts of the set-up that are relevant for the calibration test will be explained here. In short: the SM7020-D PSU is controlled in LabVIEW and provides an electrical current to the VTDC actuator, the actuator then induces a magnetic force on the AE-TB-5m, the resulting change in displacement of the pendulum arm is measured by the CS2 sensor and the measurement data is stored on the cleanroom computer with help of the DT6220/DL6230 DAQ.

AE-TB-5m

The AE-TB-5m, a pendulum thrust bench, this device was thoroughly investigated in the thesis of Bijster (2014) [23], after which it was improved and validated by Jansen (2016) [8]. It is therefore recommended to read these two thesis works to get a more in depth understanding about the AE-TB-5m, since the thrust bench will only be discussed here concisely. An overview of all the thrust bench components can be found in Figures 3.9 and 3.10. Note that for the calibration test the configuration of Figure 3.9 was used, since in Figure 3.10 the rotary spring and fluidic tube were not included. Also, in Figure 3.9 the AE-TB-5m was placed next to the vacuum chamber, while during the calibration test the thrust bench was placed inside the vacuum chamber.

Looking at the top of Figure 3.9, it can be seen that there is a "Balance fine tuner" present, which was 3D-printed and had the purpose of changing the balance point at which the pendulum arm fluctuates. By adding weights and/or changing the location of the weights, the balance point can be adjusted. It can be seen in the figure that one weight was sufficient for the set-up of the AE-TB-5m calibration test. Note that the bolts were used to restrict the rotation of the balance fine tuner.

The "Counter mass" is just below the balance fine tuner, which has the purpose of the adjusting the center of gravity and therefore the sensitivity and stability of the pendulum arm. Note that in the thesis of Jansen (2016) [8] it was mentioned that there were in total five counter masses, but only two of the five could be found as can be seen in Figure 3.9. Furthermore, the reason why there is a distance between the counter mass and the cross-beam, was because it was found through experimentation that this was needed for amplitude of the pendulum arm displacement to converge to a value between $10 - 15[\mu m]$. When this distance was reduced to zero the displacement amplitude would exhibit unstable behavior, for example: the amplitude would first converge to a value of $50[\mu m]$, after which it would diverge to (about) $160[\mu m]$, which was again followed by a convergence towards $30[\mu m]$.

The "Rotary spring" is located next to the cross-beam and has a spring constant of $0.64[Nm/rad]$. The purpose of the spring is to decrease the sensitivity, which results in an increased thrust range but a reduced accuracy. A typical measurable thrust range when using the rotary spring was about $0.1 - 15[mN]$ as found by Jansen (2016) [8]. Since the expected thrust range of the MEMS-VLM chip lies within $0 - 2[mN]$, it was investigated if it would be advantageous to exclude the spring. The opposite was found: it was necessary to include the spring for two reasons. The main reason was that without the spring the sensitivity would be to small: a magnetic force of $2[mN]$ caused the change in displacement to exceed $3000[\mu m]$, which exceeded the measurement capability / measurement range of the CS2 sensor. Another reason was that the amplitude of the displacement was very sensitive for disturbances, making it harder to directly observe the behavior of the displacement. Therefore, it is recommended to purchase a rotary spring with a lower spring stiffness. This would shorten the measurable thrust range and increase the accuracy, while maintaining a resistance against disturbances. It can also be useful to buy multiple springs with each having a different stiffness, since this will increase the flexibility of the thrust bench regarding the measurable thrust ranges and corresponding accuracies.

It can also be seen Figures 3.9 and 3.10 that the 1st gen. interface was attached to the bottom of the pendulum arm, which was done with a single M4 screw. Because of this, the interface can be misaligned and during the thrust bench test it is important to align the interface (and thus the thrust force direction) with the swing direction of the pendulum arm. Although, by doing a quick calculation it can be seen that the effect of misalignment is negligible. It was found in practice that it was easy to obtain a pointing accuracy of $10[^\circ]$. Therefore, let's say that the thrust force direction has an offset of $10[^\circ]$ with respect to the swing direction. Using simple trigonometry it can be seen that this will result in a measured thrust force that is merely $99.5[\%]$ of the true thrust force.

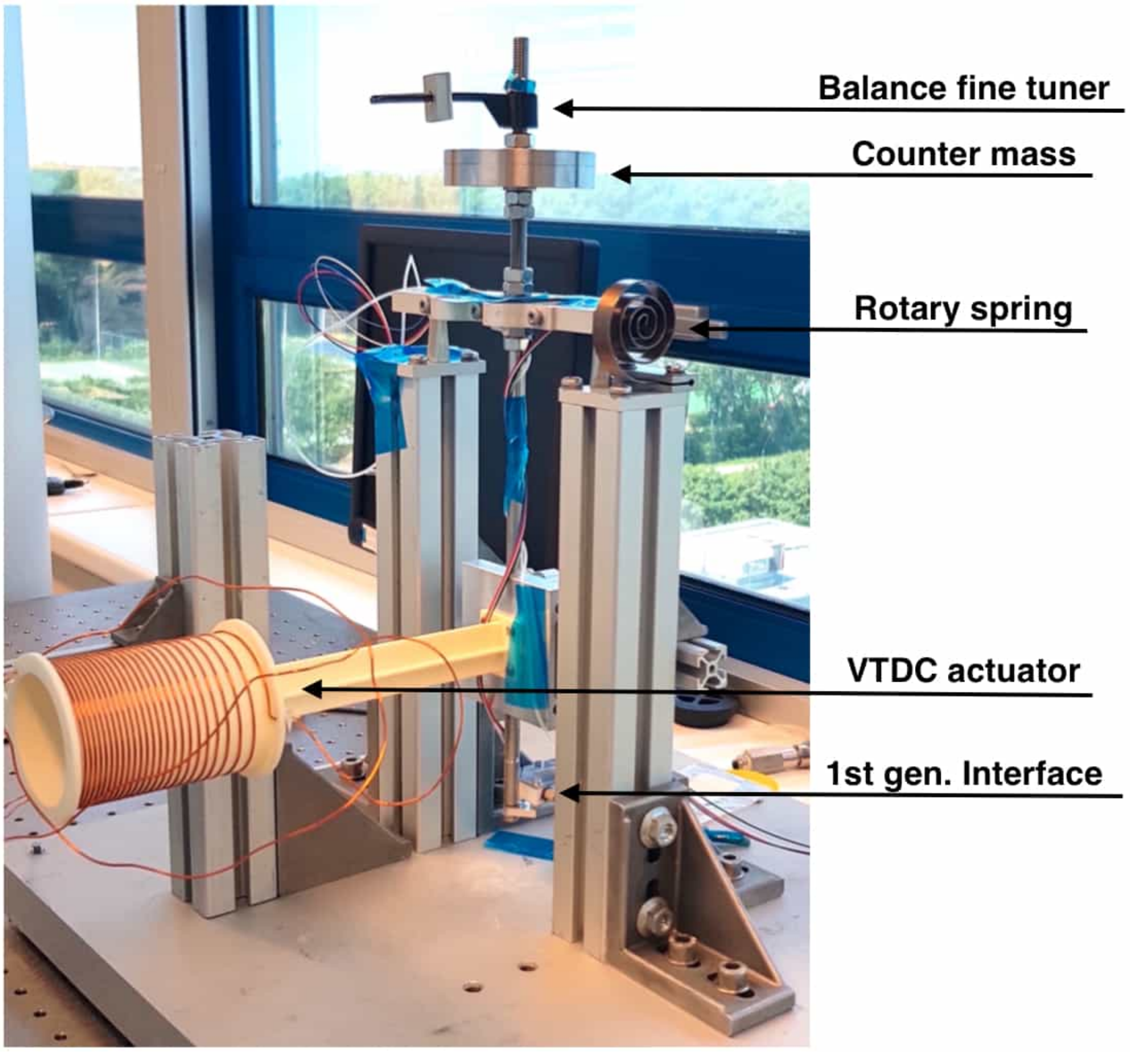

Figure 3.9: Overview of the thrust bench components with the 1st gen. interface (including the 3rd gen. MEMS-VLM) attached to the AE-TB-5m. It can be seen that the side of the VTDC with the high turn density is (at the left/) pointed away from the pendulum. Note that this configuration was used for the calibration test and that this set-up was placed inside the vacuum chamber.

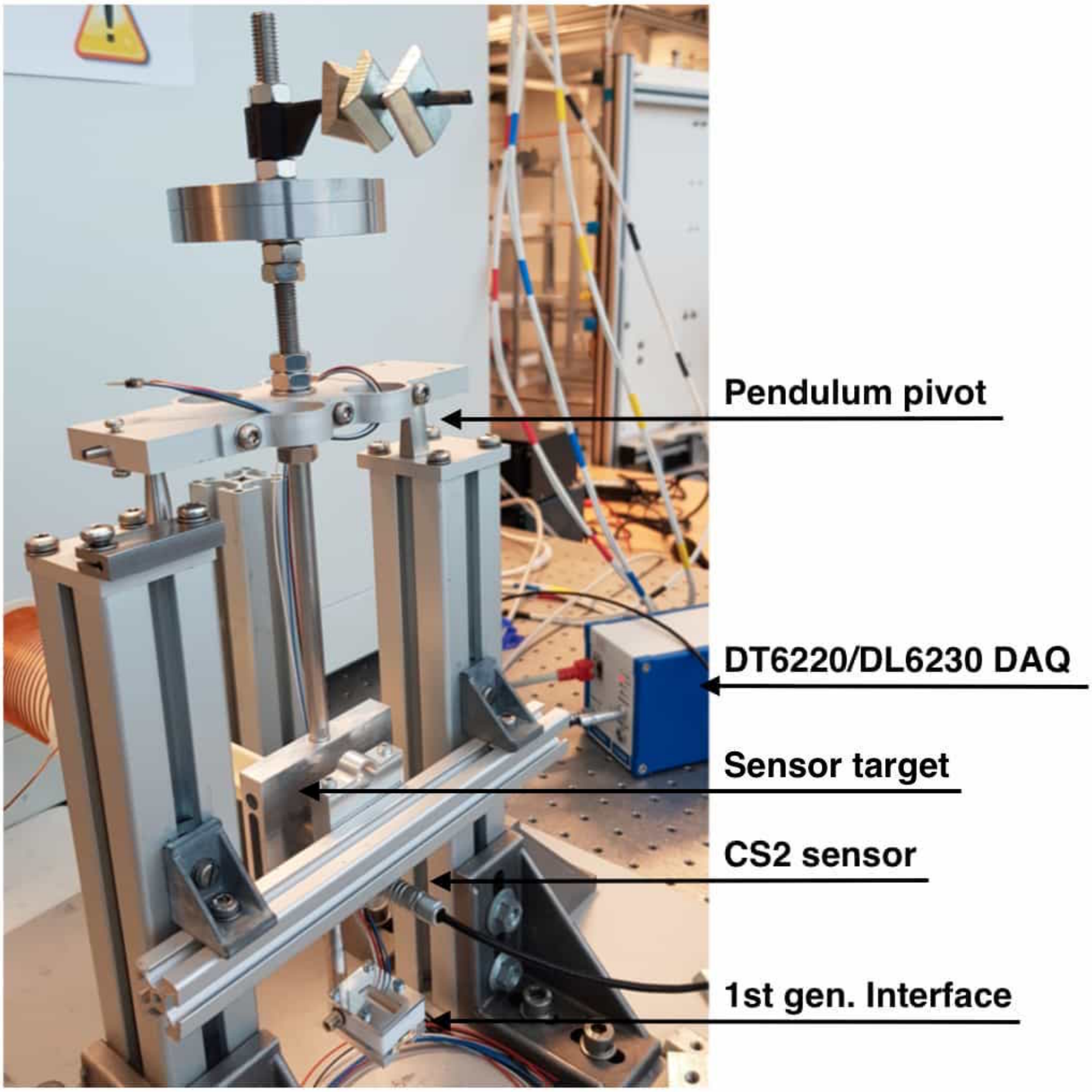

Figure 3.10: Overview of the thrust bench components with the 1st gen. interface (including the 3rd gen. MEMS-VLM) attached to the AE-TB-5m. Note that this configuration was not used for the calibration test as the rotary spring and fluidic tube were not included.

VTDC

During the calibration test the 3rd gen. MEMS-VLM chip was not used, but the VTDC actuator (see Figure 3.9 or 3.11) was used to provide a calibration force. As mentioned before, the VTDC actuator provides a magnetic force when an electrical current runs through it and the actuator has a sensitivity of $0.827[mN/A]$ as was determined by Jansen (2016) [8]. This electrical current was provided by the Delta Elektronika SM7020-D, which is the lower PSU in Figure 3.12a. The wiring was set up as follows: the common/negative (black) and positive (red) wires were connected from the SM7020-D (see Figure 3.12b) to two ports of the (female) banana connector row outside of the vacuum chamber (see Figure 4.18). This row was again wired to another (female) banana connector row inside the vacuum chamber via the power feedthrough line. Note that the banana connector rows are both colored and numbered in order to distinguish how the individual ports are linked to each other. Finally, the wires of the VTDC were plugged into two ports of the banana connector row inside the vacuum chamber. As for the current levels these were controlled with the program LabVIEW (see file ”Pendulum Calibration Required Range Exploration.vi”) on the cleanroom computer. In the LabVIEW file a simulated signal for the electrical current is sent to the SM7020-D, after which the SM7020-D outputs the real electrical currents, which are also measured in LabVIEW. Note that the simulated signal can be adjusted to the user's needs. Also, the LabVIEW file automatically stores the measurement data in a preselected folder.

Now that the operation of the VTDC actuator has been described, an explanation will be given about the displacement of the pendulum arm. Movement in the pendulum arm is induced because of the following. A magnetic holder is attached to the sensor target and inside the magnetic holder (see Figure 3.11) a magnet has been placed. When a constant electrical current runs through the VTDC a parallel homogeneous magnetic field is created within the coil, which results in a constant magnetic force that is exerted on the magnet inside the magnetic holder and thus on the pendulum arm. As described by Jansen (2016) [8], the center of the magnetic holder should be aligned with the center axis of the VTDC, though a maximum axial offset resulted in merely an increase of $+2.7[\%]$ in sensitivity ($0.849[mN/A]$). Furthermore, the distance of the magnetic holder w.r.t. the high-turn-density-side of the VTDC should be $7[cm]$. Jansen (2016) [8] found that the influence of this distance on the sensitivity was greater: a distance of $6[cm]$ resulted in a sensitivity of $0.775[mN/A]$, and a distance of $8[cm]$ resulted in a sensitivity of $0.786[mN/A]$. That is why during the preparation of the set-up for the AE-TB-5m calibration test, this distance was verified using a digital caliper. It is therefore recommended when preparing the set-up of the AE-TB-5m to use measurement tools (e.g. a digital caliper) to ensure that: the center of the magnetic holder is aligned with the center axis of the VTDC, and that the distance between the magnetic holder and the high-turn-density-side of the VTDC is $7[cm]$.

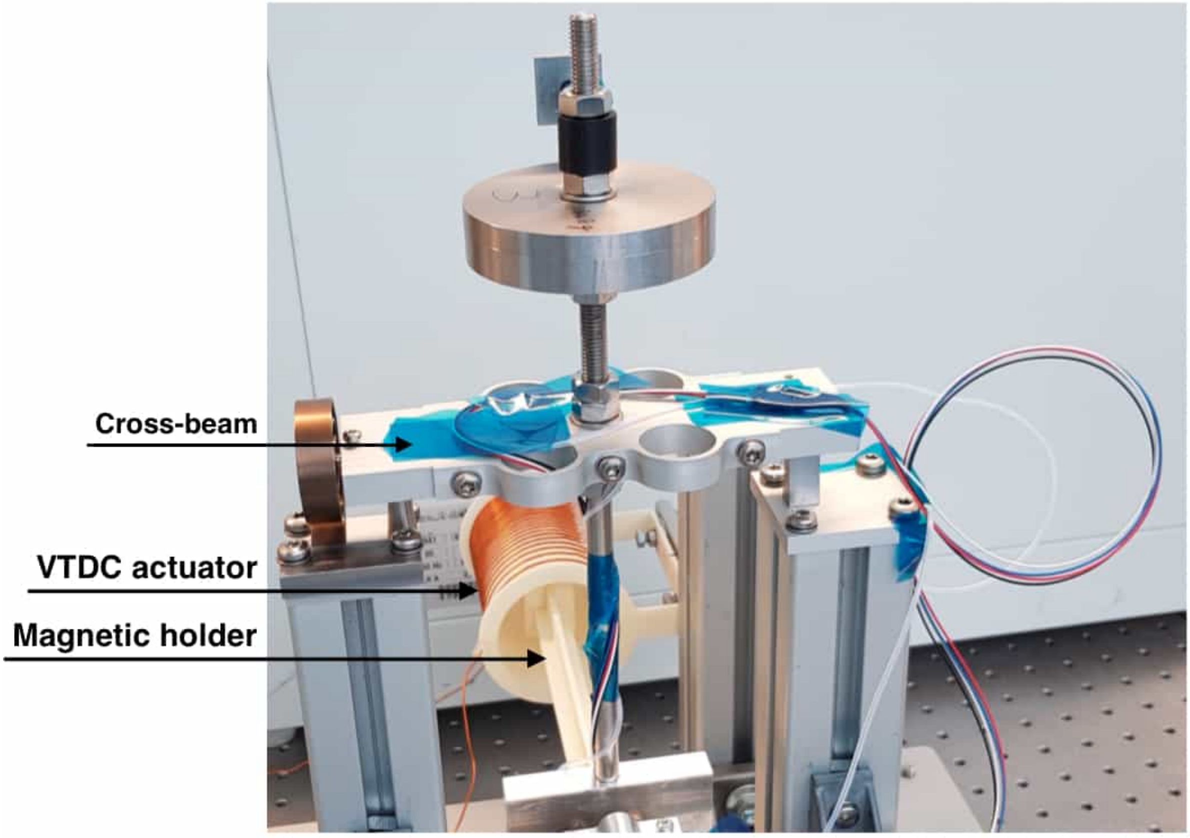

Figure 3.11: View of the magnetic holder, which is attached to the sensor target, inside the VTDC actuator. It can also be seen that in order to reduce effect of the tube and wires on the displacement, a 'loop configuration' was applied: the tube and wires are rotated around the pendulum arm, taped on top of the pendulum cross-beam, looped in the air and taped to the (Boikon profile) support pillar. Note that this configuration was used for the calibration test and that this set-up was placed inside the vacuum chamber.

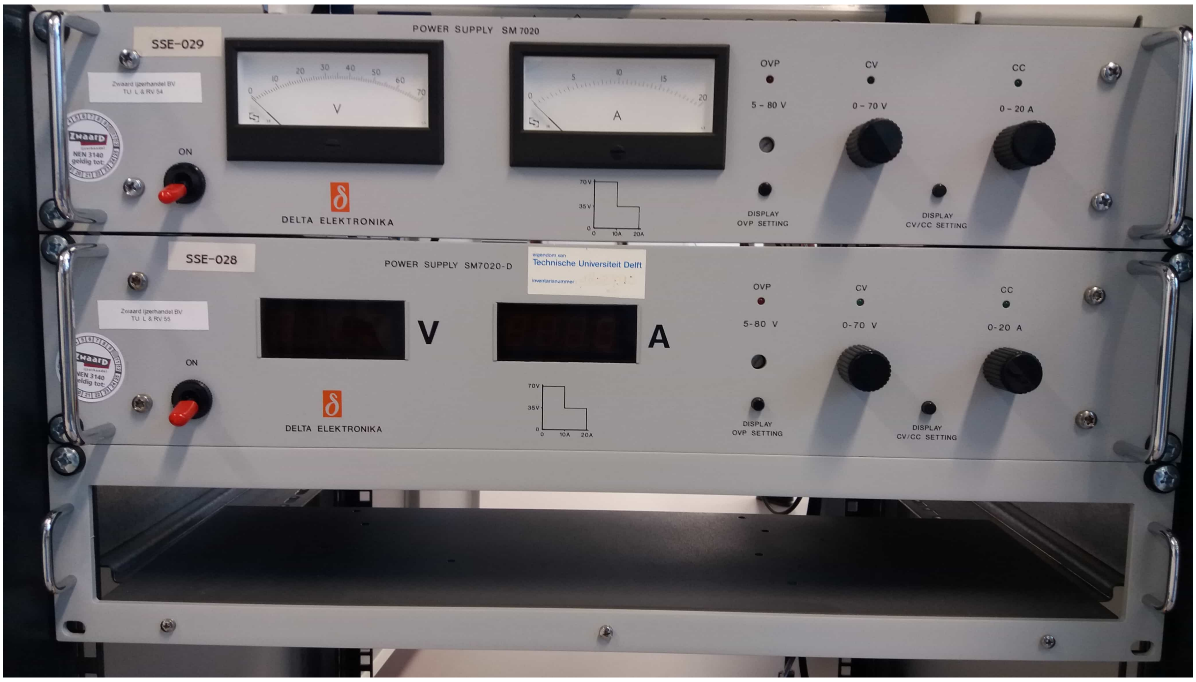

(a) Front view with the SM7020 (upper) and SM7020-D (lower) power supply units.

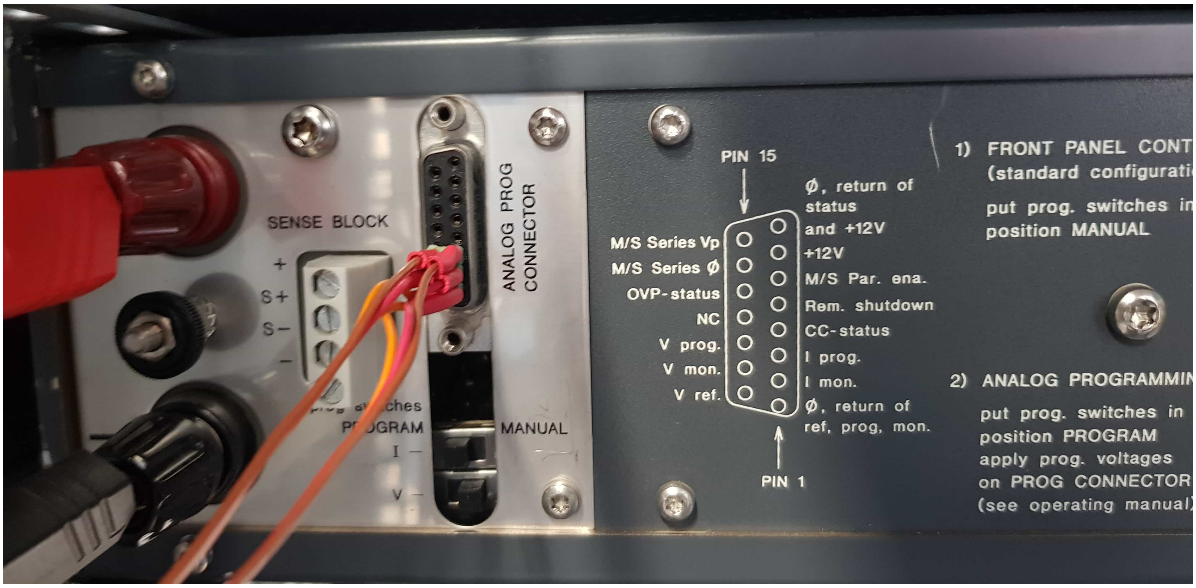

(b) Back view with only the SM7020-D power supply unit.

Figure 3.12: The Delta Elektronika SM7020 (upper) and SM7020-D (lower) power supply units are located between the vacuum chamber and the cleanroom computer. Note that SM7020-D was used for the AE-TB-5m calibration test and that SM7020 can be used to provide power to the heaters of the MEMS-VLM chip. Also, the required settings for calibration test can be seen in the back view: the current "I" is set to "PROGRAM" and the voltage "V" is set to "MANUAL".

Displacement measurement

As for the measurement of the pendulum arm displacement, this was done with the CS2 sensor, which is a capacitive (displacement) sensor purchased from the company Micro-Epsilon. The sensor has a specified range of 0-2 $[mm]$, though in practice it was found that the sensor has a range of 0-5 $[mm]$. Although the author did not find any problems when measuring displacement values between $2-3[mm]$, it is recommended to stay within the specified range of $0-2[mm]$ as the sensor was calibrated for this range. The reason why the author did not stay within the specified range, was because during the experiments it was not clear what sensor was used and it was falsely assumed that it was the CS5 sensor. This assumption was made because the range in practice was found to be $0 - 5[mm]$. Only afterwards it was found in the work of Jansen (2016) [8] that the CS2 sensor was used. This was verified by performing measurements with a (digital) caliper as the CS2 sensor has a specific shape and dimensions (see [24]). An overview of the CS2 sensor specifications can be found in Table 3.14. The presented accuracy of the sensor in the table was based on the calculations of Jansen (2016) [8]. However, the accuracy is not relevant for the force-displacement relations, since the relative displacement is needed for these relations. This is because the systematic error (accuracy) is filtered out when the difference of two measured values are taken. This does mean that random errors are still present, but these can be found and reduced by repeating the experiment multiple times.

The location of the CS2 sensor can be found in Figure 3.10, where it can be seen that the sensor is pointed towards the sensor target, which is thus the reference plane for the displacement measurements. It can also be seen that a (capaNCDT) sensor cable connects the CS2 sensor with the DT6220/DL6230 DAQ, which is specifically made to process the produced data of the CS2 sensor. The DAQ is connected to the cleanroom computer via an ethernet cable. Note that when the AE-TB-5m is placed inside the vacuum chamber, the CS2 sensor needs to be connected to the sensor cable that is present inside the vacuum chamber. This sensor cable was connected to the feedthrough connection specifically made for this application. The other sensor cable was connected to the DAQ and the outside feedthrough connection of the vacuum chamber (see Figure 4.18). Also note that it is stated in the manual of the CS2 that the DT6220/DL6230 should be switched off when plugging in or removing the sensor cables.

Table 3.14: Overview of the CS2 displacement sensor of Micro-Epsilon [24].

Sensor Type	CS2
Measured Parameter	Displacement of sensor target w.r.t. CS2 sensor: X_{disp} $[\mu m]$
Linearity CS2	1 $[\mu m]$ / 0.05 $[\%]$ FSO (Full Scale Output)
Controller/Demodulator Type	DT6220/DL6230 DAQ
Linearity DT6220/DL6230	4 $[\mu m]$ / 0.2 $[\%]$ FSO (Full Scale Output)
Repeatability DT6220/DL6230	0.02 $[\mu m]$ / 0.001 $[\%]$ FSO (Full Scale Output) [8]
Accuracy: CS2 and DT6220/DL6230	± 5.02 $[\mu m]$ [8]
Specified Range	0-2 $[mm]$
Range in Practice	0-5 $[mm]$

3.3.3. Test procedure

In this section the required steps for the pendulum calibration test are described in Tables 3.15-3.16. Note that since this test is done before (and after) the thrust bench test, many steps of the procedure overlap with the procedure of the thrust bench tests presented in Section 4.3. After the procedure has been carried out the experimental data will be obtained. The data can be processed in MATLAB (see file "$PCT11\_Data\_Analysis.m$" for PCT-11, "$PCT12\_Data\_Analysis.m$" for PCT-12, etc.) and the resulting data can be found in Subsection 3.3.4.

3.3.4. Test results & analysis

It was already displayed in Figure 3.1 that for each thrust bench test, one AE-TB-5m calibration test is done beforehand and one calibration test afterwards. As will be explained in Chapter 4, two thrust bench tests were considered successful: TT-04 and TT-05. For TT-04 the (pendulum) calibration tests PCT-11 and PCT-12 were performed, and for TT-05 the calibration tests PCT-13 and PCT-14 were performed. In this subsection only the test results of PCT-11 will be explained in detail, since the test results of the other calibration tests were obtained in a similar manner. First the electrical current data and the displacement data are presented, respectively. Hereafter, the current-displacement relation and force-displacement relation are elaborated upon. Finally an overview is given about the results of all the calibration tests.

Table 3.15: Detailed procedure for the pendulum calibration test (Part 1).

Step	**Description**	**Performed Y/N**	**Date & time**
1.	Use Section 4.2 and Table 4.7 to verify if the test set-up is complete: the MEMS-VLM chip has been integrated in the 1st gen. interface and the interface has been attached to the AE-TB-5m thrust bench, the thrust bench has been configured and placed inside the vacuum chamber, all the tubes between the 1st gen. interface and the GPF are connected, all the sensors are connected to the cleanroom computer.		
2.	Turn on the required devices/equipment simultaneously and wait 1 hour for the devices to reach a stable temperature, before performing step 5:		
	1. Turn on the PSU SM7020-D (See Figure 3.12), which has an 1 hour warm-up time.		
	2. Turn on the DT6220/DL6230 DAQ of the CS2 sensor (See Figure D.8), which has a 15 minutes warm-up time.		
	3. Turn on the clean room computer and log in with the local administrator account. The current login is *".\localadmin"* and the current password is *"sse_cr03"*).		
3.	Perform the following checks: Open the *"Pendulum_Calibration_Required_Range_Exploration.vi"* LabVIEW file, check if the data will be saved to the right folder, run the file, check if all the sensors read out measurements (that make sense) and if the PSU is providing the expected currents, stop the file and close the program. Note that if the program produces an error, the user should figure out the source of the error and solve it.		
4.	Close the vacuum chamber door, turn on the vacuum pump and wait at least 15 minutes in order to reach a P_a of 30 [Pa].		

Table 3.16: Detailed procedure for the pendulum calibration test (Part 2).

Step	**Description**	**Performed Y/N**	**Date & time**
5.	Perform the AE-TB-5m calibration test:		
	1. Open the *"Pendulum_Calibration_Required_Range_Exploration.vi"* LabVIEW file and the "DT6200 DAQ Tool"		
	2. Wait until the displacement has reached its minimum amplitude and observe wether it remains at this amplitude (1 minute is sufficient). Note that the minimum amplitude depends on the thrust bench configuration and this value can be determined by analyzing the long term (about 12 hours) behavior of the displacement. For example, the author found that the minimum amplitude of the displacement was between is between 10-15 $[\mu m]$.		
	3. Start logging the displacement data with the "DT6200 DAQ Tool" by clicking "Protocol" and run LABVIEW by clicking on the arrow button at the top left of the LabVIEW interface.		
	4. Wait and observe that the PSU provides the preset current(s) and that the displacement sensor measures the induced displacement(s). Note that the author had to wait for about 15 minutes.		
	5. Either wait for the LabVIEW program to stop itself or stop the program when the preset current(s) has been provided. After this stop the "DT6200 DAQ Tool" by clicking "Stop daq". Hereafter, localize the stored data and copy the experimental data to a separate folder or a USB device.		
6.	Perform the thrust bench test procedure described in Section 4.3.		
7.	Perform a second AE-TB-5m calibration test!		
8.	Turn off all the devices described in step 2.		
9.	Remove the test set-up from the vacuum chamber if no other tests will be carried out.		

Electrical current and magnetic force

The raw experimental data for the electrical current and voltage that was produced by the SM7020-D PSU during PCT-11 is presented in Figure 3.13. It can be seen that both the electrical current and voltage are increased incrementally as expected. Since only the amperage data was needed to obtained the magnetic force, this was further analyzed as can be seen in Figure 3.14. In the figure the amperage values were found using the MATLAB function 'findpeaks'. These measured values are compared to the simulated values in Table 3.17. It can be seen that measured amperage values are consistently lower (about $0.04[A]$) than the simulated amperages, which is about the same offset that was found by Jansen (2016) [8]. However, this does not impose any problems as the VTDC actuator still provides a magnetic force range of $0-2[mN]$. The magnetic force was calculated with the amperage data and Equation 3.1, which is based on the experimental results of Jansen (2016) [8].

$$F_{magnetic} = 0.827[mN/A] \cdot I[A] \pm 1.31e\text{-}2[mN] \tag{3.1}$$

As mentioned in the introduction of this chapter, the VTDC calibration test was not carried out during this thesis project due to time constraints. However, this does not impose a problem as the test has already been performed twice: first by Bijster (2014) [23] who found a sensitivity of $0.833[mN/A]$, hereafter by Jansen (2016) [8] who found the sensitivity as presented in Equation 3.1. Because over the two years the sensitivity value remained within the margin of error, it can be assumed that the same holds for this thesis project, which was done in 2018. Though it is interesting to investigate a possible change in the sensitivity of the VTDC actuator, it was concluded that it was not required to perform the VTDC calibration test.

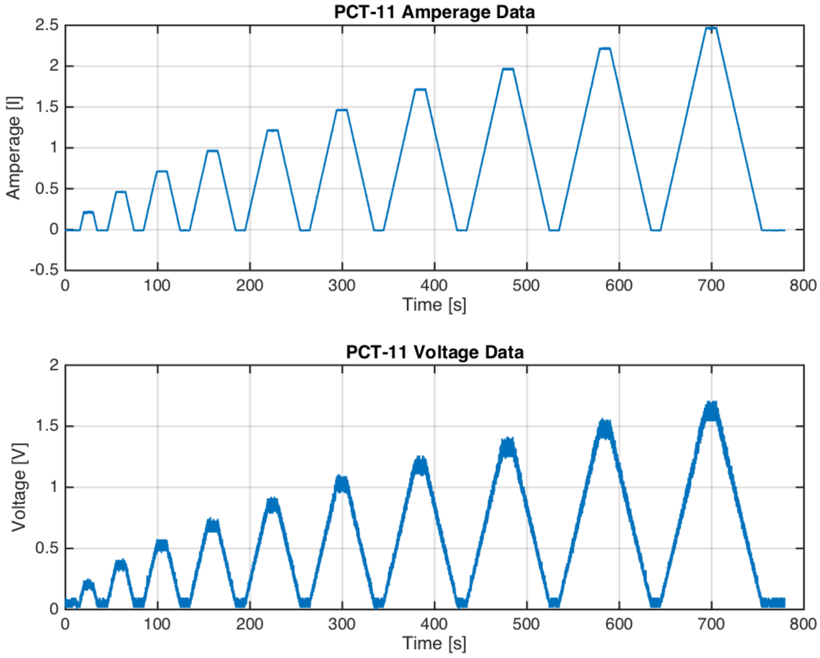

Figure 3.13: Raw electrical current and voltage data obtained from the SM7020-D during PCT-11 and sampled at a frequency of 100 [Hz].

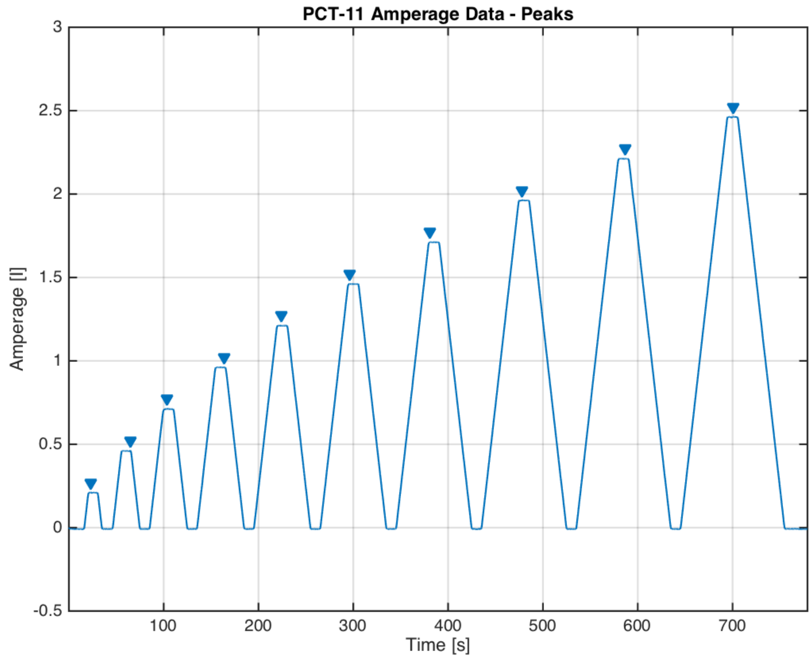

Figure 3.14: Filtered electrical current data obtained from the SM7020-D during PCT-11. The standard 'filter' function of MATLAB was used: 'a' was equal to 1 and 'b' was a 1x100 vector filled with values of 0.01. The blue triangles indicate the found electrical current values, which was done with the function "findpeaks" in MATLAB.

Table 3.17: Comparison between the simulated amperage in LabVIEW and the measured amperage that was produced by the SM7020-D. Furthermore, the simulated induced magnetic force and the real induced magnetic force produced by the VTDC actuator are included as well.

Simulated Amperage [A]	**Measured Amperage** [A]	**Difference** [A]	**Simulated Magnetic Force** [mN]	**Real Magnetic Force** [mN]
0	-0.009	0.009	0	0
0.25	0.211	0.039	0.2067	0.1747
0.50	0.462	0.038	0.4135	0.3819
0.75	0.713	0.037	0.6202	0.5895
1.00	0.962	0.038	0.8270	0.7955
1.25	1.212	0.038	1.0337	1.0021
1.50	1.462	0.038	1.2405	1.2087
1.75	1.713	0.038	1.4472	1.4163
2.00	1.963	0.037	1.6540	1.6237
2.25	2.213	0.037	1.8607	1.8300
2.50	2.464	0.036	2.0675	2.0380

Displacement

The raw experimental data for the displacement measured by the CS2 sensor during PCT-11 is presented in Figure 3.15. It can be seen that the data follows the same pattern as the electrical current of Figure 3.14. However, the data still has fluctuations that need to be reduced, which was done with the MATLAB function based on a moving average filter: the function 'smooth' with a span of 1200. The value for the span was found through trial and error. For example, a span of 1 does not provide any smoothing of the data, while a span of 5000 does not maintain the shape of the raw experimental data. It can be seen in Figure 3.16 that the smoothing function with a span of 1200 both reduces the fluctuations in the data and maintains the shape of the original data set. Hereafter, the displacement values were found using the MATLAB function 'findpeaks', which can be seen in Figure 3.17. Note that the function is not perfect as some data points were chosen that did not correspond to the peak displacement but to the baseline displacement. An overview of the results can be found in in Table 3.18. In the table the average measured displacement values are presented in the first column and the changes in the average displacement in the third column including the relative uncertainty. These uncertainties are based on the uncertainty in the the zero baseline displacement value of the second column. The reason why this was added was because there is a slight fluctuation inthebaseline displacement. It can be seen in Figure 3.16 that for each displacement peak there is a difference between the baseline displacement before and after the peak.

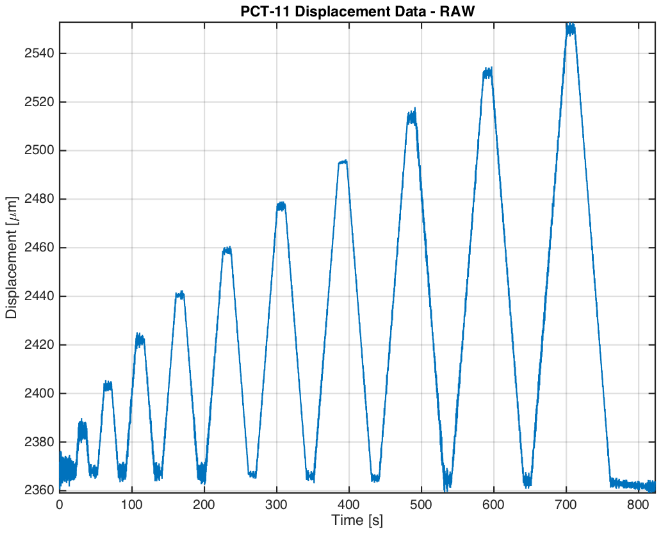

Figure 3.15: Raw experimental displacement data from the CS2 sensor in the AE-TB-5m, thrust bench, which was obtained during PCT-11 and sampled at a frequency of 104 [Hz].

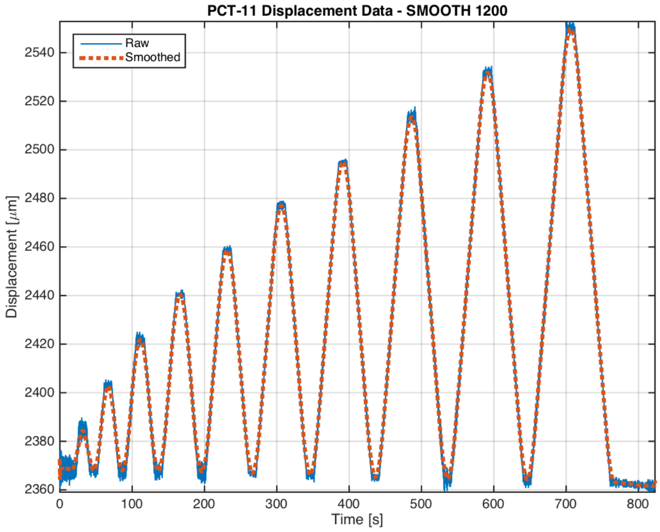

Figure 3.16: Raw experimental displacement data of PCT-11 with the filtered/smoothed superimposed, which was obtained with the function 'smooth' using a span of 1200 in MATLAB.

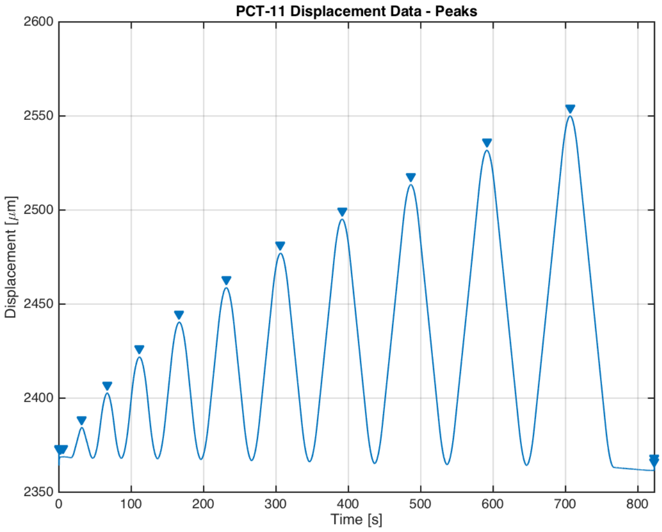

Figure 3.17: Filtered / smoothed displacement data for PCT-11, where the peaks / plateaus were found and indicated with blue triangles using the "findpeaks" function in MATLAB.

Table 3.18: Overview displacement data for PCT-11, which includes the measured displacement, the 'zero' or baseline uncertainty and the relative displacement.

X_{disp} [μm]	**Baseline Displacement Uncertainty** [μm]	Δ_{disp} [μm]
2384.4	± 0.14	16.3 ± 0.87 [%]
2402.8	± 0.05	34.8 ± 0.15 [%]
2421.9	± 0.11	54.1 ± 0.21 [%]
2440.4	± 0.18	72.9 ± 0.25 [%]
2458.8	± 0.28	91.7 ± 0.30 [%]
2477.1	± 0.33	110.6 ± 0.30 [%]
2495.2	± 0.44	129.5 ± 0.34 [%]
2513.6	± 0.32	148.7 ± 0.21 [%]
2531.8	± 0.19	167.4 ± 0.11 [%]
2550.0	± 0.50	186.3 ± 0.27 [%]

Relations

Now that the electrical current, magnetic force, and displacement data have been presented, the relationship between these data can be established. An overview of the data can be found in Table 3.19. The data sets have been shortened to a current range of $0 - 1.21[A]$ and a magnetic force range of $0 - 1.0[mN]$, since it was found that the experimental thrust range was between $0 - 1[mN]$ (see Section 5.13). The relationship between the (absolute) displacement and the amperage can be found in Figure 3.19. Note that this relationship was determined with the MATLAB function "fit" using "poly1" as the fit-type, which provides a regression line for input data and includes the Root Mean Square Error (RMSE). More information about the function can be found by typing "help fit" in MATLAB. The same 'fit' function was used to establish the relationship between the (relative) displacement and magnetic force, which is presented in Figure 3.19. The 'fit' function also provides the equation for the regression line, which is also included in the figure. This means that now an equation is available that relates the change in the pendulum arm displacement with the induced force on the pendulum arm.

Table 3.19: Overview test data for PCT-11, which includes the measured electrical current and corresponding magnetic force, the measured displacement and the relative displacement.

I [A]	$F_{magnetic}$ [mN]	X_{disp} [μm]	Δ_{disp} [μm]
0	0	2367.7	0
0.21	0.17	2384.4	16.3
0.46	0.38	2402.8	34.8
0.71	0.59	2421.9	54.1
0.96	0.80	2440.4	72.9
1.21	1.00	2458.8	91.7

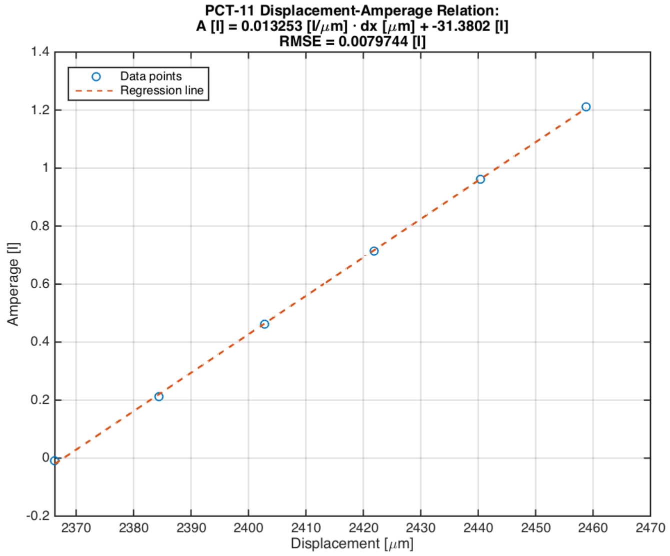

Figure 3.18: Regression line using the absolute displacement and amperage data of PCT-11, which was obtained with the function 'fit' using 'poly1' as fit-type in MATLAB.

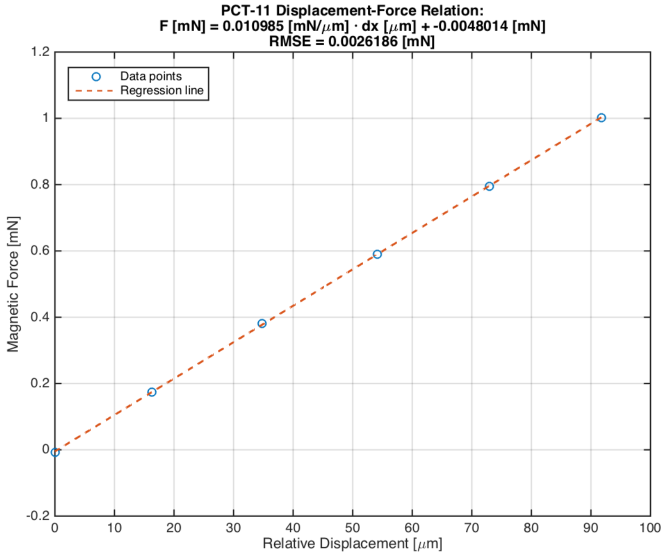

Figure 3.19: Regression line using the relative displacement and magnetic force data of PCT-11, which was obtained with the function 'fit' using 'poly1' as fit-type in MATLAB.

Overview results: PCT11-PCT14

All the steps have been explained about how the displacement-force relation was established for PCT-11. However, it was mentioned before that PCT-11 was done before the thrust bench test TT-04 and that PCT-12 was done afterwards. This means that the displacement and force data of both PCT-11 and PCT-12 can be combined in order to obtain a more precise displacement-force relation (F_{TT04}). The same holds for PCT-13 and PCT-14, which correspond to TT-05. All these relations including the uncertainty can be found in Table 3.20. It can be seen in the table that the displacement-force relations are about the same, which demonstrates the repeatability of the AE-TB-5m calibration test. For example, a Δ_{disp} of $90[\mu m]$ results in a F_{TT04} of $1.0967[mN]$ and a F_{TT05} of $1.0952[mN]$, which is a difference of merely $0.0015[mN]$. Even though this difference is small, the author still recommends to perform two calibration tests for each thrust bench test (one before and one after), since this ensures that the set-up has not been damaged in any way during the thrust bench test. Also, each calibration test only takes about 15 minutes.

The total uncertainty in Table 3.20 consists of the following (using δ_{TT04} as an example): the absolute error of the VTDC actuator ($\delta_{VTDC} = \pm 1.31e\text{-}2[mN]$) and the RMSE of F_{TT04} ($\delta_{RMSE-TT04} = \pm 2.4e\text{-}3[mN]$). Since these errors are dependent, the errors can simply be summed. Also, because the absolute error is constant, the relative error will become smaller for larger values of Δ_{disp}. A visualization of this can be found for F_{TT04} in Figure 3.20, where the relative error is given for a Δ_{disp} range of $5 - 100[\mu m]$, which corresponds to a force range of $0.039 - 1.10[mN]$. It can be seen that in order to keep the error below $10[\%]$ it is required to have minimum Δ_{disp} of $15[\mu m]$, which corresponds to a force of $0.149[mN]$.

Table 3.20: Overview of the displacement-force relations for PCT-11, PCT-12, PCT-13 and PCT-14. The average relations and the uncertainties are included as well.

PCT11	F_{PCT11} [mN] = 0.010985 $[mN/\mu m]$ · dx $[\mu m]$ – 0.0048014 $[mN]$; with $\delta_{RMSE-PCT11}$ = ± 0.0026186 $[mN]$
PCT12	F_{PCT12} [mN] = 0.011053 $[mN/\mu m]$ · dx $[\mu m]$ – 0.0055413 $[mN]$; with $\delta_{RMSE-PCT12}$ = ± 0.0017349 $[mN]$
Combined	F_{TT04} [mN] = 0.011019 $[mN/\mu m]$ · dx $[\mu m]$ – 0.0051714 $[mN]$; with $\delta_{RMSE-TT04}$ = ± 0.0023702 $[mN]$
Uncertainty	δ_{TT04} [mN] = δ_{VTDC} + δ_{TT04} = $\pm(1.31e\text{-}2 + 2.4e\text{-}3) = \pm 1.55e\text{-}2$
PCT13	F_{PCT13} [mN] = 0.010951 $[mN/\mu m]$ · dx $[\mu m]$ – 0.0076817 $[mN]$; with $\delta_{RMSE-PCT13}$ = ± 0.0017982 $[mN]$
PCT14	F_{PCT14} [mN] = 0.011096 $[mN/\mu m]$ · dx $[\mu m]$ – 0.0067317 $[mN]$; with $\delta_{RMSE-PCT14}$ = ± 0.0009341 $[mN]$
Combined	F_{TT05} [mN] = 0.011024 $[mN/\mu m]$ · dx $[\mu m]$ – 0.0072067 $[mN]$; with $\delta_{RMSE-TT05}$ = ± 0.0054494 $[mN]$
Uncertainty	δ_{TT05} [mN] = δ_{VTDC} + δ_{TT05} = $\pm(1.31e\text{-}2 + 5.4e\text{-}3) = \pm 1.85e\text{-}2$

3.3.5. Summary

Looking back at Table 3.13, all the success criteria have been met: the measurement data of the displacement and electrical current have been stored, each increase in amperage resulted in an increase of the average displacement and it was demonstrated that the AE-TB-5m calibration test is repeatable. This means that test can be concluded successful. This also indicates that the goal stated in Subsection 3.3.1 has been achieved. The relationship between the change in pendulum arm displacement and the magnetic force of the VTDC was established for TT-04 and TT-05:

$$F_{TT04}[mN] = 0.011019[mN/\mu m] \cdot \Delta_{disp}[\mu m] - 0.0051714[mN] \tag{3.2}$$

$$F_{TT05}[mN] = 0.011024[mN/\mu m] \cdot \Delta_{disp}[\mu m] - 0.0072067[mN] \tag{3.3}$$

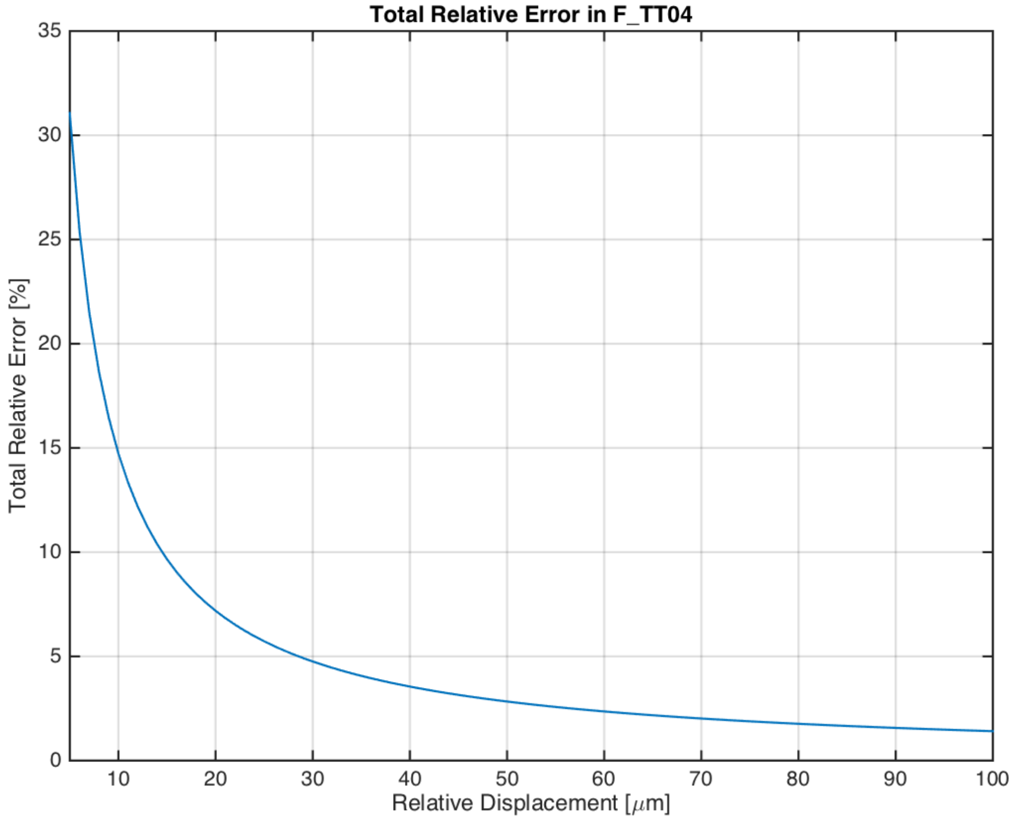

Figure 3.20: Total relative error (ϵ_{TT04}) for the average displacement-force relation F_{TT04} for a relative displacement (Δ_{disp}) range of $5 - 100[\mu m]$.

As for the recommendations, the author found many:

- Before doing the calibration test, read through the thesis works of Bijster (2014) [23] and Jansen (2016) [8], since these theses provide a more in depth explanation about the AE-TB-5m, the VTDC and the calibration test.
- When preparing the test set-up, use measurement tools (e.g. a digital caliper) to ensure that: the center of the magnetic holder is aligned with the center axis of the VTDC, and that the distance between the magnetic holder and the high-turn-density-side of the VTDC is $7[cm]$. Any deviation results in a change of the VTDC sensitivity.
- When performing the calibration test, always stay within the specified range of the CS2 sensor. Though the sensor has an actual range of $0 - 5[mm]$, it has only been calibrated for a range of $0 - 2[mm]$.
- Perform two calibration tests for each thrust bench test (one before and one after), since this ensures that the set-up has not been damaged in any way during the thrust bench test.
- Purchase and integrate a rotary spring with lower spring stiffness in the test set-up. This will shorten the measurable thrust range and increase the accuracy, while maintaining a resistance against disturbances.
- Purchase a set of rotary springs with each having a different spring stiffness. This increases the flexibility of the thrust bench as this enables the user to choose for different thrust ranges and corresponding accuracies.

3.4. AE-TB-5m FCF Test

In this section the AE-TB-5m FCF test is described. First, in Subsection 3.4.1 the test plan is described, which includes the goal of the test, the measured parameters and the success criteria. The test set-up, procedure and results are presented in Subsection 3.4.2.

3.4.1. Test plan

Purpose and relevant parameters

In this test the vertical distance (height) between the pendulum pivot and both the CS2 sensor and the nozzle exit of the MEMS-VLM chip will be measured. This is because the magnetic force produced by the VTDC actuator is applied at the same height of the of CS2 sensor, but the thrust force of the MEMS-VLM chip is located lower respectively. This means that arm w.r.t. the pendulum pivot is larger for the thrust force compared to the magnetic force. Therefore a force correction factor (FCF) will be needed to determine the actual thrust for the thrust bench test.

Success criteria

In order to determine if the test was considered successful, a few success criteria were created, which are presented in Table 3.21.

Table 3.21: Success criteria for the AE-TB-5m FCF test.

Criteria	**Test Acceptance**
SC-fr-01	The vertical distance between the pendulum pivot and the center of the CS2 sensor has been measured.
SC-fr-02	The vertical distance between the pendulum pivot and the nozzle exit of the MEMS-VLM chip has been measured.

3.4.2. Test set-up, procedure and results

For performing this test only two items were required: the AE-TB-5m thrust bench with the 1st gen. interface integrated at the bottom of the pendulum arm and a measuring tool. The tool that was used to perform the measurements was a digital caliper (Mitutoyo Absolute). The test was considered successful as it was found that:

- The vertical distance between the pendulum pivot and the center of the CS2 sensor was: $179.66[mm]$.
- The vertical distance between the pendulum pivot and the nozzle exit of the MEMS-VLM chip was: $245.07[mm]$.
- With these distances, the force correction factor FCF was determined to be: $0.7331[-]$.

4

Nitrogen Thrust Bench Test - Plan, Set-up & Procedure

In this chapter all the required information for performing the nitrogen thrust bench test is described in detail. First, in Section 4.1 the test plan is presented, which includes the goal of the test, the relevant parameters, the expectations of the test and the success criteria. Hereafter, the test set-up and test procedure are presented in Sections 4.2 and 4.3, respectively.

4.1. Test Plan

4.1.1. Purpose

Since the nitrogen thrust bench test is the main test, the purpose of this test is to help answer the main research question and meet the main objective and some sub-goals presented in Section 1.2. Therefore, with the experimental results of this test a relationship will be established between the throat Reynolds number and the nozzle performance. Furthermore, the test will provide insight about the highest achievable Reynolds number for the current test set-up. Another subgoal was making the test reproducible, which is a reason why a detailed test set-up and test procedure will be given in this chapter. Finally, it was a subgoal to provide recommendations about the test procedure (and set-up), the design of the 1st gen. interface, the design of the 3rd gen. MEMS-VLM chip and the operating conditions (e.g. input pressure).

4.1.2. Relevant parameters

In order to calculate the nozzle performance parameters (C_d,ξ_F,ξ_s and ξ_b), Equations 2.1-2.12 are needed, which were already explained in Subsection 2.2.1. These equations were implemented in MATLAB and an overview of all the parameters can be found in Figure 4.1. It can be seen in the figure that the blocks of the flow chart are colored differently: the three upper blocks are blue and represent the required input data, while the other green blocks represent the calculated / output data. The blue block with ”Measured Parameters” will be determined with the experimental results of the thrust bench test presented in Section 5. From the ”Measured Parameters” (and the NIST data base [1]) the blue block with ”Propellant Properties” will be determined and this is presented later on in Table 6.1. As for the blue block with ”Nozzle Geometry”, this was already determined in Table 3.11 in Subsection 3.2.4. When all the blue input data blocks are known, the green blocks ”Theoretical Parameters”, ”Experimental Parameters”, ”Reynolds Number” and ”Performance Parameters” will be determined.

4.1.3. Expectations

In this subsection it is calculated (using ideal rocket theory and corrections) what can be expected from the nitrogen thrust bench test. As mentioned before, during the thrust bench test the ”Measured

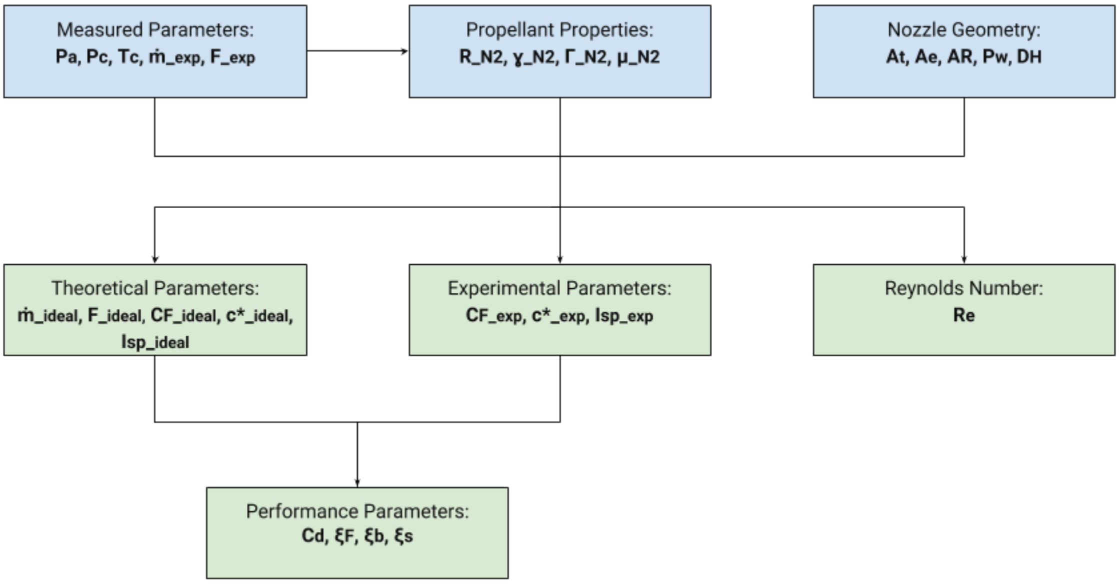

Figure 4.1: Overview of all the parameters needed for determining the nozzle performance. The flowchart represents the calculations that were made in MATLAB, where the top three blue blocks represent the required input parameters and the other green blocks represent the calculated / output parameters.

Parameters" of Figure 4.1 will be determined, which includes the ambient pressure (P_a), the chamber pressure (P_c), the chamber temperature (T_c), the mass flow ($\dot{m}$) and the thrust force (F). From these parameters, P_c will be used as a control variable and F and $\dot{m}$ are the corresponding dependent variables. It was chosen not to use T_c as a control variable since this would add complexity to the test set-up. This means that T_c can be assumed to be equal to a normal temperature ($293.15[K]$). Note that for future tests, it is recommended that the effect of this parameter is explored as well. As for P_a this will be controlled by turning on the pump connected to the vacuum chamber during the whole test. It was found through experimentation that a (near-vacuum) pressure of $30[Pa]$ could be achieved within fifteen minutes with the current set-up. Coming back to P_c, it was initially planned to vary this between $2[bar]$ and $6[bar]$. However, for the experiments this range was reduced to $2-5[bar]$ in order to ensure no leakage would occur. Now all the information is complete that is needed to apply ideal rocket theory and calculate the ideal mass flow ($(\dot{m})_{ideal}$), thrust ($(F)_{ideal}$) and specific impulse ($(I_{sp})_{ideal}$), which can be seen in Table 4.1. It can also be seen that the corrected values (see Subsection 2.2.2) are included in the table as well, which are based on divergence loss, the loss factor due to viscous effects (Spisz *et al.*, 1965) [9] and boundary layer formation in the nozzle throat (Tang and Fenn, 1978) [17]. Note that the nozzle divergence angle was already determined to be $20.5[^\circ]$ (see Table 3.11). Furthermore, comparisons between the ideal values and corrected values are presented in Figures 4.2-4.4.

Table 4.1: Overview of the expected results based on ideal rocket theory for the thrust bench test for the 01-LS2-02 chip, where a pressure range of $2-6[bar]$, a constant chamber temperature of $293.15[k]$ and a constant ambient pressure of $30[pa]$ were used. Note that the corrected values are based on divergence loss, viscous loss and boundary layer loss.

P_c [bar]	P_a [Pa]	T_c [K]	$(\dot{m})_{ideal}$ [mg/s]	$(\dot{m})_{corr.}$ [mg/s]	$(F)_{ideal}$ [mN]	$(F)_{corr.}$ [mN]	$(I_{sp})_{ideal}$ [s]	$(I_{sp})_{corr.}$ [s]	$(R_e)_{ideal}$ [−]
2	30	293.15	0.66	0.62	0.48	0.27	74.69	44.40	876
3	30	293.15	0.98	0.94	0.72	0.46	74.73	49.73	1315
4	30	293.15	1.31	1.26	0.96	0.66	74.73	52.89	1755
5	30	293.15	1.64	1.59	1.20	0.86	74.72	55.04	2200
6	30	293.15	1.97	1.91	1.44	1.06	74.70	56.62	2637

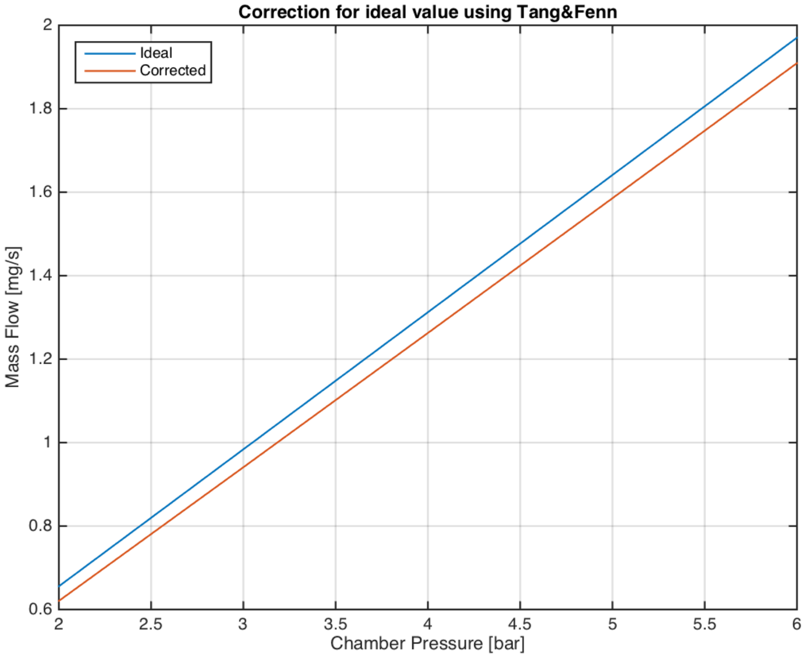

Figure 4.2: Expected mass flow for the 01-LS2-02 chip for a pressure range of $2-6[bar]$, constant chamber temperature of $293.15[k]$ and constant ambient pressure of $30[pa]$: ideal rocket theory and corrections based on throat boundary layer formation (Tang and Fenn, 1978) [17].

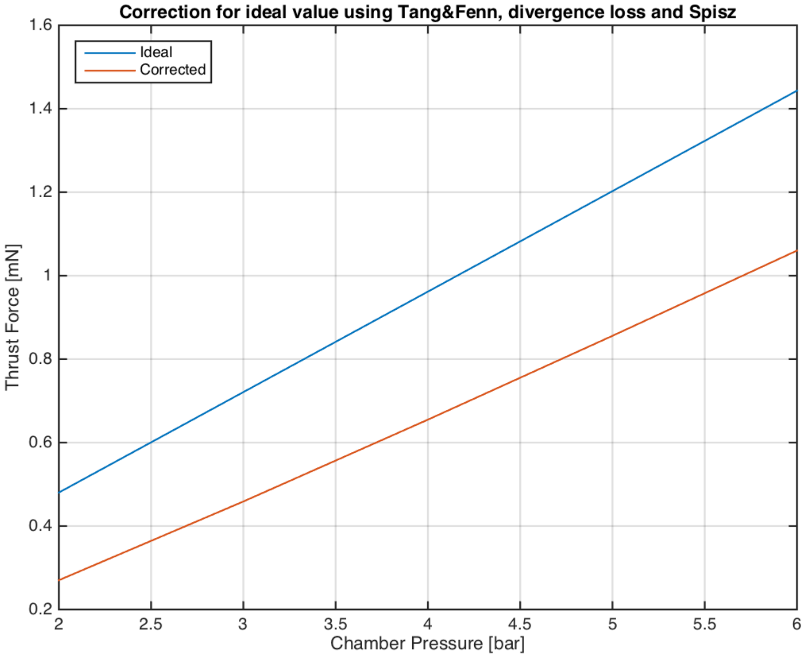

Figure 4.3: Expected thrust force for the 01-LS2-02 chip for a pressure range of $2-6[bar]$, constant chamber temperature of $293.15[k]$ and constant ambient pressure of $30[pa]$: ideal rocket theory and corrections based on throat boundary layer formation (Tang and Fenn, 1978) [17], divergence loss and viscous loss (Spisz *et al.*, 1965) [9].

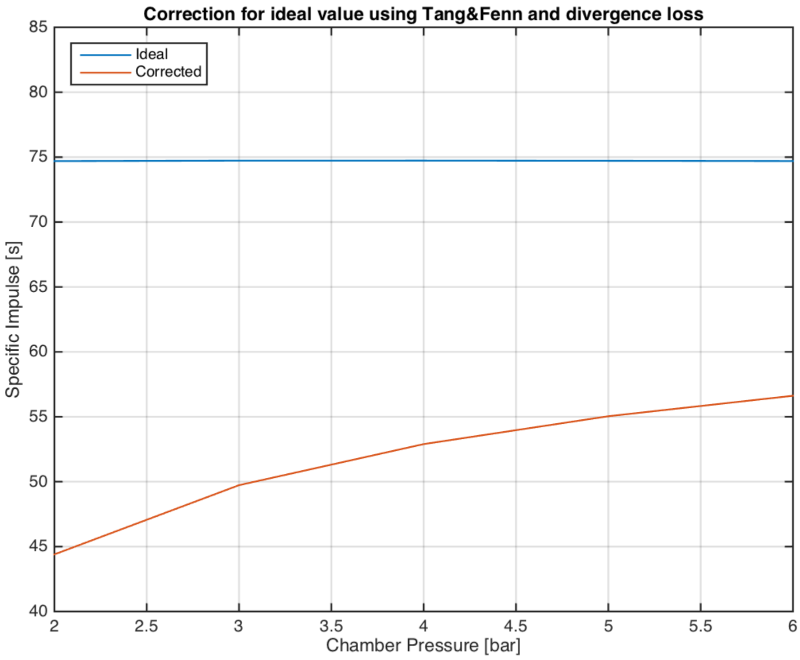

Figure 4.4: Expected specific impulse for the 01-LS2-02 chip for a pressure range of $2-6[bar]$, constant chamber temperature of $293.15[k]$ and constant ambient pressure of $30[pa]$: ideal rocket theory and corrections based on divergence loss and viscous loss (Spisz *et al.*, 1965) [9].

4.1.4. Success criteria

In order to determine if the test was considered successful, success criteria were created, which are presented in Table 4.2.

Table 4.2: Success criteria for the thrust bench test.

Criteria	**Test Acceptance**
SC-TT-01	Measurements of P_a, P_c, T_c, $(\dot{m})_{exp}$, $(F)_{exp}$ were made and documented.
SC-TT-03	Higher values of P_c, result in higher values of $(\dot{m})_{exp}$ and $(F)_{exp}$.
SC-TT-04	No leakage has occurred during the thrust bench test.
SC-TT-05	It has been proven that there was no leakage detected by the mass flow controller, both before and after the thrust bench test.
SC-TT-06	It has been demonstrated that the thrust bench test is repeatable.

4.2. Test Set-up

The equipment needed to properly perform the nitrogen thrust bench test is elaborated in this section. First in Subsection 4.2.1 the propellant feed system is described. Hereafter, in Subsections 4.2.2 and 4.2.3 information about the Brooks mass flow controller and the Lee Company's solenoid valve is presented, respectively. This is followed by the pressure/temperature sensos that was integrated in the 1st gen. interface, which can be found in Subsection 4.2.4. As for explanations about the vacuum chamber, pressure sensor and vacuum pump, these are all presented in Subsection 4.2.5. Furthermore, the cleanroom computer and the DAQs are described in Subsection 4.2.6, while the AE-TB-5m pendulum thrust bench is described in Subsection 4.2.7. Finally, a summary is given in Subsection 4.2.8.

4.2.1. Propellant feed system

In this subsection relevant information is given regarding the propellant feed system that was used for the thrust bench test. This includes all the elements of the feed system through which the nitrogen gas passed through. This is between the N2 storage bottle the fluidic input of the 1st gen. interface. To start off, the same General Purpose Feed system (GPF) was used that Van Wees (2017) [3] and Jansen (2016) [8] used to provide nitrogen gas for their thrust bench tests with the 2nd gen. MEMS-VLM chip and T3μPS, respectively. As can be seen in Figure 4.5 the GPF includes many elements. At the backside of the GPF a N2 storage bottle that contains 10 liter nitrogen at $200[bar]$ is present, which is connected to the line-in rotary valve. In case the storage bottle does not have sufficient amount of pressurized nitrogen, a request for a new bottle should be sent to "$gassenteamfmvg@tudelft.nl$", who will send an employee to replace the bottle.

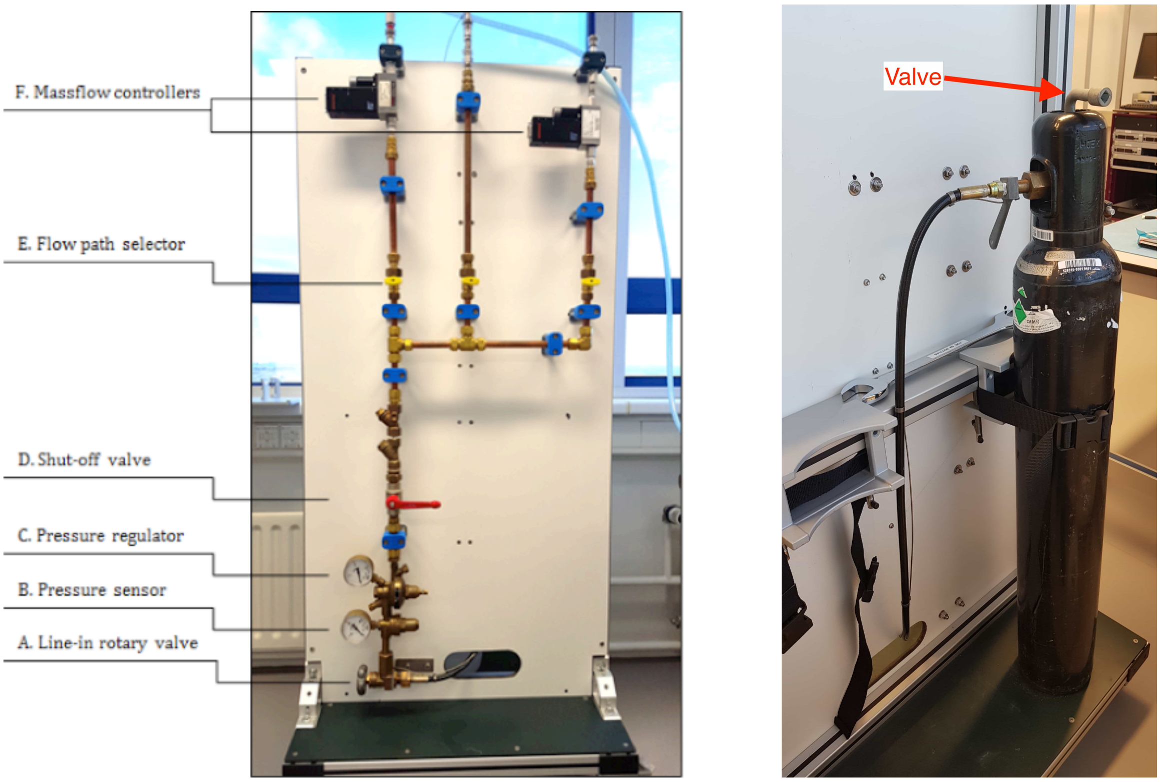

(a) Front view with a description of the components [8].

(b) Back view with the N2 bottle.

Figure 4.5: Front and back view of the GPF.

When the valve of the N2 storage bottle and the line-in rotary valve are opened, it will result in nitrogen gas flowing through the pressure gauge and the pressure regulator. The (analogue) pressure gauge can display a $0 - 315.0[bar]$ range and has an accuracy of $\pm 2.5[bar]$. The (analogue) pressure regulator can control a range of $0 - 16.0[bar]$ with an accuracy of $\pm 0.25[bar]$. Note that Jansen (2016) [8] detected a small leak between the line-in rotary valve and the shut-off valve: both valves were closed but the pressure gauge yet indicated a slow decrease in pressure over time. A solution for this leak could not be found as the leak could not be localized. Thus, in order to prevent the de-pressurization of the N2 storage bottle, it is important when no nitrogen flow is needed to close the N2 storage bottle valve, the line-in rotary valve and the shut-off valve.

When the shut-off valve is also opened, the nitrogen gas can flow to either a line with or without a mass flow controller, depending on which of the three flow path selectors is open. More details about the utilized mass flow controllers are presented in Subsection 4.2.2. A flexible tube with a diameter of $4[mm]$ is then connected between the mass flow controller and the "GN2" feedthrough (outside) of the vacuum chamber using Legris 4 5/32 push-in fittings, which can be seen in Figure 4.6. Note that the pressure/temperature sensor that is displayed in the figure was not used during the thrust bench test because this data was not needed.

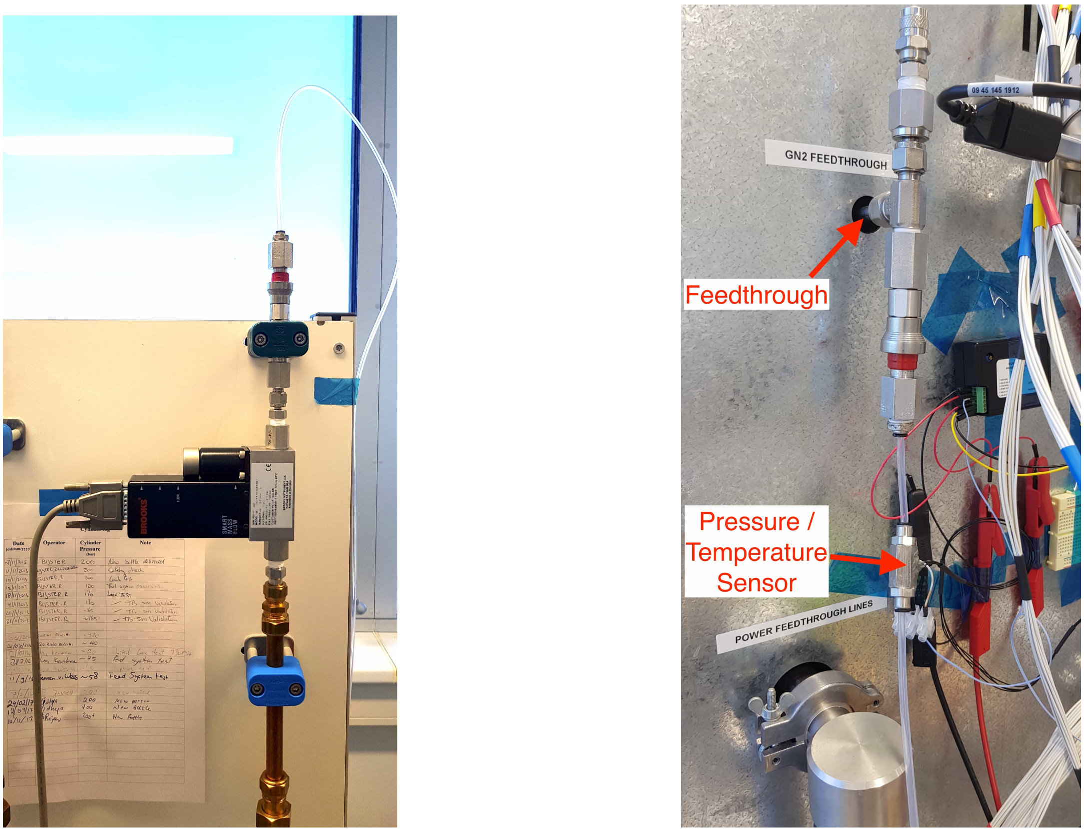

(a) Connection between the tube and the mass flow controller.

(b) Tube connected to the vacuum chamber's "GN2" feedthrough channel.

Figure 4.6: Tubing between the mass flow controller and the "GN2" feedthrough channel of the vacuum chamber using Legris 4 5/32 push-in fittings. Note that the pressure/temperature sensor was not used as the data for this location was not required for determining the thrust performance.

The feedthrough (inside) of the vacuum chamber has a Swagelok SS-QC4-D-400 fitting, which is made to quickly and easily (dis)connect with other Swagelok fittings. Attached to this fitting, is the combined Swagelok SS-QC4-B-400 fitting and SS-400-R-1 adapter, which can be seen in Figure 4.7. Furthermore, a tube with a measured outer diameter of $2.0[mm]$ goes from the Swagelok adapter to the Lee Company's 062 MINSTAC - LFA Tubing Adapter (see Figure C.5). Note that the measurement was done using the Mitutoyo Absolute digital caliper and the reason why it was measured was because the diameter of the tube was unknown as there was no data sheet or purchase order data available. Also, it can be seen that blue tyraps were added to prevent the connections from detaching at high pressures reaching $7[bar]$. Although this approach sufficiently helped in preventing the detachment, it was an improvised solution. It is therefore recommended that more suitable components are purchased and implemented, which are also designed to operate at pressures reaching $7[bar]$ or higher.

The tube with the Lee Company's 062 MINSTAC - LFA Tubing Adapter was connected to the Lee Company's "VHS-M/M-24V" solenoid valve as presented in Figure 4.8. More details about the solenoid valve are presented in Subsection 4.2.3. It can be seen that at the other side of the solenoid valve another tube with a fitting is connected: the Lee Company's 062 MINSTAC fitting system (see Figures C.3 & C.4), which consists of a 0.062 inch $(1.57[mm])$ O.D. Teflon® tube that has two 0.138-40 UNF nozzles at each fitting end. As can be seen in Figure 4.9, the tube is configured in a certain manner: the tube is first taped to the Boikon profile support pillar, subsequently looped once in the air and taped to the pendulum cross beam, after which it is rotated (and taped) downwards the pendulum arm. Introducing this loop greatly reduced the drift in the displacement of the pendulum sensor target (see Appendix E.1). It can also be seen that same configuration was done with the electrical wiring of the pressure/temperature sensor, which shall be explained in more detail in Subsection 4.2.4. Note

(a) Connection between the tube and the vacuum chamber's "GN2" feedthrough channel.

(b) Connection between the tube and the tube adapter.

Figure 4.7: Connection between the vacuum chamber's "GN2" feedthrough channel and the Lee Company's "062 MINSTAC - LFA Tubing Adapter". Note that the blue tyraps were needed to prevent the connections from detaching at the high pressures up to 7 [bar].

that there is a small difference: the electrical wires make a complete loop, while the fluidic tube makes a partial loop.

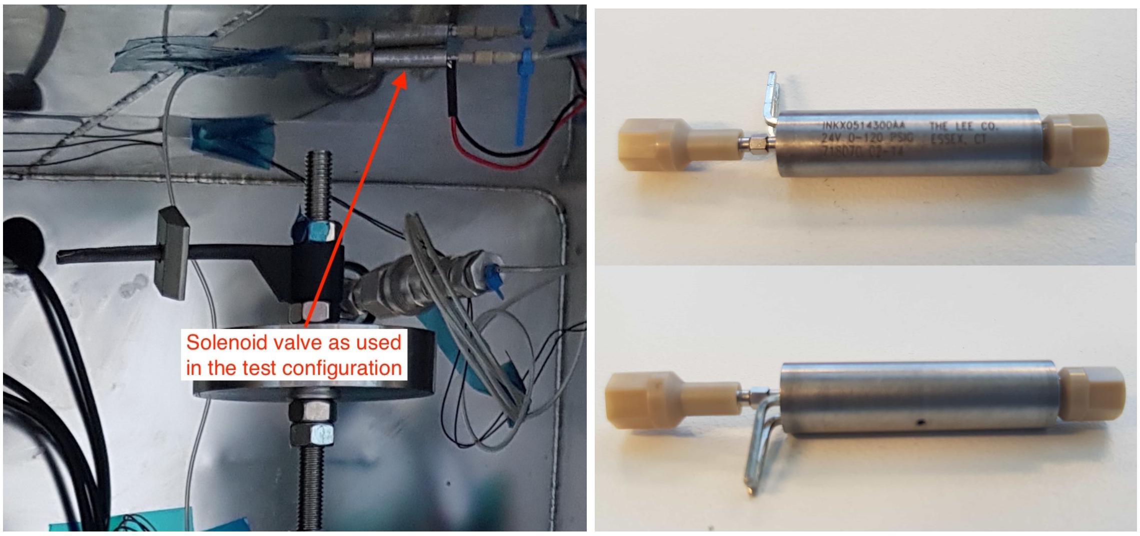

(a) Solenoid valve as used in the thrust bench test.

(b) Two close-up side views of the solenoid valve.

Figure 4.8: The Lee Company's "VHS-M/M-24V" solenoid valve as used in the thrust bench test with the 062 MINSTAC - LFA Tubing Adapter connected to one side and the 062 MINSTAC fitting system connected to the other side, which can be seen in (a). Close-up views are presented in (b). Note that the valve is designed to have a flow in only one direction: the side with the contact pins is the inlet port and the opposite side is the outlet port.

Finally, the other fitting end of the Lee Company's 062 MINSTAC fitting system is used to connect to the last part of the feed system: the Lee company's '062 MINSTAC to 125/156 MINSTAC Adapter', which is integrated in the fluidic input of the 1st gen. interface (see Figure 4.14a) with added silicone to reduce the leakage.

4.2.2. Mass flow controller

In this subsection information is given regarding the mass flow controller that was used during thrust test. Note that even though this device is a mass flow controller, which means that it has the ability to control the mass flow, it was only used as a mass flow sensor. The reason for this was that the controlling function of the device did not produce stable mass flow values, whereas using the pressure regulator as a controller did result in stable mass flow values. This is why the mass flow controller was used in its sensing mode, while the pressure regulator was used as a controller. Switching from the controlling mode to the sensing mode can simply be done activating the valve-override function, which shall be explained later in this subsection.

(a) View from inside the vacuum chamber.

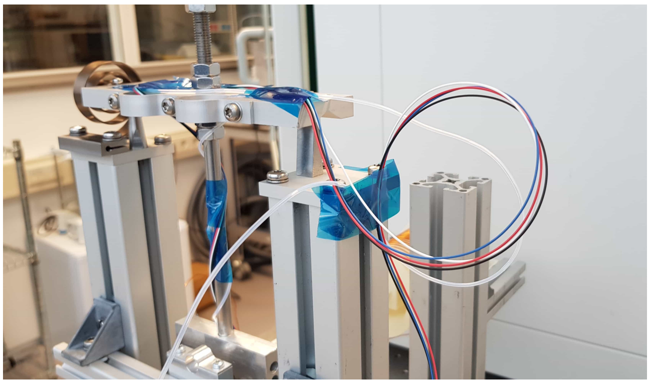

(b) Side view of the AE-TB-5m removed from the test set-up.

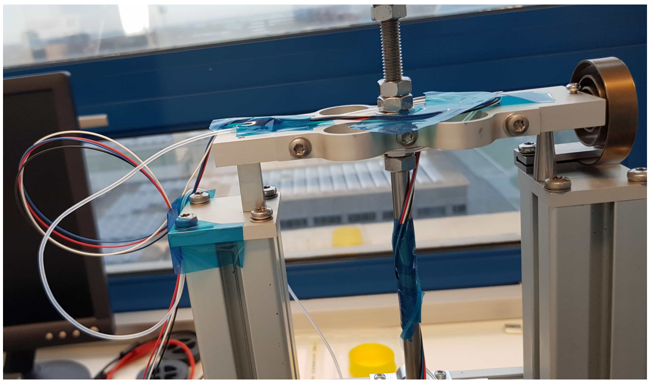

(c) Side view of the AE-TB-5m removed from the test set-up.

Figure 4.9: 'Loop' configuration of the fluidic tube and the electrical wires of the pressure/temperature sensor. Both the tube and wires are: rotated and taped around the pendulum arm, taped on the pendulum cross-beam, looped in the air and taped to the (Boikon profile) support pillar. Note that fluidic tube makes a partial loop and the electrical wires make a complete loop.

To start off, three mass flow controller are available in the cleanroom that were purchased from the company Brooks Instrument BV and all were calibrated for nitrogen gas. One Brooks 5851S mass flow controller is stored in the locker of the micro-propulsion group and two Brooks 5850S mass flow controllers are integrated in the GPF as was displayed in Figure 4.5. A close-up of the two devices in the GPF can be found in Figure 4.10.

(a) The Brooks 5850S (/BC 1K A 1 A A0 B B 1 B1) mass flow controller that has a range of 0-2000 [mln/min] and was used for the thrust bench test.

(b) The Brooks 5850S (/BC 1K A 1 B A0 B A 1 B1) mass flow controller that has a range of 0-144 [mln/min]. Note that this controller was not used for the thrust bench test.

Figure 4.10: The Brooks mass flow controllers that were integrated in the GPF. Note that the label of the mass flow controller in the right picture is clear, while the label of the other mass flow controller has faded.

It can be seen in Figure 4.10 that the mass flow controller that was used for the thrust bench test has a label that is partly faded, which is why some data about this device is unknown. For example, it is not known what the required operating pressure is for using the controlling function. Also, the serial number of the mass flow controller is unknown. When a call was made to the company Brooks Instrument BV in order to retrieve information (e.g. most recent calibration date) about the device, the serial number was necessary to search in their data base. Thus, it is advised to send the device to the company in order to both recover the missing data and recalibrate the mass flow controller.

Fortunately, the missing data did not inhibit the usage of the mass flow controller for the thrust bench test as sufficient information was available. An overview with the specifications of the device is presented in Table 4.6. The mass flow controller is a Brooks 5850S model and has a configuration code of BC 1K A 1 A A0 B B 1 B1, which for example indicates that this device has a fast response time that is smaller than $0.2[s]$. More information about this configuration code can be found in the manual [25]. Furthermore, the device has a $0-5[V]$ measurement/control signal for a measuring/control range of $0-2000[mln/min]$, where the unit is in milliliters per minute and the letter 'n' indicates that the calibration with nitrogen gas was done at normal conditions, which means at a temperature of $0[^{\circ}C]$ and a pressure of $1[atm]$ [25]. Since the measurement read out is in normal volumetric flow ($\dot{V}$) [mln/min], conversion to mass flow [kg/s] for **all measurement data** is done by using the density of nitrogen at normal conditions (ρ_{N2_n}), which is $1.2498[kg/m^3]$. This is because the device is a thermal mass flow meter, which functions based on a specific working principle. The working principle is best explained with Figure 4.11 and Equation 4.1.

Table 4.3: Overview of the Brooks 5850S mass flow controller. Note that '% F.S.' stands for the percentage of the Full Scale (or measurement range of the device) and '% S.P.' stands for the percentage of the Set Point (or measured value).

Model Type / Configuration Code	Brooks 5850 S / BC 1K A 1 A A0 B B 1 B1
Measured Parameter	Volumetric flow rate: $\dot{V}$ [mln/min]
Range & Accuracy	0 – 2000 [mln/min] ± 0.2% of F.S. or ± 0.7% of S.P.
Measurement/Control Signal	0 – 5 $[V]$
Warm Up Time	45 minutes to reach specified accuracy. Note: a warm up time of 10 minutes or smaller, will result in a ± 1.0% of F.S.
Repeatability	± 0.25% of S.P.
Stability	Smaller than ± 0.5% of S.P. per year
Last Time Calibrated	Unknown
Response Time	<0.2 [s]

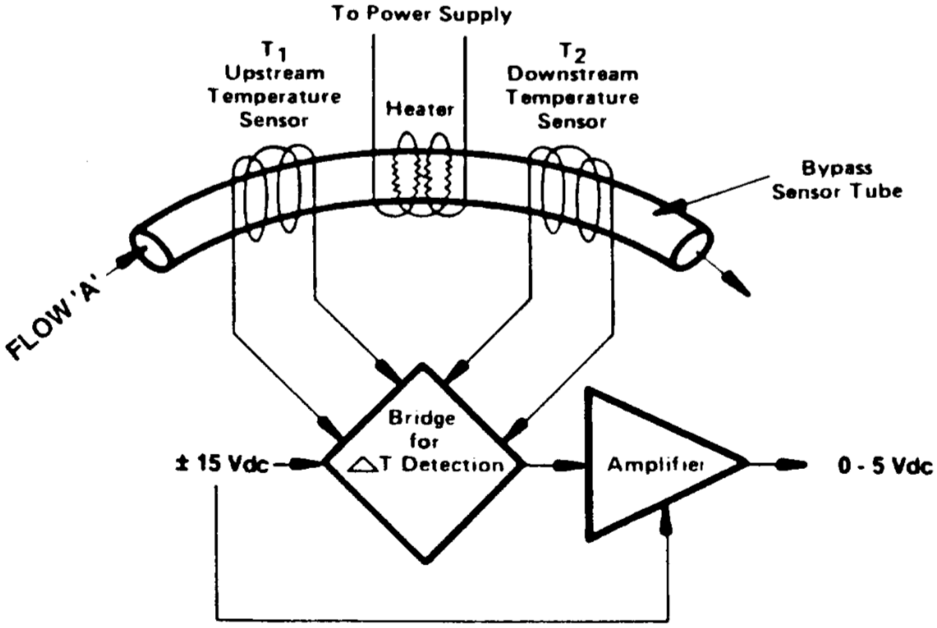

Figure 4.11: Working principle of a thermal mass flow meter as done by the Brooks 5850S mass flow controller [25].

$$\Delta T = A \cdot P \cdot Cp \cdot \dot{m} \tag{4.1}$$

Where:

- ΔT is the temperature difference between T1 and T2 $[K]$
- A is the constant of proportionality $[s^2 \cdot K^2/kJ^2]$ (defined by Brooks [25])
- P is the heater power $[kJ/s]$
- Cp is the specific heat of the gas at constant pressure $[kJ/kg \cdot K]$

A small part of main mass flow goes through a very narrow bypass tube that is thin-walled and made from stainless steel, which is displayed in Figure 4.11. In the middle of the bypass tube is a heater that provides constant power and there are two temperature sensors present. One temperature sensor

(T1) is upstream and the other sensor (T2) is downstream w.r.t. the heater. When there is no flow, both temperature sensors will measure the same temperature because both sensors will obtain the same amount of heat from the heater. In this case it would mean that ΔT in Equation 4.1 is zero, which also means that $\dot{m}$ is zero. When there is a nitrogen gas flow, the gas will prevent the heat from reaching $T1$ and carry all the heat that is generated by the heater to $T2$. This results in a temperature difference between $T1$ and $T2$, which is converted to a electrical signal using the bridge circuit and amplifier. This temperature difference is directly proportional to the nitrogen mass flow as can be seen in Equation 4.1. Also, Cp is the only parameter that is influenced by pressure and temperature differences. However, the influence of temperature and pressure changes on Cp is very small and thus neglected. For example, an employee of the company Brooks Instrument BV stated that changing the pressure from $1[bar]$ to $5[bar]$ would only result in an added measurement uncertainty of $\pm 0.39[\%]$.

Now that the working mechanism has been explained, information about the connection with the cleanroom computer shall be explained. The mass flow controller has a 15 pin D-type male connector (See Figure B.1) and is via a DB-cable 15M/F (see Figure 4.6a) connected to a new Printed Circuit Board (PCB) as can be seen in Figure 4.12. It can also be seen that the previous configuration of the DB-cable 15M/F was chaotic. Therefore, the new PCB was created, which was done with the help of the current cleanroom manager: Sevket Uludag. Apart from looking more orderly, the new PCB came with a few more advantages. Previously, a big power supply unit was needed to power the mass flow controller, while now only a small adapter (Voltcraft FPPS: $24[Vdc]$, $0.75[A]$) can be plugged in the PCB connection (see Figure B.4) to provide power. Furthermore, it was mentioned before that the mass flow controller can be switched from the controlling mode to the sensing mode by activating the valve-override function, which fully opens the valve inside the mass flow controller. This valve-override function can be induced by sending a constant $5[V]$ signal to PIN 12 of the 15 pin D-type male connector (See Figure B.1). Previously, this was done a second power supply unit, while now simply the voltage divider on the new PCB can be switched on (See Figure B.2). Looking again at Figure 4.12a, it can be seen that four wires are connected between the new PCB and the NI CB-68LP breakout board. Two wires are connected to pin 2 ("Flow Signal[V](0)+") and pin 10 ("FlowSignal(0)-"), which together provide the signal for the volumetric flow rate measurement. Alhough not used for this thrust test, the other two wires are connected to pin 1 ("SetPoint CommonInput(0)-") and pin 8 ("SetPoint[V](I)+"), which together can be used to the control the volumetric flow rate. Note that the NI CB-68LP breakout board that is connected to the cleanroom computer shall be explained in more detail in Subsection 4.2.6.

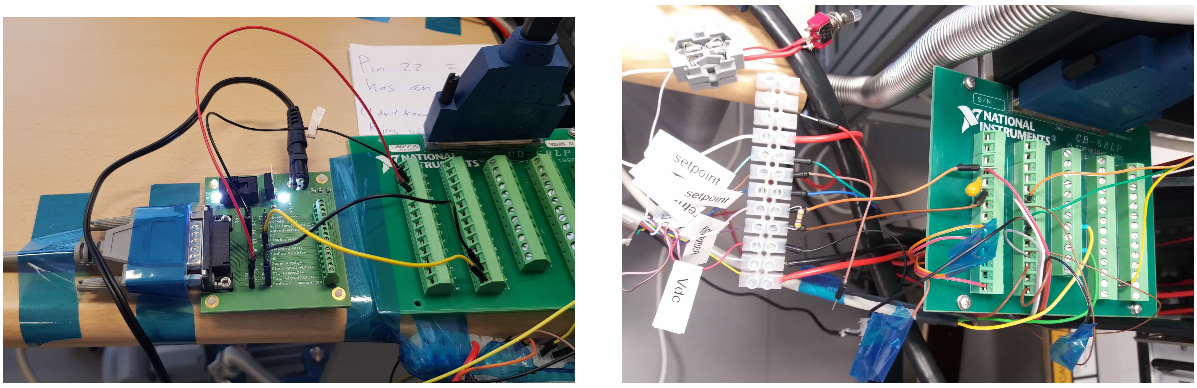

(a) Improved connection of the DB-cable 15M/F.

(b) Previous connection of the DB-cable 15M/F.

Figure 4.12: Previous and current configuration of the DB-cable 15M/F. Previously, the cable was cut open in order to connect the wires to the NI CB-68LP breakout board. Currently, the cable is connected to the new PCB from which four wires are connected to a second NI CB-68LP breakout board.

4.2.3. Solenoid valve

The VHS-M/M-24V solenoid valve that was mentioned in Subsection 4.2.1 (see Figure 4.8) was purchased from the Lee Company, which is a company that focusses on micro-fluidic systems. This solenoid valve was needed as it enabled easy control over the thrust bursts: thrust (de)activation was simply done with the push of a button in the LabVIEW interface. Without the solenoid valve, the only option to control the thrust bursts would be to manually open/close the shut-off valve or flow path selector of the GPF. Also, it is likely that the solenoid valve will be used for the propulsion system of the Delfi-PQ satellite.

The solenoid valve, and actually every component provided by the Lee Company, is quite fragile and thus needs to be handled with extreme care at all times. For example, it is mentioned in the specification sheet in Figure C.2 that when connecting a (.138-40 UNF) fitting to the ports of the solenoid valve, the fitting must be tightened with a torque between 0.035 and 0.07[N·m] while holding the port. Else the torque will be induced on that valve body, which will result in damage to the valve. For this specific purpose the MINSTAC torque wrench (see Figure C.1) was ordered that is able to fasten fittings to ports of the solenoid valve with a torque of 0.035 or 0.07[N·m]. Note that extensive usage of the wrench causes wear, which results in lower torque values. In Figure C.2 it can also be seen that one port of the solenoid valve is the inlet and the other port the outlet. This needs to be taken into account when connecting the fittings as the flow is designed to only move in one direction. Furthermore, the solenoid valve has an allowed operating pressure range between 0 and $8.27[bar]$. An overview of important specifications of the solenoid valve is presented in Table 4.4.

It can be seen in Table 4.4 and Figure C.2 that in order to operate the valve, a specific operating sequence is needed. First, a spike voltage of $24[V]$ needs to be applied for a duration of $0.35 - 2[ms]$. Hereafter, a constant voltage of $3.2[V]$ needs to be sustained. In case needed, the Lee Company also provides the same type of valve with different operating voltages: $12[V]$ spike and $1.6[V]$ constant. The required voltages were provided by two Power Supply Unit (PSU): the Delta Elektronika E 030-1 and the Delta Elektronika D 030-1), which are presented in Figure 4.13a. These PSU were connected to the input channels of the Lee Company's Spike & Hold Driver, which is presented in Figures C.7 and C.6. The output channel of the driver provides an output voltage that can be rapidly switched between the voltage level of one PSU and the other. It can be seen in Figure 4.18 that the driver's output channel is connected to the "Experiment" feedthrough (outside) of the vacuum chamber via two wires. As will be explained in Subsection 4.2.5 the vacuum chamber has many feedthrough channels and each channel has been labeled with a different name. The "Experiment" feedthrough (inside) of the vacuum chamber has a D-sub 9 connector through which the voltages to the solenoid valve are provided via two wires as presented in Figure 4.13b. Note the D-sub 9 connector also has other wires that are connected to a different power supply unit: the Delta Elektronika SM7020 (see Figure 3.12). It was intended that these wires would be used to provide power to the heaters of the 3rd gen. MEMS-VLM chip, but the heaters were not used during this thesis project due time constraints.

Table 4.4: Overview of the Lee Company's "VHS-M/M-24V" solenoid valve.

Model Type	VHS-M/M-24V
Operational Pressure Range	0-120 [psig] (=0-8.27 [bar])
Designed Flow Direction	From the inlet port to the outlet port as displayed in Figure C.2.
Port Connection Type	.620 Lee MINSTAC Boss
Required Torque	A torque between 0.035-0.07 $[N \cdot m]$. Note that it is highly recommended to use the MINSTAC torque wrench when connecting the fittings to the ports.
Required Operating Sequence	1. Induce a 24 [V] spike voltage between 0.35 and 2 [ms]. 2. Reduce the voltage to a constant value of 3.2 [V]. (Note that this is the recommended value and that 4.5 [Vdc] is the maximum)

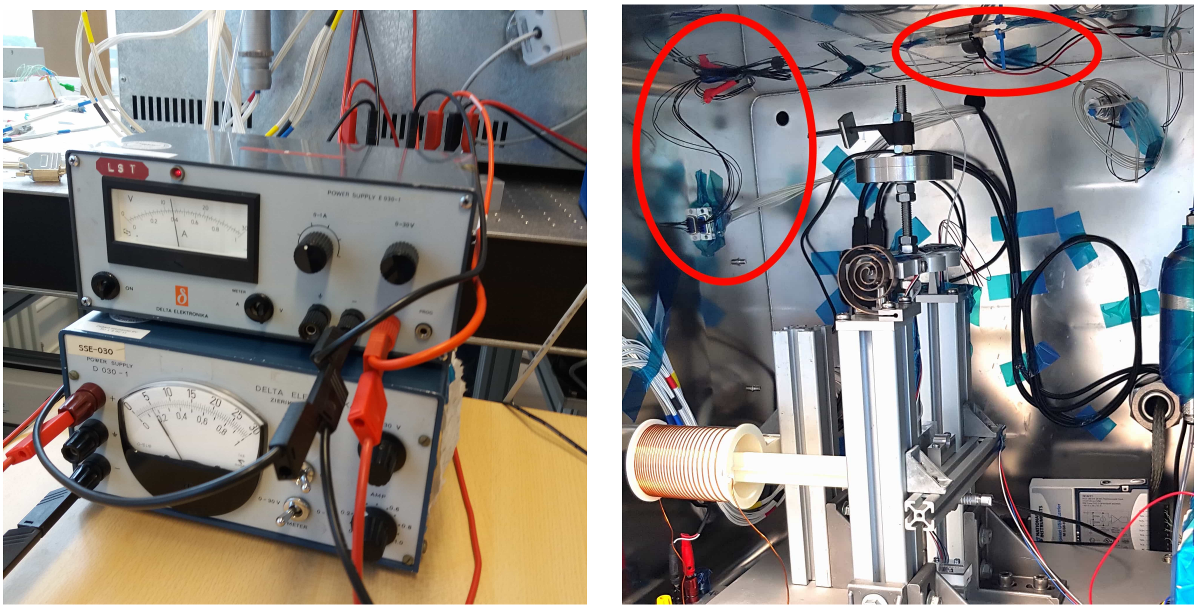

(a) Power supply units that are connected to the "Experiment" feedthrough channel. The upper unit (Delta Elektronika E 030-1) should be set at 24 [V] and the lower unit (Delta Elektronika D 030-1) at 3.2 [V].

(b) Set-up in the vacuum chamber: the left marked area indicates the "Experiment" feedthrough channel connector from which two wires are connected to the solenoid valve in the right marked area.

Figure 4.13: Power supply units and the connections to the "Experiment" feedthrough channel , which are needed to provide the voltages to the Lee Company's solenoid valve.

4.2.4. Pressure/temperature sensor

The MS5837-30BA pressure/temperature sensor was purchased from the company TE Connectivity and integrated in the 1st gen. interface, which was explained in Subsection 2.1.2. The reason why this sensor was required, was because it was able to measure two important parameters: P_{int} and T_{int}. These two parameters best represent the gas conditions (P_c and T_c) in chamber of the 3rd gen. MEMS-VLM chip before the gas flows through the nozzle. It was shown in Table 4.5 that different accuracies apply for different measurement ranges. For example, during the thrust bench test the pressure was within the range of 0 and $6[bar]$ and the temperature was within the range of 0 and 25[°C]. This means that the corresponding accuracies were $\pm 0.05[bar]$ and ± 1.5[°C], respectively.

Table 4.5: Overview of the TE Connectivity's MS5837-30BA pressure/temperature sensor [22].

Model Type	MS5837-30BA
Measured Parameters	Absolute pressure: P_{int} [bar] Temperature: T_{int} [$°C$]
Ranges & Accuracies - P_{int}	0 – 6 [bar] ± 0.05 [bar], 0 – 20 [bar] ± 0.1 [bar], 0 – 30 [bar] ± 0.2 [bar], For 0<T_{int}<40 [$°C$]
Ranges & Accuracies - T_{int}	0 – 25 [$°C$] ± 1.5 [$°C$], 0 – 60 [$°C$] ± 2.0 [$°C$], -20 – 85 [$°C$] ± 4.5 [$°C$], For 0<P_{int}<10 [bar]
Protocol	I^2C

As mentioned before in Subsection 4.2.1 (see Figure 4.9c), the electrical wiring was configured the same as the fluidic tube: it was rotated around the pendulum arm, taped on the pendulum cross-beam, looped in the air and taped to the support pillar. This configuration of the electrical wires (and fluidic tube) greatly reduces the amount of displacement drift measured by the CS2 displacement sensor about which more information is provided in Subsection 4.2.7. However, the length of the electrical wires or sensor cable was limited and could therefore not be connected with the Data Acquisition System (DAQ) directly. For this reason, an (F/M) extension cable was created. The sensor cable has a 4-pin male connector at its end, which was connected with the female connector of the extension cable. This connection can be seen in the marked area of Figure 4.15. The blue tape was applied because slight movements in the connection resulted in a signal loss error and subsequently in a shutdown of the LabVIEW program. This indicates that this connection still has some room for improvement. The 4-pin male connector of the extension cable was plugged into the breadboard ports J60 up to J63 as can be seen in Figure 4.16. Note that the red wire needs to be plugged into port J60, else LabVIEW will not be able to run as it will give an error message. From this breadboard a connection was made to the DAQ and subsequently the cleanroom computer, which shall be explained in more detail in Subsection 4.2.6.

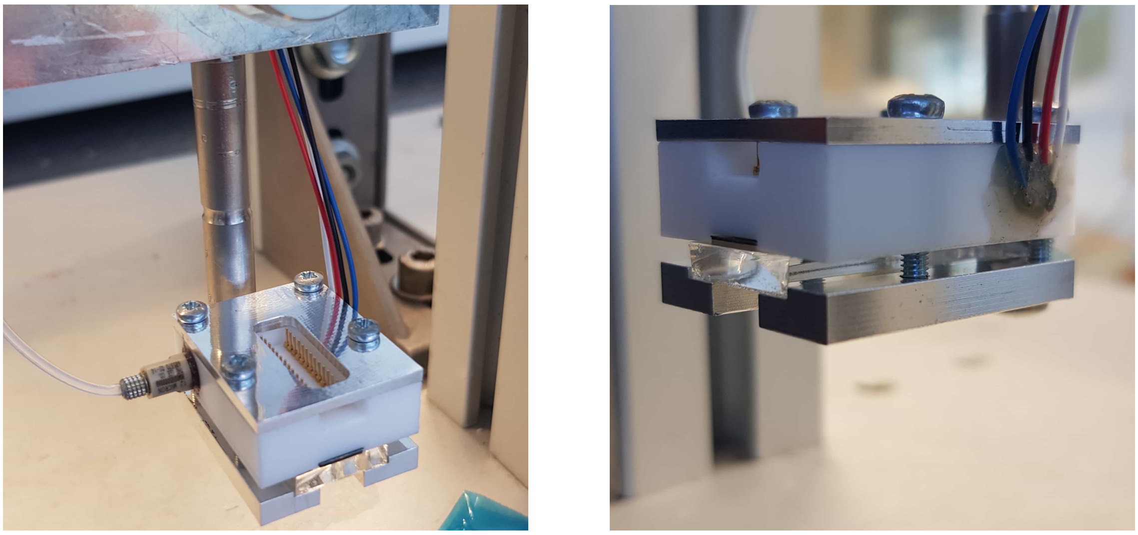

(a) View of the side with the fluidic input.

(b) View of the side with the sensor.

Figure 4.14: View of the fluidic input and pressure/temperature sensor of the 1st gen. interface as used during the thrust bench test.

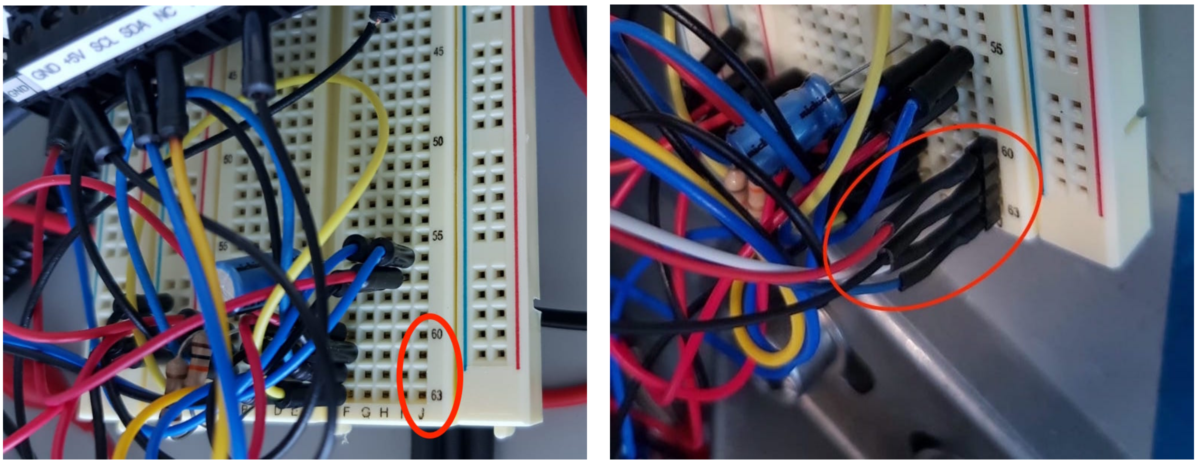

(a) Breadboard without the extension cable.

(b) Breadboard with the extension cable.

Figure 4.16: The breadboard in which the extension cable for the pressure/temperature sensor was plugged in. It was connected to port codes J60 up to J63, where the red wire was connected to port J60. Note that in the near future usage of this type of breadboard in the vacuum chamber will be prohibited according to new rules regarding maximum allowable outgassing.

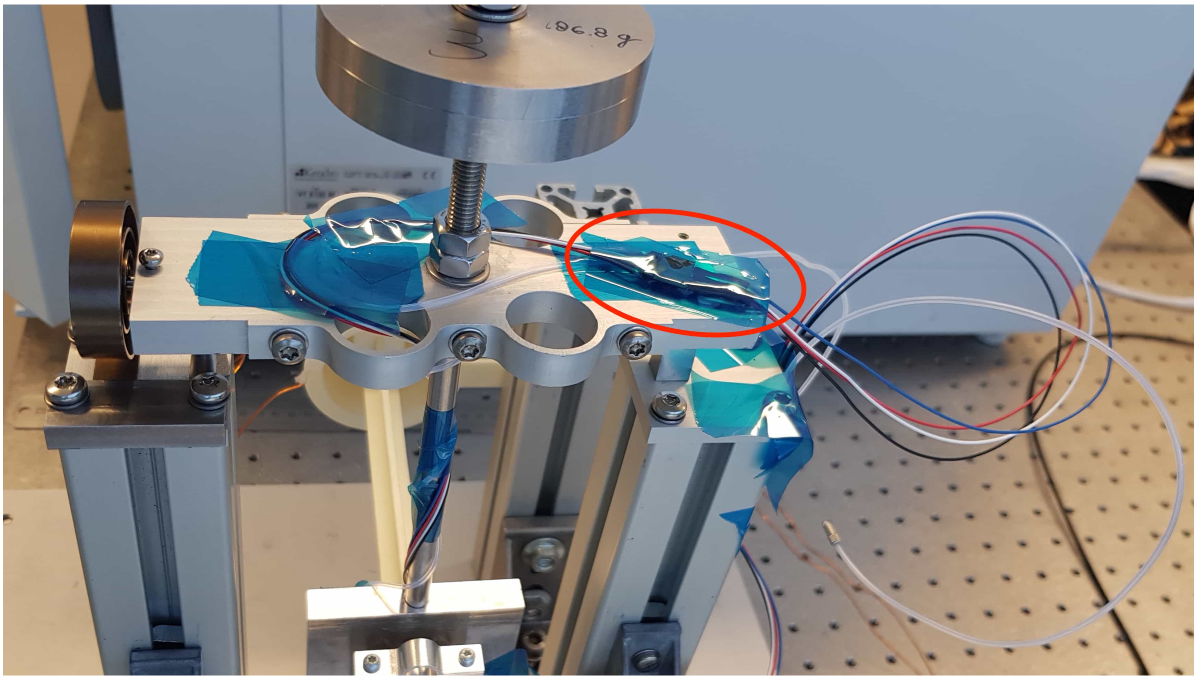

Figure 4.15: Cable of the pressure/temperature sensor connected to the extension cable on the pendulum cross beam as can be seen in the marked area. Note that the (blue) tape was necessary to prevent small movements of the connection, since this would result in errors in the LabVIEW program.

4.2.5. Vacuum chamber, pressure sensor and vacuum pump

As mentioned before, the thrust bench test was done inside a vacuum chamber: the Heraeus Vacutherm vacuum oven as presented in Figure 4.17. The reason why it is called a vacuum oven is because it has the ability to add heat to the environment inside the chamber, although this function was not used for the thrust bench test. It was also stated before that the vacuum chamber has many feedthrough channels for electrical wires, fluidic tubes etc. Each feedthrough channel has been labeled and this can be seen in Figure 4.18. More information about the Heraeus Vacutherm can be found in the manual [26].

Creating a vacuum environment inside the vacuum chamber was achieved using the Vacuubrand's RZ 6 rotary vane vacuum pump. This vacuum pump, which is presented in Figure 4.19, is owned by the micro-propulsion team and is able to reduce P_a to a pressure of $30[Pa]$ within 15 minutes. Apart from air or nitrogen gas, the pump can also safely remove water vapor from the vacuum chamber. However, for removing water vapor, the black gas ballast valve on the pump should always be pointed towards the reservoir. More information about the vacuum pump can be found in the manual, which is stored in the cleanroom.

It should be noted that before the pump is switched on, the valve line connected with the vacuum pump and the release valve should be open, which are located at the top left of the vacuum chamber in Figure 4.17. Also note that in case the pump is shut off while there is a (vacuum/) low pressure in the vacuum chamber, the valve line should be closed beforehand. Else, the outside air will flow back into the vacuum chamber via the pump and valve line. This was not an issue during the thrust bench test as the vacuum pump was switched on during the whole experiment. Only after completing the thrust bench test and opening the release valve, the vacuum pump was shut off.

Both the Vacuubrand's VACUU VIEW vacuum gauge and the DCP 3000 vacuum gauge system with a VSP 3000 pressure sensor are connected to the vacuum chamber, which can be seen in Figure 4.20. The latter was used to determine P_a as it can measure very low pressure values. An overview of the specifications of the device is presented in Table 4.6. It should be noted that in the sixth row of the table ”uncertainty” is used instead of ”accuracy”, because this terminology was also used in the manual [11]. Uncertainties in measurements can be caused by systematic errors (gain error, linearity error,

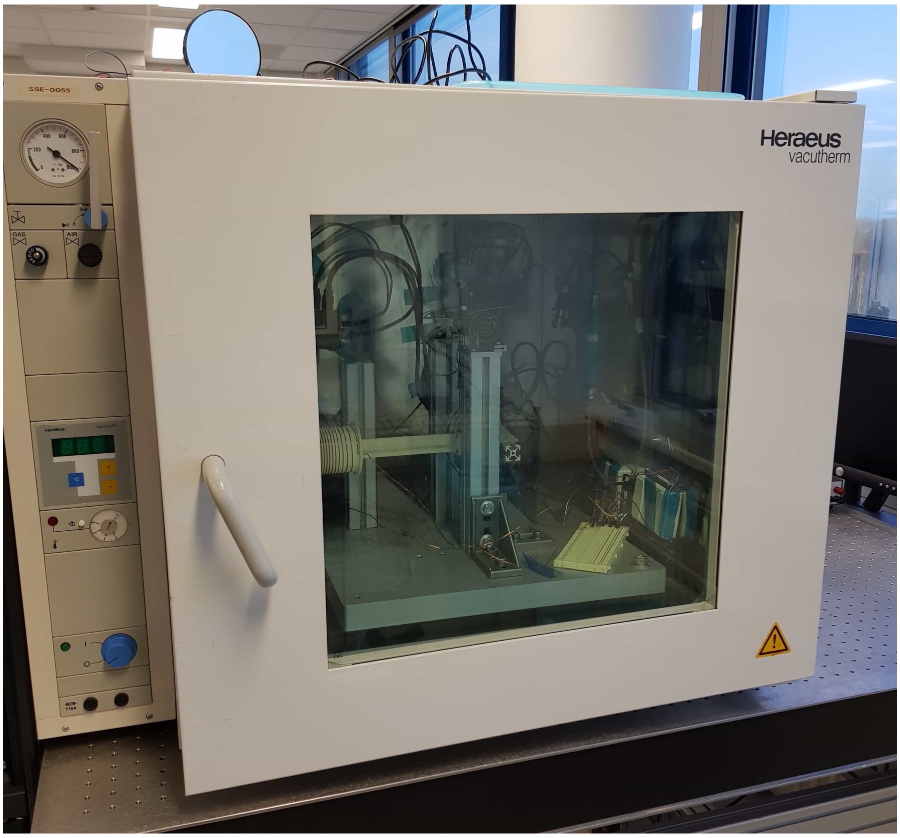

Figure 4.17: Front view of the Heraeus Vacutherm vacuum oven, where the test configuration for thrust bench test is inside the chamber. Note that this vacuum chamber also has the ability to add heat to the inside environment.

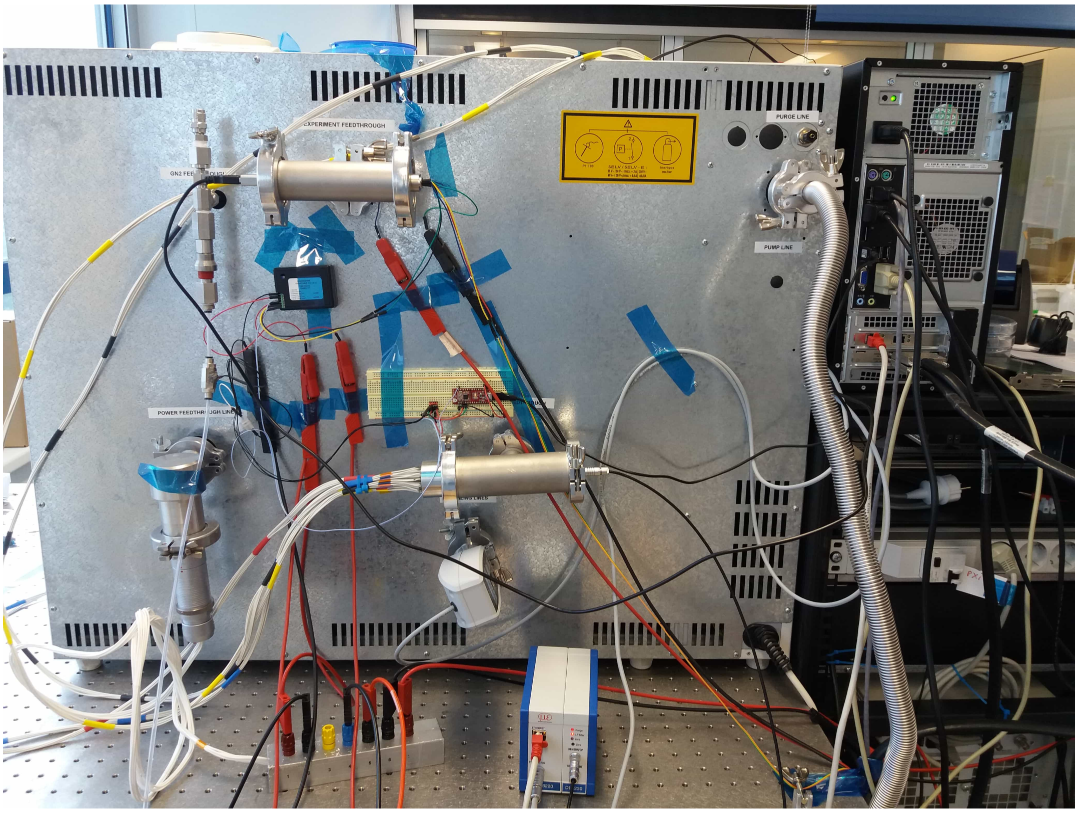

Figure 4.18: Back view of the Heraeus Vacutherm vacuum oven, where all the different feedthrough channels can be seen.

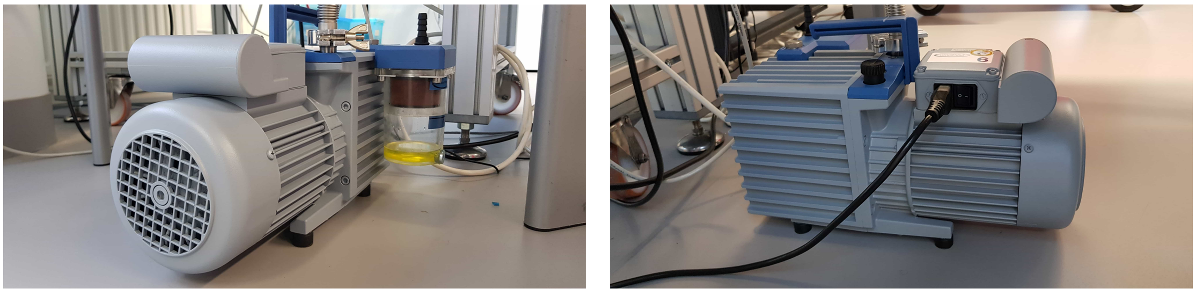

(a) Isometric view, where the reservoir and pump line are located.

(b) Side view, where the power button and plug are located.

Figure 4.19: Two views of the Vacuubrand's RZ 6 rotary vacuum pump. Note that when pumping an environment with water vapor, the arrow on top of the (black) gas ballast valve should be pointed towards the reservoir.

etc.) that relate to the accuracy and by random errors that relate to precision or repeatability (Coleman and Steele, 2009) [27]. Since it is not specifically stated what type of uncertainty is applicable, it shall be assumed that it is a systematic uncertainty and thus relates to the accuracy. This assumption was made because the uncertainty caused by random fluctuations in the data is significantly smaller than the $\pm 15[\%]$ value presented in the table. This can be found later on in Table 5.1, where for the initial pressure the mean equals $28.77[Pa]$ and the standard deviation $0.0791[Pa]$, which results in a $0.27[\%]$ uncertainty. This means that it is safe to assume that it is not a random uncertainty, but a systematic uncertainty.

(a) The DCP 3000 gauge connected with the VSP 3000 vacuum sensor.

(b) The VACUU VIEW vacuum gauge at the backside of the vacuum chamber.

Figure 4.20: The two pressure sensors connected to the vacuum chamber. Note that the DCP 3000 with the VSP 3000 was used to perform the measurements as it could measure very low pressures.

4.2.6. Cleanroom computer and DAQs

There are many devices in the set-up of the thrust bench test that gather measurement data and a few that have controlling functions. All these devices were connected to the cleanroom computer located next to the vacuum chamber. An overview of the connected devices can be found in Figure D.1 in Appendix D. Three devices were directly connected to the cleanroom computer: a USB hub with a USB

Table 4.6: Overview of the DCP 3000 vacuum gauge system and VSP 3000 pressure sensor specifications [11].

Vacuum Gauge System	DCP 3000
Pressure Sensor	VSP 3000
Measured Parameters	Absolute pressure inside the vacuum chamber: P_a [mbar]
Pressure Range	$1.0 \cdot 10^3$ - $1.0 \cdot 10^{-3}$ [mbar]
Operational temperature range	$283.15 - 313.15 [K]$
Uncertainty	± 15 [%] of measured value, For pressures smaller than 1000 [Pa]

3.0 cable, the DT6220/DL6230 DAQ with an ethernet cable and the NI PCI-6229 DAQ integrated in the cleanroom computer.

To start off with the USB hub, this device was taped to the wall inside the vacuum chamber as can be seen in Figure 4.21. It can also be seen that the hub requires a power supply and has a maximum connectivity of four devices excluding the computer. Three DAQ devices were connected to the hub via USB: the NI USB-9162 + NI 9211, the NI USB-6008 and the NI USB-8451. The NI 9211 is integrated with the NI USB-9162 (see Figure D.2), which together can be used to measure temperature via thermocouples. Although the thermocouples were not used during the thrust bench test, the DAQ needs to be plugged in because the LabVIEW code incorporates the measurements of this device. Without the DAQ, LabVIEW will give an error message and abort the program. As for NI USB-6008 and the NI USB-8451, these DAQ devices were both connected to the breadboard as can be seen in Figures D.4-D.3. It was mentioned before in Subsection 4.2.4 that the pressure/temperature sensor cable was plugged into this breadboard. Note that for thrust bench tests with liquid water, a liquid flow sensor can be connected to the breadboard, which is explained in more detail in Appendix A.

Figure 4.21: The USB hub taped to the wall inside of the vacuum chamber. Note that apart from being connected to the clean computer, the power supply cable needs to be plugged in as well. Also, it has the maximum connection capacity of five devices including the computer.

As for the DT6220/DL6230 DAQ, this device was specifically designed for the CS2 displacement sensor [24]. The device, presented Figure D.8, was placed outside the vacuum chamber. Also, it was connected to the cleanroom computer with an ethernet cable as was mentioned before. As could be seen in Figure 4.18, the DAQ was connected to the feedthrough of the vacuum chamber, which was connected to the CS2 displacement sensor inside the vacuum chamber.

As can be seen in Figure D.7, the NI PCI-6229 was integrated in the cleanroom computer. The NI PCI-6229 was connected to the two NI CB-68LP breakout boards (see Figure 4.12a and 4.22) using two thick 68-pin cables. Each breakout board has 68 numbered (female) plugs in which (male) wires can be plugged into. However, every plug number has a different channel name and a different purpose. For example, some plugs can only be used for analogue input signals (Ai) or data acquisition, while others can only be used for analogue output signals (Ao) or control functions. A layout of the pins (or plug numbers) and the corresponding channel names for the NI PCI-6229 are presented in Figure D.6 in Appendix D. Note that in LabVIEW the channel names are detected and not the plug numbers.

The breakout board presented in Figure 4.12a was connected to the new PCB and Brooks 5861 S mass flow controller, which was already discussed in Subsection 4.2.2. However, it should be noted that plug 22 (=Ao0) of this breakout board should not be used. It is likely damaged as an error message in LabVIEW occurred when plug 22 was attempted to be used. The other breakout board, which is presented in Figure 4.22, was connected to many other devices: the SM7020 PSU, the SM7020-D PSU and the Spike & Hold Driver. The SM7020 was able to provide power to the heaters of the 3rd gen. MEMS-VLM chip, though this was not used for the thrust bench test. The other PSU, the SM7020-D, was used to provide electrical currents to the VTDC actuator in order to calibrate the AE-TB-5m pendulum thrust bench. As for the Spike & Hold Driver, this device was used to control the VHS-M/M-24V solenoid valve with the help of the (Delta Elektronika) E 030-1 and D 030-1 PSU.

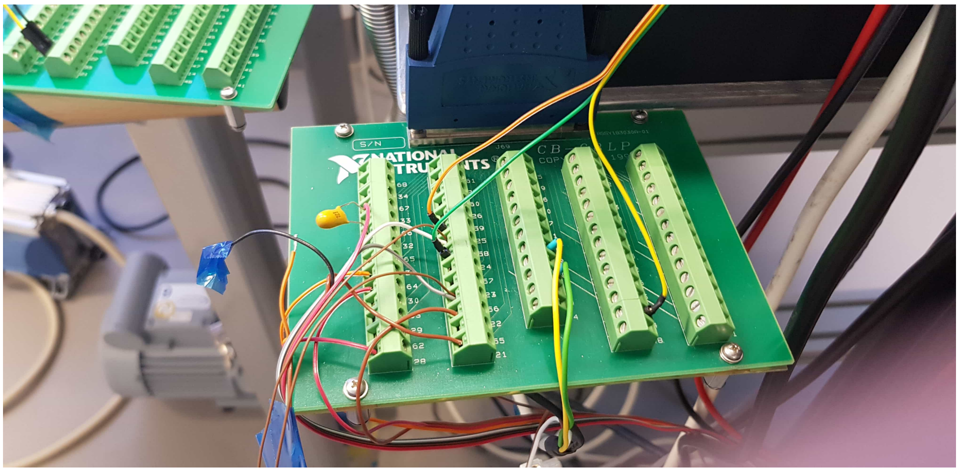

Figure 4.22: The NI CB-68LP breakout board connected to SM7020, SM7020-D and the Spike & Hold Driver.

4.2.7. AE-TB-5m thrust bench

Since the AE-TB-5m pendulum thrust bench had the same configuration as used during the pendulum calibration test as explained in Section 3.3, it is not required to again describe the whole set-up.

4.2.8. Summary

The equipment needed to properly perform the Nitrogen thrust bench test can be found in Table 4.7 and the measured parameters in Table 4.8.

4.3. Test Procedure

In this section the required steps for the thrust bench test are described in Tables 4.9 and 4.10. After these steps were performed the experimental data was obtained, which was processed in MATLAB (see file "$TT04\_Data\_Analysis.m$" for TT-04 and "$TT05\_Data\_Analysis.m$" for TT-05) and these results can be found in Section 5.

Table 4.7: Equipment needed to perform nitrogen thrust bench tests for the 01-LS2-02 chip.

Item Name:	**Description:**
Pendulum thrust bench: AE-TB-5m (see Figure 3.10)	Used to determine thrust force of the 01-LS2-02 chip by measuring the displacement of the pendulum arm. The DT6220/DL6230 DAQ is used to convert the CS2 displacement sensor's measurements into digital data on the cleanroom computer.
VTDC actuator (see Figure 3.9)	Used to calibrate the AE-TB-5m.
Propellant feed system (see Figure 4.5)	Provides gaseous Nitrogen to the 01-LS2-02 chip with the ability to control mass flow using the Brooks 5850S mass flow controllers.
Vacuum oven: Heraeus Vacutherm (see Figure 4.17)	Used to measure the ambient pressure and to provide a vacuum environment that shall be needed for a few thrust bench tests.
Pressure sensor (MS5837-30BA) integrated in the interface [22]	Used to measure the pressure near the inlet of the 01-LS2-02 chip from which the chamber pressure shall be deduced. Can also be used to provide additional information about the temperature of the propellant near the inlet.
Power supply: SM7020 and SM7020-D (see Figure 3.12)	The SM7020-D was needed for calibrating the AE-TB-5m before and after each thrust bench test. The SM7020 was intended to be used for providing power the heaters of the 01-LS2-02 chip.
DAQs and cleanroom computer (see Figures D.8-D.3)	Used to measure and digitalize all the experimental data. The available DAQs are: NI PXI-8331, NI PXI-6229 and NI PXI-4220.

Table 4.8: Overview of the measurement equipment that was needed to determine the measured parameters during the thrust bench tests. Note that 'F.S.' stands for Full Scale and 'S.P.' stands for Set Point.

Parameters	**Measurement Device / Sensor**	**Range & Accuracy**
P_a [Pa]; Absolute pressure in the vacuum chamber.	DCP3000 + VSP3000	0.1 – 106000.0 [Pa] ± 15% of displayed value For P <1000 [Pa] and 283.15<T<313.15 [K]
P_{int} [bar]; Absolute pressure in the interface for the 3rd gen. MEMS-VLM chip.	MS5837-30BA	0 – 6 [bar] ± 0.05 [bar] For 0<T<40 [$°C$]
T_{int} [$°C$]; Temperature in the interface for the 3rd gen. MEMS-VLM chip.	MS5837-30BA	0 – 25 [$°C$] ± 1.5 [$°C$] For 0<P<10 [bar]
$\dot{V}$ [ml/min]; Measured flow rate of Nitrogen.	Brooks 5850 S	0 – 2000 [ml/min] ± 0.2% of F.S. or ± 0.7% of S.P.
X_{disp} [μm]; Displacement of the sensor target w.r.t. the displacement sensor.	CS2	Specified: 0 – 2 [mm] ± 5.02 [µm] In practice: 0 – 5 [mm]

Table 4.9: Detailed procedure for the thrust bench test - Part 1

Step	**Description**	**Performed Y/N**	**Date & time**
1.	Check the most recent calibration date of the sensors (namely the Brooks 5850 S) that are used in the set-up. In case this was a long time ago, depending on the sensor, the sensor should be sent to the manufacturer for recalibration.		
2.	Use Section 4.2 and Table 4.7 to verify if the test set-up is complete: the MEMS-VLM chip has been integrated in the 1st gen. interface and the interface has been attached to the AE-TB-5m thrust bench, the thrust bench has been configured and placed inside the vacuum chamber, all the tubes between the 1st gen. interface and the GPF are connected, all the sensors are connected to the cleanroom computer.		
3.	Turn on the required devices/equipment simultaneously and wait 1 hour for the devices to reach a stable temperature, before performing step 5:		
	1. Turn on the PSU SM7020-D (See Figure 3.12), which has a 1 hour warm-up time.		
	2. Turn on the E030-10 and D030-10 PSU (See Figure 4.13a), which have a 1 hour warm-up time.		
	3. Turn on the Brooks 5850 S sensor (See Figure 4.10a), which has a 45 minutes warm-up time.		
	4. Turn on the DT6220/DL6230 DAQ of the CS2 sensor (See Figure D.8), which has a 15 minutes warm-up time.		
	5. Turn on the clean room computer and log in with the local administrator account. The current login is *".\localadmin"* and the current password is *"sse_cr03"*).		
	6. Turn on the USB hub that connects the cleanroom computer with the NI-USB-6008 (,NI-USB-9262) and NI-USB-8451 DAQ.		
4.	Perform the following checks:		
	1. Open the *"main_marsil_TEST_wDisplacementSensor.vi"* LabVIEW file, check if the data will be saved to the right folder, run the file, check if all the sensors read out measurements (that make sense), check if the valve is able to open/close (produces clicking sound), stop the file and close the program. Note that if the program produces an error, the user should figure out the source of the error and solve it.		
	2. Check if the N2 storage bottle has a sufficient amount of pressurized nitrogen gas by opening the line-in rotary valve and reading the pressure indicator of the pressure gauge. In case this is false, follow the advice in Subsection 4.2.1.		
5.	Close the vacuum chamber door, turn on the vacuum pump and wait at least 15 minutes in order to reach a P_a of 30 [Pa].		

Table 4.10: Detailed procedure for the thrust bench test - Part 2

Step	Description	Performed Y/N	Date & time
6.	Perform the AE-TB-5m calibration test as described in Subsection 3.3.3. Note that some of the steps mentioned above might overlap with the steps needed for the calibration test, since the same equipment used is required.		
7.	Open the *"main_marsil_TEST_wDisplacementSensor.vi"* LabVIEW file.		
8.	Perform the thrust bench test:		
	1. Click on the arrow button at the top left of the LabVIEW interface in order to run the program.		
	2. Set the pressure regulator at X [bar] gauge pressure, which is X+1 [bar] absolute pressure.		
	3. Open both the shut-off valve and the flow path selector valve.		
	4. Wait until the displacement has reached its minimum amplitude and observe wether it remains at this amplitude (1 minute is sufficient). Note that the minimum amplitude depends on the thrust bench configuration and this value can be determined by analyzing the long term (about 12 hours) behavior of the displacement. For example, the author found that the minimum amplitude of the displacement was between is between 10-15 $[\mu m]$.		
	5. Open the VHS-M/M-24V valve by turning on the button *"Open valve"* in LabVIEW in order to induce a thrust force on the AE-5M-TB.		
	6. Wait until the displacement amplitude has reached its minimum value, which depends on the jump in displacement, which depends on pressure X.		
	7. After this it is recommended to wait for another 60 seconds, since the author found through experiments that the displacement needed more time as it was converging to its new balance point.		
	8. Close the VHS-M/M-24V valve by turning off the button *"Open valve"* in LabVIEW in order to stop the thrust force.		
	9. Close both the shut-off valve and the flow path selector valve.		
	10. Repeat steps 5.2-5.9 for the same/other pressure(s) if required.		
9.	Stop the LabVIEW program, localize the stored data and copy the experimental data to a separate folder or a USB device.		
10.	Perform a second AE-TB-5m calibration test.		
11.	Make sure that the N2 bottle, line-in rotary, shut-off and flow path selector valves are properly closed.		
12.	Turn off all the devices described in step 2.		
13.	Remove the test set-up from the vacuum chamber if no other tests will be carried out.		

5

Nitrogen Thrust Bench Test - Experimental Results

In this chapter the test results of the nitrogen thrust bench test are presented. In total six thrust bench tests were performed and all experimental data are stored on the shared micropropulsion-group folder. However during TT-01, TT-02, TT-03 and TT-06 an unacceptable amount of leakage occurred (see SC-TT-05 in Subsection 4.1.4) and this is why the data of these tests could not be used. Luckily, the data of TT-04 and TT-05 was considered valid as no leakage occurred. During each test, five different parameters were measured: the ambient environment in the vacuum chamber (P_a), the pressure (P_{int}) and temperature (T_{int}) in the 1st gen. interface, the mass flow rate of the N2 propellant ($(\dot{m})_{exp}$) and the thrust force ($(F)_{exp}$) produced by the '01-LS2-02' 3rd gen. MEMS-VLM chip. Furthermore, each test consists of four thrust phases (p1-p4): in each phase a thrust force was produced at a different (constant) pressure. How each parameter was determined, will be explained in more detail in Sections 5.1-5.5 taking the experimental data of TT-04 as an example. Note that the experimental results of TT-05 is included as well. The measurement equipment that was needed to determine these parameters were already explained in detail in Section 4.2 and an overview of the sensors with their range and accuracy can be found in Table 4.8. Note that the Brooks SLA5850/60 sensor measured $\dot{V}$ and the CS2 sensor measured X_{disp}, which were converted to $(\dot{m})_{exp}$ and $(F)_{exp}$, respectively. This will be explained in Sections 5.4 and 5.5. Finally, a summary is given in Section 5.6.

5.1. Vacuum chamber pressure

The experimental data produced by the DCP3000 + VSP3000 sensor about the absolute ambient pressure in the vacuum chamber is presented in Figure 5.1 and in Table 5.1. The figure illustrates that the pressure curve starts out almost constant, which is because the vacuum pump was reaching its limit in providing the lowest possible pressure for this test configuration. The change in pressure was $0.4[Pa]$ over $84[s]$, which was small enough to be considered constant as will be explained later on. Hereafter, the pressure increased because the first thrust phase (p1) was induced and thus nitrogen gas was added to the vacuum chamber environment. After the first phase the solenoid valve was closed and thus the thrust force was stopped. This means that the pressure decreased again as the vacuum pump was still on and kept removing (nitrogen) gas from the vacuum chamber. The same process happened for the remaining three phases (p2-p4).

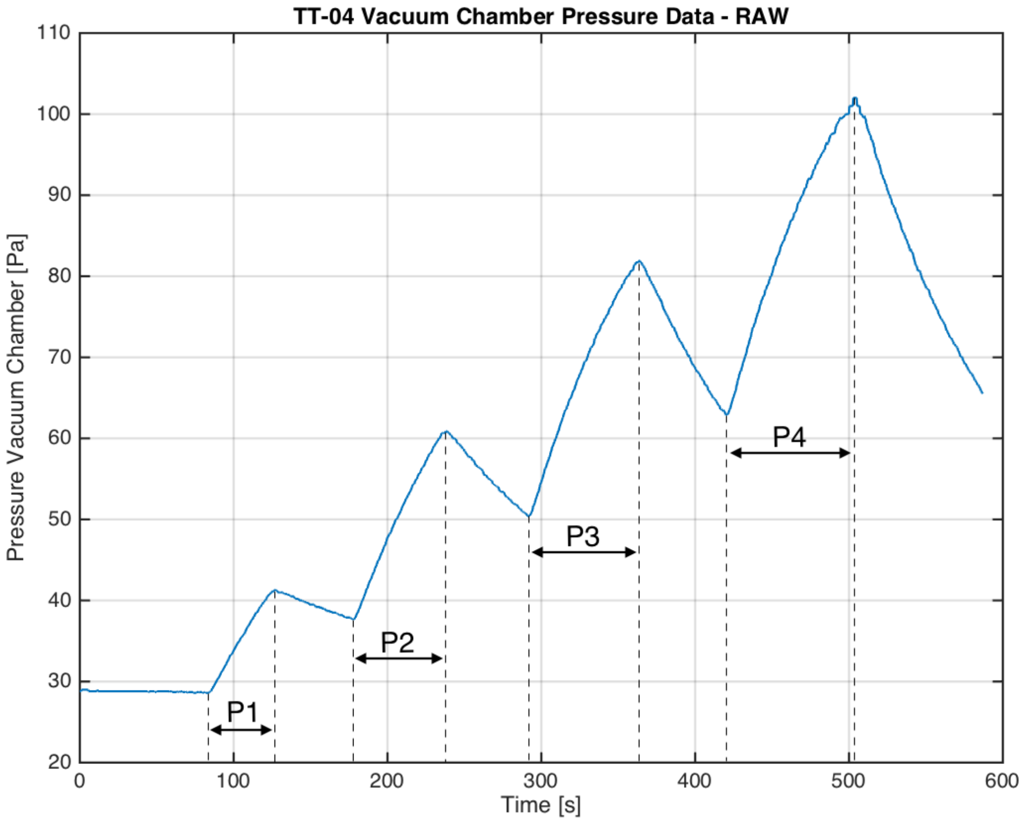

Figure 5.1: Raw absolute pressure data from the sensor (DCP3000 + VSP3000) in the vacuum chamber, which was obtained during thrust test TT-04 and sampled at a frequency of $3.56[Hz]$. Both the effects of the nitrogen gas produced and the vacuum pump are noticeable in the graph. Note that p1 up to p4 correspond to the four thrust phases of the test, where each phase was at a different pressure level.

In Table 5.1 (and 5.2) the six mean values are presented for the P_a data: the initial condition, each of the four phases and the end condition. The table also includes the standard error of the mean (δ_{SEM-Pa}), sensor uncertainty ($\delta_{Sensor-Pa}$) and the total uncertainty (ϵ_{Pa}). The mean was taken because P_a is one of the parameters needed to calculate ideal thrust force ($(F)_{ideal}$). The ideal thrust force needs to be constant when compared to the experimental thrust force ($(F)_{exp}$), since the experimental thrust force was also assumed constant. The mean and standard deviation values were calculated with standard MATLAB commands. From the standard deviation the standard error of the mean was determined with Equation 5.1. The reason why this was taken, was because the standard deviation only displays what the variability is of each measurement compared to the sample mean, while δ_{SEM} displays how far the sample mean likely lies from the true mean.

The relative uncertainty caused by the sensor was $\pm 15[\%]$ for each measurement (as mentioned before in Table 4.6 or 4.8) and this was converted into the absolute sensor uncertainty ($\delta_{Sensor-Pa}$). As for the total uncertainty, this was calculated using Equation 5.2 (Coleman and Steele, 2009) [27]. In the equation the root sum square was used, which can only be applied when uncertainties are independent. This is because δ_{SEM-Pa} is a random error and $\delta_{Sensor-Pa}$ is a systematic error. Note that if the uncertainties would be dependent, then it would be required to summate the uncertainties. The total uncertainty is acceptable as its impact is negligible. This can be explained using "TT-04_p1" as an example: an increase of $+21[\%]$ in P_a results in an increase of $+0.07[\%]$ for $(F)_{ideal}$. Looking back at the initial pressure, it is now clear that the change in pressure over time is small enough to consider the initial pressure to be constant.

$$\delta_{SEM} = \frac{\delta_{std}}{\sqrt{N}} \tag{5.1}$$

$$\epsilon_{Pa} = \frac{1}{P_a}\sqrt{\delta_{SEM-Pa}{}^2 + (\delta_{Sensor-Pa})^2} \cdot 100\% \tag{5.2}$$

Where:

- δ is the absolute uncertainty/erorr given in the measured unit
- SEM standard error of the mean / uncertainty in the mean (given in the measured unit)
- std is the standard deviation of the measurements (given in the measured unit)
- N is the sample size or number of measurements
- ϵ is the relative uncertainty/error given in percentage

Table 5.1: Measurement data produced by the DCP3000 + VSP3000 about the (absolute) ambient pressure inside vacuum chamber including the uncertainties during thrust test TT-04. The different rows are for: the initial condition, the conditions during each of the four phases and the condition at the end.

Test Label	P_a [Pa]	δ_{SEM-Pa} [Pa]	$\delta_{Sensor-Pa}$ [Pa]	ϵ_{Pa} [%]
TT-04_init	29	± 3.9e-5	± 4.3	± 15
TT-04_p1	35	± 3.0e-3	± 5.3	± 16
TT-04_p2	50	± 4.7e-3	± 7.5	± 16
TT-04_p3	68	± 5.7e-3	± 10	± 16
TT-04_p4	85	± 6.6e-3	± 13	± 16
TT-04_end	80	± 5.9e-3	± 12	± 16

Table 5.2: Measurement data produced by the DCP3000 + VSP3000 about the (absolute) ambient pressure inside vacuum chamber including the uncertainties during thrust test TT-05. The different rows are for: the initial condition, the conditions during each of the four phases and the condition at the end.

Test Label	P_a [Pa]	δ_{SEM-Pa} [Pa]	$\delta_{Sensor-Pa}$ [Pa]	ϵ_{Pa} [%]
TT-05_init	30	± 1.8e-4	± 4.5	± 15
TT-05_p1	35	± 2.7e-3	± 5.3	± 15
TT-05_p2	54	± 5.0e-3	± 8.1	± 15
TT-05_p3	69	± 5.7e-3	± 10	± 15
TT-05_p4	83	± 6.7e-3	± 12	± 15
TT-05_end	82	± 6.0e-3	± 12	± 15

5.2. Chamber pressure

In order to perform calculations with ideal rocket theory, it is required to determine the chamber pressure P_c. However, it was not possible to include a pressure sensor inside the chamber of the MEMS-VLM. That is why the MS5837-30BA pressure sensor was integrated in the 1st gen. interface, which upstream w.r.t. the chamber. Since the sensor was not located far from the chamber, it was assumed that P_c was about the same as the pressure inside the 1st gen. interface (P_{int}). In reality P_c is smaller than P_{int} because the chamber is downstream compared to the measurement and thus a pressure drop will occur. However, this pressure drop could not be measured/quantified. It is therefore recommended to adjust the design of the MEMS-VLM chip such that the true chamber pressure can be measured in future experiments and to help determine if the assumption ($P_c \approx P_{int}$) was valid.

As for the measurements made by the MS5837-30BA sensor, the experimental data for the absolute pressure is presented in Figure 5.2 and in Table 5.3. It can clearly be seen in the figure when the four thrust phases were induced: a sudden jump in the pressure caused by opening the valve, a certain time duration in which the pressure level was stable and a sudden drop in the pressure caused by closing the solenoid valve. Note that the author defined stability as: the maximum change in pressure during the thrust phase is $1[\%]$. The reason why this was acceptable, can be explained with the results of Table 5.3: increasing the pressures with $1[\%]$ only results in a $0.9[\%]$ increase in $(F)_{ideal}$ and a $1[\%]$ increase in $(\dot{m})_{ideal}$.

Coming back to Figure 5.2, though it cannot clearly be seen, the initial pressure in the interface has a value of about $3200[Pa]$. However, the DCP3000 + VSP3000 sensor measured an initial pressure of $28.77[Pa]$ and was more accurate for low pressures, which is why it was used to correct the pressure data of the MS5837-30BA sensor. This was done by taking the difference between the initial pressure of the two sensors ($= 3171.23[Pa]$) and subtracting this from all the P_{int} data. This adjusted experimental data was used for Table 5.3. Note that this would mean that the $\pm 4.3[Pa]$ sensor uncertainty of the DCP3000 + VSP3000 sensor needs to be added to the total uncertainty in Table 5.3. However, compared to the $\pm 5000[Pa]$ ($= \pm 5.0e-02[bar]$) sensor uncertainty of the MS5837-30BA sensor, the $\pm 4.3[Pa]$ uncertainty is small and was thus neglected.

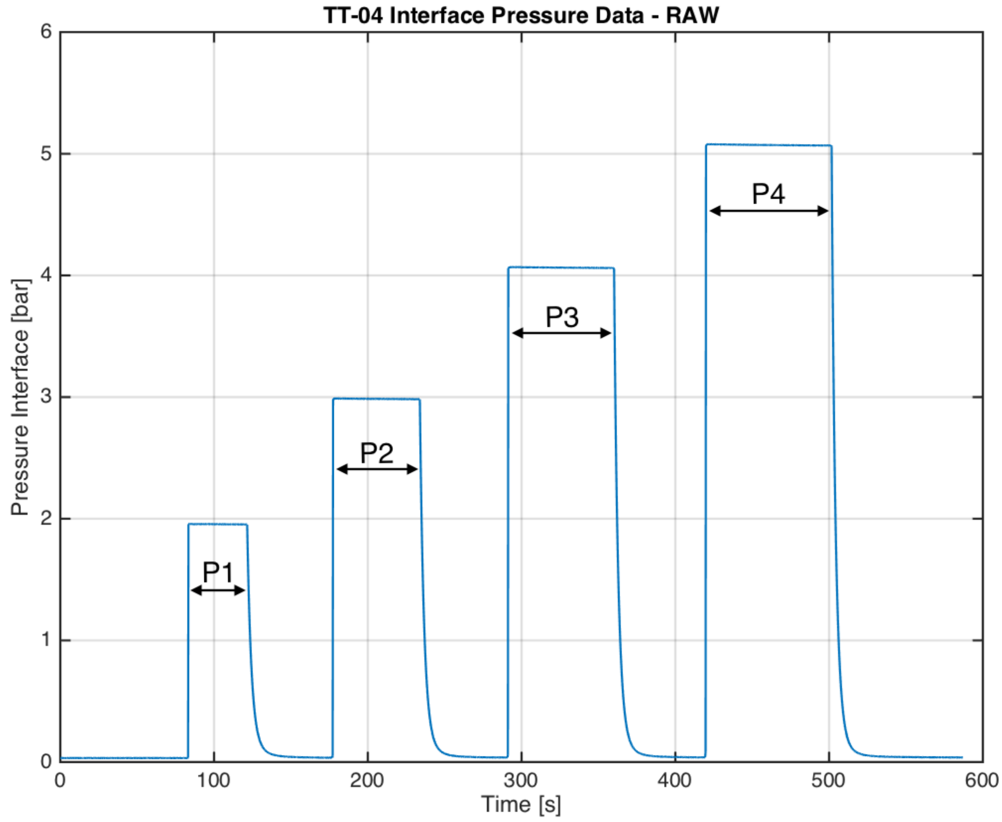

Figure 5.2: Raw absolute pressure data from the sensor (MS5837-30BA) in the 1st gen. interface, which was obtained during thrust test TT-04 and sampled at a frequency of $3.56[Hz]$.Note that p1 up to p4 correspond to the four thrust phases of the test, where each phase was at a different pressure level.

In Table 5.3 (and 5.4) four mean values (corresponding to p1-p4) of the P_{int} data are presented. The table also includes the standard error of the mean ($\delta_{SEM-P_{int}}$), sensor uncertainty ($\delta_{Sensor-P_{int}}$) and the total uncertainty ($\epsilon_{P_{int}}$). The standard error of the mean was again calculated with Equation 5.1. As for the uncertainty caused by the sensor accuracy, this depends on the pressure (and temperature) range as can be found in the manual [22]. For this pressure range the sensor has an accuracy of $\pm 0.05[bar]$, which was already shown in Table 4.8. It can be seen in Table 5.3 that $\delta_{Sensor-P_{int}}$ is much more dominant than $\delta_{SEM-P_{int}}$. As for the total uncertainty, this was calculated with Equation

5.3. Again, the root sum square was taken since $\delta_{Sensor-P_{int}}$ is a systematic error and $\delta_{SEM-P_{int}}$ is a random error.

$$\epsilon_{P_{int}} = \frac{1}{P_{int}}\sqrt{\delta_{SEM-P_{int}}{}^2 + (\delta_{Sensor-P_{int}})^2} \cdot 100\% \tag{5.3}$$

Table 5.3: Adjusted measurement data of the absolute interface pressure of thrust test TT-04 including the uncertainties. The different rows are for the four phases: p1-p4.

Test Label	P_{int} [bar]	$\delta_{SEM-P_{int}}$ [bar]	$\delta_{Sensor-P_{int}}$ [bar]	$\epsilon_{P_{int}}$ [%]
TT-04_p1	1.92	± 9.0e-05	± 5.0e-02	± 2.6
TT-04_p2	2.95	± 1.2e-04	± 5.0e-02	± 1.7
TT-04_p3	4.03	± 1.4e-04	± 5.0e-02	± 1.2
TT-04_p4	5.04	± 1.8e-04	± 5.0e-02	± 1.0

Table 5.4: Adjusted measurement data of the absolute interface pressure of thrust test TT-05 including the uncertainties. The different rows are for the four phases: p1-p4.

Test Label	P_{int} [bar]	$\delta_{SEM-P_{int}}$ [bar]	$\delta_{Sensor-P_{int}}$ [bar]	$\epsilon_{P_{int}}$ [%]
TT-05_p1	1.82	± 6.0e-05	± 5.0e-02	± 2.7
TT-05_p2	2.98	± 1.8e-04	± 5.0e-02	± 1.7
TT-05_p3	4.03	± 1.0e-04	± 5.0e-02	± 1.2
TT-05_p4	5.06	± 1.5e-04	± 5.0e-02	± 1.0

5.3. Chamber temperature

The chamber temperature T_c was assumed to be equal to the temperature of the nitrogen gas inside the 1st gen. interface (T_{int}). The experimental data for the temperature in the 1st gen. interface was produced by the MS5837-30BA sensor and is presented in Figure 5.3 and in Table 5.5. The temperature data seems a bit more noisy than the pressure data because the measured temperatures lie within a narrow range. Also, the effects of the increased pressure can be seen in the behavior of the temperature: the sensor reads slightly higher temperatures during the phases that have higher pressures. The reason for this behavior was not investigated because the temperature difference was so small that the influence on $(c^*)_{ideal}$ was negligible: while using a constant Γ and R, a temperature difference of $0.33[K]$ resulted in a $0.056[\%]$ difference for $(c^*)_{ideal}$. Apart from the pressure related behavior, another trend is noticeable: the temperature slightly increases over time. This effect was also not investigated as the temperature difference is even smaller ($0.08[K]$) compared to the $0.33[K]$ difference. It could be investigated by taking temperature measurements over a longer period with the same test set-up. Furthermore, the figure displays that for each phase the temperature spikes before reaching stability. The author claims that this is caused by the sudden jump in pressure that causes the signal to overshoot. The fact that the spike becomes higher for higher pressure jumps, is evidence for this assumption. In Table 5.5 (and 5.6) the six mean values are presented for the T_{int} data: the initial condition, each of the four phases and the end condition. Note that the values in the table were converted to Kelvin because calculations with temperature in Ideal Rocket Theory are done in Kelvin. The table also includes the standard error of the mean ($\delta_{SEM-T_{int}}$), sensor uncertainty ($\delta_{Sensor-T_{int}}$) and the total uncertainty ($\epsilon_{T_{int}}$). The standard error of the mean was again calculated with Equation 5.1. As for the sensor uncertainty, this depends on the temperature (and pressure) range as can be found in the manual [22]. For this temperature range the sensor has an accuracy of $\pm 1.5[K]$, which was already presented in Table 4.8. It can be seen that $\delta_{Sensor-T_{int}}$ is much more dominant than the uncertainty caused by $\delta_{SEM-P_{int}}$. As for the total uncertainty, this was calculated with Equation 5.4. Again, the root sum square was taken since $\delta_{Sensor-T_{int}}$ is a systematic error and $\delta_{SEM-T_{int}}$ is a random error.

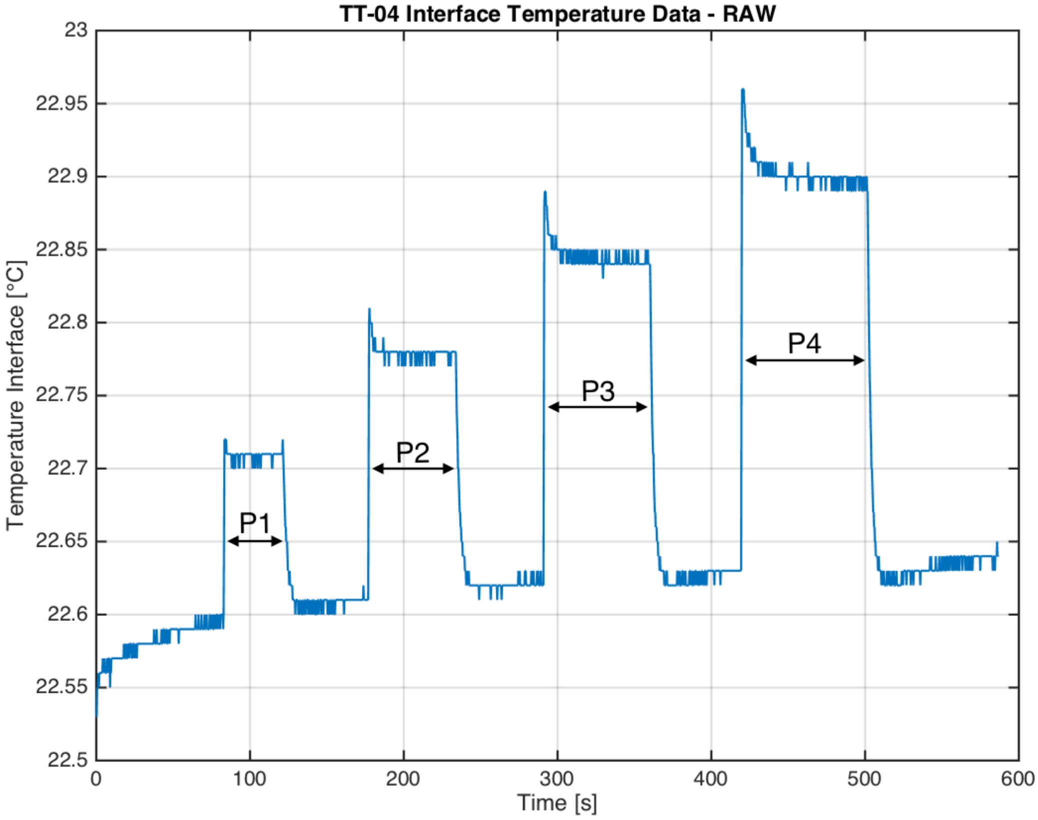

Figure 5.3: Raw experimental temperature data from the sensor (MS5837-30BA) in the 1st gen. interface, which was obtained during thrust test TT-04 and sampled at a frequency of $3.56[Hz]$.

$$\epsilon_{T_{int}} = \frac{1}{T_{int}} \sqrt{\delta_{SEM-T_{int}}{}^{2} + (\delta_{Sensor-T_{int}})^{2}} \cdot 100\% \tag{5.4}$$

Table 5.5: Measurement data of the interface temperature including the standard deviation and uncertainties for thrust test TT-04. The different rows are for: the initial condition, the conditions during each of the four phases and the condition at the end.

Test Label	T_{int} [K]	$\delta_{SEM-T_{int}}$ [K]	$\delta_{Sensor-T_{int}}$ [K]	$\epsilon_{T_{int}}$ [%]
TT-04_init	295.7	± 6.1e-04	± 1.5	± 0.51
TT-04_p1	295.9	± 3.1e-04	± 1.5	± 0.51
TT-04_p2	295.9	± 2.4e-04	± 1.5	± 0.51
TT-04_p3	296.0	± 3.1e-04	± 1.5	± 0.51
TT-04_p4	296.1	± 3.0e-04	± 1.5	± 0.51
TT-04_end	295.8	± 4.4e-04	± 1.5	± 0.51

Table 5.6: Measurement data of the interface temperature including the standard deviation and uncertainties for thrust test TT-05. The different rows are for: the initial condition, the conditions during each of the four phases and the condition at the end.

Test Label	T_{int} [K]	$\delta_{SEM-T_{int}}$ [K]	$\delta_{Sensor-T_{int}}$ [K]	$\epsilon_{T_{int}}$ [%]
TT-05_init	294.0	± 7.0e-04	± 1.5	± 0.51
TT-05_p1	294.1	± 3.7e-04	± 1.5	± 0.51
TT-05_p2	294.2	± 1.5e-04	± 1.5	± 0.51
TT-05_p3	294.2	± 3.1e-04	± 1.5	± 0.51
TT-05_p4	294.3	± 1.9e-04	± 1.5	± 0.51
TT-05_end	294.0	± 4.0e-04	± 1.5	± 0.51

5.4. Volumetric flow and mass flow rate

As mentioned before, the Brooks 5850S reads out the volumetric flow rate, which means that the data needs to be converted in order to obtain the mass flow. However, before this conversion shall be done, first the raw experimental data for the flow rate as presented in Figure 5.4 and Table 5.7 shall be explained. It can be seen in the figure that there are four plateaus of constant flow rates, which correspond to the four thrust phases. The spikes that are higher than $500[ml/min]$ are caused by adjusting the pressure regulator. The spikes that are lower than $500[ml/min]$ and are followed by a constant plateau, are caused by a sudden opening of the valve. This kickstarts the flow rate and causes the flow signal to overshoot, after which a split second is needed before the sensor is able to produce a stable value.

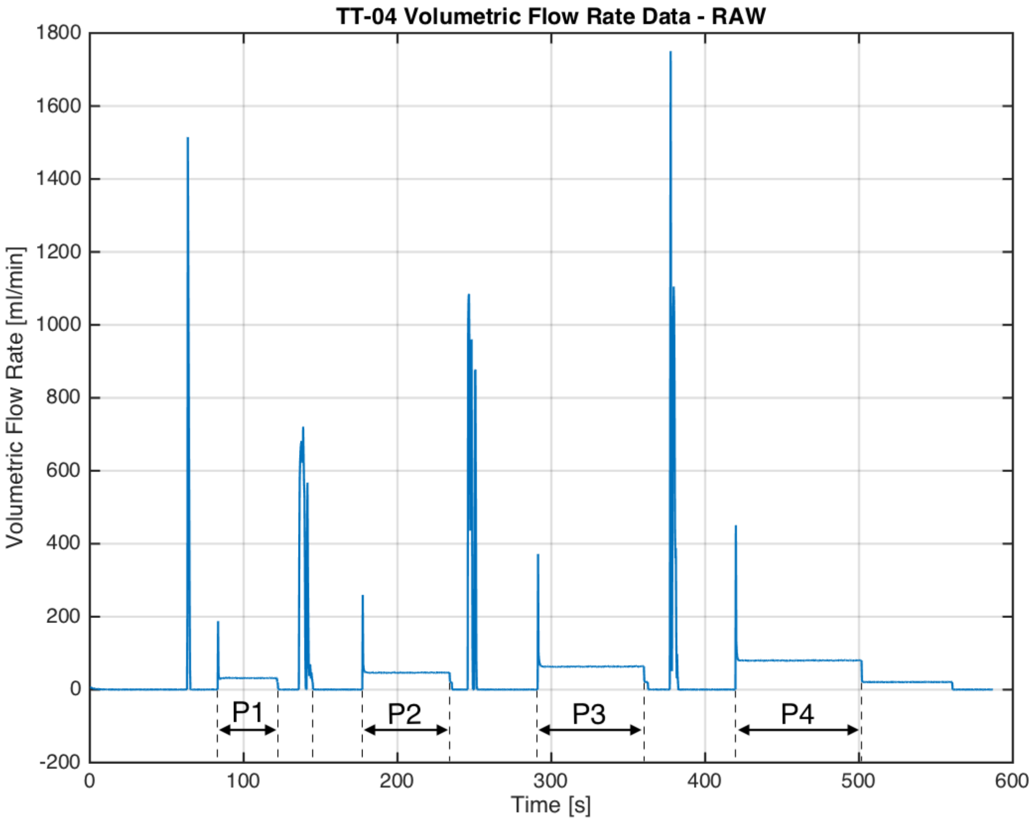

Figure 5.4: Raw experimental volumetric flow rate data from the sensor (Brooks SLA5850) in the feed system, which was obtained during thrust test TT-04 and sampled at a frequency of $3.56[Hz]$.

In Table 5.7 the six mean values are presented for the $\dot{V}$ data: the initial condition, each of the four phases and the end condition. It can be seen in the second column that the mean values of $\dot{V}$ at the initial and end conditions are not zero. Because these values should be zero, a correction was applied that resulted in $\dot{V}_{corrected}$ in the third column. The correction was done by taking the average of the volumetric flow rate at the initial and end conditions ($0.2601[ml_n/min]$) and subtracting this from the other volumetric flow rate values. Hereafter, the initial and end values become $0.0141[ml_n/min]$ and $-0.0141[ml_n/min]$, respectively. In order to present the initial and end values as zero, the zero uncertainty (δ_{zero}) of $\pm 0.0141[ml_n/min]$ needs to be added to the total uncertainty ($\epsilon_{\dot{V}}$).

Table 5.7 also includes the standard error of the mean ($\delta_{SEM-\dot{V}}$) and the sensor uncertainty ($\delta_{Sensor-\dot{V}}$). The standard error of the mean was again calculated with Equation 5.1. As for the uncertainty that resulted from the sensor accuracy, this was mentioned in Table 4.8 to be either $0.2[\%]$ of the full scale value of $2000[ml_n/min]$ or $0.7[\%]$ of the measured value, depending on which uncertainty value is bigger. In this case it is $0.2[\%]$ of the full scale, which equals $4[ml_n/min]$. It can be seen that this source of uncertainty is much more dominant than the uncertainty caused by $\delta_{SEM-\dot{V}}$ or the zero uncertainty. As for the total uncertainty, this was calculated with Equation 5.5. Again, the root sum square was taken since $\delta_{Sensor-\dot{V}}$ is a systematic error and $\delta_{SEM-\dot{V}}$ and the zero uncertainty are both a random error. Note that the reason why the total uncertainty for the flow rate is zero at the initial and end conditions is because the measured value of the initial and end $\dot{V}_{corrected}$ should also be zero.

$$\epsilon_{\dot{V}} = \frac{1}{\dot{V}}\sqrt{{\delta_{SEM-\dot{V}}}^2 + (\delta_{Sensor-\dot{V}})^2 + (\delta_{zero})^2} \cdot 100\% \tag{5.5}$$

Table 5.7: Measurement data of the volumetric flow rate including the uncertainties for thrust test TT-04. The different rows are for: the initial condition, the conditions during each of the four phases and the condition at the end. Note that the number of significant digits was given to show the difference between the uncorrected and corrected volumetric flow rate, and to show the difference in the uncorrected volumetric flow rate between "TT-04_init" and "TT-04_end".

Test Label	$\dot{V}$ $[\mathbf{ml_n/min}]$	$\dot{V}_{corrected}$ $[\mathbf{ml_n/min}]$	$\delta_{SEM-\dot{V}}$ $[\mathbf{ml_n/min}]$	$\delta_{Sensor-\dot{V}}$ $[\mathbf{ml_n/min}]$	$\epsilon_{\dot{V}}$ $[\%]$
TT-04_init	0.27	0	0	0	0
TT-04_p1	31.7	31.4	± 6.9e-2	± 4	± 12.7
TT-04_p2	46.5	46.2	± 5.6e-2	± 4	± 8.7
TT-04_p3	63.2	62.9	± 5.0e-2	± 4	± 6.4
TT-04_p4	79.9	79.7	± 4.2e-2	± 4	± 5.0
TT-04_end	0.25	0	0	0	0

Now that the flow rate data processing has been explained, the step towards the mass flow conversion can be taken. As was explained in Subsection 4.2.2, the mass flow can be calculated by dividing the volumetric flow rate with the density of nitrogen at normal conditions (ρ_{N2_n}= $1.2498[kg/m^3]$). The resulting mass flow values can be found in Table 5.8 and for TT-05 in Table 5.9. It can again be seen that the total uncertainties are quite high. As mentioned before, the major source of uncertainty is caused by the accuracy of the sensor, which relates to systematic errors. This means that repeating the measurements will not help in reducing the uncertainty as this only works for random errors (Coleman and Steele, 2009) [27]. Systematic errors can only be reduced by a extensive calibration procedure, which was already done by the company Brooks Instrument BV. This means that the problem lies somewhere else: range of the Brooks 5850 S mass flow controller is too large. As mentioned before the range was $0-2000[mln/min]$ and the sensor accuracy was $\pm 0.2[\%]$ of the full scale, which resulted in the $\pm 4[ml_n/min]$ uncertainty. This means that a smaller range will result in a smaller uncertainty caused by the full scale error. A solution could be using the other Brooks 5850 S mass flow controller integrated in the General Purpose Feed system (GPF) (see Figure 4.5a) because this device has a range of $0-144[mln/min]$, which would greatly reduce the sensor uncertainty. However, it should be noted that this device has a slower response time, only controls mass flow with amperage and is able to provide measurements/readings in voltages.

Table 5.8: Measurement data of the mass flow rate including the standard deviation and uncertainties for thrust test TT-04. The different rows are for: the initial condition, the conditions during each of the four phases and the condition at the end.

Test Label	$(\dot{m})_{exp}$ $[\mathbf{mg/s}]$	$\delta_{SEM-\dot{m}}$ $[\mathbf{mg/s}]$	$\delta_{Sensor-\dot{m}}$ $[\mathbf{mg/s}]$	$\epsilon_{\dot{m}}$ $[\%]$
TT-04_init	0	0	0	0
TT-04_p1	0.65	± 1.4e-3	± 8.33e-2	± 12.7
TT-04_p2	0.96	± 1.2e-3	± 8.33e-2	± 8.7
TT-04_p3	1.31	± 1.80-3	± 8.33e-2	± 6.4
TT-04_p4	1.66	± 8.7e-4	± 8.33e-2	± 5.0
TT-04_end	0	0	0	0

Table 5.9: Measurement data of the mass flow rate including the standard deviation and uncertainties for thrust test TT-05. The different rows are for: the initial condition, the conditions during each of the four phases and the condition at the end.

Test Label	$(\dot{m})_{exp}$ $[\mathbf{mg/s}]$	$\delta_{SEM-\dot{m}}$ $[\mathbf{mg/s}]$	$\delta_{Sensor-\dot{m}}$ $[\mathbf{mg/s}]$	$\epsilon_{\dot{m}}$ $[\%]$
TT-05_init	0	0	0	0
TT-05_p1	0.59	± 1.4e-3	± 8.33e-2	± 14.1
TT-05_p2	0.94	± 8.9e-4	± 8.33e-2	± 8.8
TT-05_p3	1.29	± 9.90-4	± 8.33e-2	± 6.5
TT-05_p4	1.64	± 9.4e-4	± 8.33e-2	± 5.1
TT-05_end	0	0	0	0

5.5. Displacement and thrust force

In order to obtain the thrust force values as was presented in Table 5.14, the following steps were needed:

1. The large fluctuations in the raw experimental data of the pendulum displacement were filtered out with function 'smooth' in MATLAB.
2. The smoothed function was used to determine: the average displacement (X_{disp}) during each phase, the variation in the baseline displacement and the relative change between the baseline and average displacement (Δ_{disp}).
3. The relative displacement (Δ_{disp}) was used together with the results PCT-11 and PCT-12 in order to determine the force exerted on the pendulum arm. Note that this is not the thrust force because force-displacement relation was established with the magnetic force of the Varying Turn-Density Coil (VTDC) actuator, which induces a force on the pendulum arm that is located higher w.r.t. the thrust force produced by the MEMS-VLM chip.
4. A force correction factor was applied in order to determine the experimental thrust force ($(F)_{exp}$).

5.5.1. Displacement

To begin with, the displacement of the AE-TB-5m pendulum arm was measured and the experimental data was stored. As was explained in Subsection 4.2.7, the CS2 sensor measured this displacement. The raw experimental data for the displacement can be found in Figure 5.5 in which the four different thrust phases are indicated with 'p1-p4'. It can be seen in the figure that the baseline displacement changes over time: it starts just below $2360[\mu m]$ and over time it keeps decreasing slightly. Therefore, the author defines displacement drift as follows: a constant increase or decrease in the average displacement over time (>10[s]). This should not be confused with signal drift, which is a drift in the measurement signal that can be caused by warmup of the measuring device. This displacement drift was investigated for different configurations for a long period (>10 hours), which is presented in Appendix E.1. It was found that the configuration of the fluidic tube and electrical wires had a huge impact on the displacement drift. For example, reconfiguring the tube and wires from a 'waterfall' configuration to a 'loop' or 'sideways' configuration greatly reduced the displacement drift: from about 2000 $[\mu m]$ over 14 hours down to about 35 $[\mu m]$ over 15 hours. The drift that was still present after the reconfiguration could also be caused by the change in ambient temperature, which was also hypothesized by Jansen (2016) [8] after performing a similar test. It is therefore recommended that the temperature influence should be investigated by repeating the long period displacement behavior test, while also measuring the ambient temperature inside the vacuum chamber. Furthermore, it can also be seen in Figure 5.5 that during each thrust phase the data has a lot of fluctuations. This is caused by the jump in displacement due to the sudden increase in pressure and induced thrust force. It can be seen that at higher jumps in pressure the fluctuation in the displacement is also higher. These fluctuations were reduced in order to enable further data processing.

The reduction in the data fluctuations can be found in Figure 5.6 where the smoothed data is indicated in red. This was done with a MATLAB function based on a moving average filter: the function 'smooth' with a span of 1200. The value for the span was found through trial and error. For example, a span of 1 does not provide any smoothing of the data, while a span of 5000 does not maintain the shape of the raw experimental data. It can be seen in Figure 5.6 that the smoothing function with a span of 1200 both reduces the fluctuations in the data and maintains the shape of the original data set. However it can be seen that the smoothed data does not perfectly coincide with the original raw data. This behavior is caused by the shape of the experimental data in combination with the 'smooth' function that uses a moving average. For better understanding of this function one should look up the reference page for the function 'smooth' (MATLAB command: 'help smooth'). Segmenting the raw data in different pieces is a solution for making the smoothed data better coincide with the raw data, as is explained in more detail in Appendix F.2. However, it was found that segmentation had a negligible effect on the thrust force and the corresponding uncertainty. This can be explained by taking "TT-04_p3" of Table 5.11 as an example: with the complete data set X_{disp} was found to be $2410.1[\mu m] \pm 0.17[\mu m]$ and $(F)_{exp}$ $0.4529[mN] \pm 2.44[\%]$, while for a segmented data set X_{disp} was $2410.0[\mu m] \pm 0.32[\mu m]$ and $(F)_{exp}$

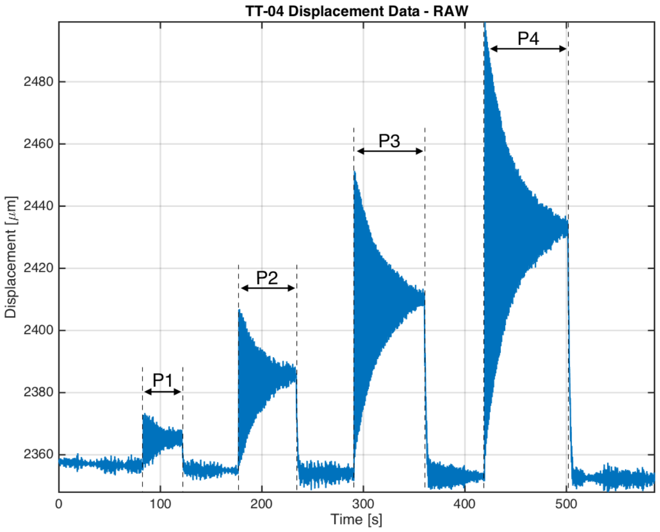

Figure 5.5: Raw experimental displacement data from the sensor (CS2) in the thrust bench (AE-TB-5m), which was obtained during thrust test TT-04 and sampled at a frequency of $104[Hz]$.

$0.4518[mN] \pm 2.49[\%]$. Therefore, the data processing was done for the complete data set and not for a segmented data set.

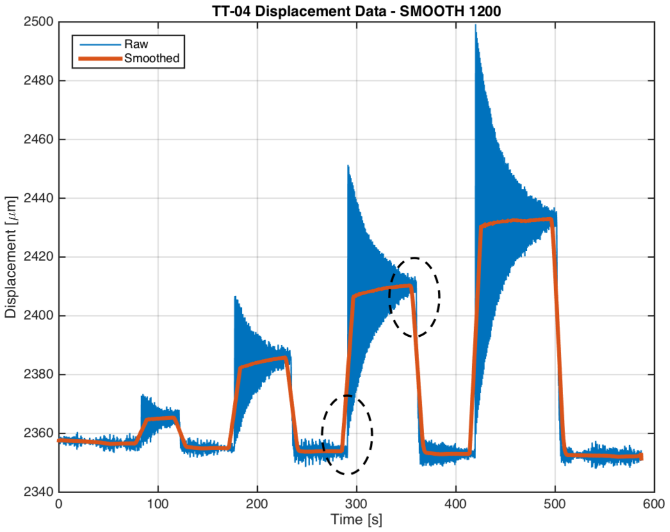

Figure 5.6: Raw experimental displacement data during thrust test TT-04 with the filtered/smoothed superimposed, which was obtained with the function 'smooth' using a span of 1200 in MATLAB, where the dotted circles indicate locations were misalignments occur.

After the smoothed data was obtained, the MATLAB function 'findpeaks' was used in order to simplify the data processing. As presented in Figure 5.7 the function is able to indicate data points that lie at a peak / plateau. This would ideally safe the trouble of manually looking through the data and trying to find the data points corresponding to each thrust phase. However, in Figure 5.7 it can be seen that for thrust phases 'p2-p4' the displacement needs time (about 30 seconds) before it converges to a relatively 'stable' value. Therefore, the data points within the stable regions were located and used for further calculations. Note that the author considered the following to be stable: a maximum change in displacement of $1[\mu m]$ for a minimum of $10[s]$. This is acceptable because this definition of stability resulted in small standard error of the mean values as presented in Table 5.11.

Coming back to the displacement drift, it is interesting that the displacement increases during the thrust phases, while the baseline displacement decreases over time. This indicates that another force is exerted on the pendulum arm during the thrust phase. The author hypothesizes that the exerted force is the result of the sudden spike in pressure, which causes an increased stiffness of the fluidic tube. Evidence for this can be found in the test 'ATV-01' that is presented in Appendix E.2, where the effect of shifting from standard pressure to vacuum on the displacement is described. It can be seen in Table 5.10 that for ATV-01 the displacement changes $20[\mu m]$ over 5 minutes. This indicates that a pressure difference between the fluidic tube and the vacuum chamber environment can shift the balance of the pendulum arm. However, this does not prove the hypothesis and there are even some questions left unanswered. Table 5.10 demonstrates that the displacement drift is not consistently increasing with higher pressure levels (or thrust phases). This would be expected if a higher pressure resulted in an increased stiffness of the fluidic tube. Therefore it is recommended to perform the test with a closed nozzle such that the effect of pressurization of the fluidic tube on the displacement is isolated. Another option could be performing the test with the 1st gen. interface rotated $90[\mathrm{deg}]$ horizontally, thus perpendicular w.r.t. the movement of the pendulum arm. However, it would be difficult to determine if the pressurization effect on the stiffness is completely isolated, since the thrust force could still have an influence on the displacement due to small offsets in the configuration. Using "TT-04_p4" of Table 5.13 as an example, let's say that the thrust force of $0.64[mN]$ pointed perpendicular w.r.t. the movement of the pendulum arm. Because the uncertainty is $\pm 1.7[\%]$, this means that resolution is $\pm 3.4[\%]$. From this it can be calculated that the thrust force needs to be pointed within $1.9[^\circ]$ accuracy, so that the pendulum arm displacement is not affected by this force.

Table 5.10: The interface pressure, displacement drift and duration for ATV-01 and the different thrust phases 'p1-p4' during TT-04 are presented. Note that the interface pressure of ATV-01 is not included because it was not constant.

Test Label	P_{int} [bar]	**Displacement Drift** [μm]	**Duration** [s]
ATV-01	-	20	300
TT-04_p1	1.92	0.74	38
TT-04_p2	2.95	3.6	56
TT-04_p3	4.03	4.24	69
TT-04_p4	5.04	3.3	81

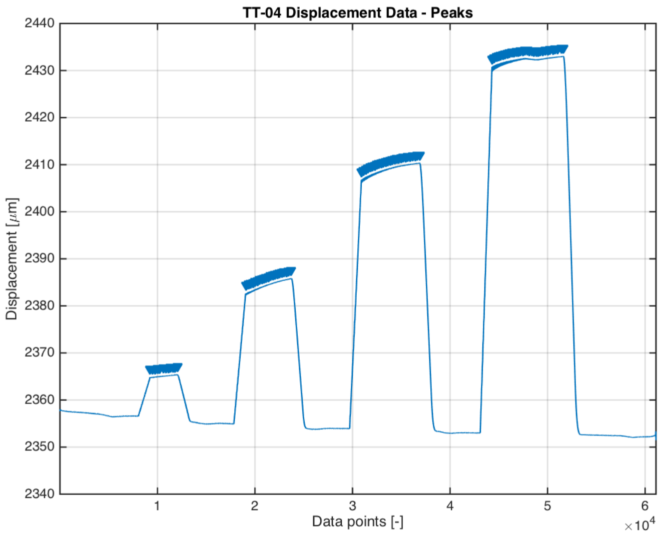

Figure 5.7: Filtered / smoothed displacement data for thrust test TT-04, where the peaks / plateaus were found and indicated with blue triangles using the "findpeaks" function in MATLAB.

In Table 5.11 the displacement data for TT-04 is presented together with the uncertainties. As mentioned before, only data points within the stable regions were used for the calculations. The mean and standard error of the mean ($\delta_{SEM-X_{disp}}$) for the displacement data of each thrust phase are presented in the second and fourth column of the table, respectively. The standard error of the mean was again calculated with Equation 5.1. In the third column the relative displacement (Δ_{disp}) is presented, which will be needed to calculate the thrust force. The Δ_{disp} was calculated for each thrust phase as follows: the average of the two neighboring baseline displacement values (before and after the thrust phase) was taken, which was subtracted from the displacement during the thrust phase. This means that the average baseline displacement acts as the zero reference value. However, the baseline displacements are not constant and thus include the standard error of the mean. Also, the two baseline displacement (mean) values are not equal, which adds another uncertainty. All these uncertainties together form the zero uncertainty (δ_{zero}) in the fifth column of the table by taking the root sum square. As for the total displacement uncertainty ($\epsilon_{\Delta_{disp}}$), this was calculated with Equation 5.6. The root sum square was taken since δ_{zero} and $\delta_{SEM-X_{disp}}$ were considered independent. Note that the sensor uncertainty, which was presented in Table 4.8, can be neglected as the displacement sensor was calibrated with the VTDC actuator.

$$\epsilon_{\Delta_{disp}} = \frac{1}{\Delta_{disp}}\sqrt{\delta_{SEM-X_{disp}}{}^{2} + (\delta_{zero})^{2}} \cdot 100\% \tag{5.6}$$

Table 5.11: Measurement data of the displacement including the uncertainties for thrust test TT-04. The different rows are for the four phases: p1-p4.

Test Label	X_{disp} [μm]	Δ_{disp} [μm]	$\delta_{SEM-X_{disp}}$ [μm]	δ_{zero} [μm]	$\epsilon_{\Delta_{disp}}$ [%]
TT-04_p1	2365	9	± 3.4e-3	± 0.78	± 8.3
TT-04_p2	2385	31	± 6.7e-3	± 0.52	± 1.69
TT-04_p3	2410	57	± 4.6e-3	± 0.46	± 0.88
TT-04_p4	2433	80	± 3.4e-3	± 0.25	± 0.31

5.5.2. Thrust force

Now that the displacement data has been processed and explained, the thrust force can be calculated. This was done with the results of the pendulum calibration test, which was explained in Section 3.3. As mentioned before, the calibration test PCT-11 was done before TT-04, while PCT-12 was done after TT-04. From these tests it was determined that the average force-displacement relationship was determined to be:

$$F_{TT04}[mN] = 0.011019[mN/\mu m] \cdot \Delta_{disp}[\mu m] - 0.0051714[mN] \tag{5.7}$$

With this relationship the force on the pendulum arm was calculated and the result can be found in the second column of Table 5.13 for the 'p1-p4'. However, Equation 5.7 does not provide the actual thrust force of the 3rd gen. MEMS-VLM chip. This is because the (magnetic) force exerted on the AE-TB-5m pendulum arm during the calibration procedure was at a higher location compared to the (thrust) force during the thrust bench test. This was also displayed in Figures 3.9 and 3.10, where the magnetic holder was located at a higher position with respect to the 1st gen. interface and thus the 3rd gen. MEMS-VLM chip. Therefore, a force correction factor (FCF) was needed and this was determined to be 0.733, which was described in detail in Subsection 3.4. The corrected force or actual thrust force was determined with Equation 5.8.

$$F_{exp}[mN] = F_{TT04} \cdot 0.733076 \tag{5.8}$$

The corrected force or actual thrust force is presented in the third column of Table 5.13 for the 'p1-p4'. It can be seen that apart from the displacement uncertainty ($\epsilon_{\Delta_{disp}}$), two more sources of uncertainty are present: the calibration uncertainty (ϵ_{TT04}) and the force correction uncertainty (ϵ_{fr}). As mentioned before in Subsection 3.3.4, the calibration uncertainty consists of: the error in the estimated force when using the calibration curve and the measurement error of the VTDC actuator. Note that in Subsection 3.3.4 the absolute error was given (δ_{TT04}) and here the relative error is given (ϵ_{TT04}). As for the force correction (factor) uncertainty, it was already explained in Subsection 3.4 that this was the result of taking measurements with the Mitutoyo Absolute digital caliper. The total uncertainty was calculated with Equation 5.9, where it can be seen that the relative errors are summed, which is because the errors are dependent. Furthermore, it can be seen that except for 'p1', the total uncertainties are quite low. It can also be seen that the calibration uncertainty and the displacement uncertainty are the most dominant sources, though these become smaller for higher thrust values. That is why it is recommended for future experiments to avoid chamber pressures below 3 [bar] or to improve the set-up such that the uncertainties are reduced.

$$\epsilon_{(F)_{exp}} = \epsilon_{TT04} + \epsilon_{fr} + \epsilon_{\Delta_{disp}} \tag{5.9}$$

Table 5.12: Measurement data of the thrust force including the uncertainties for TT-04.

Test Label	F_{TT04} [mN]	$(F)_{exp}$ [mN]	ϵ_{TT04} [%]	ϵ_{fr} [%]	$\epsilon_{\Delta_{disp}}$ [%]	$\epsilon_{(F)_{exp}}$ [%]
TT-04_p1	9.8e-2	7.2e-2	± 15.7	± 0.22	± 8.3	± 24.4
TT-04_p2	0.34	0.25	± 4.6	± 0.22	± 1.69	± 6.5
TT-04_p3	0.62	0.45	± 2.5	± 0.22	± 0.88	± 3.5
TT-04_p4	0.87	0.64	± 1.8	± 0.22	± 0.31	± 2.3

Table 5.13: Measurement data of the thrust force including the uncertainties for TT-05.

Test Label	F_{TT05} [mN]	$(F)_{exp}$ [mN]	ϵ_{TT05} [%]	ϵ_{fr} [%]	$\epsilon_{\Delta_{disp}}$ [%]	$\epsilon_{(F)_{exp}}$ [%]
TT-05_p1	8.7e-2	6.4e-2	± 21.2	± 0.22	± 6.8	± 28.2
TT-05_p2	0.37	0.27	± 5.0	± 0.22	± 2.83	± 8.1
TT-05_p3	0.63	0.46	± 2.9	± 0.22	± 1.51	± 4.7
TT-05_p4	0.89	0.65	± 2.1	± 0.22	± 0.48	± 2.8

5.6. Summary

All the test results including the uncertainties for TT-04 and TT-05 are presented in Table 5.14. Note that there are some differences between the planned (see Table 4.1) and measured/actual values for P_a, P_{int} and T_{int}. Starting off with the ambient pressure (P_a), it was planned that the ambient pressure would remain at $30[Pa]$. However, in reality the ambient pressure ranged between $35[Pa]$ and $85[Pa]$. The change in ambient pressure was caused both by the added nitrogen gas during the thrust phases and the vacuum pump that kept pumping gas out of the vacuum chamber during the whole test. This change is not a problem when the measured values are used for calculations instead of the planned values. The same holds for T_{int}, which was slightly higher compared to the planned value. As for P_{int}, it can be seen that the actual range is about $2-5[bar]$, while the planned range was $2-6[bar]$. The change in range was taken as a precaution to prevent any leakage. This is because it was found (see Section 3.1) that leakage over time would occur at lower chamber pressures: before starting the thrust bench tests leakage would only occur at a pressure higher than $7[bar]$, while during TT-06 leakage would already start at a pressure of $5[bar]$. Again, the difference between the planned values does not matter as long as the measured values are used for calculations instead of the planned ones. Furthermore, there are slight differences between the chamber pressure values of TT-04 and TT-05. This is because the pressure regulator (see Figure 4.5a) cannot be controlled with more precision directly. It could be more precisely controlled by opening the solenoid valve and using the P_{int} measurements. However, for this test it was not required to have exactly the same pressure because one purpose of this test was to obtain a relation between the chamber pressure and various parameters (e.g thrust force).

Table 5.14: Overview of the measured parameters during the thrust bench tests TT-04 and TT-05, where each test consisted of four phases (p1-p4) during which thrust was generated and the pressure was increased at every next phase.

Test Label	P_a [Pa]	P_{int} [bar]	T_{int} [K]	$(\dot{m})_{exp}$ [mg/s]	$(F)_{exp}$ [mN]
TT-04_p1	35 ± 4	1.92 ± 5e-2	295.9 ± 1.5	0.65 ± 8.3e-2	7.2e-2 ± 1.7e-2
TT-04_p2	50 ± 6	2.95 ± 5e-2	295.9 ± 1.5	0.96 ± 8.3e-2	0.25 ± 1.6e-2
TT-04_p3	68 ± 8	4.03 ± 5e-2	296.0 ± 1.5	1.31 ± 8.3e-2	0.45 ± 1.6e-2
TT-04_p4	85 ± 11	5.04 ± 5e-2	296.0 ± 1.5	1.66 ± 8.3e-2	0.64 ± 1.5e-2
TT-05_p1	35 ± 5	1.82 ± 5e-2	294.1 ± 1.5	0.59 ± 8.3e-2	6.4e-2 ± 1.8e-2
TT-05_p2	54 ± 8	2.98 ± 5e-2	294.2 ± 1.5	0.94 ± 8.3e-2	0.27 ± 2.2e-2
TT-05_p3	69 ± 10	4.03 ± 5e-2	294.2 ± 1.5	1.29 ± 8.3e-2	0.46 ± 2.2e-2
TT-05_p4	83 ± 12	5.06 ± 5e-2	294.3 ± 1.5	1.64 ± 8.3e-2	0.65 ± 1.8e-2

6

Nitrogen Thrust Bench Test - Analysis

In this chapter the test results of the nitrogen thrust bench test will be thoroughly analyzed. Section 6.1 describes how performance characteristics were determined for TT-04 and TT-05. This is followed by Section 6.2 and Section 6.3, where the discharge factor and heating quality are analyzed, respectively. Hereafter, an analysis is given about the nozzle quality in Section 6.4. Finally, in Section 6.5 a summary of this chapter given.

6.1. Nozzle performance calculation

The experimental results of the nitrogen thrust bench test have been presented in Chapter 5. Now, the experimental data are processed such that the nozzle performance of the '01-LS2-02' 3rd gen. MEMS-VLM chip can be calculated. An overview of the process was presented in Figure 4.1. The "Nozzle Geometry" block was determined in Section 3.2.4 and the "Measured Parameters" block was determined in Section 5. This leaves the block "Propellant Properties", which is described in Subsection 6.1.1. Hereafter, in Subsection 6.1.2 the mass flow adjustmet is explained. This is followed by Subsection 6.1.3, where the blocks "Theoretical Parameters" and "Experimental Parameters" are elaborated. Finally, in Subsection 6.1.4 the blocks "Performance Parameters" and "Reynolds Number" are explained.

6.1.1. "Propellant Properties"

NIST data base [1] was used to determined that R_{N2} has a constant value of $296.8[J/kg/K]$. As for the other parameters, these can be found in Table 6.1.

The "Propellant Properties" data in Table 6.1 is about the nitrogen gas during TT-04 and TT-05. Starting off with γ_{N2}, this was determined using P_{int}, T_{int} and the NIST data base [1], which provides various gas properties for different input pressure and temperature ranges. In the third column Γ_{N2} is presented, which was determined using γ_{N2} and the relation provided by Zandbergen 2016 [13]. As for the isentropic throat temperature (T_t), this was included as well and calculated using γ_{N2} and T_{int} in Equation 2.15. The calculation of T_t was needed because it was used to determine the dynamic viscosity of the propellant at the nozzle throat (μ_{t_N2}), which was again done utilizing the NIST data base. The dynamic viscosity at the throat was needed because it helps determine the experimental throat Reynolds number ($(R_e)_{exp}$).

Furthermore, because P_{int} and T_{int} were used to perform the calculations, this would mean that the uncertainties of these values (see Tables 5.3 and 5.5) would normally propagate to the parameters in Table 6.1. However, the propagated uncertainties were negligible and thus not included. For example, the uncertainty of P_c ranged between $1 - 2.6[\%]$ (see Table 5.3), and a pressure increase of $+2.6[\%]$

Table 6.1: Overview of the "Propellant Properties" data of the thrust bench tests TT-04 and TT-05. The parameters were determined using the NIST data base [1]. Furthermore, the amount of significant numbers for γ_{N2}, Γ_{N2} and μ_{t_N2} is given to display the slight variations in the parameters due to the different pressure levels of each phase. Also, the uncertainties are not included as these are negligibly small.

Test Label	γ_{N2} $[-]$	Γ_{N2} $[-]$	T_t $[\mathbf{K}]$	μ_{t_N2} $[\mathbf{kg/m/s}]$
TT-04_p1	1.403	0.6852	246.2	1.532e-5
TT-04_p2	1.405	0.6855	246.2	1.531e-5
TT-04_p3	1.407	0.6859	246.0	1.531e-5
TT-04_p4	1.409	0.6862	245.8	1.530e-5
TT-05_p1	1.403	0.6852	244.8	1.525e-5
TT-05_p2	1.405	0.6855	244.7	1.524e-5
TT-05_p3	1.407	0.6858	244.5	1.523e-5
TT-05_p4	1.408	0.6862	244.4	1.523e-5

for "TT-04_p1" would result in a $6e\text{-}3[\%]$ increase for γ_{N2}, which is very small.

6.1.2. Mass flow adjustment

Before moving on to Subsection 6.1.3, where calculations are done using the experimental data (obtained from Section 5), an adjustment for the mass flow needs to be investigated. This is needed because the mass flow measurements ($(\dot{m})_{exp}$) for TT-04 are high compared to both the ideal mass flow ($(\dot{m})_{ideal}$) and the corrected theoretical mass flow ($(\dot{m})_{corr.}$), which can be seen in Table 6.2. Note that $(\dot{m})_{corr.}$ was determined by multiplying $(\dot{m})_{ideal}$ with $(C_d)_{bd\_loss}$ (see Section 6.2 for a further explanation for calculating $(C_d)_{bd\_loss}$). When comparing the experimental mass flow with the ideal mass flow, it can be seen that the discharge factor is about $1[-]$. While Van Wees 2017 [3] did an experiment with a similar nozzle and found a discharge factor between $0.66 - 0.68[-]$.

However, Van Wees 2017 [3] used the short range (0-144 [mln/min]) Brooks 5850S, while for TT-04 and TT-05 the long range (0-2 [ln/min]) Brooks 5850S was used, which could explain the difference. Furthermore, it could be argued that the experimental mass flow of TT-04 is acceptable, because $(\dot{m})_{corr.}$ does lie within the error bounds. This can be seen in the experimental mass flow values of TT-05, which is lower than the values of TT-04 and lies consistently between $(\dot{m})_{ideal}$ and $(\dot{m})_{adj.}$. Also, the high $(\dot{m})_{exp}$ cannot be caused by leakage as the leak tests in Section 3.1 indicated that there were no (unacceptable) leaks for this pressure range.

Nevertheless, the most recent calibration date of the long range Brooks 5850S was unknown. It is suspected that this was many years ago. Therefore, the author wanted to compare the long range (0-2 [ln/min]) Brooks 5850S with the short range (0-144 [mln/min]) Brooks 5850 S in order to validate the mass flow measurements. That is why two additional tests, MFT-01 and MFT-02, were carried out with the "01-LS2-02" in order to determine the relation between the experimental mass flow and chamber pressure for both mass flow controllers. The results of both tests can be found in Table 6.3 and in Figure 6.1, where it can be seen that the short range Brooks 5850S provides measurements that are on average $0.15[mg/s]$ lower than the long range Brooks 5850S at about the same pressure levels. This difference was subtracted from $(\dot{m})_{exp}$ in order to calculate the adjusted experimental mass flow ($(\dot{m})_{adj.}$) in Table 6.2. It can be seen that the adjusted mass flow lies even further away from $(\dot{m})_{corr.}$. This could be because the short range Brooks 5850S was also calibrated many years ago. That is why for further calculations both $(\dot{m})_{exp}$ and $(\dot{m})_{adj.}$ will be used to see which mass flow value makes more sense.

Thus, the following conclusions can be made. The experimental data produced by the long range Brooks 5850S in Figure 6.1 shows repeatability: the data points at each pressure of the different experiments lie close to each other within the error bounds. Since both the short and long range have been calibrated many years ago and because the $(\dot{m})_{exp}$ data of MFT-01 falls outside the error bounds of MFT-02, it is recommended that both devices are sent to the company Brooks Instrument BV for recalibration. After this it is suggested to repeat the mass flow test for both devices, which could be used to validate MFT-01 and MFT-02. Note the difference in mass flow measurement was only done in a later phase of this thesis, which is why there was no time left for recalibration and repeating the experiments.

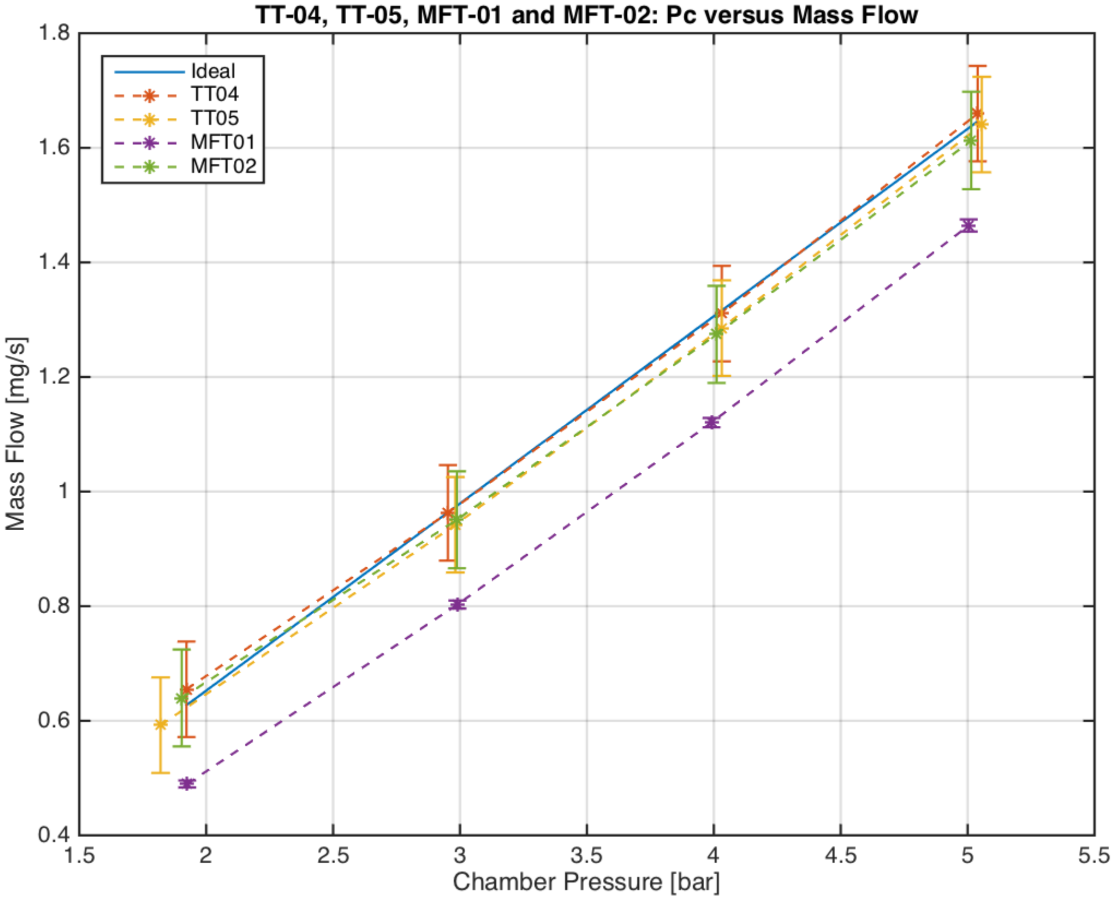

Figure 6.1: Chamber pressure (P_c) versus experimental mass flow ($(\dot{m})_{exp}$) and ideal mass flow ($(\dot{m})_{ideal}$) for the tests TT-04, TT-05, MFT-01 and MFT-02. Note that the error bars for the ideal values are not given in order to maintain the clarity of the graph.

Table 6.2: Different mass flow values are presented here: the experimental values, the ideal values, the corrected theoretical values (using Equation 2.20) and the adjusted experimental values (based on MFT-01 and MFT-02).

Test Label	$(\dot{m})_{exp}$ [mg/s]	$(\dot{m})_{ideal}$ [mg/s]	$(\dot{m})_{corr.}$ [mg/s]	$(\dot{m})_{adj.}$ [mg/s]
TT-04_p1	0.65 ± 8.3e-2	0.63	0.59	0.50 ± 8.3e-2
TT-04_p2	0.96 ± 8.3e-2	0.96	0.92	0.81 ± 8.3e-2
TT-04_p3	1.31 ± 8.3e-2	1.32	1.27	1.16 ± 8.3e-2
TT-04_p4	1.66 ± 8.3e-2	1.65	1.59	1.51 ± 8.3e-2
TT-05_p1	0.59 ± 8.3e-2	0.60	0.56	0.44 ± 8.3e-2
TT-05_p2	0.94 ± 8.3e-2	0.98	0.93	0.79 ± 8.3e-2
TT-05_p3	1.29 ± 8.3e-2	1.32	1.27	1.14 ± 8.3e-2
TT-05_p4	1.64 ± 8.3e-2	1.66	1.60	1.49 ± 8.3e-2

Table 6.3: Comparison between the short range Brooks 5850S $0-144[mln/min]$ (MFT-01) and the long range Brooks 5850S $0-2000[mln/min]$ (MFT-02): the experimental mass flow at different chamber pressures.

Test Label	P_c $[\mathbf{bar}]$	$(\dot{m})_{exp}$ $[\mathbf{mg/s}]$	Absolute difference in mass flow w.r.t. MFT-02 $[\mathbf{mg/s}]$
MFT-01_p1	1.93 ± 5.0e-2	0.49 ± 6.2e-3	0.15
MFT-01_p2	2.99 ± 5.0e-2	0.80 ± 7.1e-3	0.15
MFT-01_p3	3.99 ± 5.0e-2	1.12 ± 8.2e-3	0.15
MFT-01_p4	5.00 ± 5.0e-2	1.46 ± 1.1e-2	0.15
MFT-02_p1	1.90 ± 5.0e-2	0.64 ± 8.5e-2	-
MFT-02_p2	2.99 ± 5.0e-2	0.95 ± 8.5e-2	-
MFT-02_p3	4.01 ± 5.0e-2	1.27 ± 8.5e-2	-
MFT-02_p4	5.01 ± 5.0e-2	1.61 ± 8.5e-2	-

6.1.3. ”Theoretical Parameters” and ”Experimental Parameters”

Now that the data of all the blue blocks in Figure 4.1 have been presented, the green blocks ”Theoretical Parameters” and ”Experimental Parameters” will be determined, which are included in Tables 6.4 and 6.5. To start off with Table 6.4, this was used to compare the values of the ideal mass flow ($(\dot{m})_{ideal}$) and thrust force ($(F)_{ideal}$) to the experimental values ($(\dot{m})_{exp}$, $(\dot{m})_{adj.}$ and $(F)_{exp}$). Note that the chamber pressure (P_c) was included as it was the controlling parameter. As for the uncertainties, these were already explained for the experimental parameters, which means that the uncertainties of the ideal parameters still require an explanation. In short, the ideal parameters were calculated using the data of ”Measured Parameters”, ”Propellant Properties” and ”Nozzle Geometry”, which means that any uncertainty of the data will propagate to the ideal parameters. The calculations needed for determining the ideal parameters can be found in Subsection 2.2.1. Furthermore, to get better insight in what the data of the table means, two plots were made for thrust tests ”TT-04” and ”TT05” as can be seen in Figures 6.3 and 6.2.

In Figure 6.3 both the experimental mass flow ($(\dot{m})_{exp}$) and the adjusted experimental mass flow ($(\dot{m})_{adj.}$) are compared with the ideal mass flow. It can be seen that the regression line consists of the eight data points of TT-04 and TT-05. Furthermore, as mentioned before the experimental mass flow is about the same as the ideal mass flow, while the adjusted mass flow is a bit lower than the ideal mass flow, which makes more sense. As for Figure 6.2, here the ideal thrust force and the experimental thrust force are plotted against the chamber pressure for thrust bench test TT-04 and TT-05. It can be seen that the experimental values are lower than the ideal values, but both the ideal and experimental thrust increase linearly with chamber pressure. It can be concluded that the thrust values are repeatable as the experimental data of TT-04 and TT-05 coincide and fall within each other’s error bound.

Table 6.5 shows the comparison of experimental values of the specific impulse ($(I_{sp})_{exp}$ and $(I_{sp})_{adj.}$), characteristic velocity ($(c^*)_{exp}$) and thrust coefficient ($(C_F)_{adj.}$) with the corresponding ideal values ($(I_{sp})_{ideal}$, $(c^*)_{ideal}$ and $(C_F)_{ideal}$). Note that the experimental thrust coefficient was also adjusted for the mass flow difference. Furthermore, uncertainties were present in both the experimental and ideal parameters. Using the data in the table the specific impulse was visualized as presented in Figure 6.4. With the figure it can already be concluded that higher pressures are beneficial for the specific impulse. However, the increase in specific impulse does get smaller when going to higher pressures. This means that the Isp quality (ξ_s) converges, which will be discussed later on in Subsection 6.4. As for the the characteristic velocity data, this was not visualized in a graph because the experimental and ideal values were exactly the same, which is because it was assumed that no heat loss occurred since a cold gas was used. The thrust coefficient was also not visualized, since it will be explained later in Subsection 6.4 when looking at the nozzle quality (ξ_F).

Table 6.4: Overview of the ”Measured Parameters” and ”Theoretical Parameters” data of the thrust bench tests TT-04 and TT-05, where the experimental values of the mass flow and thrust force are compared to the corresponding ideal values. Note that P_c is used here as it was assumed to be equal to P_{int}.

Test Label	P_c [bar]	$(\dot{m})_{exp}$ [mg/s]	$(\dot{m})_{adj.}$ [mg/s]	$(\dot{m})_{ideal}$ [mg/s]	$(F)_{exp}$ [mN]	$(F)_{ideal}$ [mN]
TT-04_p1	1.92 ± 5.0e-2	0.65 ± 8.3e-2	0.50 ± 8.3e-2	0.63 ± 6.1e-2	7.2e-2 ± 1.7e-2	0.46 ± 6.9e-2
TT-04_p2	2.95 ± 5.0e-2	0.96 ± 8.4e-2	0.81 ± 8.3e-2	0.96 ± 9.2e-2	0.25 ± 1.6e-2	0.71 ± 1.1e-1
TT-04_p3	4.03 ± 5.0e-2	1.31 ± 8.5e-2	1.16 ± 8.3e-2	1.32 ± 1.2e-1	0.45 ± 1.6e-2	0.97 ± 1.4e-1
TT-04_p4	5.04 ± 5.0e-2	1.66 ± 8.4e-2	1.51 ± 8.3e-2	1.65 ± 1.5e-1	0.64 ± 1.5e-2	1.21 ± 1.8e-1
TT-05_p1	1.82 ± 5.0e-2	0.59 ± 8.4e-2	0.44 ± 8.3e-2	0.60 ± 5.8e-2	6.4e-2 ± 1.8e-2	0.44 ± 6.6e-2
TT-05_p2	2.98 ± 5.0e-2	0.94 ± 8.4e-2	0.79 ± 8.3e-2	0.98 ± 9.3e-2	0.27 ± 2.2e-2	0.72 ± 1.1e-1
TT-05_p3	4.03 ± 5.0e-2	1.29 ± 8.4e-2	1.14 ± 8.3e-2	1.32 ± 1.3e-1	0.46 ± 2.2e-2	0.97 ± 1.4e-1
TT-05_p4	5.06 ± 5.0e-2	1.64 ± 8.4e-2	1.49 ± 8.3e-2	1.66 ± 1.5e-1	0.65 ± 1.8e-2	1.21 ± 1.8e-1

Table 6.5: Overview of the ”Experimental Parameters” and ”Theoretical Parameters” data of the thrust bench tests TT-04 and TT-05, where the experimental values of the specific impulse, characteristic velocity and thrust coefficient are compared to the corresponding ideal values.

Test Label	$(I_{sp})_{exp}$ [s]	$(I_{sp})_{adj.}$ [s]	$(I_{sp})_{ideal}$ [s]	$(c^*)_{exp}$ [m/s]	$(c^*)_{ideal}$ [m/s]	$(C_F)_{adj.}$ [−]	$(C_F)_{ideal}$ [−]
TT-04_p1	11.1 ± 2.3	14.5 ± 2.3	75.1 ± 8.7	432.5 ± 1.1	432.5 ± 1.1	0.33 ± 5.2e-2	1.70 ± 2.0e-1
TT-04_p2	26.0 ± 2.4	30.8 ± 2.4	75.0 ± 8.7	432.3 ± 1.1	432.3 ± 1.1	0.70 ± 5.6e-2	1.70 ± 2.0e-1
TT-04_p3	35.2 ± 2.3	39.8 ± 2.3	74.9 ± 8.7	432.2 ± 1.1	432.2 ± 1.1	0.90 ± 5.3e-2	1.70 ± 2.0e-1
TT-04_p4	39.4 ± 2.0	43.3 ± 2.0	74.9 ± 8.6	432.0 ± 1.1	432.0 ± 1.1	0.98 ± 4.6e-2	1.70 ± 2.0e-1
TT-05_p1	11.0 ± 2.3	14.8 ± 2.3	74.8 ± 6.3	431.2 ± 1.1	431.2 ± 1.1	0.33 ± 5.3e-2	1.70 ± 1.9e-1
TT-05_p2	29.4 ± 2.8	34.9 ± 2.8	74.8 ± 6.5	431.0 ± 1.1	431.0 ± 1.1	0.80 ± 6.4e-2	1.70 ± 2.0e-1
TT-05_p3	36.7 ± 2.5	41.5 ± 2.5	74.7 ± 6.4	430.9 ± 1.1	430.9 ± 1.1	0.94 ± 5.6e-2	1.70 ± 2.0e-1
TT-05_p4	40.5 ± 2.1	44.6 ± 2.1	74.7 ± 6.2	430.7 ± 1.1	430.7 ± 1.1	1.01 ± 4.8e-2	1.70 ± 1.9e-1

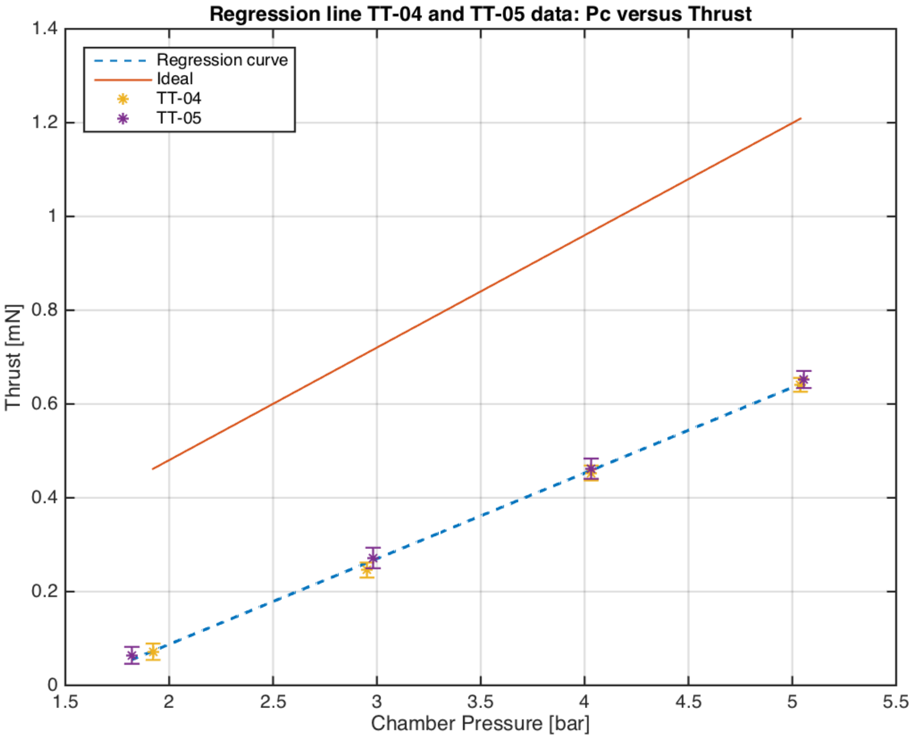

Figure 6.2: Chamber pressure (P_c) versus experimental thrust force ($(F)_{exp}$) and ideal thrust force ($(F)_{ideal}$) for thrust tests TT-04 and TT-05.

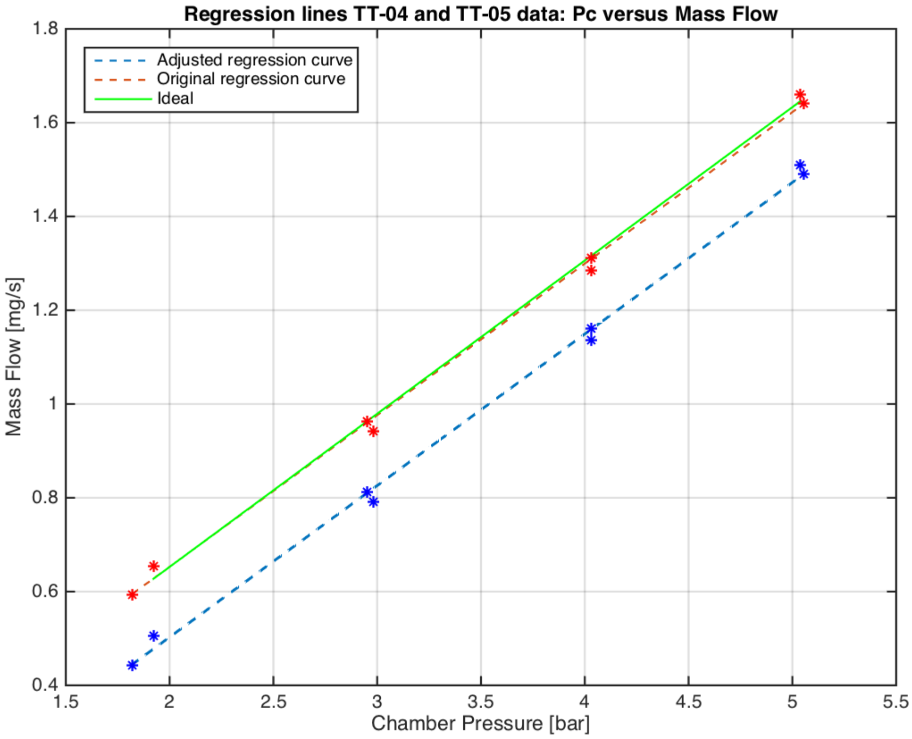

Figure 6.3: Chamber pressure (P_c) versus experimental mass flow ($(\dot{m})_{exp}$), the adjusted experimental mass flow ($(\dot{m})_{adj.}$) and ideal mass flow ($(\dot{m})_{ideal}$) for the thrust bench tests TT-04 and TT-05.

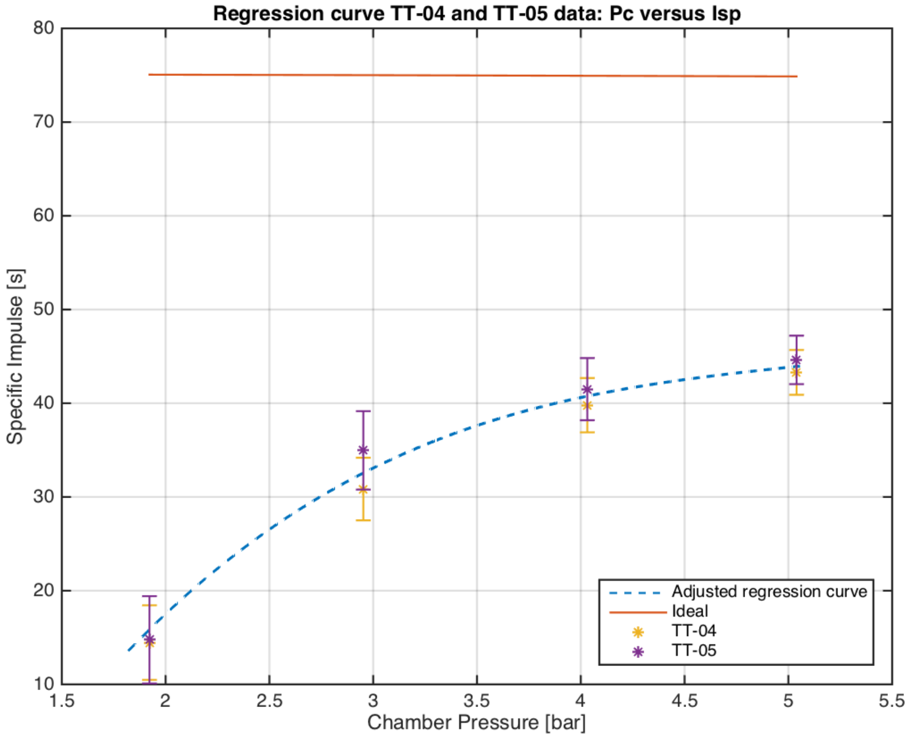

Figure 6.4: Chamber pressure (P_c) versus the adjusted experimental specific impulse ($(I_{sp})_{adj.}$) and ideal specific impulse ($(I_{sp})_{ideal}$) for thrust tests TT-04 and TT-05.

6.1.4. ”Performance Parameters” and ”Reynolds Number”

All the data has now been determined to calculate the green blocks ”Performance Parameters” and ”Reynolds Number”. Here, the parameters for both the original experimental mass flow $(\dot{m})_{exp}$ (see Table 6.6) and adjusted experimental mass flow $(\dot{m})_{adj.}$ (see Table 6.7) case will be described. Since the impact of this difference becomes much clearer when switching to the adjusted mass flow. It can be seen that the Reynolds number values $(R_e)_{exp}$ have slightly decreased. Note that $(R_e)_{exp}$ is based on both the experimental mass flow and dynamic viscosity at the throat (μ_{t_N2}), and that the equations needed for the calculations were already presented in Subsection 2.2.1. Furthermore, the discharge factor C_d now increases for higher Reynolds numbers, which makes sense considering results from literature. It can also be seen that the Isp quality ξ_s (and thus the nozzle quality ξ_F) slightly improves. As for the heating quality ξ_b, this remained $1[-]$ as expected. This is because cold nitrogen gas was used for the tests, which is why it was assumed that no heat from the propellant was lost to the nozzle walls and this means that there is no heating loss. Furthermore, a visualization of the data can be found in Figures 6.6-6.9. Also, the (adjusted) parameters will be analyzed in more depth in Subsections 6.2-6.4.

Table 6.6: Original mass flow ($(\dot{m})_{exp}$) - ”Reynolds Number” and ”Performance Parameters” data of the thrust bench tests TT-04 and TT-05.

Test Label	$(R_e)_{exp}$ $[-]$	C_d $[-]$	ξ_F $[-]$	ξ_b $[-]$	ξ_s $[-]$
TT-04_p1	8.68e2 ± 1.2e2	1.08 ± 1.7e-1	0.14 ± 2.0e-2	1.0	0.14 ± 2.0e-2
TT-04_p2	1.128e3 ± 1.4e2	1.02 ± 1.3e-1	0.34 ± 1.5e-1	1.0	0.34 ± 1.5e-1
TT-04_p3	1.74e3 ± 1.7e2	1.02 ± 1.1e-1	0.46 ± 2.3e-1	1.0	0.46 ± 2.3e-1
TT-04_p4	2.20e3 ± 2.0e2	1.03 ± 1.1e-1	0.52 ± 2.9e-1	1.0	0.52 ± 2.9e-1
TT-05_p1	7.89e2 ± 1.2e2	1.03 ± 1.7e-1	0.14 ± 2.0e-2	1.0	0.14 ± 2.0e-2
TT-05_p2	1.26e3 ± 1.4e2	0.99 ± 1.3e-2	0.39 ± 1.5e-1	1.0	0.39 ± 1.5e-1
TT-05_p3	1.71e3 ± 1.7e2	1.00 ± 1.1e-2	0.48 ± 2.3e-1	1.0	0.48 ± 2.3e-1
TT-05_p4	2.19e3 ± 2.0e2	1.00 ± 1.1e-2	0.53 ± 2.9e-1	1.0	0.53 ± 2.9e-1

Table 6.7: Adjusted mass flow ($(\dot{m})_{adj.}$) - ”Reynolds Number” and ”Performance Parameters” data of the thrust bench tests TT-04 and TT-05.

Test Label	$(R_e)_{exp}$ $[-]$	C_d $[-]$	ξ_F $[-]$	ξ_b $[-]$	ξ_s $[-]$
TT-04_p1	6.69e2 ± 1.2e2	0.81 ± 1.7e-1	0.19 ± 2.0e-2	1.0	0.19 ± 2.0e-2
TT-04_p2	1.08e3 ± 1.4e2	0.84 ± 1.3e-1	0.41 ± 1.5e-1	1.0	0.41 ± 1.5e-1
TT-04_p3	1.54e3 ± 1.7e2	0.88 ± 1.1e-1	0.53 ± 2.3e-1	1.0	0.53 ± 2.3e-1
TT-04_p4	2.00e3 ± 2.0e2	0.92 ± 1.1e-1	0.58 ± 2.9e-1	1.0	0.58 ± 2.9e-1
TT-05_p1	5.89e2 ± 1.2e2	0.60 ± 1.7e-1	0.19 ± 2.0e-2	1.0	0.19 ± 2.0e-2
TT-05_p2	1.06e3 ± 1.4e2	0.71 ± 1.3e-2	0.47 ± 1.5e-1	1.0	0.47 ± 1.5e-1
TT-05_p3	1.51e3 ± 1.7e2	0.78 ± 1.1e-2	0.56 ± 2.3e-1	1.0	0.56 ± 2.3e-1
TT-05_p4	1.99e3 ± 2.0e2	0.83 ± 1.1e-2	0.60 ± 2.9e-1	1.0	0.60 ± 2.9e-1

6.2. Discharge factor

As mentioned in Subsection 2.2.2, Tang and Fenn (1978) [17] provided Equation 2.20, which is an analytical approach for determining the discharge factor based on the specific heat ratio (γ) and the modified Reynolds number (R_{mod}). This equation was applied in order to make a comparison with the discharge factor obtained from experiments. Note that R_{mod} was determined using Equation 2.21, where R^* was $1.0[\mu m]$ and R_t was $8.7[\mu m]$ (half of W_t). It was also mentioned before in Subsection 6.1.2 that the original and adjusted experimental mass flow values ($(\dot{m})_{exp}$ and $(\dot{m})_{adj.}$) resulted in different values for the discharge factor. Therefore, a comparison was made using Figure 6.5 between the discharge factor obtained from Equation 2.20 ($(C_d)_{bd\_loss}$), and the discharge factor based on the original and adjusted mass flow. It can be seen that the regression curve of the original data set displays strange behavior: the discharge factor starts off higher than one, hereafter it reaches a valley near a Reynolds number of about $1600[-]$ and after this starts increasing towards a value higher than one. Of course, there is a large uncertainty in the data points, which means that the actual curve can have many different variations. However, when looking at the regression curve of the adjusted data it can be seen that this curve displays the same type of behavior like the analytical curve of $(C_d)_{bd\_loss}$: for increasing Reynolds numbers the discharge factor increases and converges to a value of (just below) $1[-]$. This is more evidence for concluding that the original mass flow measurements are false and that the adjusted flow is a more realistic value. Again, this is not proof as both the short and long range Brooks 5850S have been calibrated many years ago. Nevertheless, from here onwards the adjusted data set will be used to do the analyses.

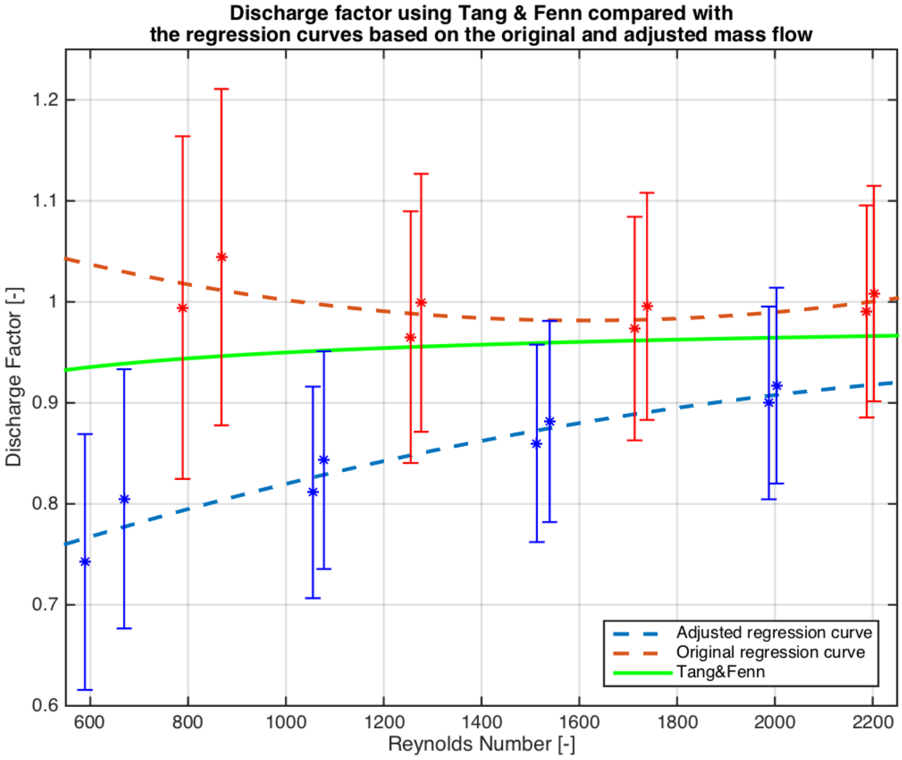

Figure 6.5: Reynolds number ($(R_e)_{exp}$) versus discharge factor (C_d), where the discharge factor based on Tang&Fenn is compared with the discharge factor regression curves (using TT-04 and TT-05) based on the original mass flow and the adjusted mass flow.

Furthermore, the adjusted regression curve does not coincide with the $(C_d)_{bd\_loss}$ curve. Even with the uncertainties, which lie between $11 - 17[\%]$, most data points do not coincide with the $(C_d)_{bd\_loss}$ curve. This is not expected, since the experimental results of Tang and Fenn (1978) [17] were much closer to the curve. The following could have caused the difference between the adjusted regression curve and the $(C_d)_{bd\_loss}$ curve. Tang and Fenn (1978) [17] used 3D conical (convergent-divergent) nozzles, while for this thesis a 2D conical nozzle was used. Depending on the real experimental mass flow, which can only be found through recalibration of the Brooks 5850S, the real discharge factor might be different. The discharge factor also depents on the $(\dot{m})_{ideal}$, which was calculated based on an estimated nozzle throat height and thus an estimated nozzle throat area (see Subsection 3.2.4). This could also result in a different discharge factor. For example, if the assumption for the estimation of the nozzle throat height was wrong and it would be $75[\mu m]$ instead of the estimated value of $81[\mu m]$), then this would result in an average C_d increase of $0.07[-]$.

Furthermore, the radius of curvature (R^*) was estimated using Figure 3.7, since a radius of curvature was not designed for the 3rd gen. MEMS-VLM chip. Looking back at Figure 2.13, it can be seen that a change in the radius of curvature has a great influence on the $(C_d)_{bd\_loss}$ curve. Nevertheless, for now it can be concluded that Equation 2.20 of Tang and Fenn (1978) [17] does provide a good indication for the expected discharge factor. Furthermore, it is again recommended to send both Brooks 5850S devices for recalibration and determine how this changes the experimental results found in this thesis. It is also recommended to always perform an optical characterization test on the MEMS-VLM chip during the manufacturing procedure before the silicon wafer is bonded to the glass wafer, such that an reliable characterization can be done for the nozzle geometry (including the radius of curvature).

Another comparison is made with the experimental results of Van Wees 2017 [3], which can be seen in Figure 6.6. Note that the nozzle geometry and experimental data of Van Wees (2017) [3] was described in more detail in Subsection 2.2.3. A few things can be seen in the figure. The discharge factor of Van Wees (2017) [3] at the Reynolds numbers is a lower compared to the adjusted regression curve. The second data point just lies outside of the error bound of the adjusted regression curve. The means that the difference must originate from somewhere else. This could be because of the different nozzle geometry. The nozzle throat area of Van Wees (2017) [3] was $3278[\mu m^2]$, while the nozzle throat area was $1411[\mu m^2]$ for the "01-LS2-02" chip used for the experiments in this thesis. Note that Van Wees (2017) [3] based the nozzle throat area value on a destructive optical inspection test on a similar nozzle, which means that there might be a slight difference in the actual nozzle throat area.

An additional comparison can be made with the data that is presented in Figure 6.7, which is from the paper of Grisnik *et al.* 1987 [2], who investigated nozzle geometry and Reynolds number influence on the discharge factor using nitrogen gas. It can be seen in the figure that for a Reynolds number range of $600 - 2000[-]$ the conical nozzle has a discharge factor between $0.85[-]$ and $0.91[-]$, while the discharge factor for the orifice is about $0.98[-]$ and only varies slightly. The MEMS-VLM chip is a 2D conical nozzle (or slit nozzle), this means that the discharge factor should be between the values of these two nozzle types. The reason for this is that ceiling and floor of the nozzle are about constant, which corresponds to an orifice, while the side wall converge and diverge, which corresponds to a conical nozzle. However, it was found that the MEM-VLM chip has a discharge factor between $0.77[-]$ and $0.91[-]$ for a Reynolds number range of $600 - 2000[-]$. This indicates that for higher Reynolds numbers the nozzle of the MEM-VLM chip corresponds to the conical nozzle, while for lower Reynolds numbers it does not.

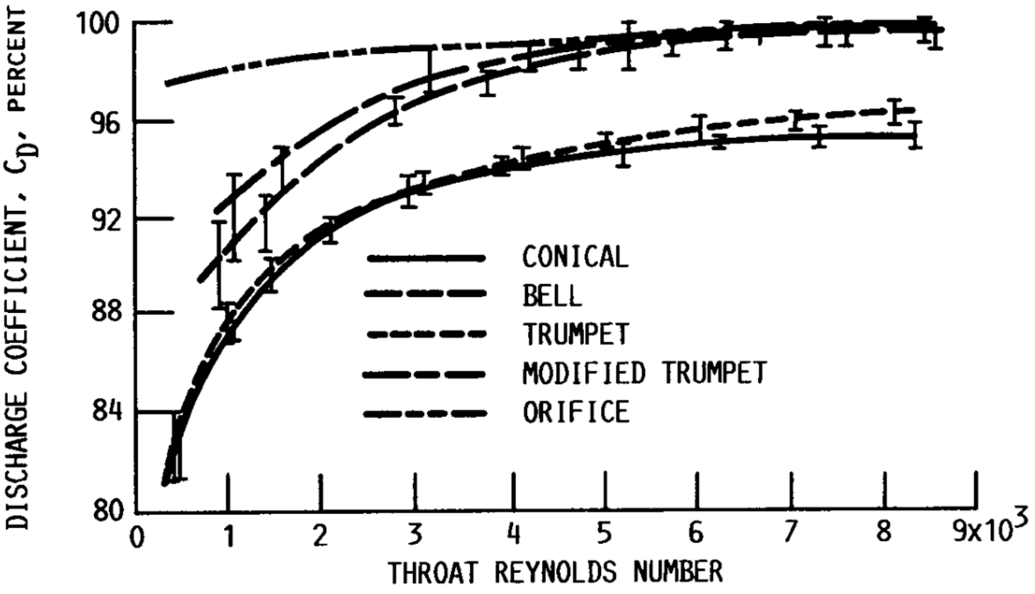

Figure 6.7: Comparison between throat Reynolds number and the discharge factor for different nozzle types, which was made by Grisnik *et al.* 1987 [2].

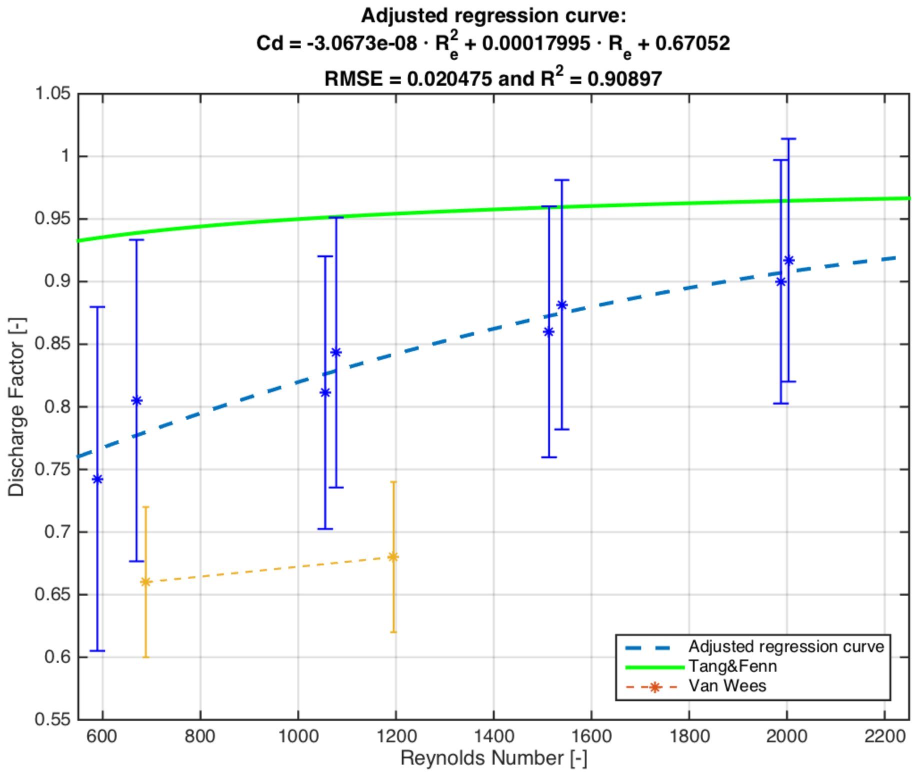

Figure 6.6: Reynolds number ($(R_e)_{exp}$) versus discharge factor (C_d), where the discharge factor regression curve (using TT-04 and TT-05) based on the adjusted mass flow is compared with the discharge factor of Van Wees 2017 [3].

6.3. Heating quality

The heating quality is described in this section. In Figure 6.8 the heating quality is presented, where the data set for both TT-04 and TT-05 are equal to 1. For now the heating quality is irrelevant. However, during water vaporization tests the heating quality could play a more important role as heat loss will be greater.

6.4. Nozzle quality

As mentioned before, the heating quality is equal to 1 and this means that nozzle quality is exactly the same as the Isp quality (see Equation 2.12), which is seen in Table 6.7. For future experiments where the propellant is heated, the heating quality is not equal 1, which will result in an difference between the nozzle quality and Isp quality. Therefore, for now only the nozzle quality will be used to prevent confusion for future experiments.

The nozzle quality data is visualized for TT-04 and TT-05 in Figure 6.9. It can be seen that the thrust bench test demonstrates repeatability regarding the calculation of the nozzle quality as the ξ_F data of TT-04 and TT-05 fall within each other's error bound. Furthermore, due to the propagation of errors in $(C_F)_{ideal}$ and $(C_F)_{exp}$, the total uncertainty for the nozzle quality lies between $13-30[\%]$. Even though this is larger than the uncertainty in the discharge factor, the difference between the ξ_F is great enough to conclude with certainty that the nozzle quality improves for higher increasing Reynolds numbers. However, the increase in nozzle quality converges as it gets smaller when going to higher Reynolds numbers. Comparing with the results of Van Wees 2017 [3], it can be seen that the improvement in ξ_F for higher Reynolds numbers is smaller compared to TT-04 and TT-05. This difference can be caused by the difference in nozzle geometry (see Subsection 2.1).

Another comparison can be made with the data that is presented in Figure 6.11, which is from the paper of Grisnik *et al.* 1987 [2], who investigated nozzle geometry and Reynolds number influence on

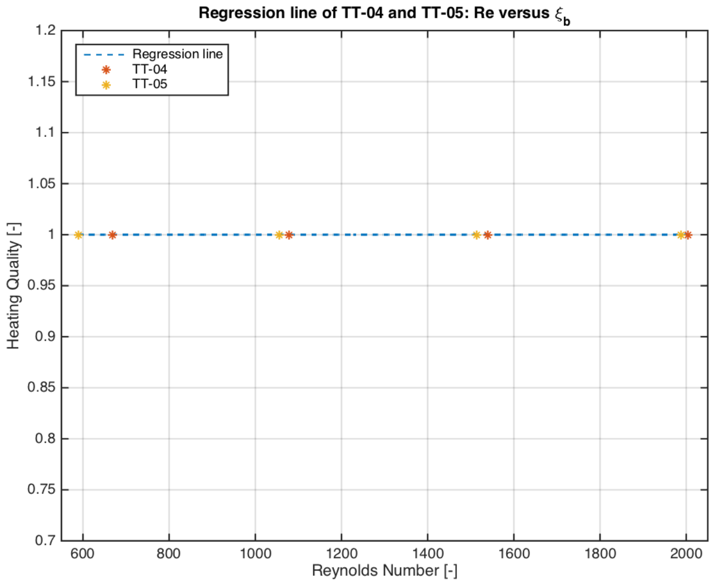

Figure 6.8: Reynolds number ($(R_e)_{exp}$) versus heating quality (ξ_b) for both TT-04 and TT-05.

the Isp quality using cold nitrogen gas. Note that since because cold nitrogen gas was used, the Isp quality in Figure 6.11 is equal to the nozzle quality. Looking at the nozzle quality (or Isp quality) of the orifice, this varies between $0.56[-]$ and $0.61[-]$ for a Reynolds number range of $600 - 2000[-]$, while for the conical nozzle this varies between $0.78[-]$ and $0.84[-]$. For the MEMS-VLM chip it was found that for Reynolds number range of $600 - 2000[-]$ the nozzle quality varies between $0.19[-]$ and $0.60[-]$. This indicates that for higher Reynolds numbers the nozzle of the MEM-VLM chip corresponds to the orifice, while for lower Reynolds numbers it does not. Note that the same behavior was found for the discharge factor, but there the data of the MEM-VLM chip resembled the data of the conical nozzle. This indicates that ideal rocket theory alone cannot provide a good prediction.

In order to give a better prediction, three effects can be considered (Zandbergen, 2016) [13]:

- The loss factor caused by a reduction in effective nozzle throat area.
- The loss factor caused by divergence of the flow ($(C_F)_{div\_loss}$).
- The loss factor caused by viscous effects ($(C_F)_{visc\_loss}$).

Starting off with the reduced effective nozzle throat area, which is caused by boundary layer formation in the throat, this increases the nozzle area ratio when the boundary layer formation in the nozzle exit is neglected. A quick calculation was done to see what its effect was on the $(C_F)_{ideal}$. Without taking the boundary layer into account $(C_F)_{ideal}$ is on average $1.701[-]$, while taking the boundary layer into account results in an average value of $1.706[-]$. It can be seen that the influence of the change in area ratio is negligible. Even for larger changes in area ratio, the influence on $(C_F)_{ideal}$ is small: for example, changing the area ratio from $30[-]$ to $20[-]$, results in an average ideal thrust coefficient of $1.684[-]$. Coming back to the change in $(C_F)_{ideal}$ caused by the throat boundary layer, because this is small it can be neglected.

As for loss factor caused by divergence of the flow, it was already explained in Subsection 2.2.2 that $(C_F)_{div\_loss}$ can be calculated by implementing θ_{nd} (equal to $20.5[°]$) in Equations 2.16 and 2.17. The results of this can be found in Table 6.8. The loss factor due to viscous effects ($(C_F)_{visc\_loss}$) is also presented in this table. This loss factor was also explained in Subsection 2.2.2 and can be estimated using the empirical relation (see Equation 2.19) provided by Spisz *et al.* (1965) [9]. However, it was mentioned before that this was only tested for Reynolds numbers in the range of $2000 - 10000[-]$. Nevertheless, Equation 2.19 was still used in order to obtain a prediction for the viscous loss.

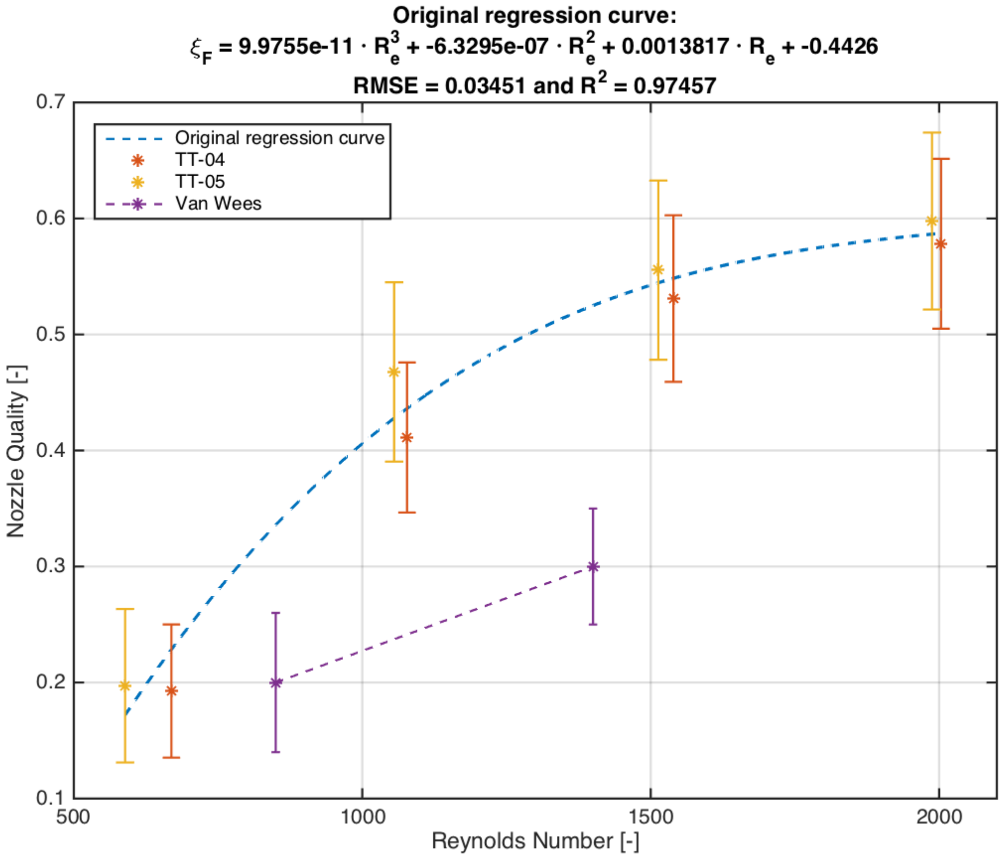

Figure 6.9: Reynolds number ($(R_e)_{exp}$) versus nozzle quality (ξ_F), where the nozzle quality regression curve (using TT-04 and TT-05) is compared with the nozzle quality of Van Wees 2017 [3].

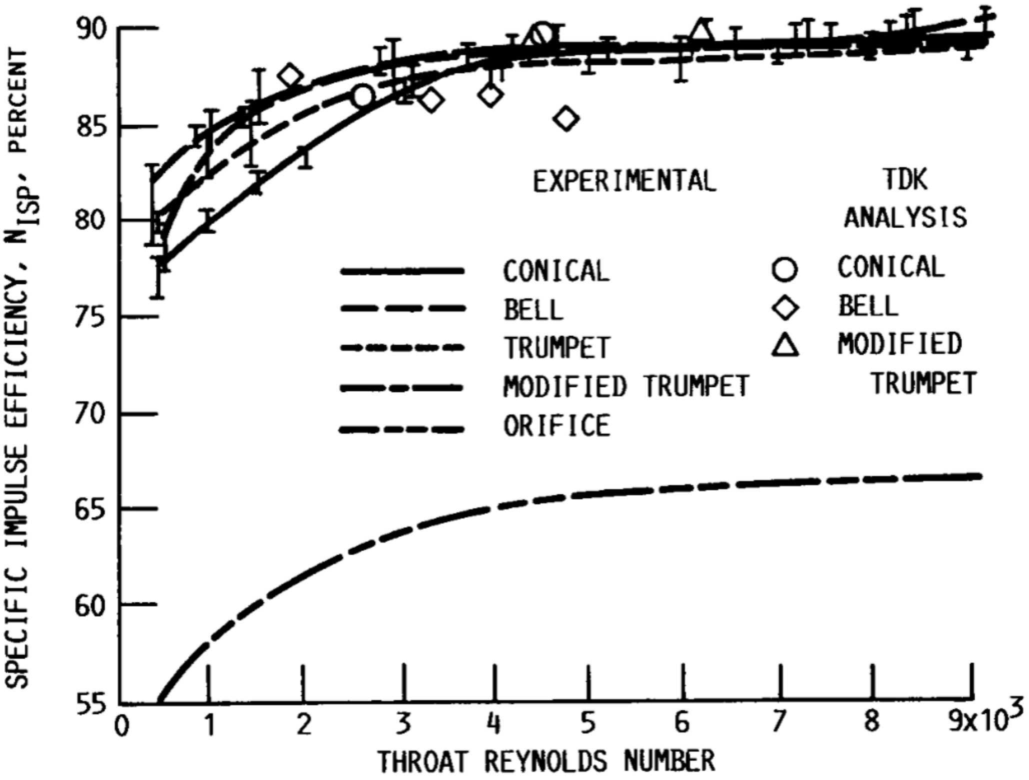

Figure 6.10: Comparison between throat Reynolds number and the Isp quality for different nozzle types, which was made by Grisnik *et al.* 1987 [2].

In Table 6.8 a comparison is made between the experimental, ideal and corrected thrust coefficient. Note that the experimental thrust coefficient ($(C_F)_{exp}$) was calculated with the adjusted mass flow ($(\dot{m})_{adj.}$). It can be seen in the table that even with both loss factors applied, there is still a difference between the experimental thrust coefficient and the corrected theoretical thrust coefficient ($(C_F)_{corrected}$). This is also visualized in Figure 6.11, where the nozzle quality is presented for both the ideal thrust coefficient and the corrected thrust coefficient. It can be seen that the corrections that were applied still do not fully account for all the losses, since the corrected nozzle quality is not equal to $1.0[-]$. Furthermore, for the highest Reynolds numbers the corrected nozzle quality is about $0.82[-]$, while for the lowest Reynolds numbers the nozzle quality is about $0.37[-]$. With this it can be concluded that Equation 2.19, which was used for calculating the viscous loss ($(C_F)_{visc\_loss}$), is indeed not suitable for Reynolds numbers lower than $2000[-]$.

The highest Reynolds numbers that were achieved in this test, were about $2000[-]$. This means that the calculation of the viscous loss at these Reynolds numbers should be valid and thus the corrected nozzle quality of $0.82[-]$ should be valid too. Furthermore, the reason why the nozzle quality value of $0.82[-]$ is not equal to $1.0[-]$ could be because of two things: there are unknown losses present apart from the viscous loss and/or the calculation of the viscous loss is not suitable for the MEMS-VLM chip. The author therefore recommends to investigate what could have caused the unknown losses (e.g. shockwaves). Looking at the latter reason, the nozzle geometry of the nozzles that were used by Spisz *et al.* (1965) [9] to establish Equation 2.19, were different from the nozzle of the MEMS-VLM chip. Non of these nozzles had the same 2D shape of the MEMS-VLM chip, for which the effect of boundary layer formation is greater as the upper and lower walls do not diverge like the sidewalls. With this a recommendation can be made about the design of the new generation MEMS-VLM chips: change the geometry of the nozzle from 2D to 3D. Apart from a better performance, the experimental data can be better compared with data from literature.

Table 6.8: Overview of the thrust coefficient: the experimental values, the ideal values, the values that include divergence loss, the values that include viscous loss and the total corrected value (includes both losses).

Test Label	$(C_F)_{exp}$ [−]	$(C_F)_{ideal}$ [−]	$(C_F)_{div\_loss}$ [−]	$(C_F)_{visc\_loss}$ [−]	$(C_F)_{corrected}$ [−]
TT-04_p1	0.33 ± 5.2e-2	1.70 ± 2.0e-1	1.67	0.95	0.92
TT-04_p2	0.70 ± 5.6e-2	1.70 ± 2.0e-1	1.67	1.11	1.08
TT-04_p3	0.90 ± 5.3e-2	1.70 ± 2.0e-1	1.67	1.21	1.17
TT-04_p4	0.98 ± 4.6e-2	1.70 ± 2.0e-1	1.66	1.27	1.23
TT-05_p1	0.33 ± 5.3e-2	1.70 ± 1.9e-1	1.67	0.90	0.87
TT-05_p2	0.80 ± 6.4e-2	1.70 ± 2.0e-1	1.67	1.10	1.07
TT-05_p3	0.94 ± 5.6e-2	1.70 ± 2.0e-1	1.67	1.20	1.17
TT-05_p4	1.01 ± 4.8e-2	1.70 ± 1.9e-1	1.66	1.27	1.23

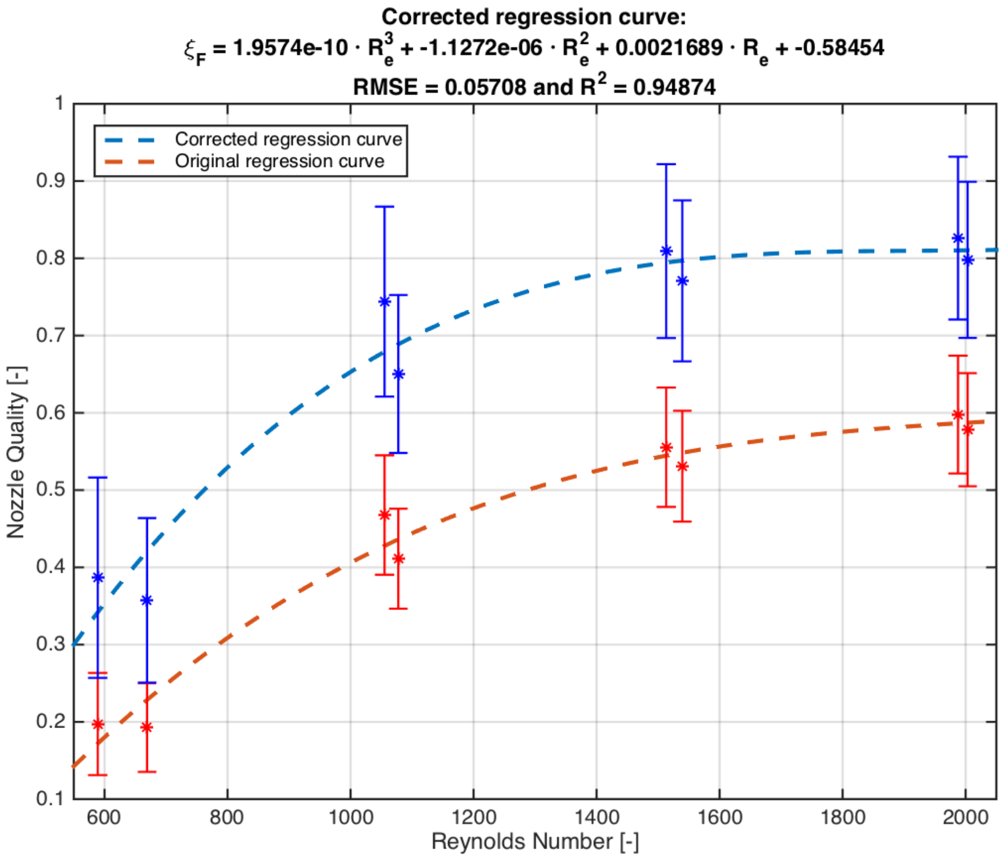

Figure 6.11: Reynolds number ($(R_e)_{exp}$) versus nozzle quality (ξ_F), where the original nozzle quality regression curve based on the ideal thrust coefficient is compared with the corrected nozzle quality regression curve based on the corrected thrust coefficient, which accounts for viscous loss and divergences loss.

6.5. Summary

Looking back at Table 4.1.4, all the success criteria have been met, which means that this test can be concluded to be successful. This means that no leakage has occurred during TT-04 and TT-05, but also that all the required data measurements were obtained. This also means that it has been demonstrated that the thrust bench test is repeatable. This can be seen in Figure 6.2 for the thrust measurements, but also in Figure 6.1 for the mass flow measurements. However, it was found that the long range Brooks 5850S that was used for the thrust bench test, provided mass flow readings that were consistently $0.15[mg/s]$ higher compared to the short range Brooks 5850S, which was found in a separate comparison test in which the chamber pressure and mass flow relations for both devices were established. Note that both devices have likely been calibrated many years ago, which is why it is recommended that the devices are sent to Brooks company for recalibration. Nevertheless, it was assumed that short range Brooks 5850S provided the correct mass flow measurements.

This assumption was made because the original mass flow measurements resulted in unrealistic discharge factor values (around $1.0[-]$). While an adjusted mass flow, which was $0.15[mg/s]$ smaller compared to the original mass flow, resulted in a discharge factor range of $0.77 - 0.91[-]$. This adjusted discharge factor made more sense when comparing it to the expected discharge factor range of $0.93 - 0.97[-]$, which was determined with the analytical relation of Tang and Fenn (1978) [17]. Even though there was a slight difference between the predicted and adjusted discharge factor, it was concluded that Equation 2.20 of Tang and Fenn (1978) [17] does provide a good indication for the expected discharge factor. The differences could have been caused by the assumed nozzle throat height, which determines the nozzle throat area and subsequently the ideal mass flow and the discharge factor. That is why it is recommended to always perform an optical characterization test on the MEMS-VLM chip during the manufacturing procedure before the silicon wafer is bonded to the glass wafer, such that an reliable characterization can be done for the nozzle geometry (including the radius of curvature). The difference between the adjusted and predicted discharge factor could also have been caused by the assumption about the chamber pressure: the pressure measured inside the 1st gen. interface was assumed to be equal to the chamber pressure. In reality there is a pressure drop, which would result in a reduced ideal mass flow and thus an increased discharge factor. It is therefore recommended that the design of the MEMS-VLM chip is adjusted in such a way that the chamber pressure can directly be measured.

Apart from improving the discharge factor, increasing the Reynolds number from $600[-]$ to $2000[-]$ increased the nozzle quality from $0.19[-]$ to $0.60[-]$. Taking into account the divergence loss and viscous loss based on Equation 2.19 of Spisz *et al.* (1965) [9], a corrected nozzle quality range of $0.37 - 0.82[-]$ was found. This indicated that Equation 2.19 is not suitable for Reynolds numbers below $2000[-]$. The highest corrected nozzle quality corresponded to a Reynolds number of about $2000[-]$, which indicates that the $0.82[-]$ value does include a valid viscous loss. The means that $0.18[-]$ of loss can be caused by other sources (e.g. shockwaves) or that Equation 2.19 does not give good prediction for 2D conical nozzles. It was therefore recommended to investigate the unknown loss source and to create a new generation MEMS-VLM chips with a 3D nozzle. Apart from a possible better performance, the experimental data can be better compared with data from literature.

7

Conclusion and Recommendations

7.1. Conclusion

The aim of the thesis project was to investigate the relationship between the throat Reynolds number and the performance characteristics of the 3rd gen. MEMS-VLM chip. This was translated to the following research question:

"What do experiments, within an accuracy of 10%, reveal about the influence of different throat Reynolds numbers on the performance characteristics by controlling the operating conditions of the 3rd gen. MEMS-VLM chip?"

This research question was expanded and translated into the following research objectives:

Subgoal 1: "Experimentally determine the relationship between the throat Reynolds number and the Isp quality / nozzle discharge factor / nozzle quality."
It can be concluded that this goal was achieved as the data produced from the experiments was documented and plotted in graphs in this thesis. Furthermore, the analytic relation of Tang and Fenn (1978) [17] provides a good prediction for the discharge factor. The prediction for Reynolds number range of $600 - 2000[-]$ was a discharge factor between $0.93 - 0.97[-]$, while the actual discharge factor was between $0.77 - 0.91[-]$. The difference could be caused by the estimated nozzle throat area, which determines the ideal mass flow and thus the discharge factor.

As for the nozzle (or Isp) quality, it was found that the quality also improved for higher Reynolds numbers: increasing the Reynolds number from $600[-]$ to $2000[-]$ increased the nozzle quality from $0.19[-]$ to $0.60[-]$. Corrections for ideal rocket theory were made, which shifted the nozzle quality from $0.37[-]$ to $0.82[-]$. These corrections included divergence loss, which was small (about $0.03[-]$), and viscous loss, which was expected to account for all the loss and was determined with the empirical relation of Spisz *et al.* (1965) [9]. However, the corrected nozzle quality was not $1.0[-]$. This meant that the empirical relation provides a poor prediction for viscous loss for low Reynolds numbers (below $2000[-]$). This also meant that the relation does not give good prediction for 2D conical nozzles or that or that other losses (e.g. shockwaves) were present.

Subgoal 2: "Explore the limit of the highest achievable Reynolds number and the corresponding performance characteristics at vacuum by controlling the operating conditions without damaging the 3rd gen. MEMS-VLM chip and 1st gen. interface."
This goal was concluded to be achieved as well, since the limit for the throat Reynolds number was found. Though this limit changed over time as became clear from the two leak tests during which a MEMS-VLM chip with a blocked nozzle was put inside the 1st gen. interface and the system was pressurized. The first leak test was performed before all the thrust bench tests, while the second leak test was performed after all these tests. During the first leak test it was found that the system could

be pressurized up to $7[bar]$ without showing any signs of leakage, but during the second leak test this value drop down to $5[bar]$. Therefore the highest achievable Reynolds number was about $1900[-]$, which corresponds to $5[bar]$.

Subgoal 3: "Obtain experimental data that is reproducible and accurate within 10% from both the preliminary tests and the thrust bench tests."
It was concluded that the goal was partly achieved as some measurements had uncertainties above $10[\%]$ and some below. However, it was mentioned in Section 1.2 that the value for the uncertainty requirement was guessed. Furthermore, it was found that a higher uncertainty does not always impose a problem for the analysis. For example, the uncertainty for the nozzle quality varied between $15-25[\%]$, but the relationship with the Reynolds number could still be noticed.

Subgoal 4: "Create detailed test procedures for both the preliminary tests and the thrust bench tests."
This goal was achieved as for all experiments detailed test procedures were created.

Subgoal 5: "Investigate through experimentation the influences of using liquid water versus gaseous nitrogen as propellant."
This goal was not achieved. The reason for this was that the nitrogen thrust bench test already took most of the timespan of the thesis project, which meant that there was not any time to perform the tests with liquid water. However, de Athayde Costa e Silva *et al.* (2017) [10] did perform a separate test with the liquid water demonstrating that it is possible to vaporize liquid water with the MEMS-VLM chip. Possible challenges will be the configuration of the additional wiring to power the heaters.

Subgoal 6: Provide recommendations for the test procedures, the 1st gen. interface design, the 3rd gen. MEMS-VLM chip design and the operating conditions.
This goal was achieved as every lesson learned during this thesis project was documented and a summary of all the recommendations can be found in Section 7.2.

In conclusion, the main research question, could partially be answered. The accuracy of $10[\%]$ was an overestimation as for the nozzle quality (and Isp quality) the uncertainties were between $15-25[\%]$ and despite the high uncertainty a relationship was established between the throat Reynolds number and the nozzle quality: increasing the Reynolds number from $600[-]$ to $2000[-]$ increased the nozzle quality from $0.19[-]$ to $0.60[-]$ and with viscous loss and divergence loss corrections increased the nozzle quality from $0.37[-]$ to $0.82[-]$. As for the relationship with the discharge factor, this range increased between $0.77-0.91[-]$, which corresponded well to the predicted range of $0.93-0.97[-]$. The corresponding operating conditions were as follows: the temperature was uncontrolled and on average at $295[K]$, while the pressure range was controlled and varied between $2[bar]$ and $5[bar]$ with increments of $1[bar]$.

7.2. Recommendations

- The following can be recommended about the test setup:
    - Recalibrate the Brooks MFC(s) before usage. All the current MFCs that are available in the cleanroom have been last calibrated over more than 10 years ago. This means that during these years the accuracy of the flow rate measurement has worsened with ±0.5[%] per year. Also, the Brooks MFC with the 0-2000 [ml/min] range has a controlling function that is currently not working, which is an issue that needs to be solved.
    - When a mass flow range of $0-2[mg/s]$ is expected, switch to the Brooks MFC with a range of 0-144 [ml/min]: because of the lower range the effect of the ±0.18[%] F.S. uncertainty will be less and thus the overall uncertainty in the measurement will reduce.
    - Buy different torsion springs that have different and lower spring constants than the one that is currently in use. This will enable future users of the AE-TB-5m pendulum thrust bench to

choose a range and accuracy that is more suitable for their experiment.
  - Investigate if baseline pendulum arm displacement change can be affected by a ambient temperature change.
- The following can be recommended about the MEMS-VLM chip:
  - Perform the thrust bench test with water as propellant.
  - Investigate the influence of the nitrogen gas temperature on the nozzle performance.
  - It was found during the optical characterization test that there are discrepancies between designed nozzle and the manufactured nozzle of the MEMS-VLM chip. The biggest discrepancy was found in the nozzle throat area, which is used to calculate the theoretical mass flow and thus has a big influence on the discharge factor. It is therefore recommended that either the manufacturing precision of the MEMS-VLM chip is improved or that for each chip an optical characterization test is done before the thrust bench tests are performed.
  - For the manufacturing procedure of the MEMS-VLM chip it is recommended that an optical characterization is carried out before the glass waver is attached to the silicon waver.
  - It is recommended that thrust bench tests for other 3rd gen. MEMS-VLM chips with different nozzle geometries are performed in order to determine the most favorable nozzle type.
- The following can be recommended about the 1st gen. interface:
  - Find a solution for the leakage. Over time leakage will occur at lower chamber pressures. As mentioned before during the first leak test this was found to be 7 [bar] and over time this was reduced to 5 [bar], which was most likely caused by the bending of the teflon block of the interface.

Bibliography

[25] *Brooks® smart-series digital mass flow meters and controllers,* (Brooks Instruments, 2008).

[3] T. Van Wees, *Characterization and Test of a MEMS-Resistojet for Small Satellite Propulsion*, Diploma thesis, Delft University of Technology (2017).

[10] M. de Athayde Costa e Silva, D. Cordeiro Guerrieri, H. Van Zeijl, A. Cervone, and E. Gill, *Vaporizing liquid microthrusters with integrated heaters and temperature measurement,* Sensors and Actuators A: Physical (2017).

[24] *capancdt - capacitive displacement sensors and systems,* (Micro-Epsilon, 2015).

[22] *Ms5837-30ba - ultra small gel filled pressure sensor,* (Sensor Solutions, 2015).

[11] *Technology for vacuum systems - dcp3000,* (Vacuubrand).

[1] N. I. of Standards and Technology, *Nist standard reference database number 69,* Last time accessed: 2018-10-10.

[17] S. Tang and J. Fenn, *Experimental Determination of the Discharge Coefficients for Critical Flow through an Axisymmetric Nozzle*, Tech. Rep. (1978).

[9] E. Spisz, P. Brinich, and J. Jack, *Thrust coefficients of low-thrust nozzles,* (1965).

[2] S. Grisnik, T. Smith, and L. Saltz, *Experimental study of low reynolds number nozzles,* in *19th International Electric Propulsion Conference* (1987).

[4] E. Gill and J. Guo, *Mems technology for miniaturized space systems: needs, status, and perspectives,* Proceedings of SPIE (2012).

[5] J. Mueller, R. Hofer, and J. Ziemer, *Survey of Propulsion Technologies Applicable to Cubesats*, Tech. Rep. 20100032899 (California Institute of Technology, 2010).

[6] T. Matthew, *Design of a MEMS micro-resistojet*, Diploma thesis, Delft University of Technology (2011).

[7] C. Hanselaar, *Evaporative Two-Phase Micro-Flow Modelling*, Diploma thesis, Delft University of Technology (2016).

[8] E. Jansen, *Improvement and validation of test stand performance for novel micropropulsion systems*, Diploma thesis, Delft University of Technology (2016).

[12] W. Larson and J. Wertz, eds., *Space Mission Analysis and Design* (California: Microcosm Press, London: Kluwer Academic Publishers, 2005) pp. 688–691.

[13] B. Zandbergen, *Thermal Rocket Propulsion (V2.04))*, Technical Report (Delft University of Technology, 2016).

[14] G. Suton and O. Biblarz, eds., *Rocket Propulsion Elements*, 7th ed. (John Wiley and Sons, 2001) pp. 62–63.

[15] D. Huzel and D. Huang, *Design of Liquid Propellant Rocket Engines*, Tech. Rep. SP-125 (National Aeronautics and Space Administration (NASA), 1971).

[16] S. Farokhi, ed., *Aircraft Propulsion*, 2nd ed. (John Wiley & Sons, 2014).

[18] R. Bayt, *Analysis, Fabrication and Testing of a MEMS-based Micropropulsion System*, Ph.D. thesis, Massachusetts Institute of Technology (1999).

[19] D. Maurya, S. Das, and S. Lahiri, *An analytical model of a silicon mems vaporizing liquid microthruster and some experimental studies,* Sensors and Actuators, A: Physical (2005).

[20] D. Maurya, S. Das, and S. Lahiri, *Silicon mems vaporizing liquid microthruster with internal microheater,* Journal of Micromechanics and Microengineering (2005).

[21] J. Cen and J. Xu, *Performance evaluation and flow visualization of a mems based vaporizing liquid micro-thruster,* Acta Astronautica (2010).

[23] R. Bijster, *Design, Verification and Validation of a Micropropulsion Thrust Stand*, Diploma thesis, Delft University of Technology (2014).

[26] *Heraeus heating and drying oven,* (Thermo Scientific, 2007).

[27] H. Coleman and W. Steele, eds., *Experimentation, Validation, and Uncertainty Analysis for Engineers*, 3rd ed. (John Wiley & Sons, 2009).

A

Thrust Bench Test - Liquid Water

Most of the time during the thesis project was spent on the nitrogen thrust bench test with the 3rd gen. MEMS-VLM chip, which means that there was not enough time for performing the thrust bench test with liquid water as propellant. However, some information relevant for the liquid water thrust bench test was gathered, which is presented in this appendix. In Section A.1 experiments performed by de Athayde Costa e Silva *et al.* (2017) [1] are discussed in short. In Section A.2 adaptions for the test set-up are described that are needed when switching from nitrogen to liquid water as propellant.

A.1. Performed experiments

Two PhD students (M. de Athayde Costa e Silva and D. Cordeiro Guerrieri) of the TU Delft, successfully demonstrated that vaporization of water was possible using the heaters of the 3rd gen. MEMS-VLM chip (de Athayde Costa e Silva *et al.*, 2017) [1]. Note that before performing the water vaporization test that de Athayde Costa e Silva *et al.* (2017) [1] performed an electrical characterization test in order to determine the temperature resistance coefficient of the heatesrs of the MEMS-VLM chip.

Furthermore, during the water vaporization test the inlet section of the MEMS-VLM chip was slowly filled with water, after which the power to the heaters was increased causing the vaporization to start. After this the mass flow rate and the heater power were manually adjusted such that full vaporization occurred within the chamber before the water reached the nozzle. This was visually checked by looking through the glass side of the MEMS-VLM chip. Apart from the heater power and mass flow, the exact location in the chamber where the liquid water transitioned into gaseous water also depended on the nozzle type and chamber shape. For more information about the experimental results it is recommended the read the paper of de Athayde Costa e Silva *et al.* (2017) [1].

After these experiments, de Athayde Costa e Silva *et al.* (2017) [1] found through optical inspection that a small amount of residue was build op in the nozzle and for some chips the residue fully clogged the nozzle throat. During the experiment demineralized water was used, which means that it could still contain some mineral particles. It is therefore recommended for future experiments to use distilled water, which does not have any mineral particles. It is also recommended to clean all the feed lines through which the water needs to flow before it reaches the MEMS-VLM chip. In case residue still builds up in the nozzle after taking these precautions, the residue could be caused by a chemical reaction between the hot water gas and the MEMS-VLM chip. Thus, it is recommended to find the cause of the residue and to find a solution.

A.2. Adaptions test set-up

In this section in short the adaptions in the test set-up are described that will be needed to perform the liquid water thrust bench test. The following adaptions are needed: electrical wiring for powering the heaters, a tank for storing the water and a liquid mass flow sensor for measuring the mass flow of the water.

The SM7020 Power Supply Unit (PSU) can be used to provide the required power to heaters. The SM7020 is connected to the ?Experiment? feedthrough of the vacuum chamber, which is connected to a D-sub 9 connector inside the vacuum chamber. From the connector the wiring to the golden pins of the 1st gen. interface still need to be established. Note that the golden pins touch the heater pads of the MEM-VLM chip and thus provide the power to the heaters. It is recommended that the wiring is configured the same as the fluidic tube: it should be first taped to the Boikon profile support pillar, subsequently looped once in the air and taped to the pendulum cross beam, after which it is rotated (and taped) downwards the pendulum arm and finally connected to the golden pins. This will reduce the influence of the stiffness of the wires on the pendulum arm displacement of the AE-TB-5m, which is needed to obtain thrust measurements with a low uncertainty.

As for the water tank and liquid mass flow sensor, these are presented in Figures A.1 and A.2. The mass flow was purchased from the company Sensiron and an overview of the specifications can be found in Table A.1 [2].

Table A.1: Overview of the SLI-0430 Liquid Flow Meter specifications [2]. Note that '% F.S.' stands for the percentage of the Full Scale (or measurement range of the device) and '% S.P.' stands for the percentage of the Set Point (or measured value).

Range	$0 - 80\ [\mu l/min]$
Accuracy	± 0.15% of F.S. or ± 5.0% of S.P.
Repeatability	± 0.01% of F.S. or ± 0.5% of S.P.
Operating Temperature	10<T<50 $[\deg C]$
Operating Pressure	maximum 50 $[bar]$
Response Time	0.040 [s]

Figure A.1: Sensiron's SLI-0430 Liquid Flow Meter that is suitable for the liquid water thrust bench test [2].

Figure A.2: Set-up that includes both the water tank and the SLI-0430 Liquid Flow Meter in the feed system.

Bibliography

[1] M. de Athayde Costa e Silva, D. Cordeiro Guerrieri, H. Van Zeijl, A. Cervone, and E. Gill, Vaporizing Liquid Microthrusters with integrated heaters and temperature measurement, Sensors and Actuators A: Physical (2017).

[2] SLI Liquid Flow Meter Series - Media Isolated Microfluidic Flow Meter, (Sensiron, 2016).

B

Brooks 5850S

In this appendix additional information about the Brooks 5850S is presented, which is a device that can both measure and control mass flow. The device has a 15 pin D-type male connector and the pinout specification is presented in Figure B.1, which was obtained from the manual [1]. A DB-cable 15M/F was used to connect the Brooks 5850S to a (new) Printed Circuit Board (PCB) created by the current cleanroom manager (Sevket Uludag). The PCB was connected to the computer via the NI CB-68LP breakout board. Pictures of the PCB are presented in Figures B.2-B.4. In Figure B.2 it can be seen that the pinout specification of Figure B.1 is displayed on the PCB. Also, each channel on the board has three connections: a female socket, a male socket and a female socket with screws. These connections can be used to connect the PCB to the NI CB-68LP breakout board.

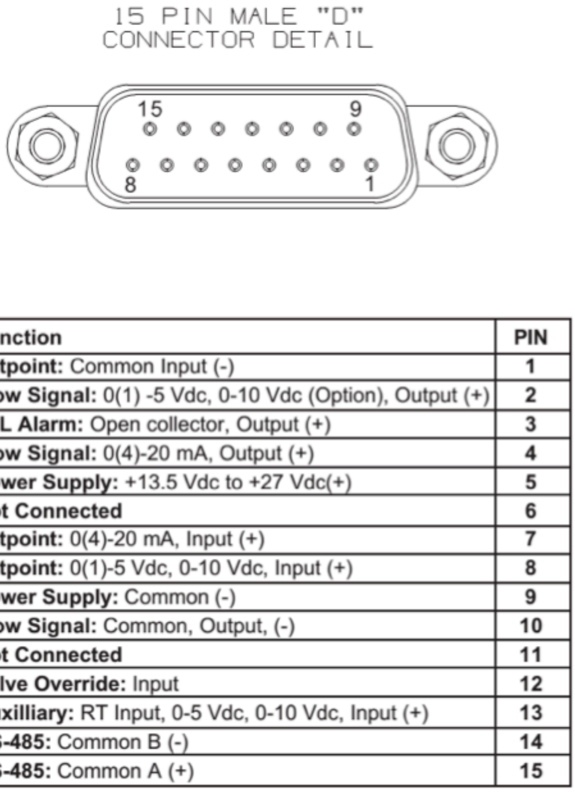

Function	PIN
Setpoint: Common Input (-)	1
Flow Signal: 0(1) -5 Vdc, 0-10 Vdc (Option), Output (+)	2
TTL Alarm: Open collector, Output (+)	3
Flow Signal: 0(4)-20 mA, Output (+)	4
Power Supply: +13.5 Vdc to +27 Vdc(+)	5
Not Connected	6
Setpoint: 0(4)-20 mA, Input (+)	7
Setpoint: 0(1)-5 Vdc, 0-10 Vdc, Input (+)	8
Power Supply: Common (-)	9
Flow Signal: Common, Output, (-)	10
Not Connected	11
Valve Override: Input	12
Auxilliary: RT Input, 0-5 Vdc, 0-10 Vdc, Input (+)	13
RS-485: Common B (-)	14
RS-485: Common A (+)	15

Figure B.1: The pin specification of the D-type male connector of the Brooks 5850S [1].

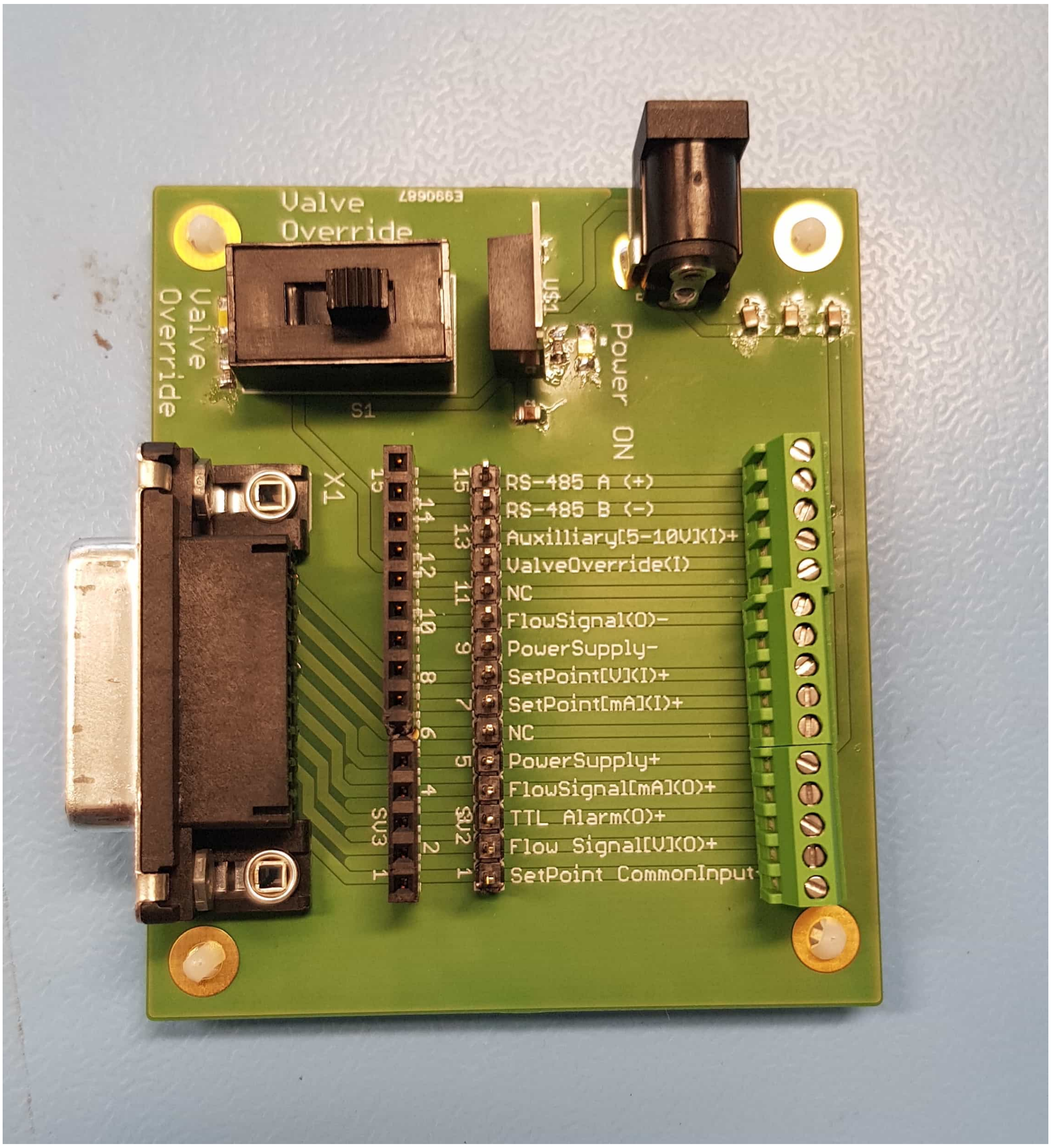

Figure B.2: Top view of the PCB that connects the Brooks 5850S with the NI CB-68LP breakout board, which is an interface between the computer and the PCB. Note that the ”NC” means that these pins have ”No Connection” with the mass flow controller.

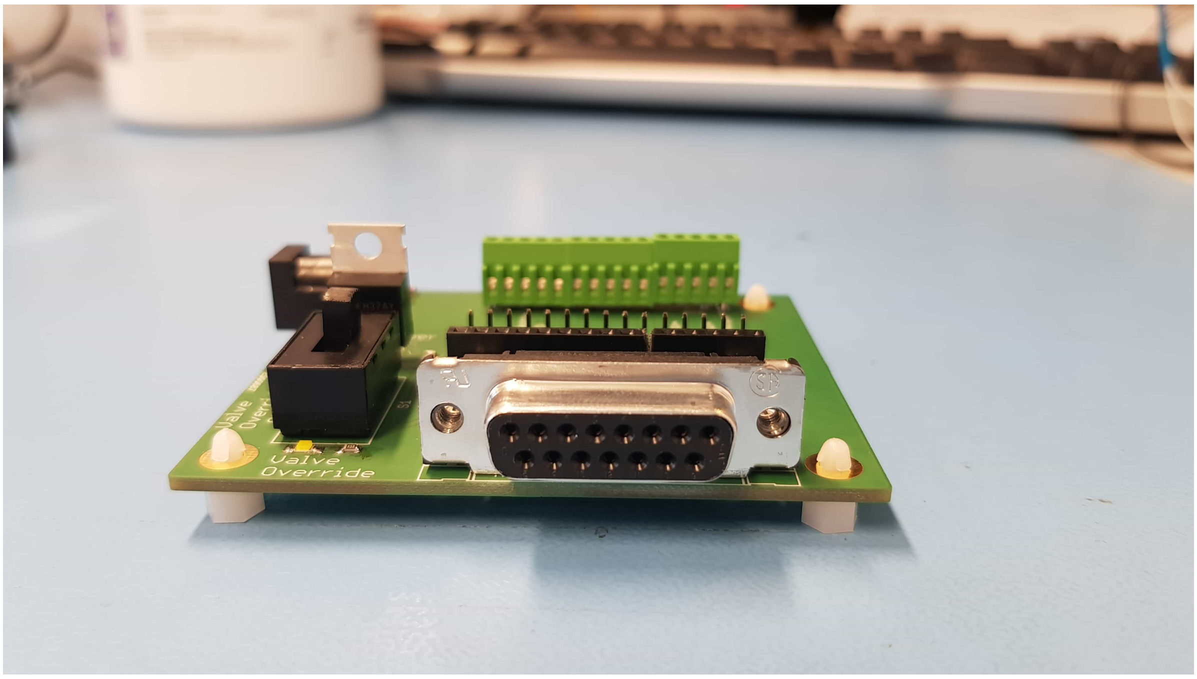

Figure B.3: Side view of the PCB, where the 15 pin D-type female connector can be connected to the 15 pin D-type male connector of the Brooks 5850S via the DB-cable 15M/F.

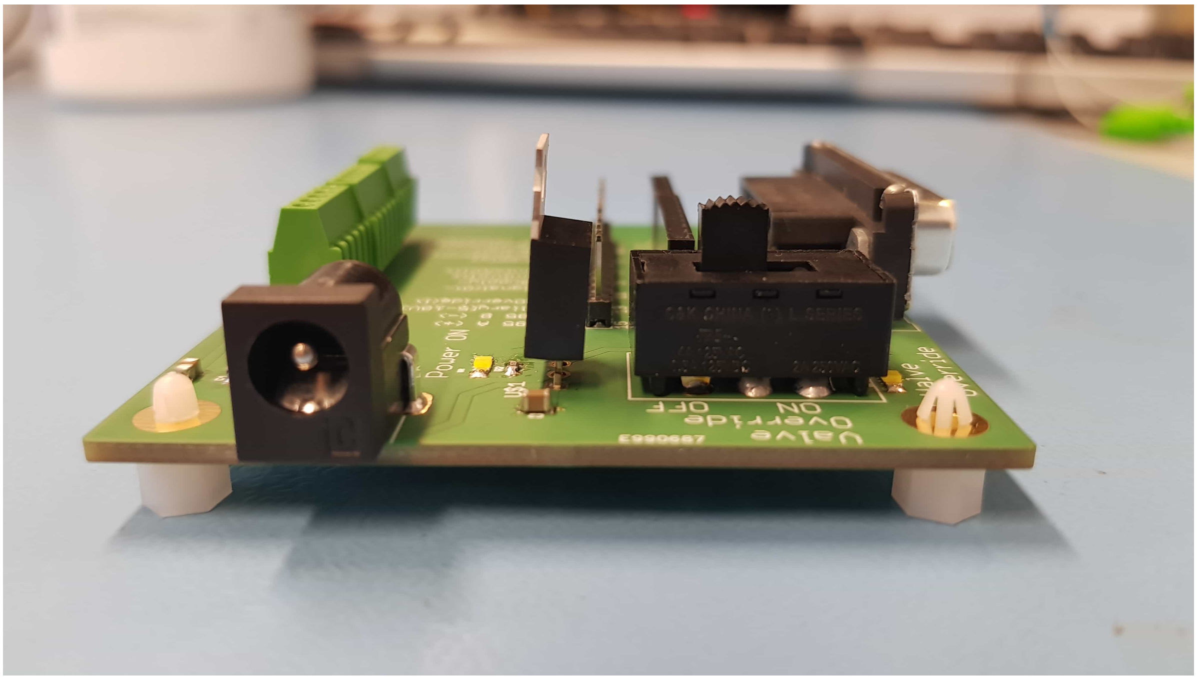

Figure B.4: Side view of the PCB, where the 2.5 [mm] connector jack can be connected to the VOLTCRAFT FPPS (24 [Vdc], 0.75[A]) adapter in order to provide power to the mass flow controller.

Bibliography

[1] Brooks® smart-series digital mass flow meters and controllers, (Brooks Instruments, 2008).

C

Lee Company Components

In this appendix a collection of Lee Company components are presented, which is a company that provides miniature fluid control products. This collection was needed for the test set-up of a nitrogen thrust bench test. Starting off, the VHS-M/M-24V solenoid valve is able to fully close/open and thus was used to control nitrogen gas feed. A technical data sheet about the solenoid valve is presented in Figure C.2 [2]. A tube with a 062 MINSTAC fitting system (see Figure C.3) is suitable to connect with the solenoid valve. The assembly of this system is presented in Figure C.4. An alternative option is to attach a tube to the 062 MINSTAC LFA Tubing Adapter (see Figure C.5), which can also be connected to the solenoid valve. For both the 062 MINSTAC fitting system and the 062 MINSTAC LFA Tubing Adapter, for attachment to the solenoid valve it is required to use the MINSTAC torque wrench (see Figure C.1). This is important as the solenoid valve is very fragile and could break if the torque applied to the fitting of the valve is too great. Furthermore, for controlling the solenoid valve it is required to use the Spike & Hold Driver as presented in Figure C.6, about which a specification sheet can be found in Figure C.7.

(a) Side that provides a torque of 0.07 $[N \cdot m]$.

(b) Side that provides a torque of 0.035 $[N \cdot m]$.

Figure C.1: The Lee Company's MINSTAC torque wrench that is strongly advised to be used for tightening the .138-40 UNF fittings to the ports of the VHS-M/M-24V solenoid valve.

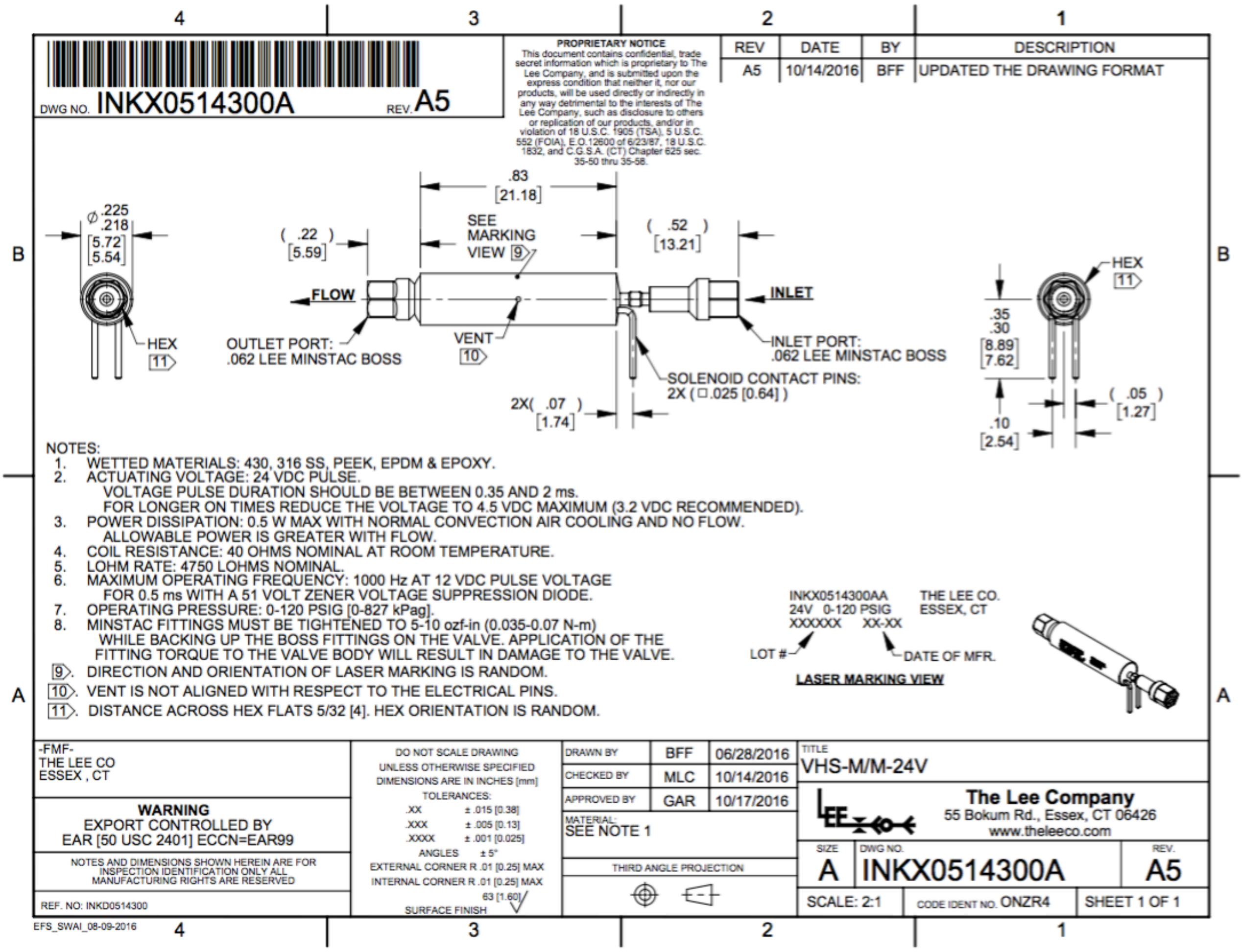

DWG NO. INKX0514300A REV. A5

PROPRIETARY NOTICE
This document contains confidential, trade secret information which is proprietary to The Lee Company, and is submitted upon the express condition that neither it, nor our products, will be used directly or indirectly in any way detrimental to the interests of The Lee Company, such as disclosure to others or replication of our products, and/or in violation of 18 U.S.C. 1905 (TSA), 5 U.S.C. 552 (FOIA), E.O.12600 of 6/23/87, 18 U.S.C. 1832, and C.G.S.A. (CT) Chapter 625 sec. 35-50 thru 35-58.

REV	DATE	BY	DESCRIPTION
A5	10/14/2016	BFF	UPDATED THE DRAWING FORMAT

NOTES:
1. WETTED MATERIALS: 430, 316 SS, PEEK, EPDM & EPOXY.
2. ACTUATING VOLTAGE: 24 VDC PULSE.
   VOLTAGE PULSE DURATION SHOULD BE BETWEEN 0.35 AND 2 ms.
   FOR LONGER ON TIMES REDUCE THE VOLTAGE TO 4.5 VDC MAXIMUM (3.2 VDC RECOMMENDED).
3. POWER DISSIPATION: 0.5 W MAX WITH NORMAL CONVECTION AIR COOLING AND NO FLOW.
   ALLOWABLE POWER IS GREATER WITH FLOW.
4. COIL RESISTANCE: 40 OHMS NOMINAL AT ROOM TEMPERATURE.
5. LOHM RATE: 4750 LOHMS NOMINAL.
6. MAXIMUM OPERATING FREQUENCY: 1000 Hz AT 12 VDC PULSE VOLTAGE
   FOR 0.5 ms WITH A 51 VOLT ZENER VOLTAGE SUPPRESSION DIODE.
7. OPERATING PRESSURE: 0-120 PSIG [0-827 kPag].
8. MINSTAC FITTINGS MUST BE TIGHTENED TO 5-10 ozf-in (0.035-0.07 N-m)
   WHILE BACKING UP THE BOSS FITTINGS ON THE VALVE. APPLICATION OF THE
   FITTING TORQUE TO THE VALVE BODY WILL RESULT IN DAMAGE TO THE VALVE.

9. DIRECTION AND ORIENTATION OF LASER MARKING IS RANDOM.
10. VENT IS NOT ALIGNED WITH RESPECT TO THE ELECTRICAL PINS.
11. DISTANCE ACROSS HEX FLATS 5/32 [4]. HEX ORIENTATION IS RANDOM.

-FMF-
THE LEE CO
ESSEX , CT

WARNING
EXPORT CONTROLLED BY
EAR [50 USC 2401] ECCN=EAR99

NOTES AND DIMENSIONS SHOWN HEREIN ARE FOR INSPECTION IDENTIFICATION ONLY ALL MANUFACTURING RIGHTS ARE RESERVED

REF. NO: INKD0514300

DO NOT SCALE DRAWING
UNLESS OTHERWISE SPECIFIED
DIMENSIONS ARE IN INCHES [mm]
TOLERANCES:

.XX	± .015 [0.38]
.XXX	± .005 [0.13]
.XXXX	± .001 [0.025]
ANGLES	± 5°

EXTERNAL CORNER R .01 [0.25] MAX
INTERNAL CORNER R .01 [0.25] MAX
63 [1.60]
SURFACE FINISH

DRAWN BY	BFF	06/28/2016
CHECKED BY	MLC	10/14/2016
APPROVED BY	GAR	10/17/2016

MATERIAL:
SEE NOTE 1

THIRD ANGLE PROJECTION

TITLE
VHS-M/M-24V

The Lee Company
55 Bokum Rd., Essex, CT 06426
www.theleeco.com

SIZE	DWG NO.	REV.
A	INKX0514300A	A5

SCALE: 2:1 CODE IDENT NO. ONZR4 SHEET 1 OF 1

EFS_SWAI_08-09-2016

Figure C.2: Specification sheet of the Lee Company's VHS-M/M-24V solenoid valve [2]. Note that there is variation of this valve available that needs a spike/pulse voltage of $12[V]$ and a constant voltage of $1.6[V]$

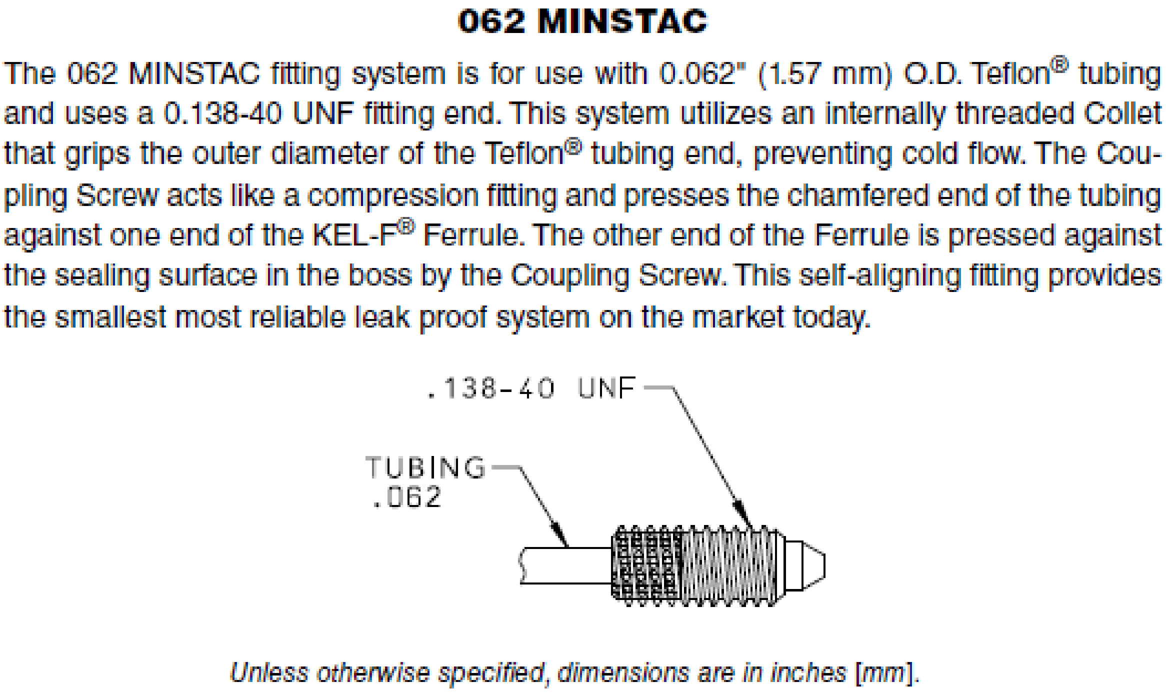

062 MINSTAC

The 062 MINSTAC fitting system is for use with 0.062" (1.57 mm) O.D. Teflon® tubing and uses a 0.138-40 UNF fitting end. This system utilizes an internally threaded Collet that grips the outer diameter of the Teflon® tubing end, preventing cold flow. The Coupling Screw acts like a compression fitting and presses the chamfered end of the tubing against one end of the KEL-F® Ferrule. The other end of the Ferrule is pressed against the sealing surface in the boss by the Coupling Screw. This self-aligning fitting provides the smallest most reliable leak proof system on the market today.

Unless otherwise specified, dimensions are in inches [mm].

Figure C.3: Snapshot of the Lee Company's manual with information about the 062 MINSTAC fitting system [1].

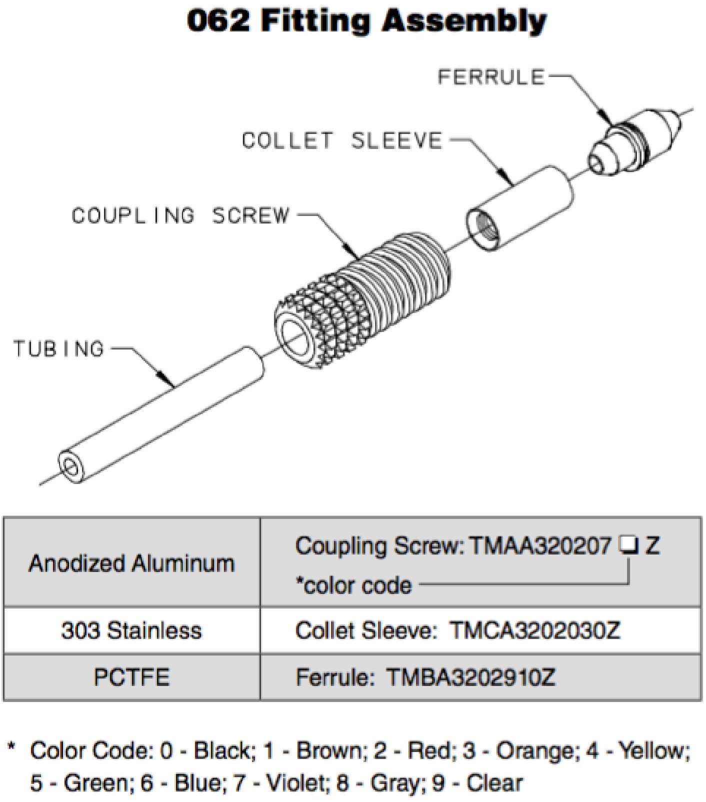

062 Fitting Assembly

Anodized Aluminum	Coupling Screw: TMAA320207 ☐ Z *color code
303 Stainless	Collet Sleeve: TMCA3202030Z
PCTFE	Ferrule: TMBA3202910Z

* Color Code: 0 - Black; 1 - Brown; 2 - Red; 3 - Orange; 4 - Yellow; 5 - Green; 6 - Blue; 7 - Violet; 8 - Gray; 9 - Clear

Figure C.4: Snapshot of the Lee Company's manual with information about the assembly of the 062 MINSTAC fitting system [1].

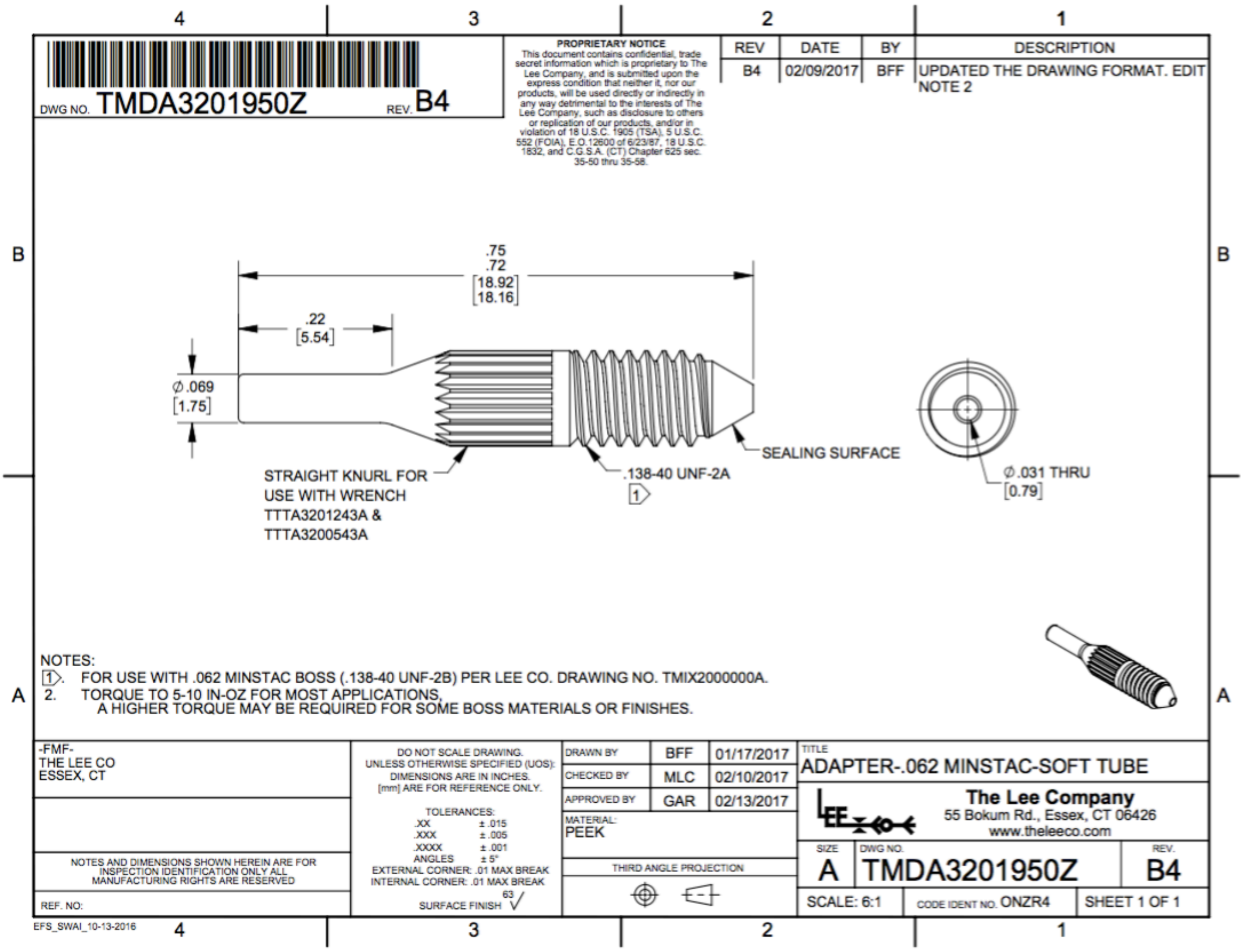

DWG NO. TMDA3201950Z REV. B4

PROPRIETARY NOTICE
This document contains confidential, trade secret information which is proprietary to The Lee Company, and is submitted upon the express condition that neither it, nor our products, will be used directly or indirectly in any way detrimental to the interests of The Lee Company, such as disclosure to others or replication of our products, and/or in violation of 18 U.S.C. 1905 (TSA), 5 U.S.C. 552 (FOIA), E.O.12600 of 6/23/87, 18 U.S.C. 1832, and C.G.S.A. (CT) Chapter 625 sec. 35-50 thru 35-58.

REV	DATE	BY	DESCRIPTION
B4	02/09/2017	BFF	UPDATED THE DRAWING FORMAT. EDIT NOTE 2

NOTES:
1. FOR USE WITH .062 MINSTAC BOSS (.138-40 UNF-2B) PER LEE CO. DRAWING NO. TMIX2000000A.
2. TORQUE TO 5-10 IN-OZ FOR MOST APPLICATIONS, A HIGHER TORQUE MAY BE REQUIRED FOR SOME BOSS MATERIALS OR FINISHES.

-FMF-
THE LEE CO
ESSEX, CT

NOTES AND DIMENSIONS SHOWN HEREIN ARE FOR INSPECTION IDENTIFICATION ONLY ALL MANUFACTURING RIGHTS ARE RESERVED

REF. NO:

DO NOT SCALE DRAWING.
UNLESS OTHERWISE SPECIFIED (UOS):
DIMENSIONS ARE IN INCHES.
[mm] ARE FOR REFERENCE ONLY.

TOLERANCES:

.XX	± .015
.XXX	± .005
.XXXX	± .001
ANGLES	± 5°

EXTERNAL CORNER: .01 MAX BREAK
INTERNAL CORNER: .01 MAX BREAK
SURFACE FINISH 63 √

DRAWN BY	BFF	01/17/2017
CHECKED BY	MLC	02/10/2017
APPROVED BY	GAR	02/13/2017

MATERIAL: PEEK

THIRD ANGLE PROJECTION

TITLE ADAPTER-.062 MINSTAC-SOFT TUBE

The Lee Company
55 Bokum Rd., Essex, CT 06426
www.theleeco.com

SIZE A | DWG NO. TMDA3201950Z | REV. B4

SCALE: 6:1 | CODE IDENT NO. ONZR4 | SHEET 1 OF 1

EFS_SWAI_10-13-2016

Figure C.5: Specification sheet of the Lee Company's 062 MINSTAC LFA Tubing Adapter [2].

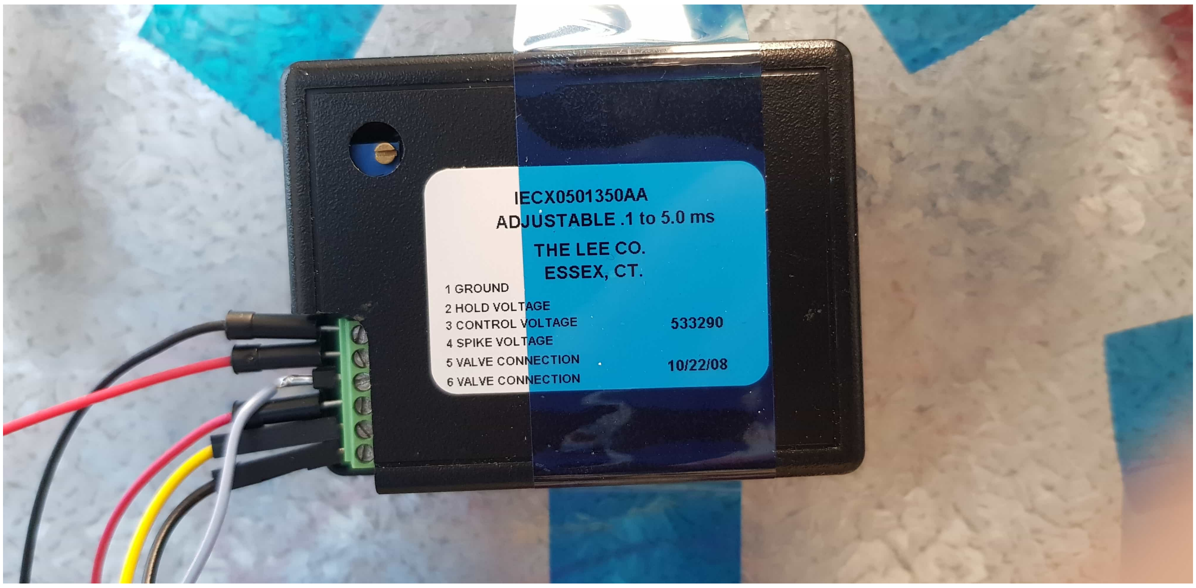

Figure C.6: The Lee Company's Spike & Hold Driver as used in the set-up of the thrust bench test.

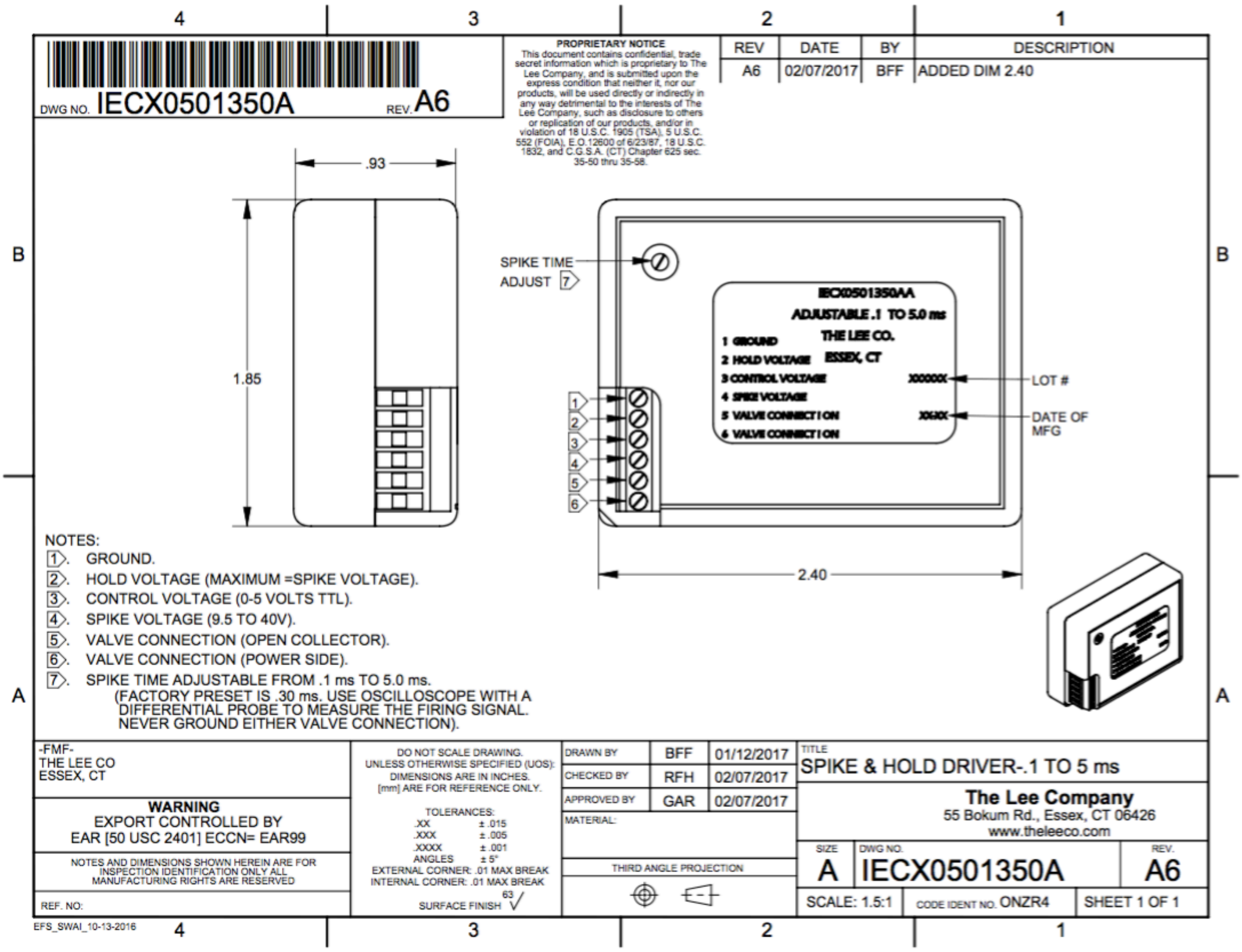

PROPRIETARY NOTICE
This document contains confidential, trade secret information which is proprietary to The Lee Company, and is submitted upon the express condition that neither it, nor our products, will be used directly or indirectly in any way detrimental to the interests of The Lee Company, such as disclosure to others or replication of our products, and/or in violation of 18 U.S.C. 1905 (TSA), 5 U.S.C. 552 (FOIA), E.O.12600 of 6/23/87, 18 U.S.C. 1832, and C.G.S.A. (CT) Chapter 625 sec. 35-50 thru 35-58.

REV	DATE	BY	DESCRIPTION
A6	02/07/2017	BFF	ADDED DIM 2.40

NOTES:
1. GROUND.
2. HOLD VOLTAGE (MAXIMUM =SPIKE VOLTAGE).
3. CONTROL VOLTAGE (0-5 VOLTS TTL).
4. SPIKE VOLTAGE (9.5 TO 40V).
5. VALVE CONNECTION (OPEN COLLECTOR).
6. VALVE CONNECTION (POWER SIDE).
7. SPIKE TIME ADJUSTABLE FROM .1 ms TO 5.0 ms.
(FACTORY PRESET IS .30 ms. USE OSCILLOSCOPE WITH A DIFFERENTIAL PROBE TO MEASURE THE FIRING SIGNAL. NEVER GROUND EITHER VALVE CONNECTION).

-FMF-
THE LEE CO
ESSEX, CT

WARNING
EXPORT CONTROLLED BY
EAR [50 USC 2401] ECCN= EAR99

NOTES AND DIMENSIONS SHOWN HEREIN ARE FOR INSPECTION IDENTIFICATION ONLY ALL MANUFACTURING RIGHTS ARE RESERVED

REF. NO:

DO NOT SCALE DRAWING.
UNLESS OTHERWISE SPECIFIED (UOS):
DIMENSIONS ARE IN INCHES.
[mm] ARE FOR REFERENCE ONLY.

TOLERANCES:

.XX	± .015
.XXX	± .005
.XXXX	± .001
ANGLES	± 5°

EXTERNAL CORNER: .01 MAX BREAK
INTERNAL CORNER: .01 MAX BREAK
SURFACE FINISH 63

DRAWN BY	BFF	01/12/2017
CHECKED BY	RFH	02/07/2017
APPROVED BY	GAR	02/07/2017

MATERIAL:

THIRD ANGLE PROJECTION

TITLE
SPIKE & HOLD DRIVER-.1 TO 5 ms

The Lee Company
55 Bokum Rd., Essex, CT 06426
www.theleeco.com

SIZE A
DWG NO. IECX0501350A
REV. A6
SCALE: 1.5:1
CODE IDENT NO. ONZR4
SHEET 1 OF 1

EFS_SWAI_10-13-2016

Figure C.7: Specification sheet of the Lee Company's Spike & Hold Driver [2].

Bibliography

[1] Electro-fluidic systems handbook, (The Lee Company, 2013).

[2] The Lee Company, `https://www.theleeco.com/products/`, Last time accessed: 2018-10-10.

D

Devices Connected To The Computer

In this appendix information is given about the nitrogen thrust bench test with the 3rd gen. MEMS-VLM chip regarding all the devices that were connected to the computer in the cleanroom. A flowchart about the cleanroom computer and the devices can be found in Figure D.1. It can be seen that the flowchart consists of: the cleanroom computer (blue), Data Acquisition System (DAQ) devices (green), miscellaneous objects (yellow), Power Supply Unit (PSU) devices (purple) and controllers/sensors (orange).

Starting off with the USB hub, this was connected to the following DAQ devices: NI USB-9162 + NI 9211, NI USB-6008 and NI USB-8451. The NI USB-9162 + NI 9211, which is presented in Figure D.2, was able to connect to thermocouples for temperature measurements. Although, this was not used for the nitrogen thrust bench test. As for the NI USB-6008 and NI USB-8451, which are presented in Figures D.3-D.5, these devices were able to connect to the MS5837-30BA sensor and a liquid mass flow sensor. The MS5837-30BA sensor was used to determine the chamber pressure and temperature of the MEMS-VLM chip. The liquid mass flow sensor was not used, but it will be needed when using liquid water as propellant.

As for the NI PCI-6229, this DAQ device was integrated inside the cleanroom computer and a pin specification can be found in Figure D.6. The device was connected with two thick 68-pin cables (see Figure D.7) to two NI CB-68LP breakout boards. One breakout board was connected to a new Printed Circuit Board (PCB) that was again connected to the Brooks 5850S. Note that the Brooks 5850S was used to measure the nitrogen gas mass flow through the MEMS-VLM chip. The other breakout board was connected to the SM7020 PSU, the SM7020-D PSU and the Spike & Hold Driver. The SM7020 PSU could be used to provide power to the heaters of the MEMS-VLM chip, which is needed for a thrust bench test in which liquid water propellant is vaporized. Although, for the nitrogen thrust bench test the SM7020 PSU was not used. The SM7020-D PSU on the other hand, was needed for the test as it was used to power the Varying Turn-Density Coil (VTDC) actuator, which was utilized to calibrate the AE-TB-5m (pendulum) thrust bench in order to obtain thrust measurements. As for the Spike & Hold Driver, this was used together with the Delta Elektronika E 031-1 PSU and D 030-1 PSU to control the solenoid valve, which functioned as a gate between the (nitrogen) propellant feed system and the inlet of the MEMS-VLM chip.

Finally, the DT6220/DL6230 DAQ device (see Figure D.8) was needed as its function is specifically to process the displacement data of the CS2 sensor. This sensor measured the displacement of the pendulum arm of the AE-TB-5m from which the produced thrust force of the MEMS-V:M chip was determined.

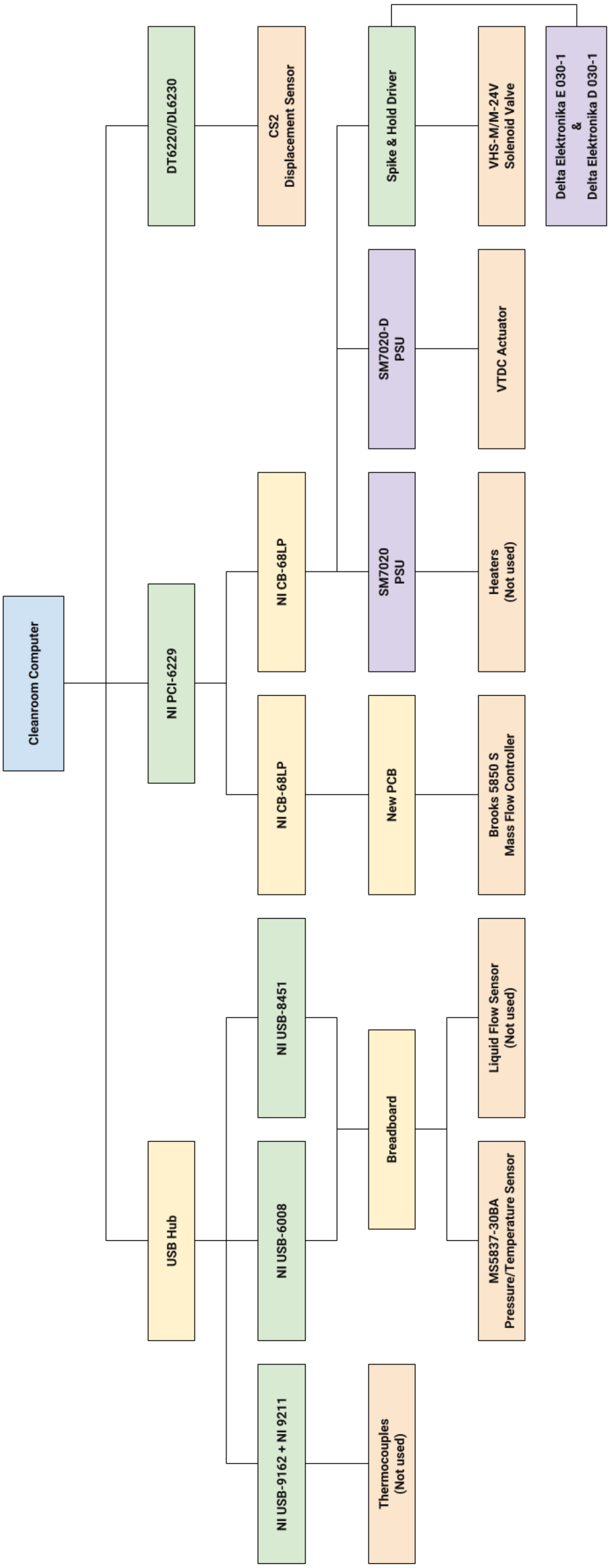

Figure D.1: Flowchart of all the connections with the cleanroom computer with different colors indicating different types of devices: blue indicates that it is the cleanroom computer, green stands for DAQ, orange means that it is either a sensor or a controller, purple indicates that it is a PSU and yellow boxes are miscellaneous objects.

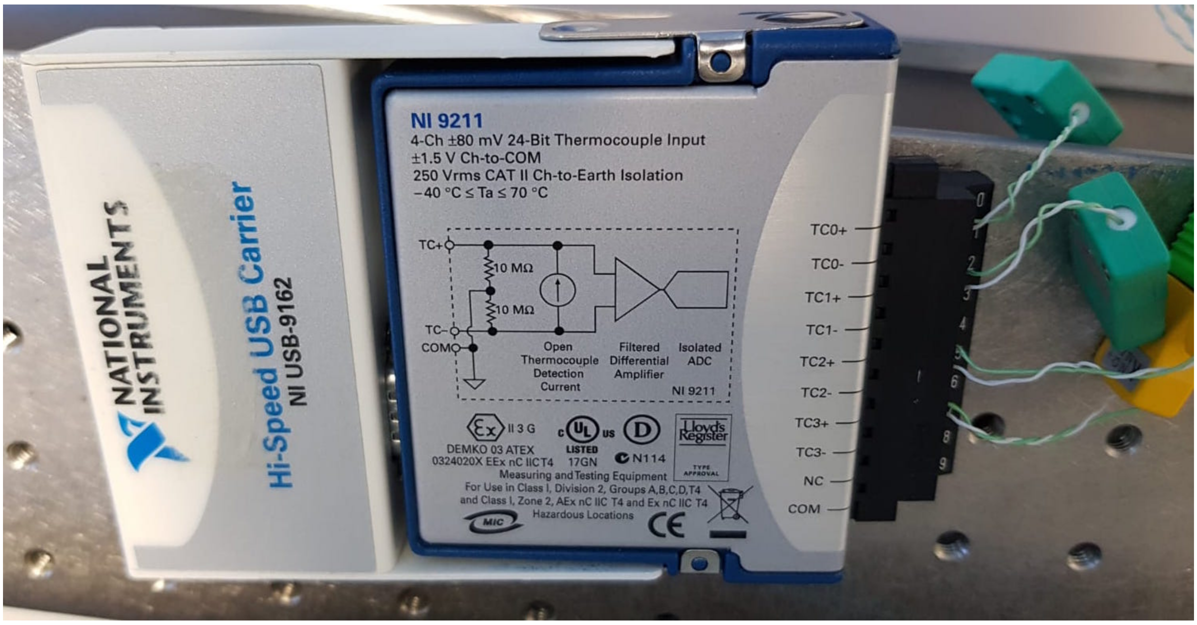

Figure D.2: The NI 9211 integrated with the NI USB-9162.

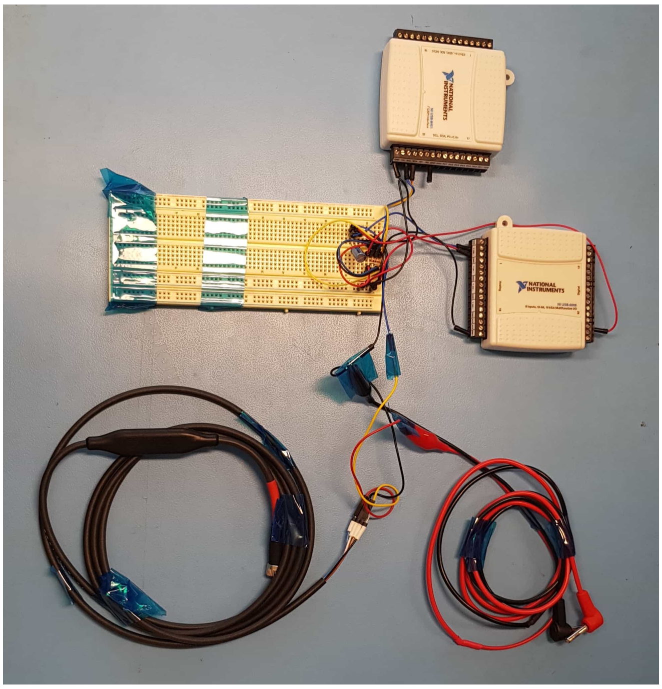

Figure D.3: The breadboard connected to the NI USB-8451 and the NI USB-6008. Note that the black wire at the left can be connected to the (Sensiron) liquid mass sensor for data acquisition. Also, the black and red wires at the right can be used to connect to a power supply for the liquid mass flow sensor.

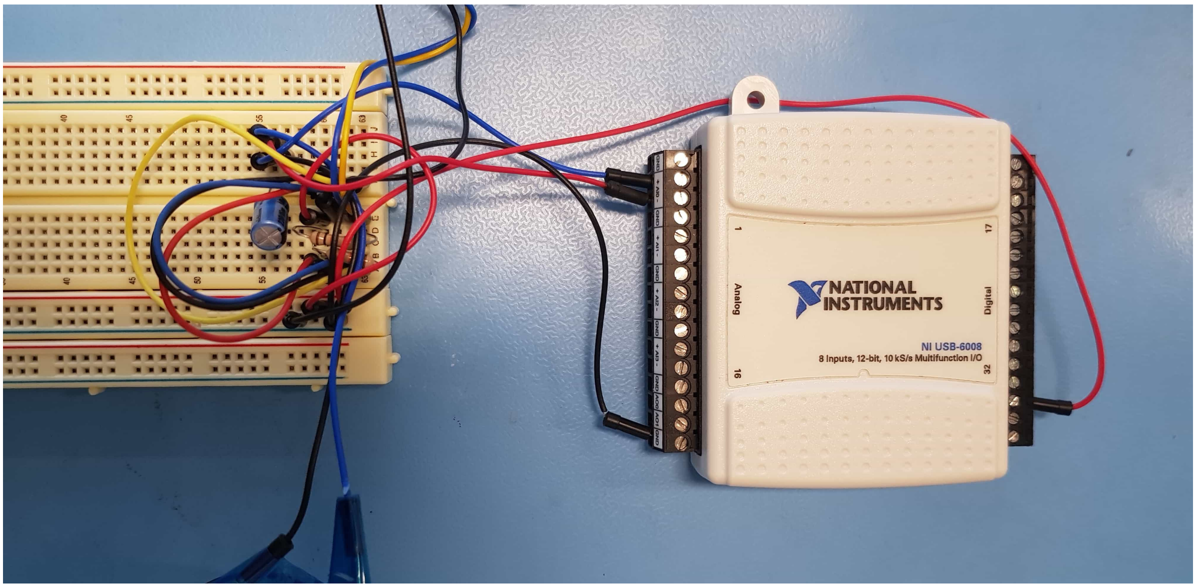

Figure D.4: The NI USB-6008 connected to the breadboard.

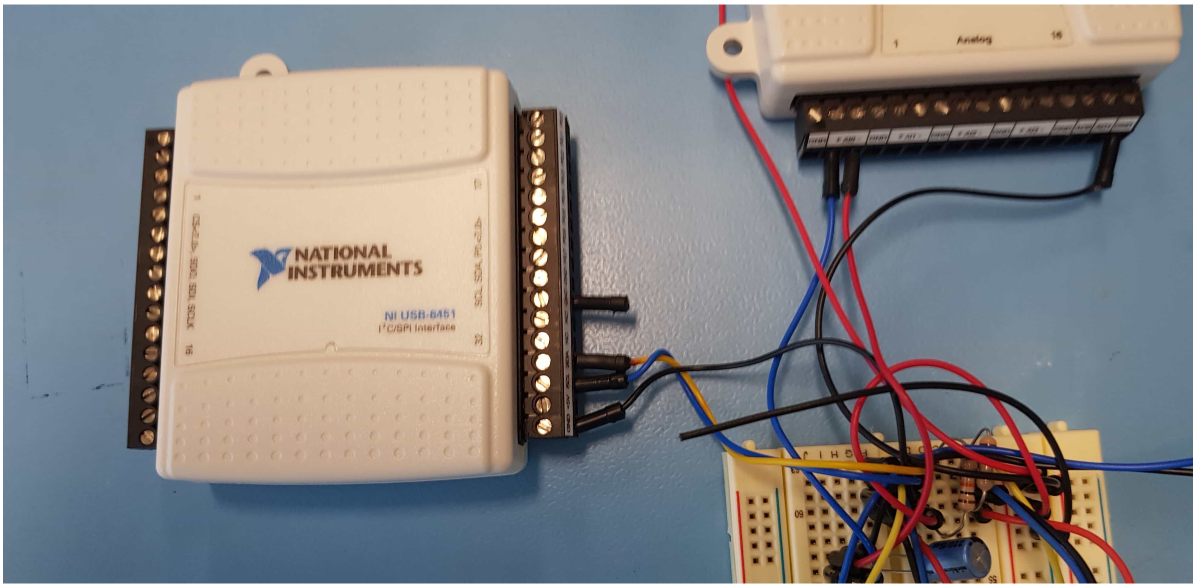

Figure D.5: The NI USB-8451 connected to the breadboard.

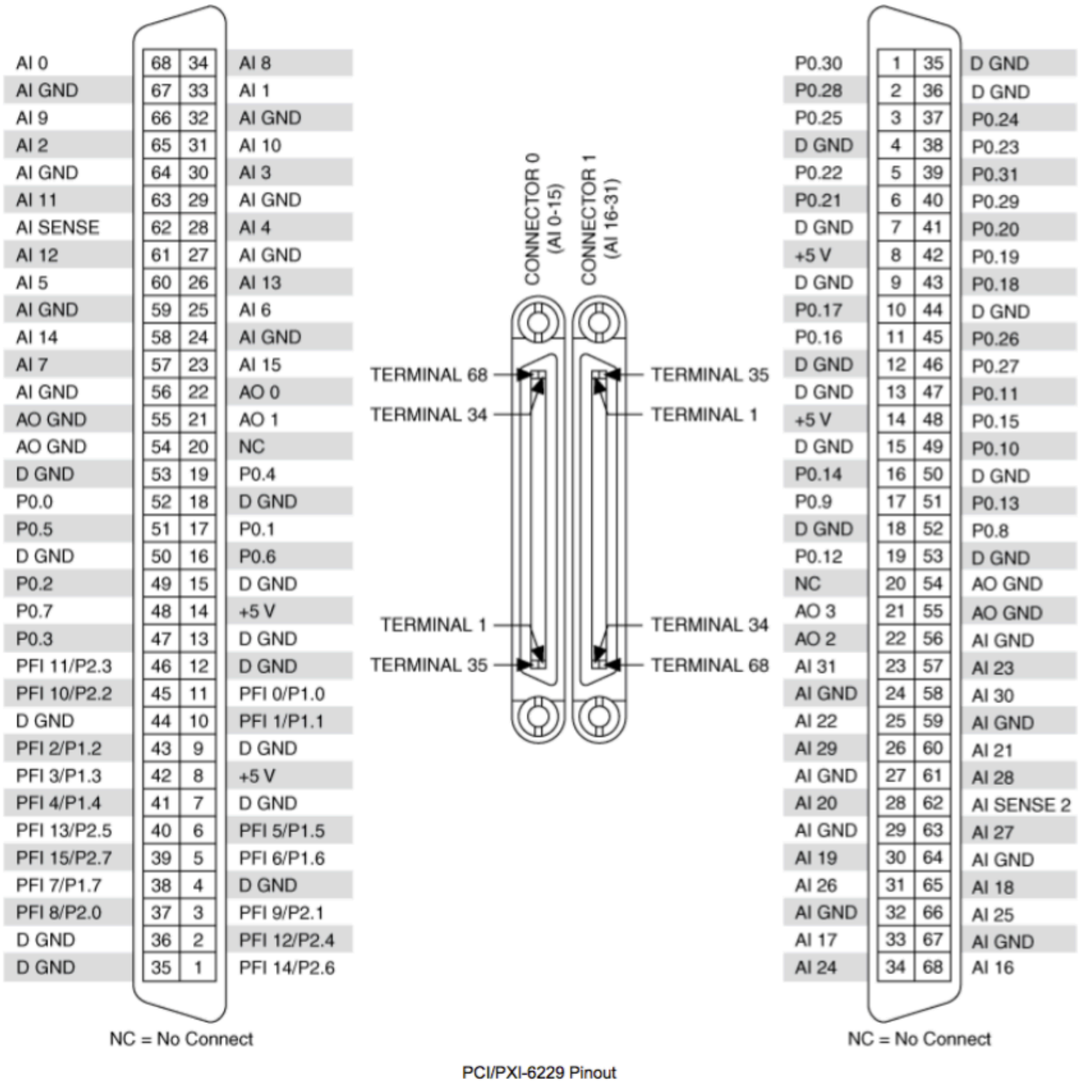

Figure D.6: Pin specification of the PCI-6229 [1].

Figure D.7: The NI PCI-6229 integrated in the cleanroom computer connected to two thick 68-pin cables. Note that the ethernet cable that can be seen here, is the one that is connected to the DT6220/DL6230 DAQ.

Figure D.8: The DT6220/DL6230 DAQ for the displacement data of the CS2 sensor.

Bibliography

[1] Low-Cost M Series Multifunction Data Acquisition - 16-Bit, 250 kS/s, up to 80 Analog Inputs, (National Instruments, 2014).

E

Pendulum Behavior Tests

In this appendix two different behavior tests of the AE-TB-5m pendulum thrust bench are explained. Firstly, three long-time behavior tests are presented in Section E.1, which were performed to investigate different AE-TB-5m configurations on the pendulum arm displacement over a long period. Secondly, an atmosphere-to-vacuum behavior test is presented in Section E.2 which was performed to investigate the influence of the pressure difference between the fluidic tube (propellant feed) and the ambient environment on the pendulum arm displacement.

E.1. Long-period-behavior Test

The behavior of the pendulum arm displacement for a long time (>10 hours) for the three different configurations is presented in Figures E.1-E.3. It can be seen that the displacement changes for all configurations over time, but the displacement behavior and the amount of change in displacement differs for each configuration. It can be concluded that the ”loop” or ”sideways” configuration results in the lowest change in displacement over time compared to the other configurations.

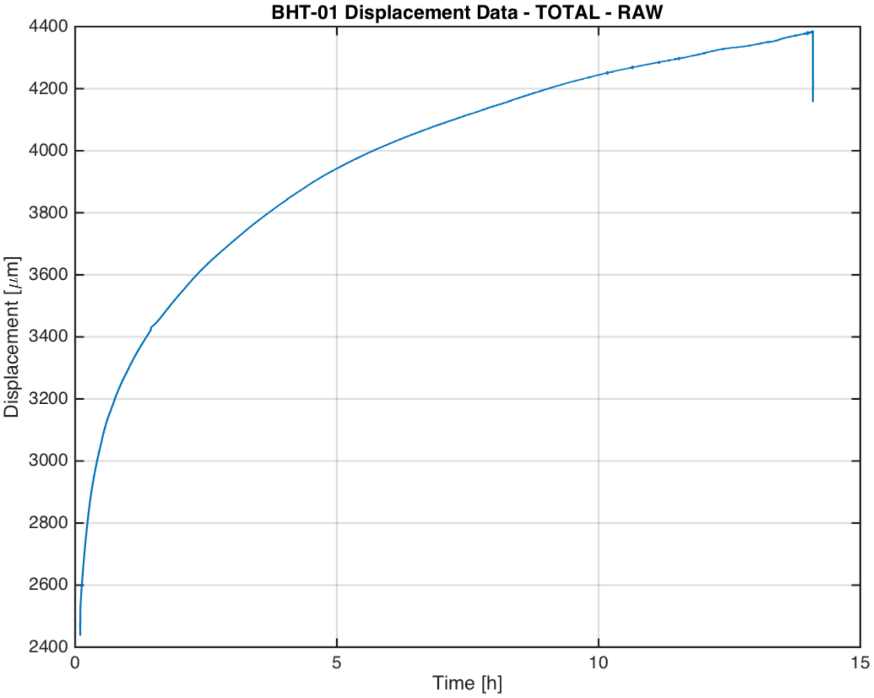

Figure E.1: Long-time behavior test in which the fluidic wires and electrical wires were directly attached to the vacuum chamber ceiling as a 'waterfall' configuration. Also, the vacuum chamber door was closed, but the pressure was kept at standard atmospheric conditions.

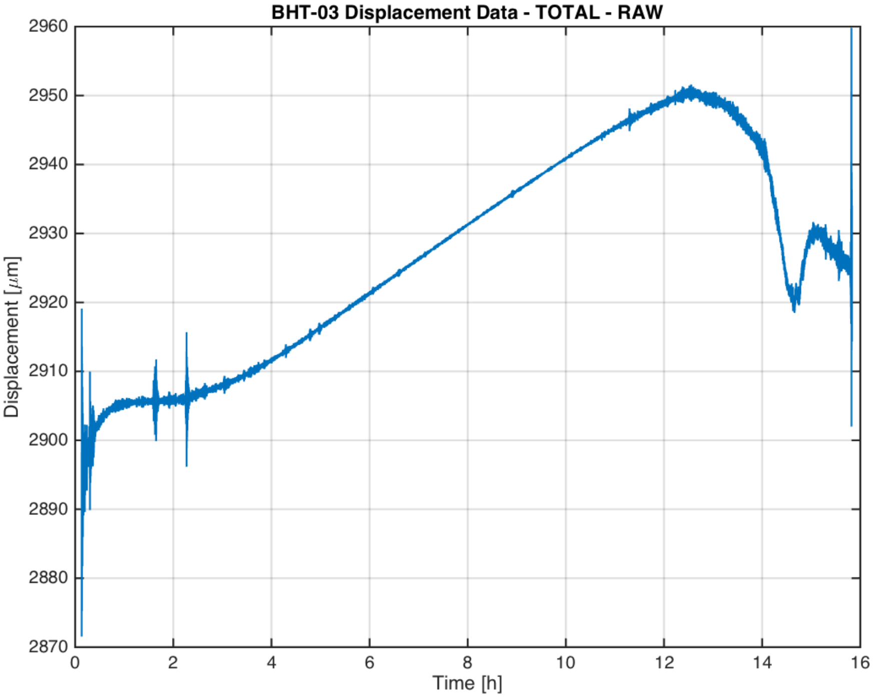

Figure E.2: Long-time behavior test in which the fluidic tube and electrical wires were disconnected from the fluidic and electrical system. In fact, the whole 1st gen. interface including the 3rd gen. MEMS-VLM chip was removed from the test set-up. Again, the vacuum chamber door was closed, but the pressure was kept at standard atmospheric conditions.

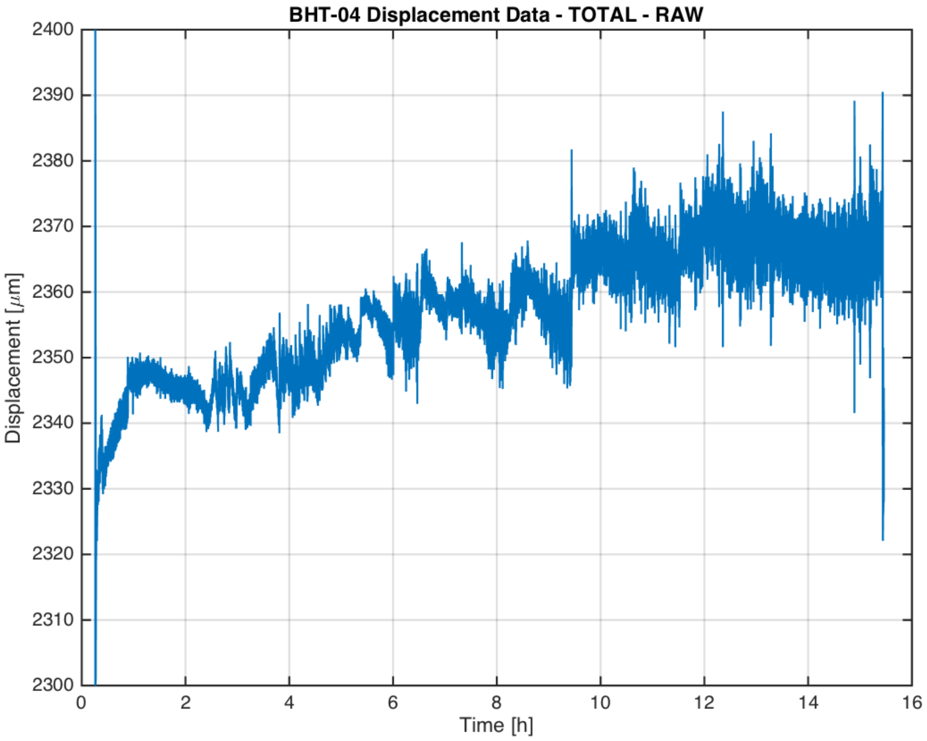

Figure E.3: Long-time behavior test in which the fluidic tube and electrical wires were rotated and taped around the pendulum arm, taped on the pendulum cross-beam and taped to the (Boikon profile) support pillar. Also, the vacuum chamber door was closed, but the pressure was kept at standard atmospheric conditions. Note that due to improper documentation it is uncertain wether the tube and wires made a loop ('loop' configuration) or were connected directly to the support pillar ('sideways' configuration).

E.2. Atmosphere-to-vacuum Test

The behavior of the pendulum arm displacement when going from standard atmosphere to vacuum is presented in Figure E.4. Note that the fluidic wires and electrical wires were in the 'loop' configuration. It can be seen that the ambient pressure decreases from $1[atm]$ to about $80[Pa]$ over, which means that the pressure difference between the fluidic tube and the ambient environment increases. This change in ambient pressure increases the balance point of the pendulum arm: the displacement starts at about $2335[\mu m]$ and it increases up to $2353[\mu m]$ within a period of $300[s]$. This means that a pressure difference of about $1[atm]$ can induce a change of $18[\mu m]$ in the balance point of the pendulum arm displacement. This also indicates that during a thrust phase of the MEMS-VLM chip the pressurization of the fluidic tube could influence the pendulum arm displacement over a long period.

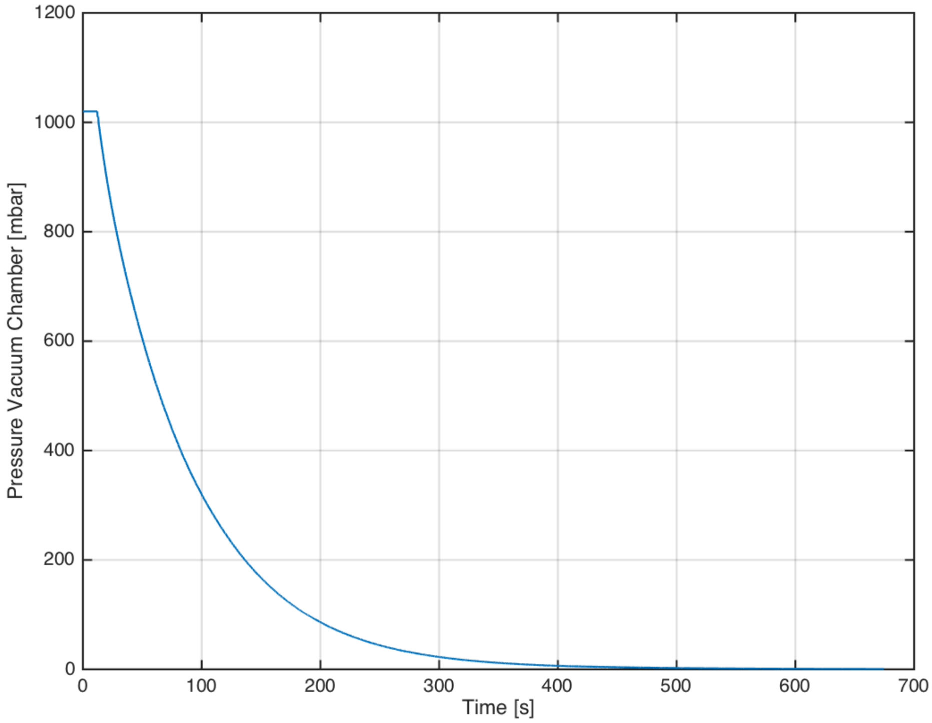

(a) Raw absolute pressure data from the sensor (DCP3000 + VSP3000) in the vacuum chamber, which was obtained during test ATV-01.

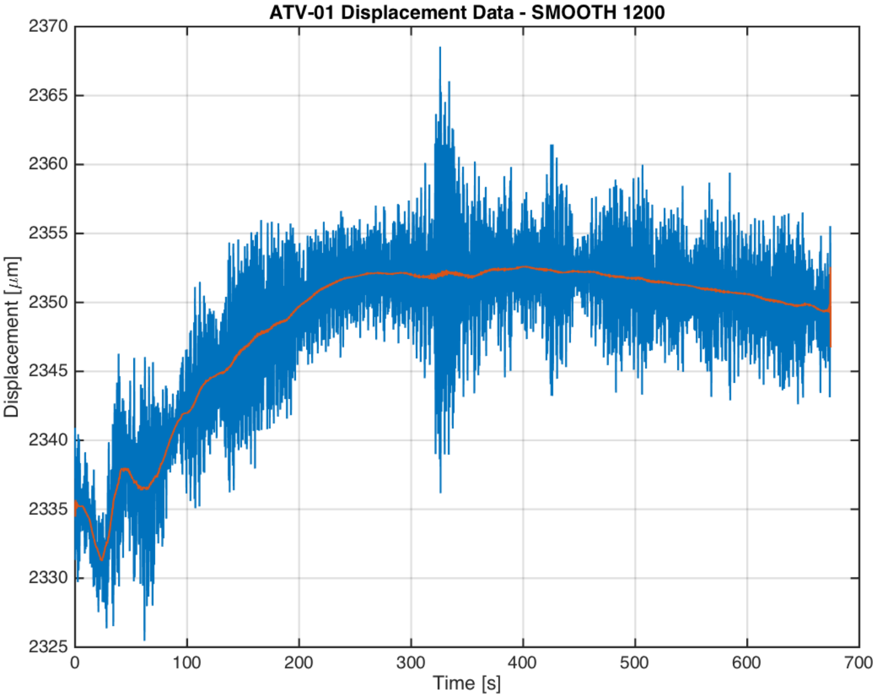

(b) Raw experimental displacement data from the sensor (CS2) in the thrust bench (AE-TB-5m), which was obtained during test ATV-01.

Figure E.4: Atmosphere-to-vacuum test in which the fluidic wires and electrical wires were in the 'loop' configuration.

F

Data Processing

In this appendix an overview is given of different processing methods for the experimental data obtained from the CS2 displacement sensor, which was integrated with the AE-TB-5m pendulum thrust bench. Firstly, in Section F.1 two methods are discussed that were used for removing fluctuations in the displacement data using a AE-TB-5m calibration test (PCT-01) as an example. Hereafter, in Section F.2 it is investigated whether segmentation of the displacement data introduces improvements regarding the thrust levels and the corresponding uncertainties, where the experimental data of a thrust bench test (TT-04) is used as an example.

F.1. 'Filter' versus 'Smooth'

Because the raw displacement data has a lot of fluctuations, data processing is required. Two methods in MATLAB were compared for the displacement data of PCT-01: the function 'filter' (see Figure F.1) and the function 'smooth' (see Figure F.2). It can be seen that the data converted by the 'filter' function does not follow the original raw data from beginning till the end. The 'filter' function suddenly spikes from zero up to the actual displacement level. Also, a time correction was needed as the 'filter' function introduces delays. The 'smooth' function does not have all of these disadvantages, which is why this function was chosen to perform the data processing.

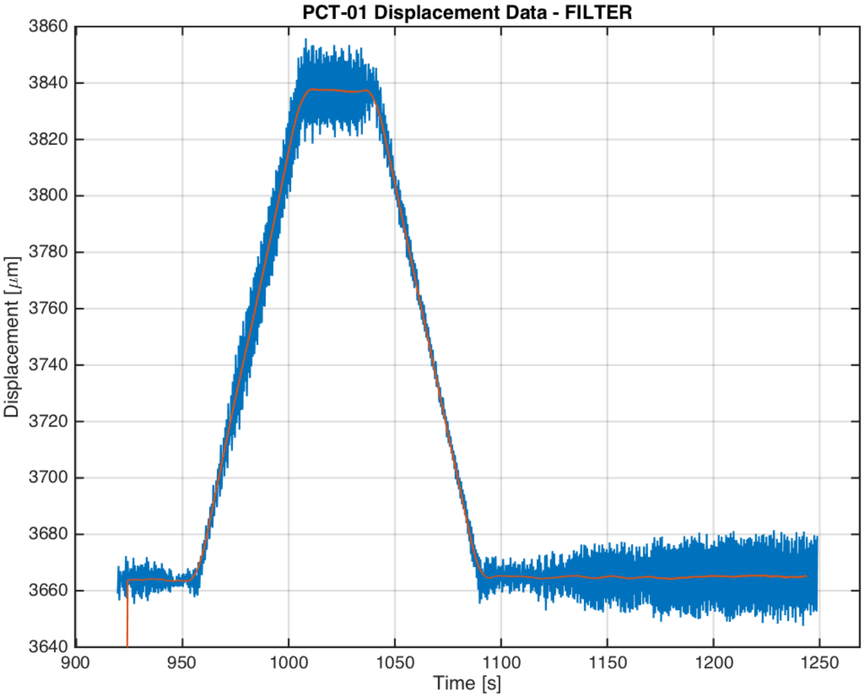

Figure F.1: Data processing of PCT-01 displacement data using the MATLAB function 'filter' and correcting for time delay

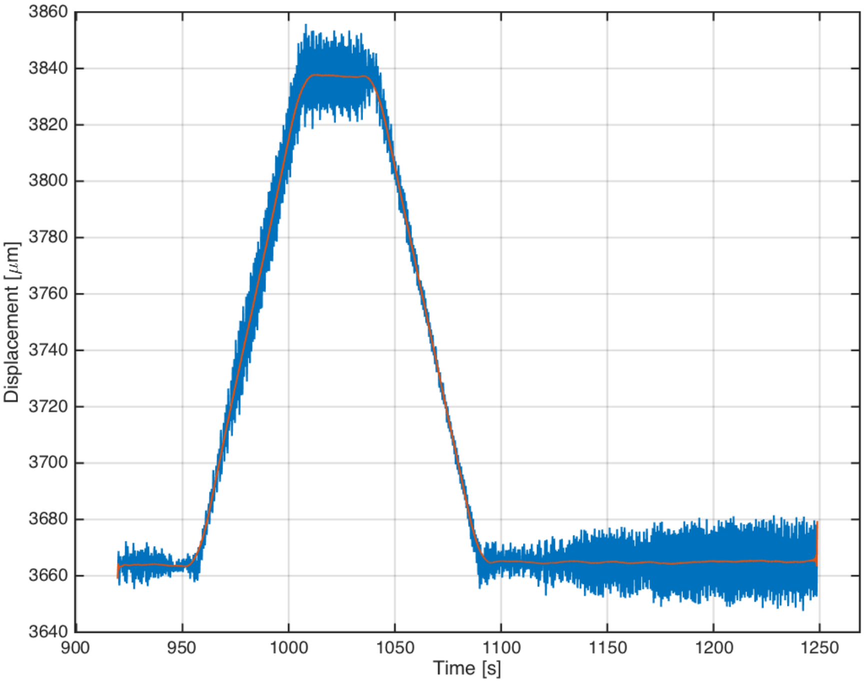

Figure F.2: Data processing of PCT-01 displacement data using the MATLAB function 'smooth'.

F.2. Segmented versus Complete Data Set.

Another form of data processing was investigated. It can be seen in Figure F.3 that the smoothed data does not completely follow the raw experimental data during the four thrust phases. It was therefore investigated whether segmenting the data (cutting the displacement data during the thrust phases) had a significant impact on the obtained thrust values and the corresponding uncertainty. In Figure F.4 the experimental data of the third thrust phase is presented, which is the thrust phase in Figure F.3 that is between the dotted circles. It can be seen that the smoothed data here does follow the original experimental data from the beginning until the end. The average of the smoothed data was taken between $328[s]$ and $359[s]$, which was done because the displacement was only considered stable between this range as the change in displacement was not more than $1.0[\mu m]$. The resulting average displacement, thrust force, standard error of the mean ($\delta_{SEM-X_{disp}}$) and the corresponding relative uncertainty ($\epsilon_{SEM-X_{disp}}$) are presented in Table F.1. It can be seen that the average displacement for both cases is the same, which means that the thrust force is also the same. As for $\delta_{SEM-X_{disp}}$ and $\epsilon_{SEM-X_{disp}}$, these values are small and the difference between the two cases is negligible. This is because the effect of $\epsilon_{SEM-X_{disp}}$ on the thrust force is also negligible: for the complete data this results in a thrust uncertainty of $\pm 4.6e-5[mN]$ and for the segmented data $\pm 3.7e-5[mN]$. Thus, for this case it can be concluded that segmentation of this thrust phase is not required as its effect is negligible. Since for the other thrust phases the difference between the raw data and smoothed data is about the same, it was assumed that effect of segmentation is also negligible for these phases.

Table F.1: Data processing of the third thrust phase of TT-04, where the segmented data is compared with the complete data. The average displacement, standard deviation and the corresponding total uncertainty in the thrust force are presented for both cases.

Data Type	X_{disp} $[\mu\mathrm{m}]$	$(F)_{exp}$ [mN]	$\delta_{SEM-X_{disp}}$ $[\mu\mathrm{m}]$	$\epsilon_{SEM-X_{disp}}$ [%]
Complete data	2410.0	0.4529	± 4.6e-3	± 8.1e-5
Segmented data	2410.0	0.4529	± 5.6e-3	± 9.9e-5

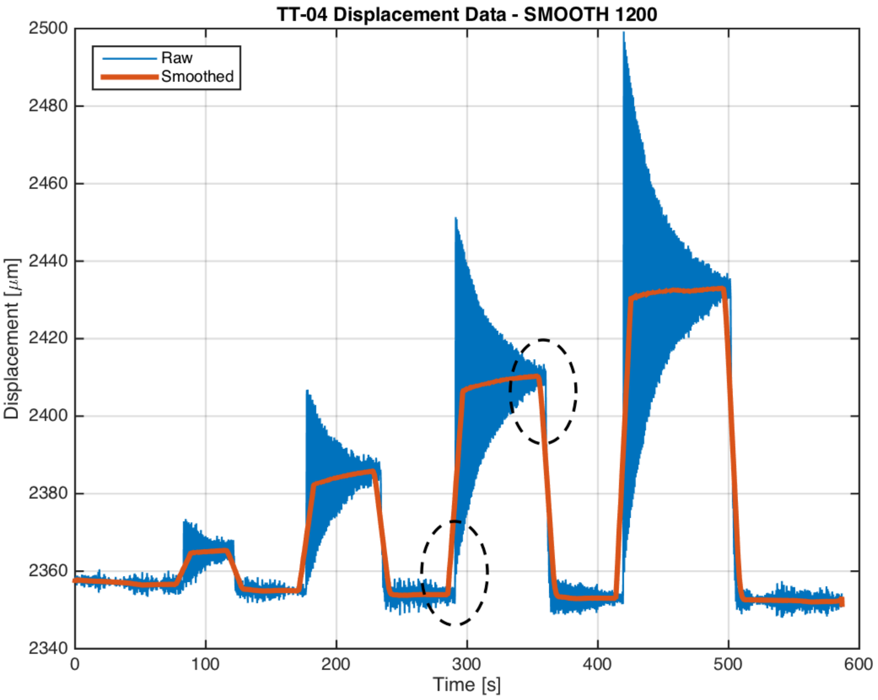

Figure F.3: Raw experimental displacement data during thrust test TT-04 with the filtered/smoothed superimposed, which was obtained with the function 'smooth' using a span of 1200 in MATLAB, where the dotted circles indicate locations were misalignments occur.

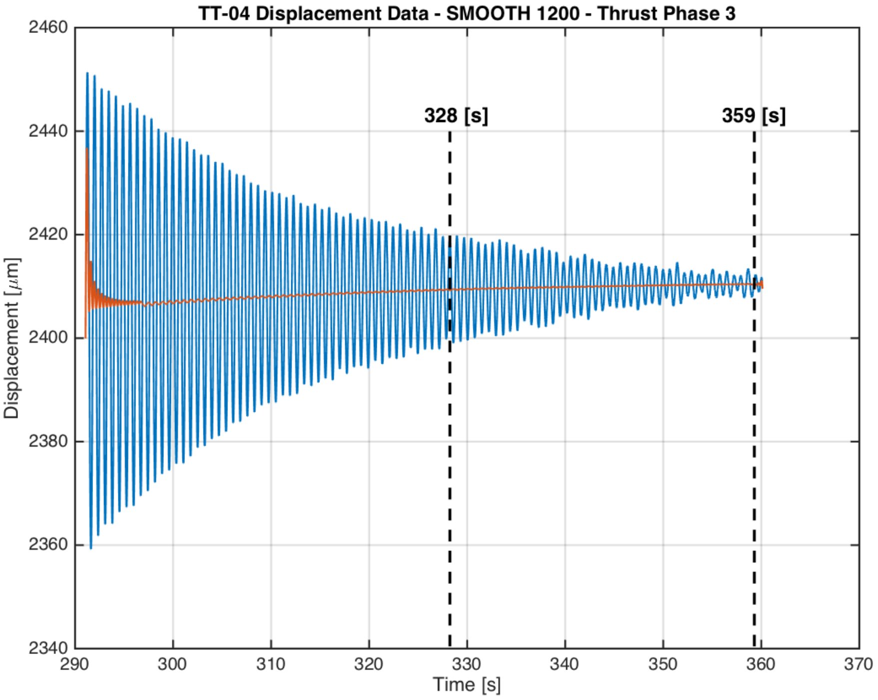

Figure F.4: Third thrust phase extracted from the complete data set of TT-04. The smooth function (with a span 1200) was applied and it can be seen that the smoothed data follows the raw data from the beginning until the end.

G

Additional Data - TT-05

In this appendix the raw experimental data of thrust bench test ”TT-05” is plotted in Figures G.1-G.5. This includes data about the vacuum chamber pressure (controlled variable), the interface temperature (uncontrolled variable), the interface pressure (controlled variable), the volumetric flow rate (dependent variable) and the displacement (dependent variable). Note that the purpose of the test is to determine the nozzle performance of the 3rd gen. MEMS-VLM chip using the measurement data.

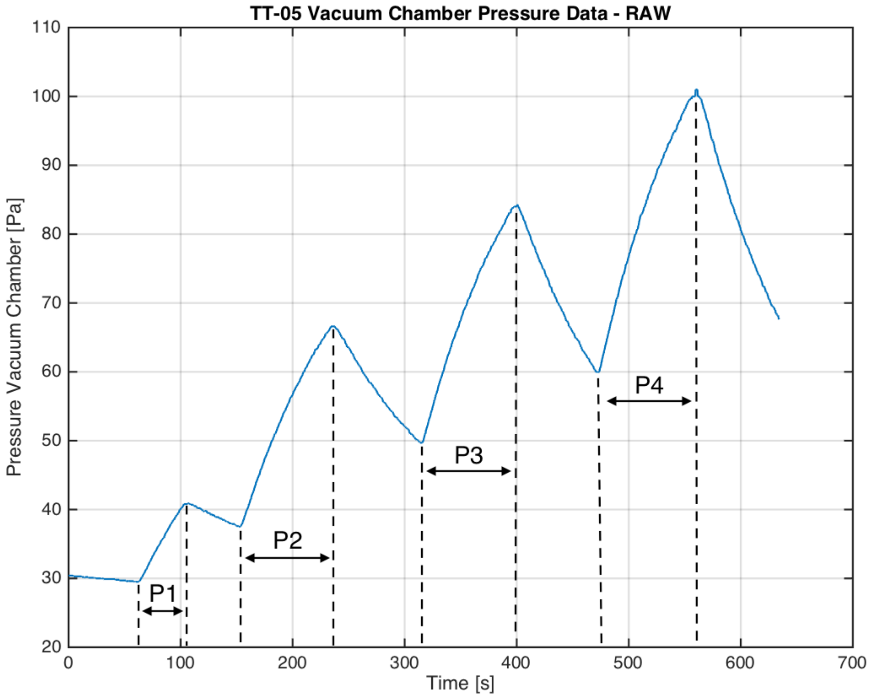

Figure G.1: Raw absolute pressure data from the sensor (DCP3000 + VSP3000) in the vacuum chamber, which was obtained during thrust test TT-05. Note that p1 up to p4 correspond to the four (thrust) phases of the test.

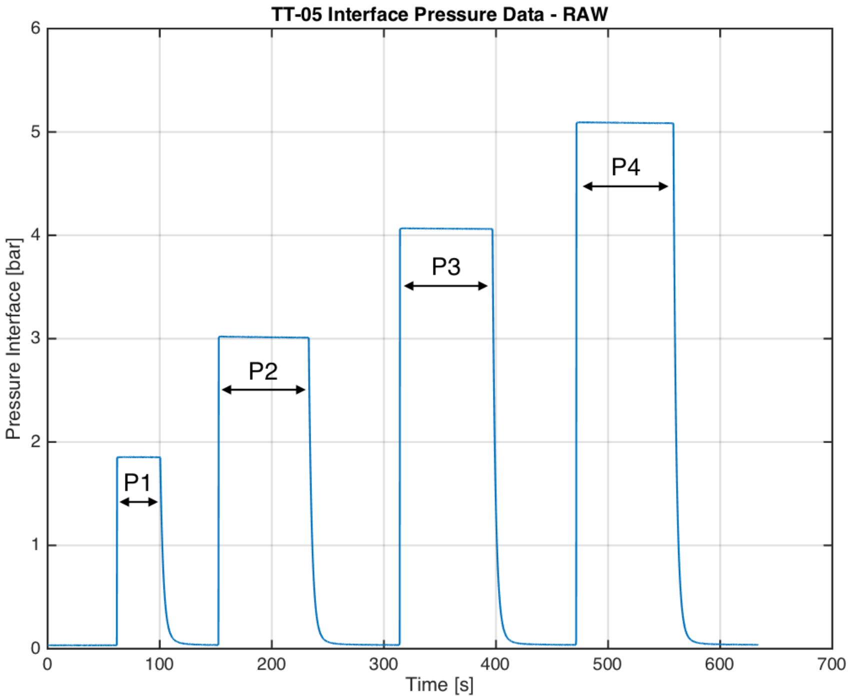

Figure G.2: Raw absolute pressure data from the sensor (MS5837-30BA) in the 1st gen. interface, which was obtained during thrust test TT-05. Note that p1 up to p4 correspond to the four (thrust) phases of the test.

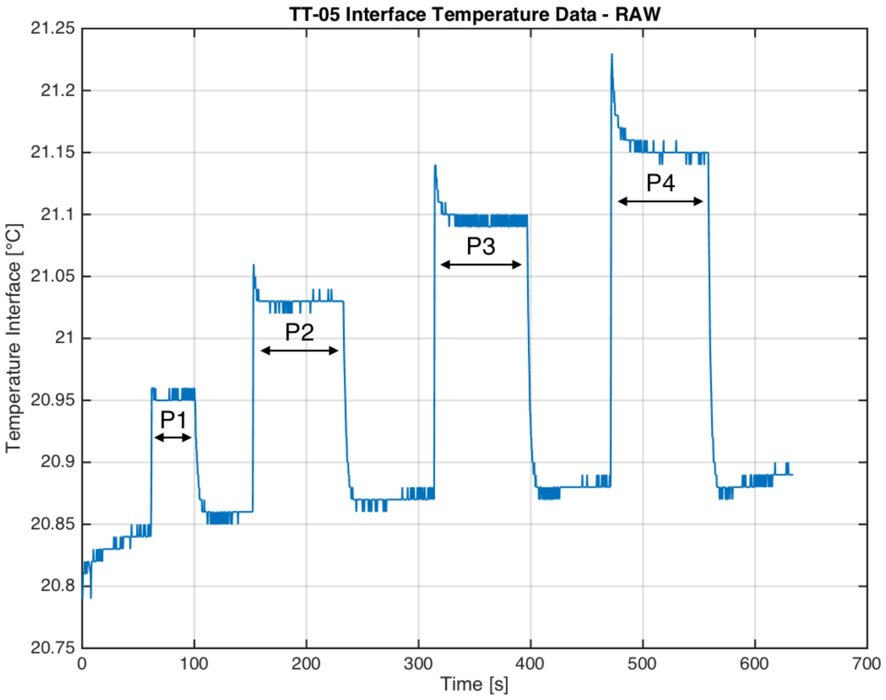

Figure G.3: Raw experimental temperature data from the sensor (MS5837-30BA) in the 1st gen. interface, which was obtained during thrust test TT-05.Note that p1 up to p4 correspond to the four (thrust) phases of the test.

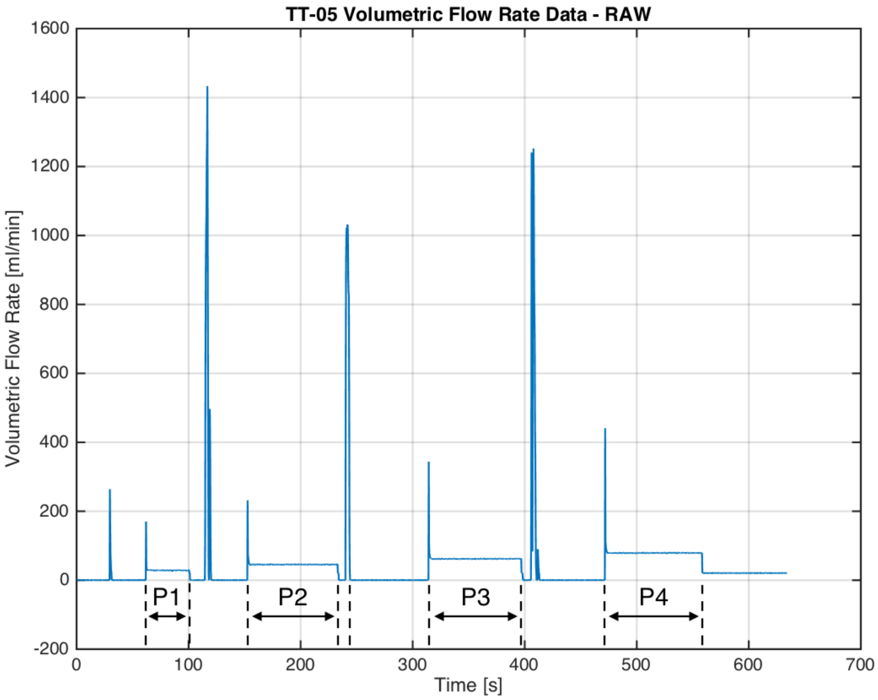

Figure G.4: Raw experimental volumetric flow rate data from the sensor (Brooks SLA5850) in the feed system, which was obtained during thrust test TT-05.Note that p1 up to p4 correspond to the four (thrust) phases of the test.

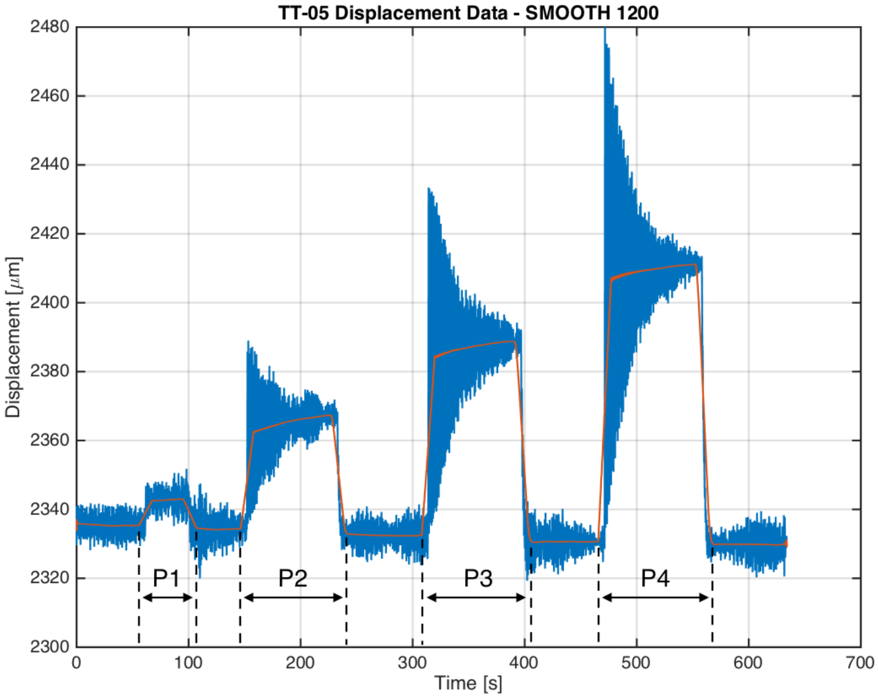

Figure G.5: Raw experimental displacement data from the sensor (CS2) in the AE-TB-5m thrust bench obtained during thrust test TT-05 with the filtered/smoothed superimposed, which was obtained with the function 'smooth' using a span of 1200 in MATLAB. Note that p1 up to p4 correspond to the four (thrust) phases of the test.

H

Previous Optical Characterization Test

In this appendix data of the (previous) optical characterization test is presented, which was performed with the VHX-2000E Digital Microscope. The lens of microscope was able to magnify between 100x-1000x. The purpose of the test was to characterize the geometry of the ”01-Ws2-01” MEMS-VLM chip and an example of a microscopic image can be found in Figure H.1. Note that this chip was not used for gaseous nitrogen thrust bench test as the interface for this chip caused leakage of the N2. This is because it was deformed due to the high temperatures it experienced during water vaporization tests. The new interface that was manufactured was only suitable for the long MEMS-VLM chips and not the short ”01-Ws2-01” chip. Hence, no N2 thrust bench tests were done with this chip. However, the optical characterization test still holds valuable information.

The test results of the parameters can be found in the second and third column of Table H.1. For most parameters multiple measurements were done using the software tools of VHX-2000E Digital Microscope in order to determine the error. That is why the average and standard deviation of the measurements are presented in the second column of Table H.1. The magnification is also included if the measurements were done at the same magnification.

For some parameters it was possible to count the amount of pixels (see third column of Table H.1), which could provide more accurate results than using the software tools of the digital microscope as these include human errors. An example of this can be found when comparing the measurements of the nozzle throat width, which were determined using Figures H.2 and H.3, where the throat width is likely 1 $[\mu m]$ smaller when using the pixel counting method. The method was carried out with the help of the standard Preview app of macOS, where the pixels (both in X and Y direction) could easily and precisely be counted by selecting a rectangular area. First the number of pixels of the reference scale was counted in order to calculate the length of one pixel. Hereafter, the number of pixels of the parameters were counted in order to determine their metric values. This method is called the ”Pixel Counting Method” as written in the third column of the table. The measurement uncertainty for each parameter was determined by counting the amount of pixels of the borderlines.

The fourth column of Table H.1 contains the designed values for the nozzle parameters. The designed values are based on [1]. In the last column the percentage difference between the designed and measured values is presented. Note that because the ”Pixel Counting Method” (third column) is more accurate, its value was compared to the designed value instead of the ”Average Measurement” (second column).

A few important points can be noticed when looking at Table H.1. The percentage difference between the designed parameters and the measurements of the manufactured parameters is in most cases small, except for the nozzle throat width (W_t). Since the difference in the throat width has a huge impact on the thrust performance, the precision of the manufacturing process needs to be improved. Furthermore, the digital microscope was not able to perform measurements inside the nozzle due to a lack of illumination. For this reason it was too dark to perform measurements for: t_{nd}, t_t, A_t and A_e.

Table H.1: Test results of the optical characterization test for the nozzle parameters, where: "R" stand for the angle between the divergent and convergent section of the nozzle, "L" stands for the length, "W" stands for the width, "t" stands for the depth/thickness, "A" stands for the area and "θ_{nd}" stands for the nozzle divergence half angle. As for the subscripts: "nc" stands for the nozzle convergent section, "nd" stands for the nozzle divergent section, "t" stands for the nozzle throat, "e" stands for the nozzle exit, "upper" stands for the upper part and "lower" stands for the lower part.

Parameters: Nozzle	**Average Measurement ± Standard Deviation**	**Pixel Counting Method ± Uncertainty**	**Designed Value**	**Difference**
$R^*_{1(upper)}$	104.3 ± 0.6 [°]	N/A	106.32 [°]	1.9%
$R^*_{2(lower)}$	104.3 ± 0.6 [°]	N/A	106.32 [°]	1.9%
L_{nc}	1480 ± 3 [μm] (100x magnification)	N/A	1500 [μm]	1.3%
W_{nc}	2950 ± 22 [μm] (100x magnification)	N/A	3000 [μm]	1.7%
L_{nd}	647.9 ± 2.8 [μm]	N/A	660 [μm]	1.9%
W_{nd}	776.6 ± 3.4 [μm]	757.53 ± 4.79 [μm] (300x magnification)	780 [μm]	2.9%
$\theta_{nd_1(upper)}$	30.5 ± 0.3 [°]	N/A	29.11 [°]	4.7%
$\theta_{nd_2(lower)}$	30.5 ± 0.3 [°]	N/A	29.11 [°]	4.7%
W_t	20.0 ± 0.4 [μm] (1000x magnification)	19.0 ± 1.4 [μm] (1000x magnification)	45 [μm]	81.3%
t_t,t_{nd}	*Too dark to perform measurement!*		100 [μm]	-
A_t	*Too dark to perform measurement!*		4500 [μm^2]	-
A_e	*Too dark to perform measurement!*		78000 [μm^2]	-

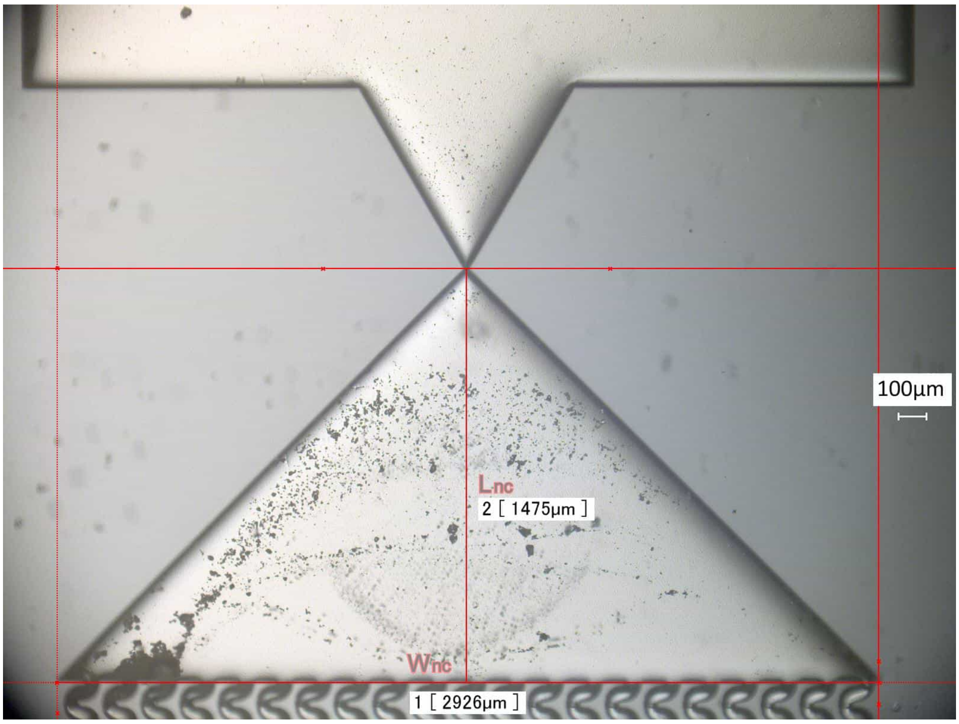

Figure H.1: Nozzle at a magnification of 100x. Data used for: L_{nc} and W_{nc}.

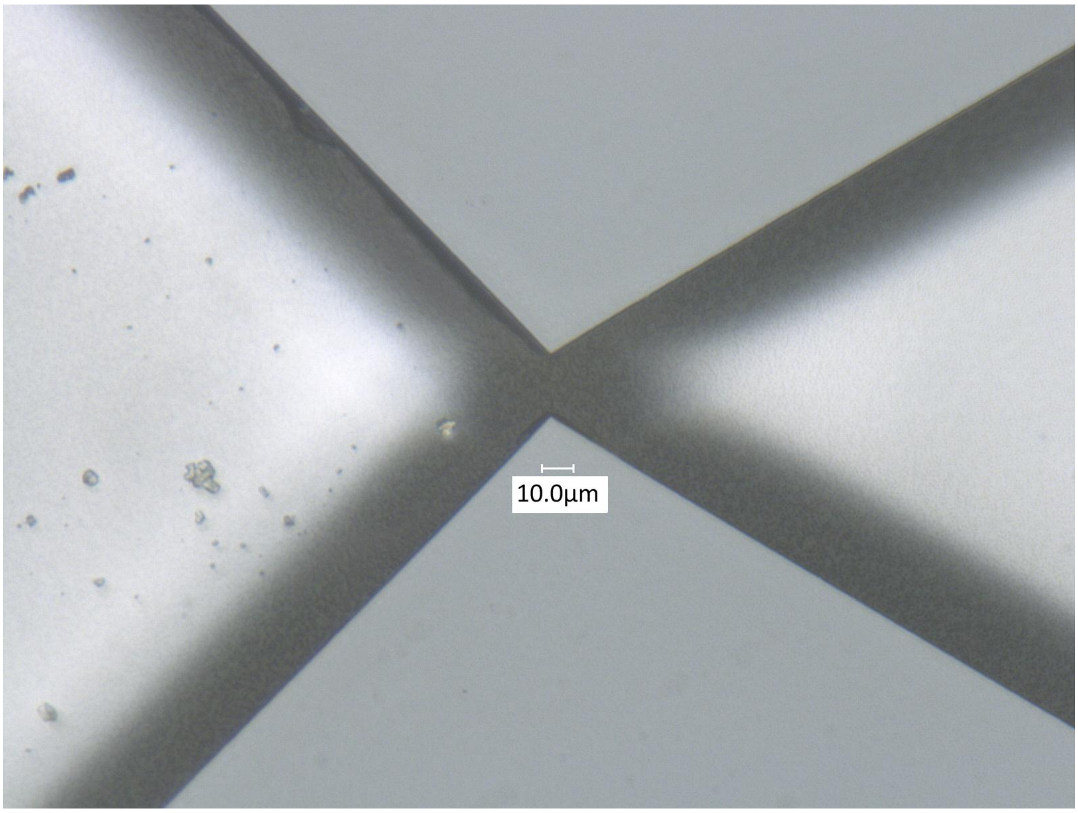

Figure H.2: Nozzle throat at a magnification of 1000x. Used for pixel counting method to determine W_t. The reference scale of 10 μm consists of 50 pixels.

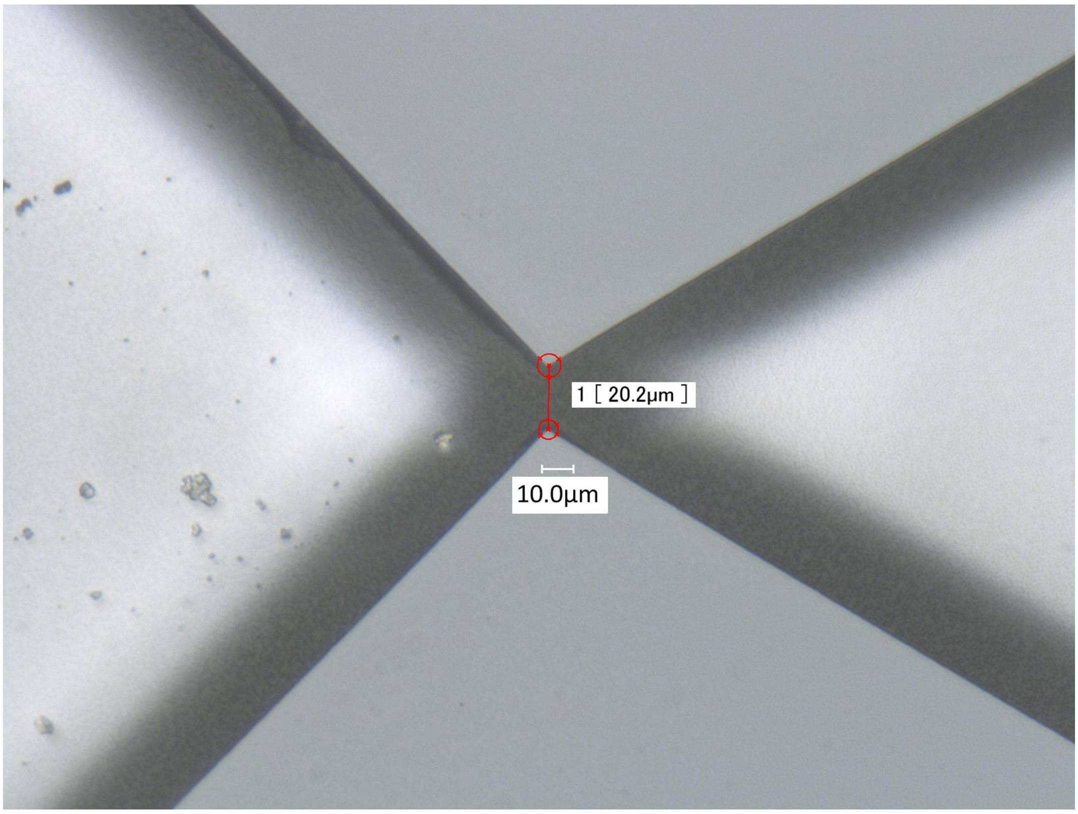

Figure H.3: Nozzle throat at a magnification of 1000x. Data used for: W_t.

Bibliography

[1] M. de Athayde Costa e Silva, D. Cordeiro Guerrieri, H. Van Zeijl, A. Cervone, and E. Gill, Vaporizing Liquid Microthrusters with integrated heaters and temperature measurement, Sensors and Actuators A: Physical (2017).